Search for production of dark matter in association with a Higgs boson decaying to $b\bar{b}$ with the ATLAS detector

M. Baca

Thesis submitted for the degree of
Doctor of Philosophy

Particle Physics Group,
School of Physics and Astronomy,
University of Birmingham.

April 19, 2018

ABSTRACT

Using 3.2 fb^{-1} of $\sqrt{s}$ =13 TeV proton-proton data collected in 2015 with the ATLAS detector at the Large Hadron Collider, new limits were imposed on the associated production of Dark Matter (DM) with a 125 GeV Higgs boson which decays into a pair of b-quarks. The final state of the signal is a pair of b-quark jets and large Missing Transverse Momentum (MET) attributed to the DM escaping the detector. Two theoretical models of the signal were considered in this analysis: a simplified model where the Higgs boson and DM pair originate from a Z' vector intermediate state and a Z'-2HDM model where the intermediate state decays to a 125 GeV Higgs boson and a heavy Higgs boson (denoted as A^0). In the latter, the A^0 decays into the DM candidates.

The dominant backgrounds were simulated. These, along with signal simulations, were subject to selection requirements to increase signal to background ratio. Three regions were designated based on the number of leptons in the event. 0 lepton events made up the signal region. Events with 1 and 2 leptons were control regions. Similar selection requirements were applied to the control regions as in the signal region, in order to examine a similar phase space. Following this, the regions were further divided into MET bins. A blinding region was established in the 0 lepton region over the m_{bb} distribution to mask where a reconstructed 125 GeV Higgs boson would appear. The control regions and the side bands in the signal region were then fit to the m_{bb} data distribution. Unblinding of the signal region did not result in the discovery of the decay channel, but allowed limits to be imposed, which are detailed later in this report.

This thesis also details the work carried out by the author on the radiation hardness testing of silicon sensors for the upgraded ATLAS detector in the High Luminosity LHC (HL-LHC). At the HL-LHC, the entire ATLAS inner detector will be replaced by silicon sensors. The strip sensors will be exposed to a fluence of 1×10^{15} 1

MeV n_{eq} cm^{-2} over 10 years. Radiation hardness tests were performed with sensor prototypes at the University of Birmingham medical cyclotron. The large dosage over a short period of time caused a heating effect which was undesirable, as the resulting annealing of the sensor would lead to misleading results regarding the detector's performance after receiving the desired fluence. This was confirmed by comparing the charge collection of sensors irradiated at Birmingham with those that had been irradiated elsewhere and then undergone a deliberate annealing process. Efforts were made to improve the cooling system of the irradiation setup and the temperature monitoring. Direct measurements of sensor temperature are not possible, as any temperature probe directly attached would also be irradiated. In order to understand the temperature of the sensor, its thermal properties were explored under controlled heating experiments. Following this, a simulation was developed to predict the temperature change of the sensor under certain irradiation conditions. The simulation results informed future irradiations of the optimal beam current and speed at which to move the beam over the sensor sample (0.5 μA at a speed of 4 mm/s).

DECLARATION OF AUTHOR'S CONTRIBUTION

The work outlined here is the result of work from many parties. Specifically those on the analysis team, those who provided feedback and everyone involved in the ATLAS experiment who contributed to the collection of the 2015 dataset.

For my part as a member of the analysis team, I contributed specifically on the development of the resolved region for both the 0 lepton (signal) and 1 lepton (control) regions. I helped develop and implement the selection criteria, for these regions as outlined in Chapter 5. I produced many cut flow plots for these regions and compared them to the results of the same analysis performed by the group focusing on the merged analysis and ensured that results were consistent across all groups. I also produced many of the input files that were later passed into the fitting algorithm in Chapter 6. I performed the trigger efficiency analysis for the MET trigger used in the signal region, which is included at the end of Chapter 2. As part of my contribution, I prepared and delivered the unblinding approval talk on behalf of the analysis team.

I contributed to the collection of data during 2015 by performing a total of 31 shifts (248 hours) working at the Trigger desk in the ATLAS control room, along with the guidance and support of the trigger experts.

In the radiation hardness tests for the HL-LHC upgrade, I ran a significant number of the irradiations performed in 2013-2014 at the University of Birmingham medical cyclotron. I performed extensive measurements of the heating of the sensors and their surroundings and contributed to the understanding of the effects through simulations to predict the change in temperature of a sensor based on beam current, speed of the moving sensor and the initial temperature conditions.

I have made contributions to publications regarding my work in both the monoHiggs analysis (see [1]) and the irradiation of Phase 2 sensor upgrade components (see [2], [3], [4] and [5]). I presented my work in each area on two separate occasions at the annual Institute of Physics conferences and have also presented my Higgs work at the annual ATLAS UK conference.

ACKNOWLEDGEMENTS

First of all I would like to thank my supervisors Kostas Nikolopoulos and Paul Thompson. They have stuck with me, given me significant amounts of their time and offered excellent advice to guide me through my PhD resulting in this thesis. I would also like to thank the others on the analysis team who also offered invaluable help in my work, including most notably Sam Meehan, Andrew Mehta, Rainer Roherig and Carl Gwilliam. Thank you to Nigel Watson and Joost Vossebeld for taking the time to read and critique my thesis during my viva and for their insightful comments.

I'd like to extend thanks to John Wilson, Paul Hodgson, Paul Dervan and Kerry Parker who helped me significantly through the upgrade work in the first year of my PhD.

Most of the fun I've had during my PhD I can attribute to the people I shared an office with over the past 3 and a half years both in Birmingham and at CERN, including (in chronological order) Andy C, Benedict, Richard, Javier, Andrew Daniells, Mark, Rhys, Alasdair, Andy F, Jamés, Tim, Briglin, Kendrick, Elliot, Jack, Russell, Rob and John. Whether it was rescuing Javier from snakes, brewing Danger Juice with Briglin or getting unreasonably angry in political debate with Elliot, the group made office life a lot of fun (more fun than many would likely approve of). I'd also like to thank Champs-Frechet kebabs for making the world a better place.

Lastly I would like to thank and send my love to my family. My parents, Linda and Ian. James and Katie, my brother and sister. My uncle George and my grandmother Beulah, who sadly passed away whilst I was writing this thesis. I thank my friends from across the country, particularly -and alphabetically- Ally, Amber, Danny, Gareth, Gemma, Jerri, Jess, John, Matt, Nik, Perry, Roxy, Ruth, Sam and Sophie for their continued love and support.

‘There is a theory which states that if ever anyone discovers exactly what the Universe is for and why it is here, it will instantly disappear and be replaced by something even more bizarre and inexplicable.’

- Douglas Adams, The Hitchhiker’s Guide to the Galaxy

'There is another theory which states that this has already happened.'

- Douglas Adams, The Hitchhiker's Guide to the Galaxy

Contents

List of Tables

List of Figures

DEFINITIONS OF ACRONYMS

LHC Large Hadron Collider

SM Standard Model

DM Dark Matter

QCD Quantum Chromodynamics

BSM Beyond the Standard Model

BEH Brout-Englert-Higgs

VEV Vacuum Expectation Value

MET Missing Transverse Momentum

ATLAS A Toroidal LHC ApparatuS

CMS Compact Muon Solenoid

LHCb Large Hadron Collider Beauty

ALICE A Large Ion Colliding Experiment

LUX Large Underground Xenon experiment

SURF Sandford Underground Research Facility

ID Inner Detector

ITk Inner Tracker

SCT Semiconductor Tracker

IBL Insertible B-Layer

TRT Transition Radiation Tracker

TR Transition Radiation

HEC Hadronic End Cap

EMEC Electromagnetic End Cap

EM Electromagnetic

LS Long Shutdown

HL-LHC High Luminosity LHC

NIEL Non-Ionizing Energy Loss

MC Monte Carlo

PDF Parton Density Function

NNPDF Neural Network Parton Density Function

ISR Initial State Radiation

FSR Final State Radiation

MPI Multi Parton Interactions

NNLO Next to Next to Leading Order

GRL Good Runs List

JES Jet Energy Scale

NP Nuisance Parameters

MLL Maximised Log-Likelihood value

CHAPTER 1

INTRODUCTION

1.1 Introduction

The mystery surrounding DM is one of the most prevalent problems in modern physics. It is known from observations in the fields of astrophysics and cosmology that DM makes up 26.8% of the universe, compared to 4.9% ordinary matter [24]. However from a particle physics point of view, very little is known about Dark Matter. If such matter does exist, a sufficiently high energy particle collider should be able to produce it. From this, an in-depth study of the properties of such a particle could proceed, shining light on to one of the biggest mysteries faced by physics today.

It is known that DM is electrically neutral. DM self interactions are very weak. Because of this, DM candidates do not interact with any part of the detector. They would manifest themselves as missing transverse energy recoiling against a number of SM particles. The discovery of the Higgs boson [25, 26] opens many new channels for DM production. Many searches were performed in Run 1, summarised in Section 1.8, looking for various Higgs boson decays in association with large MET.

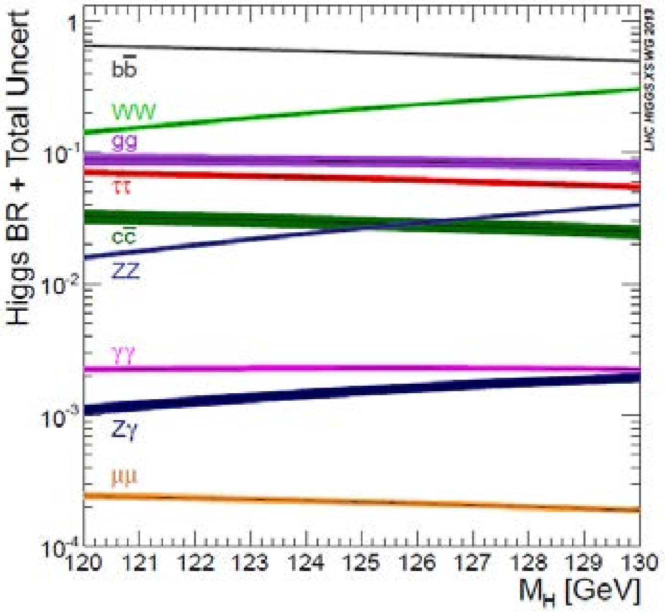

Figure 1.1: The Branching ratios of the main decays of the SM Higgs boson.

Studying a Higgs boson decay produced back to back with other known particles has another advantage over previously performed searches. Initial state radiation of Higgs bosons from quarks are Yukawa suppressed, resulting in the Higgs boson having to be produced in association with the DM candidates at the same vertex. This allows the study of the coupling of DM to SM particles.

The analysis described in this thesis extends and improves over previous searches for associated production of DM with a Higgs boson, where the latter decays into a pair of b-quarks. Higgs boson decay to a pair of b-quarks is the dominant decay channel for the 125 GeV Higgs boson as shown in Figure 1.1. The analysis is performed using 3.2 fb^{-1} of Run 2 data collected during 2015. The data represents proton-proton collisions at $\sqrt{s} = 13$ TeV, a higher centre of mass energy than Run 1.

This is just one of many different studies into the nature of dark matter from a particle physics perspective. Theory predicts a range of different dark matter signatures that could potentially be observed in the LHC. A summary of all LHC efforts searching for dark matter can be found at [27], which considers both effective field theory and simplified approaches to modelling dark matter (see Sections 1.5 and 1.6 respectively). Another report focused more specifically on simplified models can be found at Reference [28].

1.2 The Standard Model of Particle Physics

The SM of particle physics is the most complete picture we have of the fundamental building blocks that make up all matter in the universe. Interactions between the constituent parts of the model are derived via the application of a $SU(3)_C \otimes SU(2)_L \otimes SU(1)_Y$ local gauge symmetry. The SM contains two major types of particles, fermions and bosons. The fermions are point like particles which interact via the strong and electroweak forces. They are split into two categories, quarks and leptons.

The six quarks come in three pairs: up/down, charm/strange and top/bottom. In short notation, they are frequently referred to by the first letter of their names (u, d, c, s, t and b quarks respectively). Up type quarks (u, c, t) carry an EM charge of $+\frac{2}{3}|e|$ and the down type quarks (d, s, b) carry a charge of $-\frac{1}{3}|e|$. The leptons are the electron, the muon, the tau lepton and then the three associated neutrinos (e, μ, τ and $\nu_{e/\mu/\tau}$ respectively). Neutrinos carry no electric charge. The charged leptons carry -1 EM charge. The fermions also have associated anti-matter counterparts with an opposite charge. A summary of all quarks and leptons in the SM can be found in Table 1.1.

The four bosons are the force carriers. These are the photon (the carrier of the EM force), the gluon (the carrier of the strong nuclear force) and the Z and $W^{\pm}$ bosons (the carriers of the weak nuclear force). Where as the photon and gluon are massless, the Z boson has a mass of 91.1876$\pm$0.0021 GeV and the $W^{\pm}$ has a mass of 80.385$\pm$0.015 GeV[6]. In 2012, there was a new addition to the bosons of the SM

- the Higgs boson. The Higgs boson stands aside from the other four as it is a scalar particle, not a vector boson.

One of the key differences between quarks and leptons is that quarks carry colour charge, whereas leptons do not. Colour charge is required for interactions using the strong force, described by Quantum Chromodynamics (QCD) for short. QCD is a non-abelian gauge theory described by the $SU(3)_C$ symmetry. As leptons do not carry colour charge, QCD only affects quarks and is mediated by the gluon. Gluons also carry colour charge, and as a consequence can self interact. Only colourless states are observed experimentally, so quarks and gluons bind together to form colour neutral states called hadrons. This process is called hadronisation. All quarks undergo hadronisation with the exception of the top quark which decays at time scales shorter than those required for hadronisation.

Symbol	**Mass (MeV)**	**Electric Charge**
Quarks		
u	$4.8^{+0.7}_{-0.5}$	$+2/3$
d	$2.3^{+0.7}_{0.5}$	$-1/3$
c	$(1.275 \pm 0.025) \times 10^3$	$+2/3$
s	95 ± 5	$-1/3$
t	$(173.21 \pm 0.51 \pm 0.71) \times 10^3$	$+2/3$
b	$(4.18 \pm 0.03) \times 10^3$	$-1/3$
Leptons		
e	0.51100	-1
ν_e	0	0
μ	105.65	-1
ν_μ	0	0
τ	1776.8	-1
ν_τ	0	0

Table 1.1: The masses and electric charges of the known fermions in the SM [6].

Electroweak interactions are described by the $SU(2)_L \otimes SU(1)_Y$ gauge group. The theory goes on to state that fermions are made of left and right-handed fields. Left handed fields are doublets in $SU(2)$ and right handed fields are singlets. Electroweak theory must remain invariant under gauge transformations. As such, weak interactions can only act on the left handed fields. In order to achieve this, the theory introduces a weak isovector called W_μ and a weak isoscalar called B_μ which correspond to $SU(2)_L$ and $U(1)_Y$ respectively, each with their own coupling constant. A shortcoming of this theory is that it predicts massless W and Z bosons as standard Dirac mass terms would violate gauge invariance. This is the motivation for the introduction of the Brout-Englert-Higgs Mechanism.

There is a significant effort in modern particle physics to observe exotic phenomena which are categorised as Beyond the Standard Model (BSM). BSM particles characteristically have very high mass. Among the more mainstream BSM searches currently in progress are the searches for Supersymmetric particles and for Dark Matter. The analysis described in this thesis falls under the category of a search for physics beyond the Standard Model, and aims to impose limits on the cross-section of a monoHiggs boson and DM vertex and potentially observe new physics. This is an especially interesting event to analyse, as it presents us with a direct vertex coupling DM to the SM.

1.2.1 The Brout-Englert-Higgs Mechanism

The Higgs boson is responsible for generating the masses of the fermions and the vector bosons [29, 30, 31]. Electroweak interactions are mediated by four gauge bosons, $W^\mu_{1,2,3}$ and B_μ which correspond to the generators of $SU(2)_L$ and $U(1)_Y$ respectively. The $W^\pm$, Z and photon are combinations of these four gauge bosons, as shown below:

$$W^\pm_\mu = \frac{1}{\sqrt{2}}\left(W^1_\mu \mp iW^2_\mu\right) \tag{1.1}$$

$$Z_\mu = \frac{g_2 W^3_\mu - g_1 B_\mu}{\sqrt{g_2^2 + g_1^2}} \tag{1.2}$$

$$A_\mu = \frac{g_1 W^3_\mu + g_2 B_\mu}{\sqrt{g_2^2 + g_1^2}} \tag{1.3}$$

It is known that the photon should be massless and that the $W^{\pm}$ and Z should have mass as they mediate the weak force. Directly introducing a mass to these bosons would not preserve the $SU(2)_L \times U(1)_Y$ symmetry.

The Brout-Englert-Higgs (BEH) mechanism allows for particle masses and also preserves this symmetry. A complex $SU(2)$ scalar doublet is introduced:

$$\Phi = \begin{pmatrix} \mathrm{Re}\Phi^{+} + i\mathrm{Im}\Phi^{+} \\ \mathrm{Re}\Phi^{0} + i\mathrm{Im}\Phi^{0} \end{pmatrix} \tag{1.4}$$

The potential associated with this doublet is given as:

$$V(\Phi) = \mu^2 \Phi^{\dagger}\Phi + \lambda(\Phi^{\dagger}\Phi)^2 \tag{1.5}$$

Here μ^2 is the mass term of Φ and λ is a coupling constant for self interaction. If $\mu^2 < 0$ then the potential takes on a ‘Mexican hat’ shape as shown in Figure 1.2.

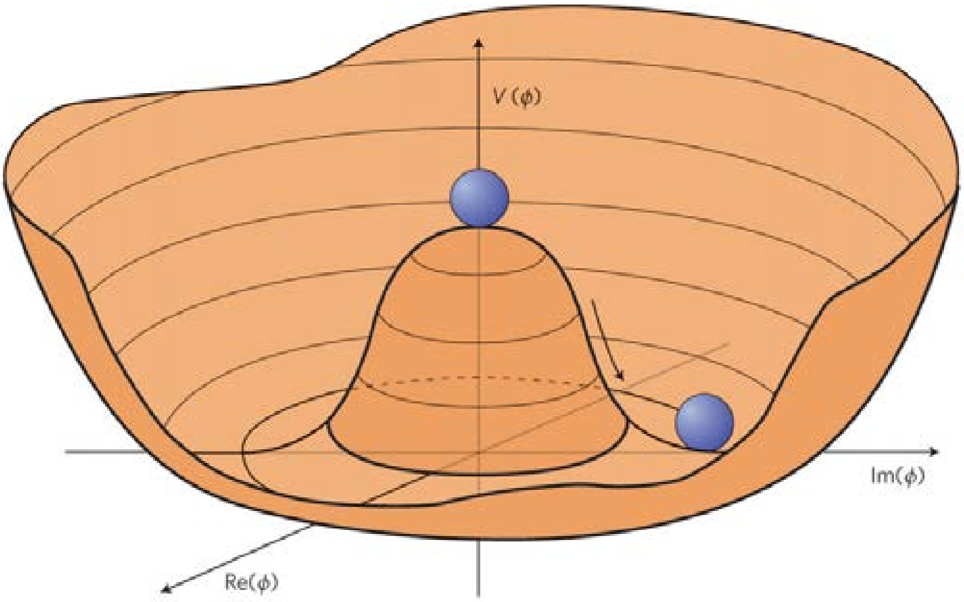

Figure 1.2: The “Mexican Hat” potential of the scalar field Φ. Image taken from [7].

As can be seen in Figure 1.2, the minimum of the potential is not at zero and is instead found at $v = \sqrt{-\mu^2/\lambda}$. This value is known as the Vacuum Expectation Value (VEV). If the particle sat at the ground state at 0, the vacuum state of the system would be symmetric. But as the particle moves toward the minimum instead of resting on top of a maximum, it is said to spontaneously break this symmetry, occupying one of infinite degenerate ground states.

The Lagrangian density can be written as:

$$L_\Phi = (D^\mu\Phi)^\dagger(D_\mu\Phi) - V(\Phi) \tag{1.6}$$

where $V(\Phi)$ is defined in Equation 1.5 and D_μ is the covariant derivative which brings in the interactions with W^a_μ and B_μ and is defined as:

$$D_\mu = \partial_\mu - ig_2\frac{\tau_a}{2}W^a_\mu - ig_1\frac{Y}{2}B_\mu \tag{1.7}$$

To derive physical fields from this doublet, we rewrite it in terms of four real fields:

$$\Phi(x) = \left(\begin{array}{c} \theta_2(x) + i\theta_1(x) \\ \frac{1}{\sqrt{2}}(v + H(x)) - i\theta_3(x) \end{array}\right) = e^{i\theta_a(x)\tau^a(x)/v}\frac{1}{\sqrt{2}}\left(\begin{array}{c} 0 \\ v + H(x) \end{array}\right) \tag{1.8}$$

where the real fields are $\theta_{1,2,3}(x)$ and $H(x)$. As any local gauge transformation can be applied to the doublet, one can be used to eliminate three of the above fields, namely $\theta_{1,2,3}$. These fields are referred to as Goldstone bosons [32, 33, 34].

$$\Phi(x) \to e^{-i\theta_a(x)\tau^a(x)/v}\Phi(x) = \frac{1}{\sqrt{2}}\left(\begin{array}{c} 0 \\ v + H(x) \end{array}\right) \tag{1.9}$$

If one then takes the definition of $\Phi(x)$ from Equation 1.9 and substitute it into

Equation 1.6, the kinetic energy term becomes:

$$\frac{1}{2}(\partial_\mu H)^2 + \frac{g_2^2}{8}(v+H)^2|W_\mu^1 + iW_\mu^2|^2 + \frac{1}{8}(v+H)^2|g_2W_\mu^3 - g_1B_\mu|^2 \tag{1.10}$$

Using the definitions of the fields $W_\mu^\pm$, Z_μ and A_μ as given in Equations 1.1-1.3, bilinear terms appear in the kinetic energy term, from which particle masses can be derived:

$$m_W = \frac{1}{2}vg_2 \tag{1.11}$$

$$m_Z = \frac{1}{2}v\sqrt{g_2^2 + g_1^2} \tag{1.12}$$

$$m_A = 0 \tag{1.13}$$

The vacuum expectation value can be given in terms of the Fermi constant for weak interactions:

$$v = 1/(\sqrt{2}G_F)^{1/2} = 246 \text{ GeV} \tag{1.14}$$

With this and measurements of g_1 and g_2, by comparing the strength of charged and neutral currents, one derives the masses of the $W^\pm$ and Z bosons. And, as expected due to bilinear term associated with the A field, the photon has no mass.

Thus far this explains how the BEH mechanism gives mass to the vector bosons. Fermion masses can be derived by looking at a Lagrangian density function describing fermion-Higgs interactions which are gauge invariant in $SU(2)_L \times U(1)_Y$ and applying the above field. For example, an electron and an electron neutrino can be described by:

$$L_f = f_e(\bar{e},\bar{\nu})_L \Phi e_R \to f_e(\bar{\nu_e},\bar{e_L})\frac{1}{\sqrt{2}}\begin{pmatrix} 0 \\ v+H(x) \end{pmatrix} e_R = \frac{f_e}{\sqrt{2}}(v+H)\bar{e_L}e_R \quad (1.15)$$

Once again, the bilinear terms lead to masses $m_e = f_e v/\sqrt{2}$ and $m_\nu = 0$.

The three degrees of freedom that are absorbed in the calculation of the vector boson masses leave one behind. This represents a physical particle, the boson associated with the Higgs field, the Higgs boson. By isolating H field bilinear terms ($\frac{1}{2}m_H^2 H^\dagger H$), the Higgs boson mass can be derived as $m_H = \sqrt{2\lambda v^2}$.

The most interesting feature of the Higgs boson is that it is a spin-0 particle. It couples to fermions in proportion to their mass and to vector bosons in proportion to the square of their mass. As an extension of this, the Higgs boson can't couple directly to the massless photons or gluons, but can be induced indirectly via quantum loops.

1.2.2 Higgs Boson Production at the LHC

Higgs bosons produced in hadron colliders such as the LHC can be generated in four main ways. These are: gluon fusion, vector boson fusion, associated production with a vector boson and production with a pair of top-quarks. These four processes are shown as Feynman diagrams in Figure 1.3. The dominant production mechanism in hadron colliders is gluon fusion.[35] The triangular quark loop depicted for this process is comprised of heavy quarks, dominated by top-quarks but with some contribution from bottom-quarks as well.

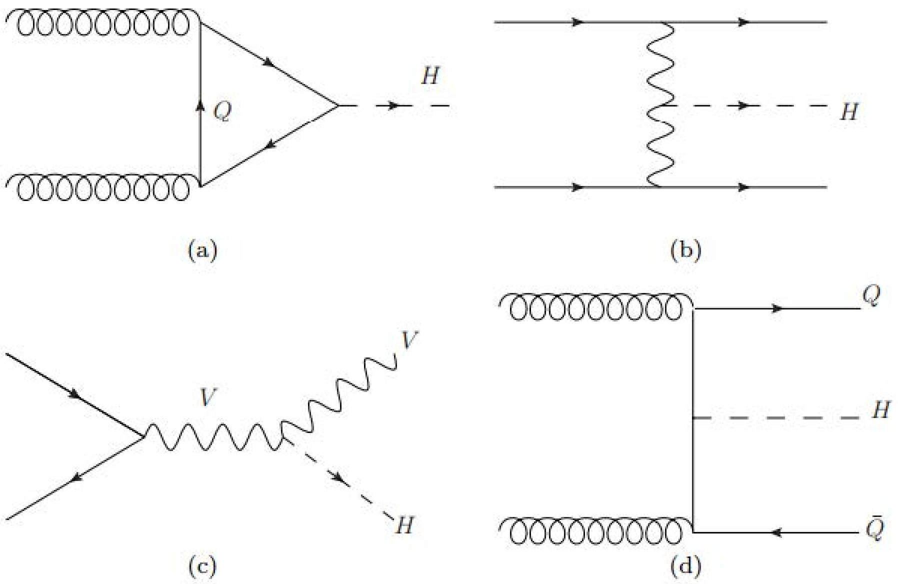

Figure 1.3: Different Higgs boson production mechanisms in the LHC: (a) gluon fusion, (b) vector boson fusion, (c) associated production with a vector boson and (d) production with a pair of top quarks. Image taken from [7].

Process	$\sqrt{s} = 8$ TeV	$\sqrt{s} = 13$ TeV
ggF	$19.27\%^{+7.2\%+7.5\%}_{-7.8\%-6.9\%}$	$43.92\%^{+7.4\%+7.1\%}_{-7.9\%-6.0\%}$
VBF	$1.578\%^{+0.2\%+2.6\%}_{-0.2\%-2.8\%}$	$3.748\%^{+0.7\%+3.2\%}_{-0.7\%-3.2\%}$
WH	$0.705\%^{+1.0\%+2.3\%}_{-1.0\%-2.3\%}$	$1.380\%^{+0.7\%+3.2\%}_{-1.5\%-3.2\%}$
ZH	$0.415\%^{+3.1\%+2.5\%}_{-3.1\%-2.5\%}$	$0.870\%^{+3.8\%+3.5\%}_{-3.8\%-3.5\%}$
ttH	$0.129\%^{+3.8\%+8.1\%}_{-9.3\%-8.1\%}$	$0.509\%^{+5.7\%+8.8\%}_{-9.3\%-8.8\%}$

Table 1.2: Table showing the production cross sections in pb at the LHC for centre of mass energies at 8 TeV and 13 TeV for a Higgs boson with mass of 125 GeV. The first uncertainty comes from scale variations and the second comes from PDF uncertainties.[7]

1.3 Dark Matter

As described in Section 1.1, there is reason to believe that DM makes up a significant portion of the matter in the universe. In the field of astrophysics, models for the shape and velocity of stars within spiral galaxies are not consistent with what is observed without the presence of a large amount of invisible matter on either side of the galactic disk. This mass needs to be able to interact through gravity, but does not interact electromagnetically, enabling light to pass directly through it.

Current theory suggests that DM is stable, has high mass and without electric charge. Cosmological constraints limit Dark Matter interactions with Standard Model (SM) particles at the weak scale or below. Searches for high mass, exotic particles from beyond the Standard Model are a common undertaking, particularly in the search for supersymmetric particles. If DM does exist, it may found as a high mass particle in a particle accelerator such as the LHC.

A number of experiments also exist which are attempting to detect DM directly. Large Underground Xenon experiment (LUX) is one of the leading direct detection experiments, consisting of a time projection chamber containing 370 kg of xenon which is itself contained within a larger water tank. It is located 1.5 km underground at Sandford Underground Research Facility (SURF) in South Dakota, USA [36].

1.4 Mono-Higgs

The Higgs boson, of mass 125 GeV, was discovered during Run 1 of the Large Hadron Collider at CERN by the A Toroidal LHC ApparatuS (ATLAS) and Compact Muon Solenoid (CMS) Collaborations, using 20.3 fb^{-1} of data[25, 26]. The data collected was from proton-proton collisions with a centre of mass energy $\sqrt{s} = 7$ TeV and $\sqrt{s} = 8$ TeV. The decay channels used for discovery were a Higgs boson decaying into four leptons and decaying into a pair of photons, the former being the most dominant decay channel for the 125 GeV Higgs boson.

The distinction that causes a Higgs boson to be labelled as a mono-Higgs, lies entirely on the topology of the event in which the boson appears. A Higgs boson produced in isolation in an event with large missing transverse energy is often referred to as a mono-Higgs. As explained in the introduction, the specific signal in this analysis is the associated production of a mono-Higgs in association with a pair of DM candidates.

There is a very small coupling between Higgs bosons and light quarks, as seen in Figure 1.1. As a result of this, initial state radiation of a Higgs boson from an intermediate particle is heavily suppressed. This means we expect to see the Higgs boson produced at the same vertex as the DM pair. This is especially useful as it provides a direct probe to couplings between the SM and DM.

1.5 Effective Field Theory

The models that can be used to describe this signal can be placed into one of two broad categories: Effective Field Theories and Simplified Theories. These are models recommended by the LHC Dark Matter forum [27]. Parameters used for the models are close to those used in the forum report.

The effective field theory attempts to model the interaction without specifying the exact UV physics that occurs at the SM-DM vertex. It relies on the introduction of non-renormalisable operators to generate the Higgs boson and E_T^{Miss}. Non-renormalisable operators coming in at dimensions 5, 6 and 8 require suppression in the form of $\frac{1}{\Lambda^{(n-4)}}$, where Λ is the effective mass scale of UV particles and n is the number of dimensions of the operator.

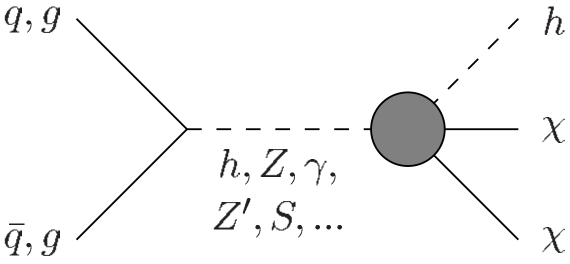

Figure 1.4: An effective operator that couples dark matter to the Higgs boson and gives rise to the mono-H signature in a collider experiment.

EFT models make use of the Higgs portal, $|H|^2$ [37, 38, 39, 40, 41, 42, 43]. In the case of scalar Dark Matter, the following operator is dimension-4:

$$\lambda \left|H\right|^2 \chi^2 \tag{1.16}$$

where λ is a coupling constant and χ is a real scalar. In the case of fermionic DM, the dimension-5 operator is used:

$$\frac{1}{\Lambda} \left|H\right|^2 \overline{\chi}\chi \tag{1.17}$$

$$\frac{1}{\Lambda} \left|H\right|^2 \overline{\chi} i\gamma_5 \chi \tag{1.18}$$

where Λ is the previously mentioned UV particle effective mass suppression to renormalise the operator.

After spontaneous symmetry breaking, the Higgs boson picks up a value expectation value:

$$\left|H\right|^2 = (\nu + h)^2 = \nu^2 + 2\nu h + h^2 \tag{1.19}$$

where ν is the vacuum expectation value and h is the observed Higgs boson at 125 GeV. When multiplied by χ^2 (scalar) or $\bar{\chi}\chi$ (fermionic), the first term becomes a mass term, the second becomes a coupling term between a Higgs boson and two DM candidates and the third becomes coupling between two Higgs bosons and two DM candidates.

In the kinematic region where $m_\chi < \frac{m_h}{2}$, invisible Higgs boson decays (H$\rightarrow \overline{\chi}\chi$) becomes viable. Here the Higgs boson decays directly into the two Dark Matter particles. The partial widths for invisible Higgs boson decays are (for scalar and fermionic DM respectively):

$$\Gamma(h \to \overline{\chi}\chi) = \frac{\lambda^2 \nu^2}{4\pi m_h} \tag{1.20}$$

$$\Gamma(h \to \overline{\chi}\chi) = \frac{\nu^2 m_h}{8\pi \Lambda^2} \tag{1.21}$$

Terms to the order of m_χ^2/m_h^2 are considered negligible and are ignored. An indirect limit is already imposed on the invisible Higgs boson decay of $Br(h \to \overline{\chi}\chi) < 38\%$ [44]. In order to satisfy this observed limit, $\lambda \leq 0.016$ for scalar DM and $\Lambda \geq 10$ TeV for fermionic DM. In regions where invisible Higgs boson decay is viable ($m_\chi > \frac{m_h}{2}$), the values of λ and Λ can go beyond these limits.

By going to dimension-6, one can introduce an operator which describes an effective h-Z-DM coupling:

$$\frac{1}{\Lambda^2}\chi^\dagger i\overleftrightarrow{\partial^\mu}\chi H^\dagger i D_\mu H \tag{1.22}$$

$$\frac{1}{\Lambda^2}\bar{\chi}\gamma^\mu \chi H^\dagger i D_\mu H \tag{1.23}$$

Where $\overleftrightarrow{\partial^\mu}$ is defined as $\alpha\overleftrightarrow{\partial^\mu}\beta = (\partial^\mu\alpha)\beta - \alpha(\partial^\mu\beta)$. The Z-coupling term comes from the unitary gauge of the above covariant derivative:

$$D_\mu = \partial_\mu - igZ_\mu \tag{1.24}$$

The Z-DM coupling leads to the possibility of Z to invisible decays if such a decay is kinematically possible ($m_\chi < m_Z/2$). Constraints on the Z to invisible decays would impose $\Lambda \geq 400$ GeV.

Lastly, the operator can be taken to dimension-8 by introducing additional SM fields:

$$\frac{1}{\Lambda^4}\overline{\chi}\gamma^{\mu}\chi B_{\mu\nu}H^{\dagger}D^{\nu}H \tag{1.25}$$

Where B is the SM U(1)$_Y$ field strength tensor, which generates qq $\rightarrow$ Z*/γ* $\rightarrow$ h$\chi\chi$. This particular model is not constrained by invisible decays.

1.6 Simplified Models

Simplified models represent the UV particles as degrees of freedom in the theory, where as the DM is the only new degree of freedom in EFT. Although EFT is more model independent, it is only reliable at parton energies $< \Lambda$ [45]. Simplified models overcome these problems by being more model dependent. Again, the dark matter can be fermionic or scalar and is assumed to be a singlet under $SU(3)_C \otimes SU(2)_L \otimes U(1)_Y$. The simplified theory has to be further broken down depending on whether the s-channel intermediate particle is a vector or a scalar.

In these models, we make the assumption that DM is fermionic and that it carries baryon number, which in turn is gauged under a local U(1)$_B$. The reasoning behind this is explained in Section 1.6.1.

1.6.1 Vector Mediator

In the vector mediator version of the simplified model, the mediator in question is assigned to be Z'. This is an already familiar vector that arises naturally as a minimal extension to the gauge structure of the SM. Z' is theorised to only couple to quarks, not leptons. A gauge extension of the SM posits that baryon number is gauged, with Z' being the gauge boson. As a result of this, Z' must carry baryon number. Therefore in order for DM to couple to Z', it must also carry baryon number [46]. Further to this, the consistency of the extension implies new stable, baryonic states which are neutral under SM gauge symmetry. These are very good

DM candidates. Carrying baryon number also prevents coupling to leptons, which is beneficial as coupling to leptons is already tightly constrained experimentally.

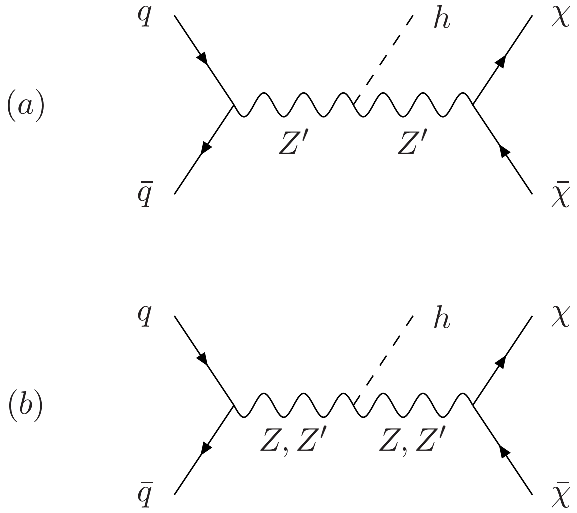

Figure 1.5: The collider production mode in a simplified model including a Z' boson which decays to $\chi\bar{\chi}$.

The Lagrangian for the vector mediator model would contain the following terms:

$$g_q \overline{q} \gamma^\mu q Z'_\mu + g_\chi \overline{\chi} \gamma^\mu \chi Z'_\mu - g_{hZ'Z'} h Z'_\mu Z'^\mu \tag{1.26}$$

where the various g variables are coupling strength coefficients. The first term describes coupling between quarks and Z', the second term couples DM to Z' and the third term represents coupling between the Higgs boson and the Z'.

1.6.2 Scalar Mediator

The use of a scalar mediator is motivated by the fact that it is easy to represent the potential for particles that couple to the SM via Higgs bosons only as:

$$V \supset a\left|H\right|^2 S + b\left|H\right|^2 S^2 + \lambda_h \left|H\right|^4 \tag{1.27}$$

The simplest way of representing the coupling of the scalar mediator to the DM is:

$$-y_\chi\overline{\chi}\chi S \tag{1.28}$$

After spontaneous symmetry breaking (SSB), there is a mixing between the h and the S after diagonalising the fields in the unitary gauge. The specific quark and DM coupling terms become:

$$-y_\chi\overline{\chi}\chi(c_\theta S - s_\theta h) - \frac{m_q}{\nu}\overline{q}q(c_\theta h + s_\theta S) \tag{1.29}$$

Many other terms also come out of this Higgs potential. The ones pertaining to coupling of the h with the S (h^2S and S^2h terms), allow for radiation of the Higgs boson from this s-channel scalar mediator.

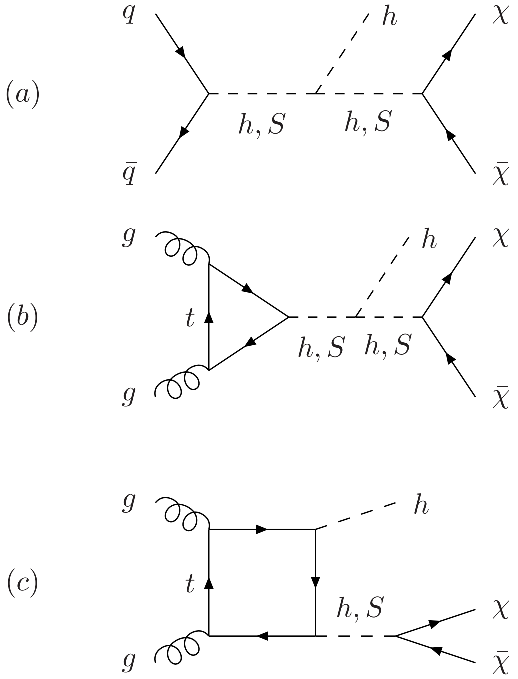

Figure 1.6: Diagram showing some collider production modes in a simplified model including a scalar S boson which decays to $\chi\bar{\chi}$.

Additionally, to account for Higgs boson radiation directly from top quark loops, the model also includes an effective gghS vertex which is derived in the large m_t limit.

1.6.3 Z'-2HDM Model

In this model, a vector mediator decays into a 125 GeV Higgs boson and a heavy pseudo-scalar Higgs boson (A^0). This heavy Higgs boson arises from a two-Higgs doublet extension to the SM. A^0 is a pseudoscalar with a large branching fraction to a DM pair.

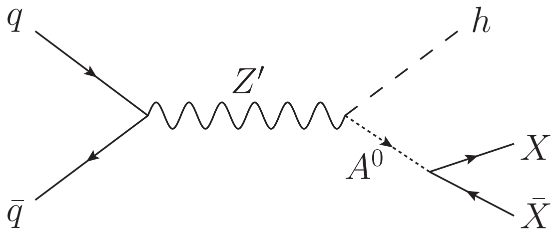

Figure 1.7: Production mechanisms for dark matter plus a Higgs boson through a new Z' coupled to a two Higgs-doublet model, where the new pseudoscalar A^0 decays primarily to dark matter.

The Lagrangian can be expressed as:

$$-L \supset y_u Q\widetilde{\Phi}_u\overline{u} + y_d Q\Phi_d\overline{d} + y_e L\Phi_d\overline{e} + h.c. \tag{1.30}$$

where the y-values are coupling strength parameters, Φ_u is the Higgs doublet that couples to up-type quarks, Φ_d is the doublet that couples to down-type quarks and leptons. u, d and e represent up-quarks, down-quarks and electrons respectively. Q and L refer to the right-handed weak isospin singlets associated with quarks and leptons.

After electroweak symmetry breaking, the Higgs doublets gain vacuum expectation values ν_u and ν_d for up and down type respectively. In unitary gauge, the doublets can now be parameterised as:

$$\Phi_d = \frac{1}{\sqrt{2}} \begin{pmatrix} -\sin\beta H^{+} \\ \nu_d - \sin\alpha h + \cos\alpha H - i\sin\beta A^0 \end{pmatrix} \tag{1.31}$$

$$\Phi_u = \frac{1}{\sqrt{2}} \begin{pmatrix} \cos\beta H^{+} \\ \nu_u + \cos\alpha h + \sin\alpha H + i\cos\beta A^0 \end{pmatrix} \tag{1.32}$$

where H and h are neutral, CP-even scalars (where h is the currently observed Higgs boson with a mass of 125 GeV) and A^0 is the above mentioned heavy Higgs which is a neutral, CP-odd scalar. The heavier Higgs bosons (H and A^0) are expected to have masses of $\geq$ 300 GeV.

We define $tan(\beta) = \nu_u/\nu_d$ and define α as the mixing angle that diagonalises the h-H mass squared matrix. We further impose that $\alpha = \beta - \pi/2$, which is an alignment limit coming from the scenario where h has SM-like couplings to gauge bosons and fermions and that $tan|\beta| \geq 0.3$ coming from the implications of perturbativity of the Yukawa top coupling.

1.7 Comparison of Topologies Between Models

As demonstrated above, there are many different types of models that can describe the signal. However these models contain unknown parameters, namely the mass of the dark matter particles and the mass of the intermediate state which appears in some form or another in all of the above models, be it as a Z' or as an A^0. As these are unknown, a broad range of values for these need to be tested. As such, Monte Carlo simulations of the signals were generated, each with a range of different masses for the DM and intermediate state.

Samples were generated with three profiles in mind: fixed low intermediate state mass (10 GeV) with increasing DM mass, fixed low DM mass (1 GeV) with increasing intermediate state mass and increasing masses of both DM and intermediate state to a keep both on a similar scale. Increasing the mass of the DM particles in the sample will result in a larger amount of MET being detected. For the Z'-2HDM analysis, samples were generated for all iterations, except those where A^0 mass would be higher than Z' mass.

A summary of all the different signal models that were used in this analysis is presented in Tables 1.4 and 1.5 which show the mass combinations for the simplified and the Z'-2HDM models respectively.

Figure 1.8 compares the MET distributions of various signal different signal models over four plots.

1.8 Earlier Experimental Searches

A similar search for dark matter in this channel was conducted by the ATLAS collaboration during Run 1, using 8 TeV data [9]. There was also a search for the same dark matter production as above, but in the case where the Higgs boson decays into two photons [47]. In the context of searching for SM particles recoiling from a pair of DM candidates, searches have been performed using recoiling hadronic jets [48, 49], b-quarks [50], a photon [51, 52] or a W/Z boson or top quark [53, 54, 55, 56, 57]. Results for the Z'-2HDM model can be found in Figure 1.9.

Regions underneath these observed limits have been excluded. With the increased statistics from Run 2, and higher centre of mass energy, this analysis hopes to improve greatly upon the results shown above.

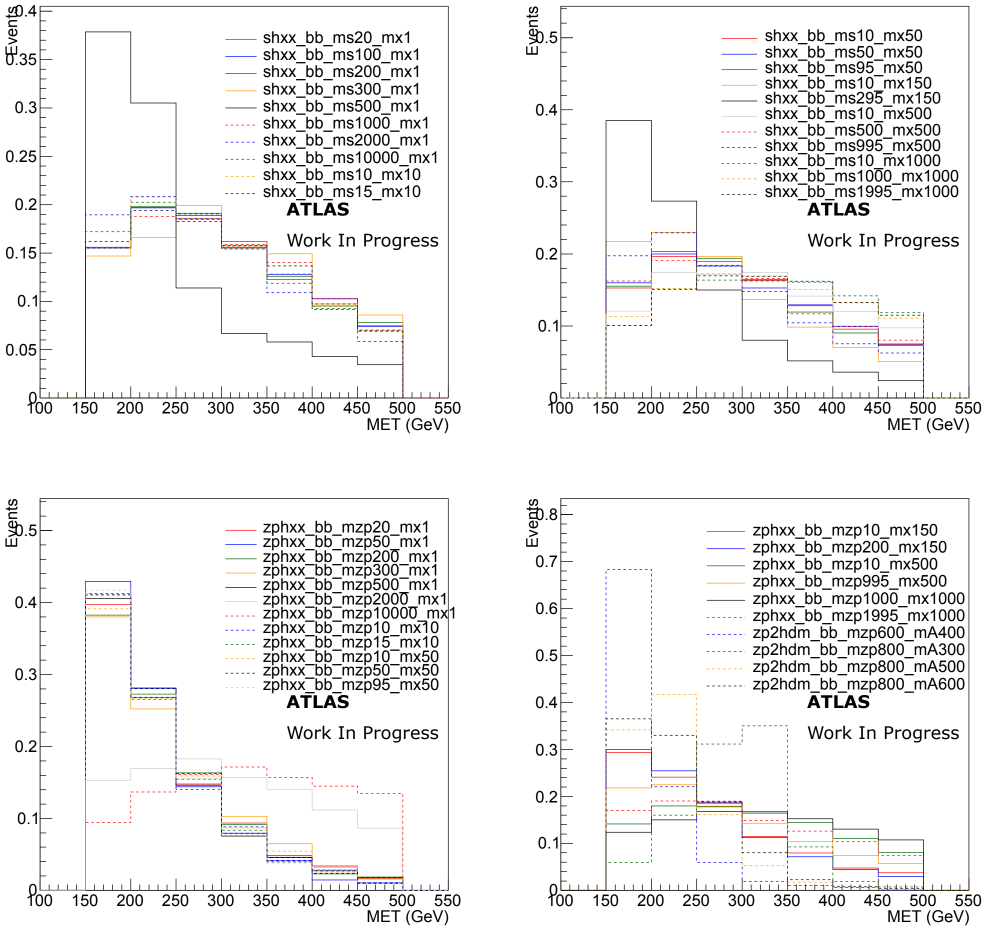

Figure 1.8: Normalised generator-level missing transverse energy distributions for the signal samples used. 'shxx_bb' refers to a simplified model with a scalar intermediate particle where 'ms' is mass of said particle. 'zphxx_bb' refers to a simplified model with a vector intermediate particle (Z') of mass 'mzp'. 'mx' is mass of the DM in the specific model. 'zp2hdm_bb' refers to the Z'-2HDM model. 'mA' is the mass of the A^0. All mass numbers are given in GeV.

Name	Lagrangian	Dim.	Parameters	Madgraph Parameters	S_χ	Higgs Portal
			EFT Models			
xxhh	$\lambda\|H\|^2\chi\chi$	4	λ	$g_{DM} = v \cdot \lambda$	0	yes
xxhhg5	$\frac{1}{\Lambda}\|H\|^2\bar{\chi}i\gamma_5\chi$	5	Λ	$g_{DM} = \frac{v}{\Lambda}$	1/2	yes
xdxhDh	$\frac{1}{\Lambda^2}\chi^\dagger i \overleftrightarrow{\partial^\mu} \chi H^\dagger i D_\mu H$	6	Λ	$y_\chi = \frac{1}{\Lambda^2}$	0	no
xgxFhDh	$\frac{1}{\Lambda^4}\bar{\chi}\gamma^\mu\chi B_{\mu\nu}H^\dagger D^\nu H$	8	Λ	$y_\chi = \frac{1}{\Lambda^4}$	1/2	no
			Simplified Models			
scalar	$\supset -y_\chi\bar{\chi}\chi S$	4	m_S, y_χ $sin(\theta)$, b	m_S, $g_{DM} = y_\chi$ $spmix = sin(\theta)$, $g_b = b$	1/2	no
zpzp	$\supset g_\chi\bar{\chi}\gamma^\mu\chi Z'_\mu$	4	$m_{Z'}$, g_χ g_q, $sin(\theta)$	$m_{Z'}$, $g_{DM} = g_\chi$ $sp = sin(\theta)$, $g_f = g_q$ $g_z = 0.3 \cdot m_{Z'}$	1/2	no
Z'-2HDM	$\supset y_u Q\tilde{\Phi}_u\bar{u} + y_d Q\Phi_d\bar{d}$ $+y_e L\Phi_d\bar{e} + \text{h.c.}$		$tan(\beta)$, g_Z m_A, $m_{Z'}$, m_χ		1/2	no

Table 1.3: The Lagrangian operators and free parameters for all models considered except the Z'-2HDM simplified model. The MadGraph parameters and other information are tabulated as well, for reference. The short naming convention is used to refer to the models throughout the text.

Intermediate Mass [GeV]	DM Masses [GeV]					
	1	10	50	150	500	1000
10	●	●	●	●	●	●
15		●				
20	●					
50	●		●			
95			●			
100	●					
200	●			●		
295				●		
300	●					
500	●				●	
995					●	
1000	●					●
1995						●
2000	●					
10000	●					

Table 1.4: Table showing the combinations of intermediate state and dark matter candidate masses used when generating the simplified models.

	A^0 Masses					
Z' Mass	300 GeV	400 GeV	500 GeV	600 GeV	700 GeV	800 GeV
600 GeV	●	●				
800 GeV	●	●	●	●		
1000 GeV	●	●	●	●	●	●
1200 GeV	●	●	●	●	●	●
1400 GeV	●	●	●	●	●	●

Table 1.5: Table showing the combinations of Z' and A^0 masses used when generating Z'-2HDM model.

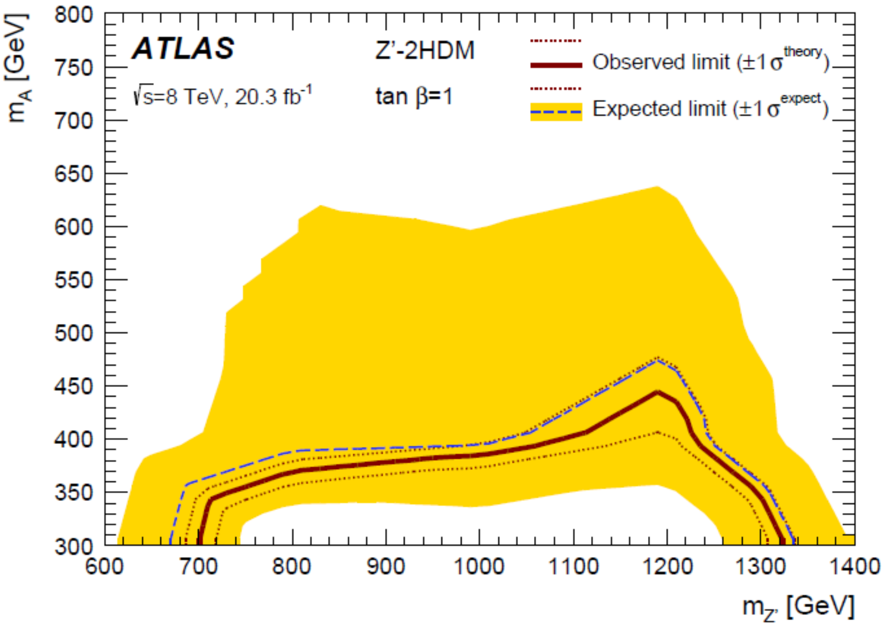

Figure 1.9: Exclusion contour for the Z'-2HDM model (see Section 1.6.3) from the Run 1 analysis using 8 TeV data. Blue line shows the expected limit with the yellow bands showing $\pm 1\sigma$ uncertainty. Solid red line shows the observed limit with the dotted red line showing the variations of the limit based on a $\pm 1\sigma$ uncertainty on the signal theoretical cross section. [9]

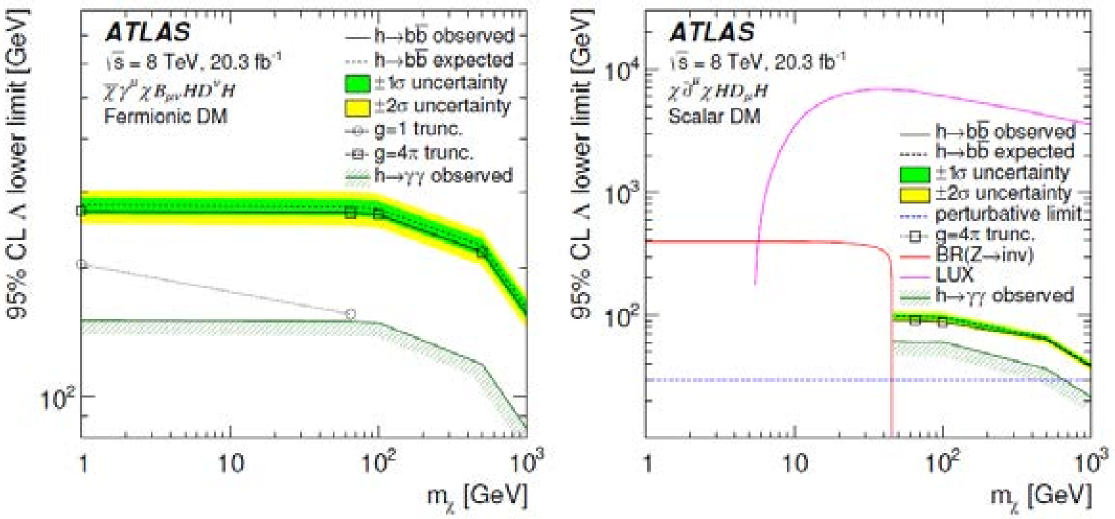

Figure 1.10: 95% confidence level lower limit on the coupling parameter Λ as a function of m_χ. [9]

CHAPTER 2

THE DETECTOR

2.1 The Large Hadron Collider

The LHC (Large Hadron Collider) is currently the world's largest particle accelerator measuring 26.7km in circumference. It is used most of the time as a proton-proton collider, however heavy ions can be injected into the beam line for proton-ion or ion-ion collision experiments.

It was completed in 2008 with the first run occurring between 2010 and 2012, with beam energies of 7 TeV (2010-2011) and 8 TeV (2012) and with a peak luminosity of $7.7 \times 10^{33}\text{cm}^{-2}\text{s}^{-1}$. During Run 1, the bunch spacing was 50 ns. Run 2 started in 2015 colliding beams with centre of mass energies of 13 TeV (near the initial target energy of 14 TeV). Bunch spacing was reduced to 25 ns and the peak luminosity reached $1.7 \times 10^{34}\text{cm}^{-2}\text{s}^{-1}$.

Protons pass through LINAC2 (linear accelerator) and then through a booster. From this they are then passed into the Proton Synchrotron (PS) and the Super Proton Synchrotron (SPS) which act to further accelerate the protons before final injection to the beam line. Full details of the injector system can be found in Figure 2.1.

Located at CERN in Geneva, the LHC consists of two superconducting rings. The rings intersect inside four large particle detectors; ATLAS, CMS, LHCb and ALICE.

- **ATLAS & CMS** - ATLAS (A Toroidal LHC ApparatuS)[58] and CMS (Compact Muon Solenoid)[59] are both general purpose particle detectors which are used to collect data for a vast range of different analyses. The detectors are constructed differently. CMS has a fully silicon inner tracker (as oppose to ATLAS's current combination of silicon and transition radiation trackers), uses different materials in its calorimeters and has a differently constructed magnetic field. Further details about the ATLAS detector can be found in the rest of this Section.
- **LHCb** - The LHCb[60] (where the b stands for beauty) experiment gets its name from being designed to focus on the search for new physics arising from bound states of bottom-quarks. The most significant research being based on measurements of processes which will further our understanding of CP-violation. It has a characteristic cone-like asymmetrical shape, being a single arm forward spectrometer.
- **ALICE** - ALICE (A Large Ion Colliding Experiment)[61] studies heavy ion collisions at the LHC for a period outside of regular proton-proton operation. The resulting high density quark-gluon plasma is comparable to early conditions of the universe shortly after the Big Bang.

The LHC ring was constructed inside the pre-existing tunnel used on the same site for the LEP experiment. The tunnels housing the LHC have an internal diameter of 3.7m. The arcs that make up the ring contain superconducting magnets which bend the beam and allow it to travel in a circular motion around the LHC. To ensure that they remain in the superconducting state, these magnets have their own dedicated cooling system running along the full length of the pipe, to achieve the required temperatures for superconducting. Pipes of superfluid helium run past the magnets at a pressure of 0.13 MPa with a temperature of 1.9 K. [62]

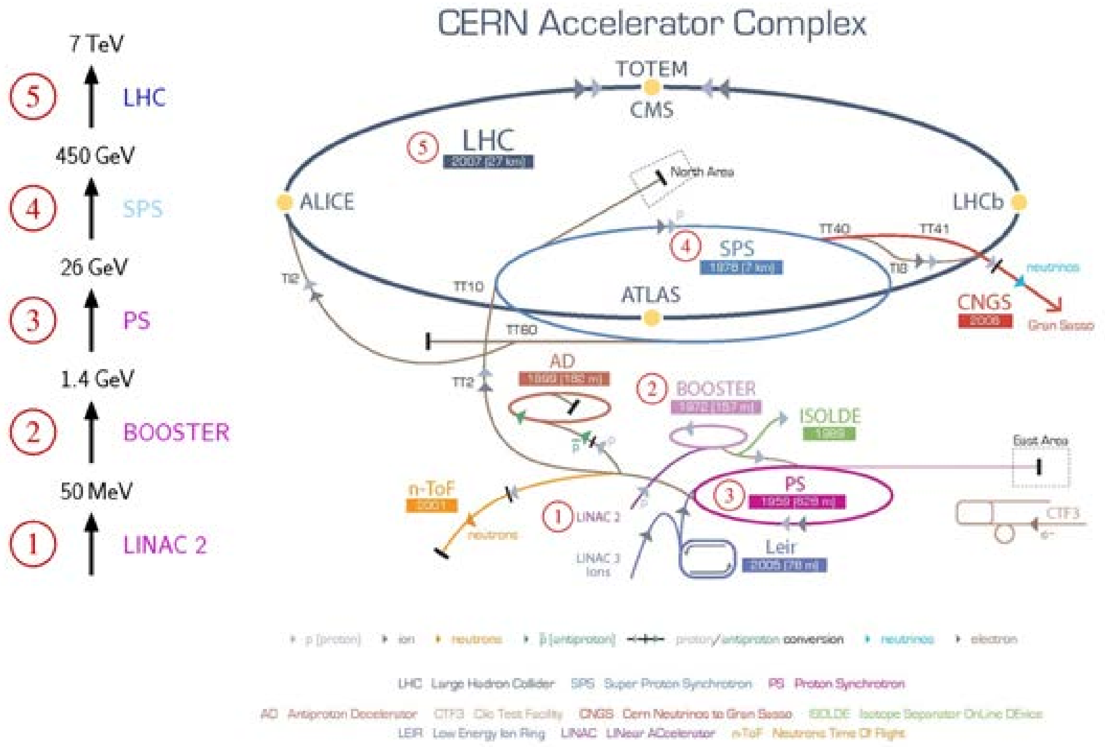

Figure 2.1: The CERN accelerator complex including the injector system for the Large Hadron Collider. Image from [10].

2.2 The ATLAS Detector

The ATLAS detector is a multi-purpose detector designed and commissioned to search for new physics. Most notably it was responsible for the discovery of the Higgs Boson in the summer of 2012. The ATLAS experiment has a cylindrical structure with two end-caps consisting of many nested layers of detectors (see Figure 2.2). Each detector has its own function and through combining data from all subdetectors, the identity of a given particle can be inferred as in Figure 2.3. The detector can be divided into three major regions: the tracking system (Section 2.2.1), the calorimeters (Section 2.2.2) and the muon spectrometer (Section 2.2.3). Integrated into this combination of detectors is the magnet system, which is described in Section 2.2.4.

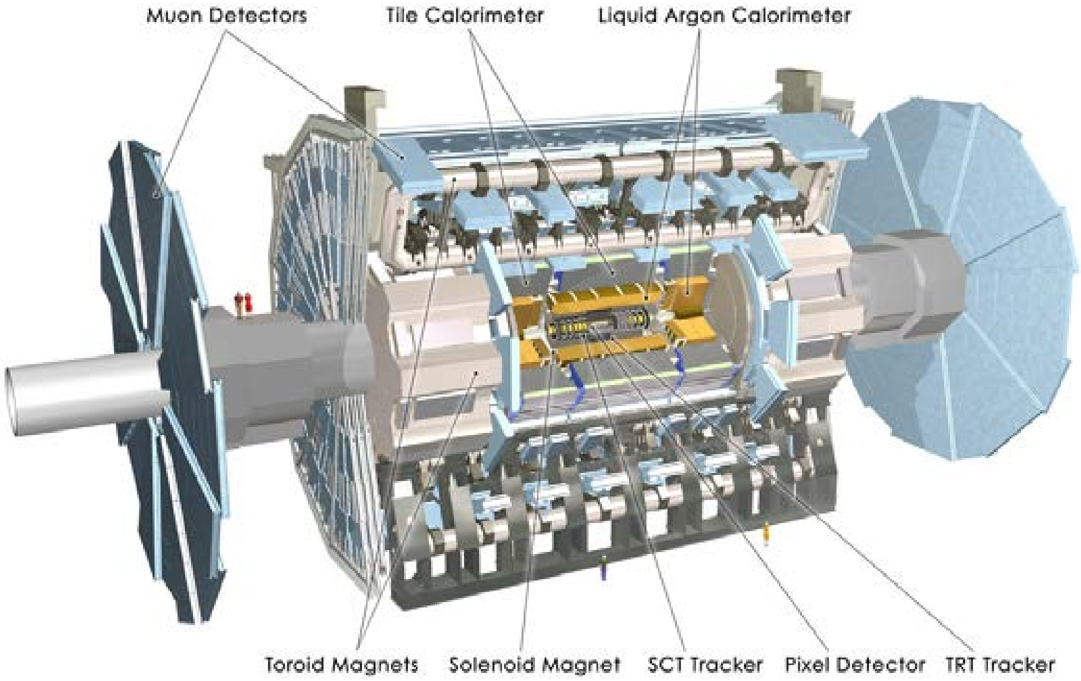

Figure 2.2: Cross-section of the ATLAS detector highlighting and labelling all the components that shall be discussed in this section. Image from [11].

The coordinate system for the detector is centred about the nominal interaction point. The beam line is defined as the z-axis with x and y describing the plane transverse to the beam. The azimuthal angle around the beam line is defined as ϕ and the angle to a certain position as measured from the beam line is defined as θ. The pseudorapidity is defined as:

$$\eta = -ln \tan\left(\frac{\theta}{2}\right) \tag{2.1}$$

Angular separation between objects in the detector is measured by ΔR, where $\Delta R = \sqrt{(\Delta\eta)^2 + (\Delta\phi)^2}$

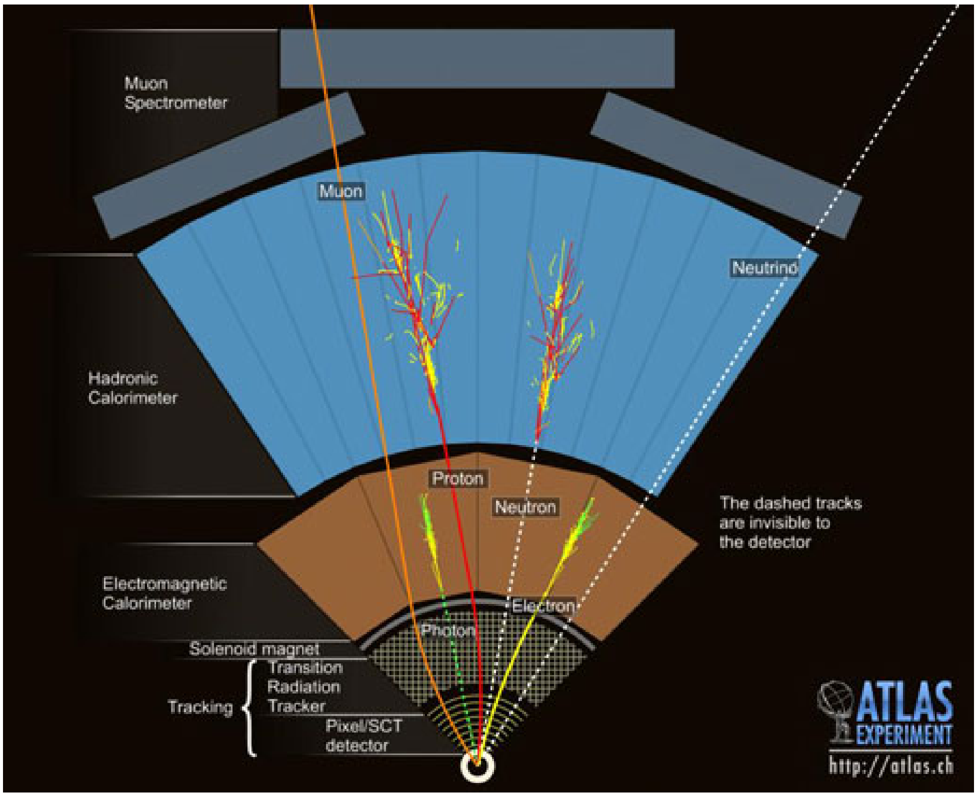

Figure 2.3: Diagram showing which particles are 'visible' in each subdetector. Image from [12].

2.2.1 Inner Detector

The innermost section of the ATLAS detector is known as the inner detector and is comprised of three components; the pixel detectors, the semiconductor tracker (SCT) and the transition radiation tracker (TRT). The tracking system uses its high granularity, its position close to the beam line and the many layers it has to calculate the position of the vertices of the interaction and the paths taken by the particles that pass through it. Only charged particles can be detected by the tracking system. Each sub-component is described in Sections 2.2.1.1-2.2.1.4. The structure of the tracking system (as it was during Run 1), can be found in Figure 2.4.

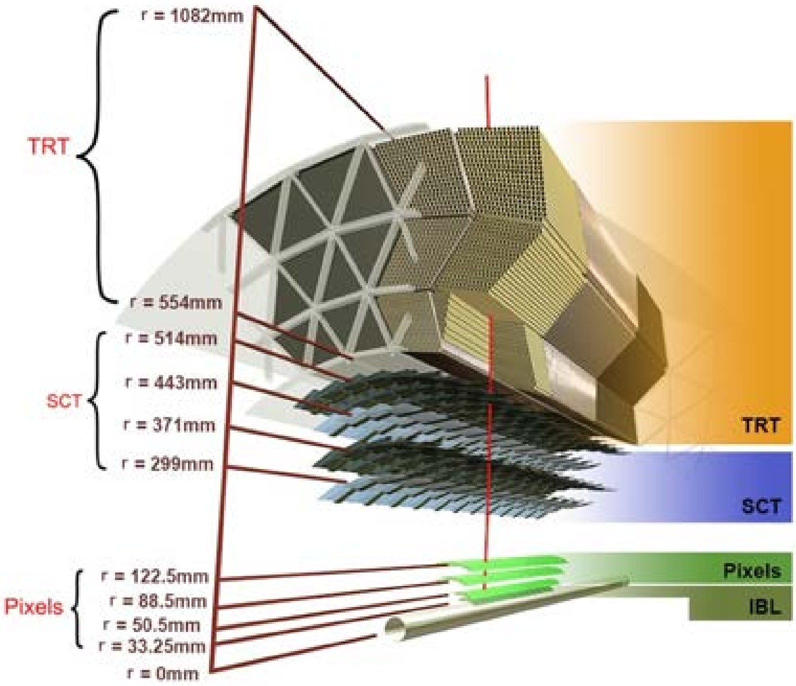

Figure 2.4: Diagram showing the structure of the pixel detectors, the SCT and the TRT in the ATLAS Tracker system as was configured in Run 1. The IBL which was added for Run 2 is not included in this diagram. Image from [13].

2.2.1.1 Pixel Detector

The pixel detector is the innermost part of ATLAS and makes up the first layer of the inner detector. The pixel detector provides high granularity and high precision very close to the beam line. It consists of three barrels of different radii nested within one another, with radii of 5 cm, 9 cm and 12 cm respectively. There are also three disks at the two ends of the barrels, each with an outermost radius at 15 cm and an innermost (as in the radius of the hole in the centre of the disk) at 9 cm from the beam line. They provide coverage over the region $|\eta| < 2.5$. The pixel detectors measure 62.4 mm by 21.4 mm each and contain 46080 pixels. This is divided up into 16 sections of 18 by 160 pixels, each section being read out by its own dedicated read out chip.

The three barrels contain 1456 mounted pixel detectors and the disks contain 288. This totals at 8×10^7 pixels operating over a surface area of 1.7m^2. It provides almost complete coverage and as such, particles normally pass through all three layers. This

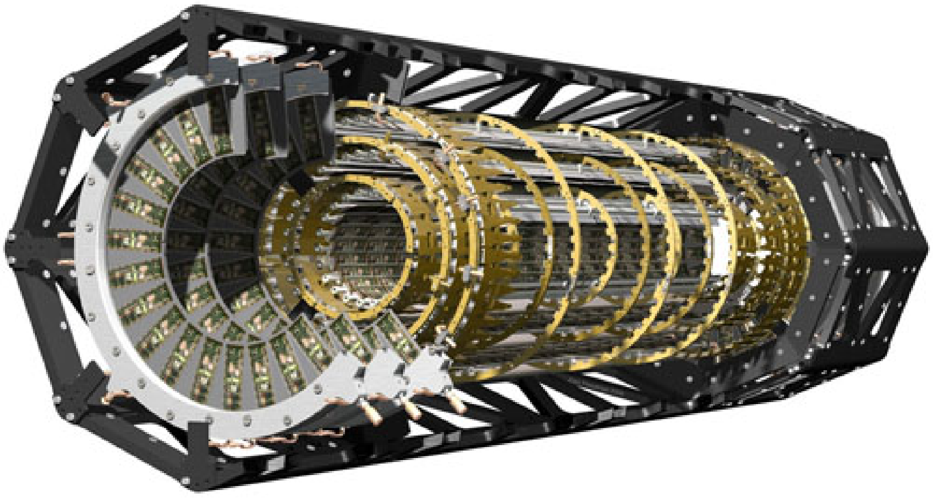

Figure 2.5: Diagram showing the structure of the pixel detector. Image from [14].

is allows the pixel detector to play a very important part in determining the impact parameter resolution. The three separate hits inside this level allow for the particle's path to be reconstructed. Another advantage of its precision, size and position is that it allows for very short lived particles to be detected.

The associated read out chips need to be radiation hardy enough to be able to cope with the intense radiation levels they will be exposed to. Over a 10 year period, each chip will receive 300 kGy from the ionising particles and 5×10^{14} neutrons/cm^2. After such a time, these would be among the components that would need replacing (see Section 3.1).

2.2.1.2 Insertable B-Layer (IBL)

During the Phase-0 Upgrade, which occurred during Long Shutdown 1 (2013-2015), a fourth layer was added to the pixel detector. The Insertable B-Layer (IBL) module was inserted inside of what was formerly the smallest radius barrel of the pixel detector. The module's design also required a section of the beam pipe to be replaced. The original beam pipe radius was set between 2.9 cm $<$ R $<$ 3.6 cm. The new radius of the new pipe installed along with the IBL is 2.5 cm $<$ R $<$ 2.9 cm. The IBL itself can be found between 31.0 mm $<$ R $<$ 40.0 mm, with the sensitive radius of the detectors within it being placed at 33 mm from the beam line.

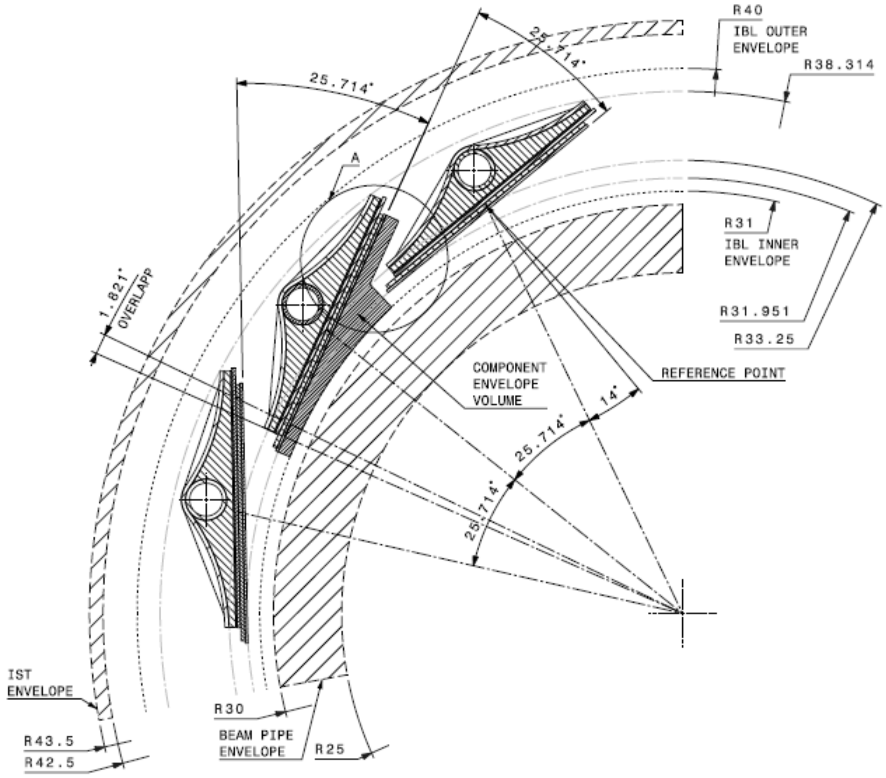

Figure 2.6: Cross section of a portion of the IBL. Image from [15].

2.2.1.3 Semiconductor Tracker (SCT)

The technology in the SCT is fundamentally very similar to the Pixel Detector. It again uses silicon sensors, but with a different geometry. Where as the pixel detector was comprised of an array of pixels in a grid-like formation on each module, each SCT module instead has a series of silicon strips. Each module measures 6.36 cm by 6.40 cm and houses 768 strips, with each strip being 80 μm wide. The modules are made of pairs and are mounted on four nested barrels of radii 30.0 cm, 37.3 cm, 44.7 cm and 52.0 cm. Each pair has one module offset at a slight angle to the other. This way each pair can be used to define the particle's position as the point of intersection of the two strips that registered a signal. A pair on each of the four barrels results in the particle passing through 8 modules in total.

The end-caps of the SCT use a similar design and follow the SCT barrels in the same manner as the pixel detector end-caps follow the pixel detector barrels. The geometry is fundamentally the same, with four disks, each covered with an offset pairs of modules. The only difference, other than the disks in place of the barrels, is that the modules taper slightly at one end in order to allow for many to fit around the inside of the disk and cover as much space as possible.

2.2.1.4 Transition Radiation Tracker (TRT)

The transition radiation tracker uses the ionisation of inert gases as a charged particle passes through it as a method for particle identification. As before, it has a basic barrel structure with an inner radius of 56 cm and an outer radius of 107 cm. The barrels are filled with 4 mm diameter straws. Each straw is filled with gas, with a gold wire of 30 μm diameter running down the centre and has a maximum length of 144 cm.

The gas used is 70% Xe, 27% CO_2 and 3% CO_3. The charged particle passes through this gas, ionising the path it makes. The electrons that are freed in this process then drift towards the wire down the centre of the straw. As they are conducted down the wire, a current is detected which indicates the presence of a charged particle having just passed through. Each straw gives a drift time measurement which is accurate within a special resolution of 170 μm.

The barrel contains 50,000 straws each in parallel to the beam line. Each straw is split in the centre. This allows for the straws to be read out at each end of the barrel and thus reduce occupancy. Two read out channels per straw means 100k read out channels for the entire barrel. The barrel is constructed in sections, each one holding between 329 and 793 straws. The central 80cm of the straws in the first six layers are deliberately left inactive in order to further reduce occupancy.

The end-caps take the form of 18 'wheels' at each end. Each wheel is made up of radial straws which are perpendicular to those in the barrel. Each end cap has

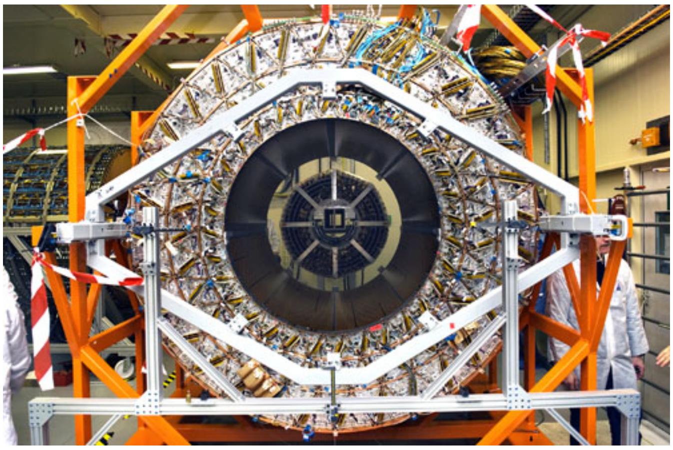

Figure 2.7: Photograph of ATLAS's TRT. Image from [16].

160,000 straws, resulting in a total across both end-caps and the barrel of 420,000 straws. Wheels 1-14 have an inner radius of 64 cm and an outer radius of 103 cm, whilst wheels 15-18 have an inner radius of 48 cm. Wheels 7-14 have half the straw-density as the rest of the end-cap.

Between each layer of drift tubes is a radiator made of polypropylene foils. Electrons passing through these radiators emit transition radiation in the form of X-rays. The photons produced from electrons via Transition Radiation (TR) are higher in energy (8-10 keV) compared to those from minimum-ionising particles such as pions (typically about 2 keV). A threshold of minimum energy deposited TRT is used to identify electrons.

2.2.2 Calorimeters

The work of a calorimeter is to slow down the incoming particles within them and then decay into a particle shower which can then be measured. ATLAS has two sets of calorimeters which are outlined in the two following sub-sections.

2.2.2.1 Electromagnetic Calorimeter

The electromagnetic calorimeter (or EM Calorimeter) measures the energy of electrons and photons as they pass through them (see Figure 2.3). The structure of the calorimeter is a repeating pattern of absorber layers followed by layers of active material. The absorber layers are made out of a very dense material which cause the particle to generate a shower. The particles that make up the shower are then detected within the active layers. The sum of the energies of all the particles in the shower that is produced is used to determine that of the incoming particle. In the case of the ATLAS EM calorimeter, lead is used for the absorber and liquid argon is used as the active material. It is due to this that the EM calorimeter is often referred to as the Liquid Argon Calorimeter.

The EM calorimeter has an interesting geometry in the form of an "accordion" structure. The motivation behind this is to ensure that the particles each travel through approximately the same amount of material. In the case of a simple barrel like structure, a particle moving at right angles to the beam line will pass through less material than a particle traveling at an angle between 0° and 90°. The structure as shown in Figure 2.8 gives an approximately even thickness to particles passing through.

This internal structure is inside of what is again over all a barrel structure. The barrel is split in two halves down the centre; one barrel covering $0 < \eta < 1.475$, the other covering $-1.475 < \eta < 0$. Each half is 3.2 m long with an inner radius of 1.4 m and an outer radius of 2 m. Each one has 1024 absorbers and weighs 57 tonnes.

2.2.2.2 Hadronic Calorimeter

The hadronic calorimeter uses steel absorbers and scintillating tiles in place of the liquid argon. To this effect it is also known as the Tile Calorimeter. The primary aim of the hadronic calorimeter is to cause hadronic matter such as protons and

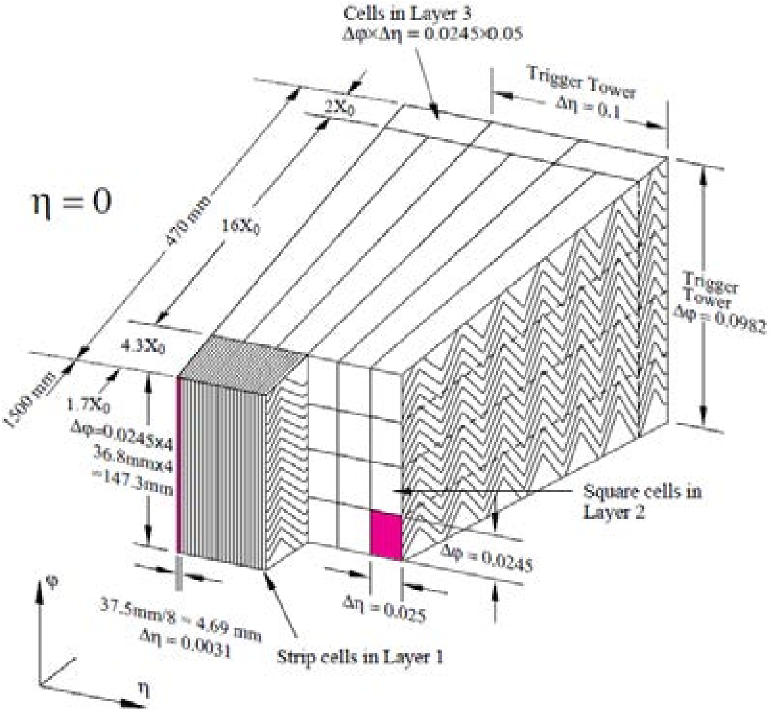

Figure 2.8: Diagram showing the ‘accordion’ geometry of the ATLAS EM Calorimeter. Image from [17].

neutrons to decay into showers, which can then be recorded.

The hadronic calorimeter is divided into three barrel-shaped sections. The central barrel is 5.8 m long with an inner and outer radius of 2.28 m and 4.25 m respectively. After a small gap, on each end of the central barrel can be found two ’extended’ barrels which are 2.6 m long and have the same radial dimensions as the central one. The barrels are each made up of 64 modules each one covering approximately 0.1 radians, providing full coverage.

To maximise coverage, the ATLAS detector also has Hadronic End Cap (HEC) calorimeters placed behind the Electromagnetic End Cap (EMEC) wheel. HEC calorimeters are made up of two wheels HEC1 (front) and HEC2 (rear). Each has a diameter of about 4 m. HEC1 has a length of 0.82 m and HEC2 has a length of 0.96 m. [63]

2.2.3 Muon Spectrometer

The outermost part of the ATLAS detector is the muon spectrometer. They are capable of measuring muon momentum to within a very high precision in the monitored drift tube chambers (or MDT chambers) which operate in the $|\eta| < 2.4$. Each chamber has a thickness of 3 to 8 pressurised drift tubes Each tube is capable of a resolution of 80 μm with each chamber over all attaining an average resolution of 35 μm.

The primary structure consists of three barrels, each one made up of 8 small modules and 8 large modules as illustrated in Figure 2.9. The barrels can be found at 5.0 m, 7.5 m and 10.0 m from the beamline.

The end caps take the form of large wheels at 7.4 m, 10.8 m, 14.0 m and 21.5 m from the interaction point. Together with the barrels, the overall structure ensures that muons pass through at least three layers of muon detectors as seen in Figure 2.10.

2.2.4 Magnet System

The ATLAS experiment has a unique magnet system. A barrel solenoid is incorporated into the calorimeter level supplying an axial 2 T magnetic field inside of it. The toroidal element of the magnet system takes the form of a barrel toroid (0.5 T) and two end-cap toroids (1 T). The toroid magnets are located in the same regions as the muon spectrometers supplying the above magnetic field to their detecting range. The barrel and end-caps are each made up of 8 magnetic coils. The overall magnetic field of the system covers a net volume of 12,000 m^3. The main barrel has an inner and outer radius of 9.4 m and 20.1 m respectively, is 25.3 m long in the z-direction and weighs 830 tonnes.

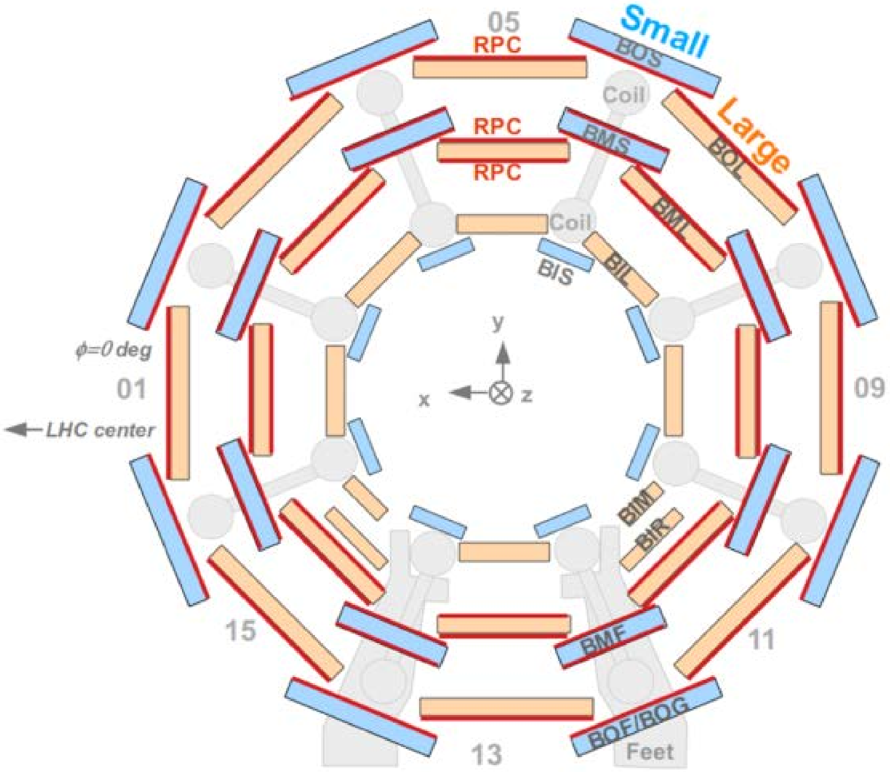

Figure 2.9: Diagram showing the arrangement of muon detectors in the r-ϕ plane. Image from [18].

2.3 Trigger System and Data Acquisition

The rate at which events occur within the ATLAS detector is far too high for every single one to be processed and stored. Nominally, the LHC can deliver a bunch crossing frequency of 40 MHz. The current limit on the recording rate is about 200 Hz. Rate reduction is achieved through a three level trigger system.

The first level is hardware based. It uses low-granularity readings from the calorimeters and the muon spectrometer to quickly identify high p_T objects and large regions of MET. The Level-1 trigger system reduces the rate to 75 kHz and highlights Regions of Interest (RoIs) where interesting structures are located (usually about 2% of the full event data).

The following layers are known as Higher Level Triggers (HLTs). Level-2 triggers

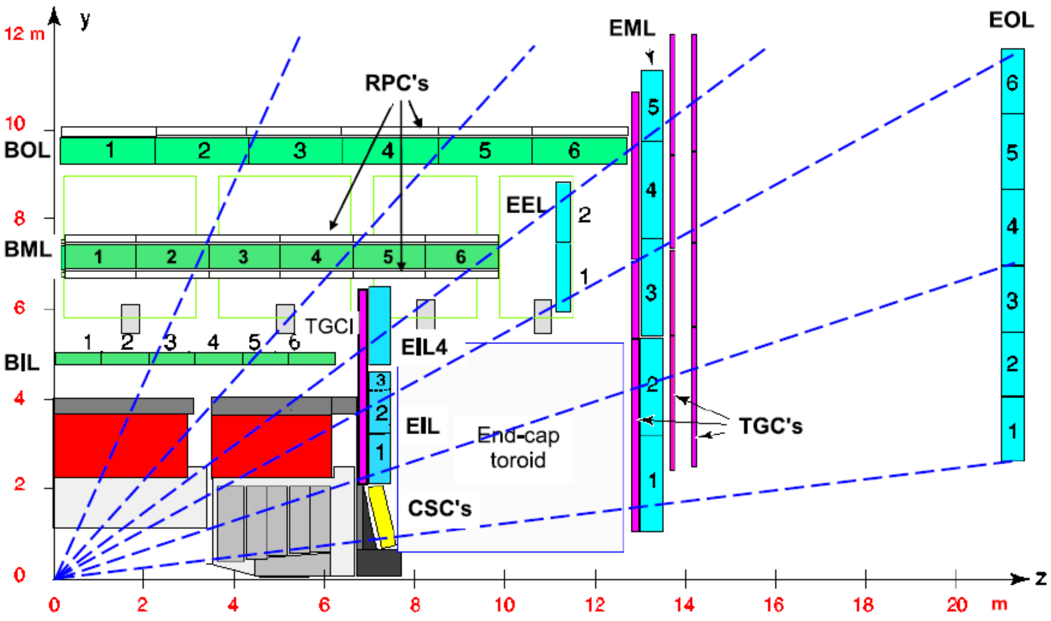

Figure 2.10: Diagram showing the arrangement of muon detectors in the r-z plane. Note how muons pass through three layers. Image from [18].

analyse these RoIs with full granularity and reduce the rates down to 3.5 kHz. Events are then passed on to the Event Filter (EF) which fully reconstructs the event and makes a decision on whether to record it or not, resulting in the final rate of approximately 200 Hz.

The signal region in this analysis makes use of a E_T^{miss} HLT trigger, motivated by the large amount of E_T^{miss} we expect to see as a result of the dark matter candidates not being detected by ATLAS. In the W+jets control region, the proxy for this E_T^{miss} recoiling against the jets is the E_T^{miss} associated with a neutrino plus the E_T of the lepton from the leptonic W decay. The E_T^{miss} trigger used above is the HLT_XE70 trigger. This trigger fires based on E_T^{miss} reconstructed from the calorimeter system and as such ignores the muon in the W+jets control region. As such, a muon trigger is also used in this region. The new E_T^{miss} is then calculated by adding back in the contribution from the muon. This modified E_T^{miss} we refer to as $E_{T,nomu}^{miss}$.

To perform a study of the efficiency of the HLT_XE70 trigger, one can look at the W+jets region (both Monte Carlo simulation and data) and use the result of the muon trigger as a baseline. By looking at events that pass the muon trigger, one can measure the turn on curve for HLT_xe70. The efficiency of the muon trigger is already known to be fully efficient from a much lower muon p_T threshold. The efficiency of HLT_xe70 is shown in Figure 2.11 below as a function of E_T^{miss}.

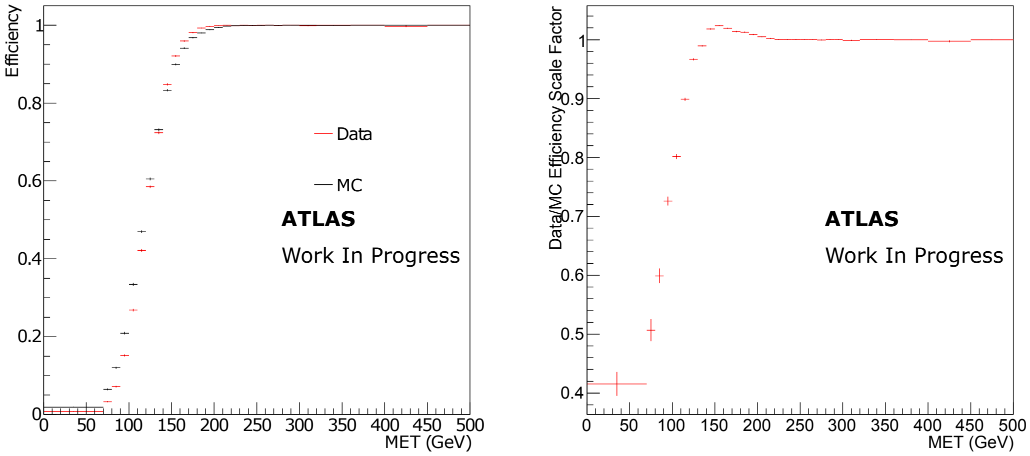

Figure 2.11: The trigger efficiency for events in data and W+jets Monte Carlo (left) for events seeded with one lepton triggers with the ratio of the efficiency in data to that in Monte Carlo (right).

For the Z+jets control region, where the recoiling proxy consists entirely of leptons, an array of muon triggers are used instead. The Z control region triggers on any of the following:

- HLT_e24_lhmedium_L1EM18VH - HLT 24 GeV electron trigger, seeded by a 18GeV EM level 1 trigger
- HLT_e24_lhmedium_L1E20VH - HLT 24 GeV electron trigger, seeded by a 20GeV EM level 1 trigger
- HLT_e60_lhmedium - HLT 60 GeV electron trigger
- HLT_e120_lhloose - HLT 120 GeV electron trigger
- HLT_mu20_iloose_L1MU15 - HLT 20 GeV muon trigger
- HLT_mu50 - HLT 50 GeV muon trigger

CHAPTER 3

PHASE II UPGRADE

This chapter details the work carried out on preparations for the Phase II upgrade of the ATLAS detector as my authorship qualification task. The work described here was largely carried out at the University of Birmingham, with input from the University of Liverpool and the University of Sheffield.

3.1 The High Luminosity LHC Upgrade

During Long Shutdown (LS) 1 over 2013-2014, the LHC and certain components of the detectors underwent the Phase-0 upgrade in order to allow the collider to run at 13 TeV, the original intended energy, ready for Run 2 (2015-2017) with a luminosity of $1 \times 10^{34}\text{cm}^{-2}\text{s}^{-1}$.

Following this, LS 2 (2018-2022) will see Upgrade Phase-I preparing for Run 3, whereby the beam luminosity of the LHC will be increased to $2 - 3 \times 10^{34}\text{cm}^{-2}\text{s}^{-1}$

[64].

One of the biggest changes comes about during LS 3 (commencing 2024 and lasting for 30 months) during which the luminosity shall be increased to $10^{35}\text{cm}^{-2}\text{s}^{-1}$. From this stage on, the accelerator will be known as the HL-LHC [65]. Over 10 years of operation, the strip sensors are expected to receive a fluence of 1×10^{15} 1 MeV neq cm^{-2}.

The increased luminosity will result in higher particle fluences passing through the components of the detectors. Those that receive the highest dose as a result of this increase are the layers closest to beam line. The types of damage this would cause are detailed in Section 3.2.

The work detailed in this chapter is contributing towards the effort to upgrade the ATLAS Inner Tracker (ITk) system in preparation for the HL-LHC. The pixel detector will have accumulated damage over the years of operation and would need to be replaced. The Semiconductor Tracker (SCT) will also need replacing by strip sensors with better granularity. It is these new sensors which require testing to assess their radiation hardness.

3.2 Radiation Damage to Sensors

As a charged particle enters the detector material in a semiconductor sensor, pairs of charge carriers are excited and gain the ability to move freely. These charge carriers are a freed electron and the hole it leaves behind. The mean energy required to create an electron-hole pair in a silicon semiconductor sensor is 3.6 eV. The amount of pairs created in the lattice is directly proportional to the energy of the incoming radiation. Electrodes positioned periodically within the detector material attract the freed charge carriers, where they are registered as an electrical current. As a result, the amount of electrical current picked up by an electrode is proportional again to the energy of the incoming radiation. This way, semiconductor sensors can be used to determine both the energy and the position of incoming charged particles.

However, in instances of very high exposure to radiation, damage to the sensors can arise. The types of radiation damage that can affect a silicon sensor can be categorised into two types; those creating defects in the lattice and ionisation of the lattice.

3.2.1 Lattice Damage

When a high energy particle hits the lattice structure of the silicon sensor, it can interact with one of the atoms. The energy transferred in this process is known as PKA energy (Primary Knock on Atom). When this transfer takes place, there is a possibility of creating a Vacancy-Interstitial pair (also known as a Frenkel pair) in the lattice whereby the atom moves out of place and leaves a hole behind. The minimum energy threshold to create a Frenkel pair in silicon is only 20 eV.

There is an imperfect energy transfer between the incoming particle and the atom due to recoil. As such, the energy required of a proton or a neutron to create a pair is 110 eV and the energy required of an electron is 260 keV (larger due to its smaller mass). After transferring a fraction of its energy, the incoming particle recoils. The amount of energy in the recoil is dependent on the type of radiation. This recoiling can have a further negative effect as it will encourage more PKA energy transfers and could result in even more Frenkel pairs being created using all available energy. This type of process is known as Non-Ionizing Energy Loss (NIEL) [66].

Ions dislodged by this process become defects within the lattice which can change its electrical characteristics. Defect clusters form around these ions which lead to secondary effects.

The effects of displaced atoms in a lattice are listed below.

3.2.1.1 Increased Leakage Current

In lattice based electronics such as the sensors used here, an integral part of the design requires a region of electrical insulation. This is achieved via the application of an electric field which sweeps away mobile charge carriers, preventing current from flowing. This region is referred to as the depletion region.A leakage current allows charge to leak away over this otherwise forbidden region. The amount of leakage current is increased through the displacement of atoms in the lattice, altering the structure that would otherwise enforce this insulation region.

The leaking current also has associated statistical fluctuations. These fluctuations can be to the order of magnitude of the signal itself, resulting in a large amount of noise in the electronic readout.

This loss of current also means that the power supplied over the sensor is no longer sufficient as a fraction would be wasted. A damaged sensor would require more power to achieve the desired effects.

Current leakage also affects the thermal properties of the sensor. The leakage current actively heats the sensor, which in turn increases the leakage current. This creates a positive feedback loop known as ‘thermal runaway’.

3.2.1.2 Dopant Concentration

N-type bulk sensors also gradually become more p-type under high radiation exposure, which generates more acceptor defects than donor defects. After a certain threshold, the bulk undergoes type inversion and picks up p-type characteristics. The more p-doped the bulk becomes, the higher the voltage required to fully deplete the sensor. This also leads to an effect called reverse annealing, where the p-dopant concentration continues to increase after irradiation. This can be prevented by keeping the sensor at a low temperature.

It is for these reasons that semiconductors normally operate under cooling. This would be another aspect, along with the required power, that would need to be re-evaluated and calibrated [66].

3.2.1.3 Trapping Drifting Charge

The rearranged atoms can create undesired potential wells which could trap charges as they move across the lattice. As a result some of the signal will be lost to these traps rather than being registered.

If there are trapped charges between two points at different potentials, the path made by an electron moving through the system could be diverted [66].

3.2.2 Ionisation

Ionisation can lead to localised areas of charge on the surface of the lattice. This can again act as a trap for drifting charges as in Section 3.2.1.3.

Ionised regions in the sensor can cause an anomalous flow of charge which can register as an event incorrectly [66].

3.3 Thermal Annealing

One method of repairing lattice damage is through a process called thermal annealing. Semiconductors are annealed when they are exposed to high temperatures for an extended period of time. Any displaced atoms gain kinetic energy. The atoms then return to the lowest energy state by returning to their original positions within the lattice, undoing the damage. Therefore it is important to avoid heating the samples during any radiation hardness tests. This is was one of the challenges that is discussed in this chapter (see Sections 3.5.2 and 3.7.3).

3.4 The Sensors

The samples being tested at the irradiation facility are strip sensors to be used in the ATLAS Phase-II upgrade (see Section 3.1)[5]. The sensors come in two geometric shapes which shall be referred to as mini-sensors and long-sensors. Mini-sensors are cut squares of silicon with an internal strip structure measuring 10mm by 10mm. Long sensors are longer cuts, measuring 15mm by 30mm. Both sensors are approximately 0.3mm thick. In order to mount these sensors at the irradiation facility, there are two types of carbon fibre frames, each designed to hold one of the two sensors. The 3x3 frames have nine 1cm by 1cm windows cut into them, arranged in a 3x3 system (Figure 3.1). The long frames have three windows; two 4.2cm by 2cm, the third being 2.3cm by 2cm (Figure 3.2). They are both compatible with the mechanism in the cold box lid (see Section 3.5.2).

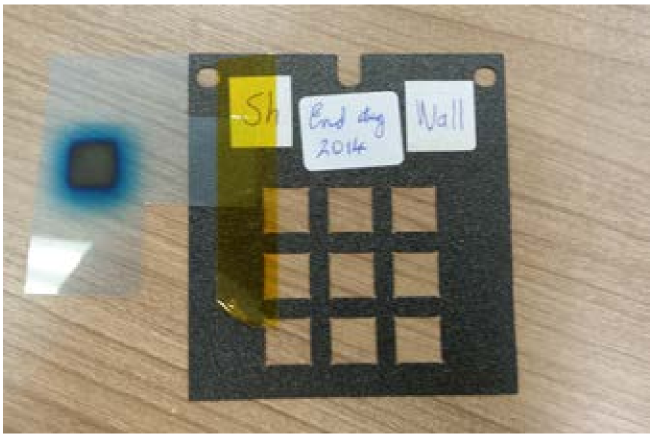

Figure 3.1: 3x3 frame designed to hold mini-sensors.

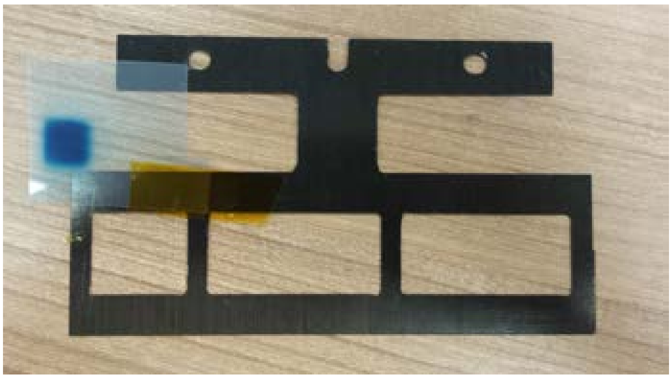

Figure 3.2: Long ‘strip’ frames designed to hold long-sensors.

3.5 The Birmingham Irradiation Facility

3.5.1 The MC40 Cyclotron

Located in the Medical Physics building at the University of Birmingham, the MC40 Cyclotron is primarily used to generate radioactive isotopes used in medical procedures. The cyclotron was originally located at the Veterans Affairs Medical Centre in Minneapolis between 1993 and 2001. In 2002, the University of Birmingham acquired the system and it was installed in the Medical Physics building in the same year. The facility has been active and operational since 2004.

The fundamental concept of a cyclotron involves two metal ‘dees’ (large, D-shaped blocks) with a small gap between them. One is held at ground whilst the other has an alternating voltage applied. A magnetic field (denoted as B) is applied uniformly across both dees. An ion source near the centre launches the ion on a path, which is soon turned into an orbit due to the magnetic field. As the ion crosses from one dee to another, the potential difference across the gap accelerates the ion, resulting in a greater orbital radius. This can be shown via:

$$\frac{mv^2}{r} = qvB \tag{3.1}$$

$$r = \frac{mv}{qB} \tag{3.2}$$

where r is the orbital radius, m is the mass of the ion, v is the velocity and q is the charge of the ion. For a positive ion to gain energy as it crosses the gap, it must be accelerated by being drawn towards a negative potential. After travelling halfway round the dee, it will have turned enough to begin its movement out again. In order to accelerate this process, the dee must gain a positive potential to repel the ion. This is why one of the dees must have an alternating voltage. It is important to maintain an alternating frequency which is the same as the orbital frequency of the ion (finer details discussed later in this section).

$$t_{Cyclotron} = \frac{2\pi r}{v} = \frac{m}{qB} \tag{3.3}$$

The University of Birmingham MC40 Medical Cyclotron differs slightly in design. Instead of two dees, it is made up of four quarter-circle sections (still referred to as dees despite not being D-shaped). Moving clockwise, they alternate in being held at ground or being at an alternating voltage. The benefit of this design is that the ions cross a voltage difference four times per cycle as opposed to two, gaining more energy per orbit.

There are two ways in which the voltage of the dees can be alternated corresponding to oscillation harmonics. In the fundamental mode (N=1), the voltage cycles once per orbit. In this case, for the voltages to be appropriate upon the arrival of the ion, the two dees need to be in antiphase. In the first harmonic mode (N=2), the voltage cycles twice per orbit. The shorter oscillation period results in the two dees now being in phase with each other. This is better understood when plotted, as in Figure 3.3.

The frequency of the dees can be manually altered between 14.5 - 26 MHz. The geometry of the paths differ between N=1 and N=2 because of the difference in gradient experienced whilst inside the dees in both cases (see Figure 3.3). As such the ion source needs to have two ways of injecting the ion initially to correspond to each mode. The ion source generates ionised isotopes of hydrogen and helium for use in the cyclotron (specifically protons, deuterons, ^{3}He and ^{4}He).

Ions normally complete 500 orbits inside the magnetic field. The more orbits it completes, the higher the energy. The stronger the magnetic field, the tighter the orbits (hence more completed before the outside of the cyclotron is reached). The maximum achievable magnetic field is approximately 1.8T. For a list of possible

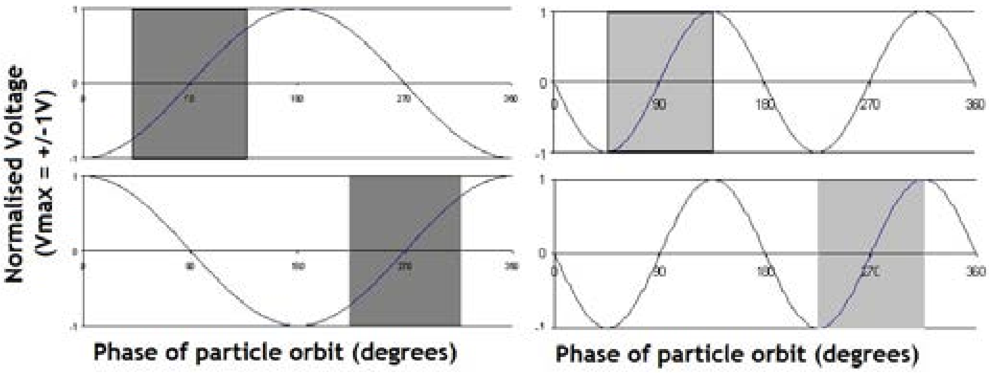

Figure 3.3: The horizontal axis shows the phase of the particle's orbit. The vertical shows the voltage normalised to $V_{Max} = \pm 1$. **Left:** N=1, where top and bottom plots show the two dees and how the normalised voltage oscillates across a period. The shaded regions depict the times within the cycle that the ion is passing through each dee respectively. Note how the dees are out of phase. **Right:** As left, but depicting N=2. Note how the dees are in phase and yet the ion experiences the same fluctuation in both.

energies see Table 3.1.

Ion	Energy Range (N=2)	Energy Range (N=1)
Protons	11 - 38 MeV	3 - 9 MeV
Deuterons	N/A	5.5 - 19 MeV
^{3}He	35 - 53 MeV	9 - 27 MeV
^{4}He	N/A	11 - 37 MeV

Table 3.1: Capable energy ranges for various ions at the MC40 Medical Cyclotron (for N=1 and N=2).

Upon its final orbit, an electrostatic deflector (with a potential difference of 50kV) extracts the ions and delivers them down one of a number of beam lines. The extraction has about 60% efficiency, but this enough to run a proton beam current of 50μA and a helium beam current of 20μA [2].

The idea was proposed to commission the building of an irradiation facility at the cyclotron site. To replicate the damage done to the inner layer of the strips in the tracker for the HL-LHC, a fluence of 1×10^{15} 1MeV neq cm^{-2} is needed. Using 27MeV protons with a beam current of 1μA a fluence of 10^{15} cm^{-2} can be achieved in 80 seconds [4].

3.5.2 The Cold Box

The energy transfer from the beam into the sensor generates high temperatures. This introduces the risk of annealing the sensors (see Section 3.3). The annealing would result in at least partially repairing the damage done to the sensor, giving misleading results that would imply that the sensor is more radiation resistant than it actually is. To avoid this problem a cooling system must be employed to maintain a low temperature during the irradiations. The sensors should also be stored at such temperatures during any time that elapses between irradiation and testing.

As such, the University of Birmingham's irradiation facility has a purpose built cold box, constructed by the University of Sheffield. The cold box measures 12 inches by 15 inches by 20 inches and is primarily made out of foam coated in plastic in order to ensure good thermal insulation. The box is accessed through a removable lid with a peg-and-hole system packed with foam to ensure a tight seal when closed. There are two 6 inch by 3 inch windows in the box (located front and back) to allow the beam to pass through.

A cooling element is placed inside the bottom of the box which is connected to a chiller that pumps low temperature glycol around the system. A series of electrical fans are mounted inside the cold box to aid in circulating the cold air. The glycol chiller can be lowered to -25°C. However, due to the imperfect heat transfer into the cold box, the average temperature of a sample before irradiation is $\approx$ -15°C. The fans and the glycol chiller are controlled from a computer via a NI RIO Real-Time programmable controller using software created in LabView. The chiller takes more than 2 hours to transition from room temperature to -25°C.

Sub-zero temperatures will result in condensation forming inside from the box from the natural levels of moisture in the air. As such, before and during any period of time where the chiller is on, the box is purged with dry nitrogen from a gas bottle in an adjacent room. A constant, low stream of nitrogen is fed into the box throughout the duration of any experiment.

The under side of the lid has a mechanism that allows carbon fibre frames to be attached, directly in the path of the beam. These frames come in various designs and are used to mount the different types of sensors (see Section 3.4).

3.5.3 Irradiation Setup

The beam sweeps out a path across the carbon fibre frame, irradiating any samples mounted there. The beam comes into the box through a collimator which reduces it to 1cm by 1cm. The collimator itself has its own additional cooling to allow for beams of up to 2μA if necessary. The beam is fixed and is unable to move. Therefore in order to sweep out the path, the cold box has been designed to move in such a way that the beam makes contact with all parts of the frame. The cold box is placed on top of a mechanical mount (Figure 3.4). Like the chiller and fan system, this mount is also connected to a NI RIO Real-Time controller and software from LabView. From a computer in the cyclotron control room, the motion of the box and mount can be pre-programmed and executed. The standard procedure used in these experiments is to allow a horizontal sweep across the frame, followed by a vertical displacement of 0.5cm and then back across the frame, proceding in this fashion until the entire sample has been irradiated.

Experiments start with the box being purged with dry nitrogen and then the chiller and fans activated some 2 to 3 hours before the intended run time to allow for the box to cool down. Samples are fitted to the appropriate carbon fibre frames (this is often prepared before the day of experimentation) and are then attached to the underside of the cold box lid. Calibration of the beam's location is required before the experiment starts in order to ensure that the programmed path will place the beam where required. This is done by attaching a piece of gafchromic film to the frame in the starting position of the beam (where it should be located by default). The box is put into its 'home position' and is briefly exposed to the beam. The irradiated part of the gafchromic film will turn blue, indicating a 1cm by 1cm square (with some haloing effects - for examples, see Figures 3.1 and 3.2). By observing

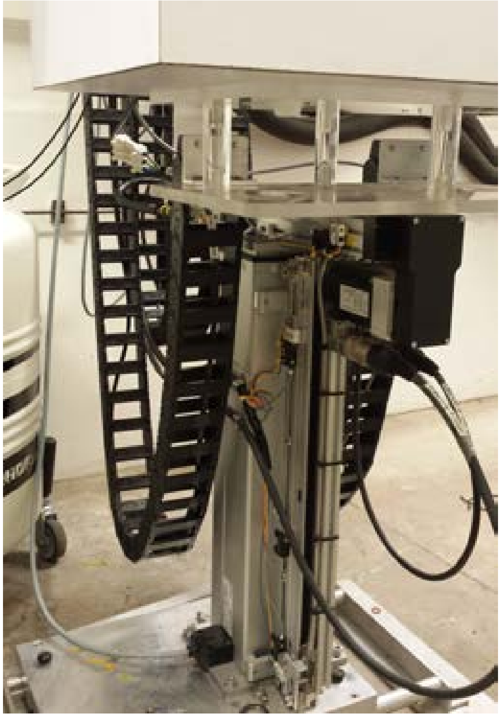

Figure 3.4: Photograph of the electronic mount that moves the cold box.

this position and extrapolating where path of the beam would go (based on the programmed instructions), the experiment will proceed or not. Depending on the path, these irradiations can take from 10 - 30 minutes.

3.5.4 Assessing Radiation Damage

Once irradiated, the samples are stored in a refrigerator to keep them below room temperature until they are shipped to the University of Liverpool where the damage is assessed. The system used to assess the damage is called the ALiBaVa (Analogue Liverpool Barcelona Valencia) readout system. It uses analogue electronics to readout many channels of data from silicon sensors with high sensitivity toward low signal strength and high readout speed. The electronics used in the connections to the sensors are based on technologies used for data readout in the LHCb VELO system.

The system can read out up to 128 data channels simultaneously. The signals are passed though a front-end amplifier and a 10 bit Analogue to Digital Converter (ADC). The system has a clock speed of 40 MHz. Beetle chips from the LHCb VELO design are placed on a 'daughter' board. Normally there are two chips per board, each chip reading 128 channels, resulting in 256 channels per daughter board. The sensors being tested are wire bonded to the beetle chips. The daughter boards are then stored in a cooled environment and are wired up to a 'mother' board which is allowed to operate at room temperature. The mother board is also connected to a triggering system which tells the system when the sensor is being hit. This occurs when electrons (from a β^- radioactive decay) pass through the trigger and are detected by the scintillator. The mother board communicates with a computer where it is controlled and read out data is stored.

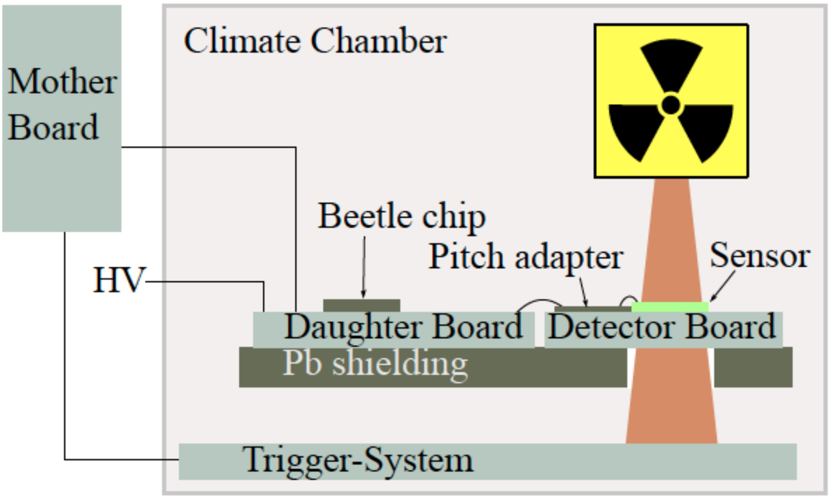

Figure 3.5: Diagram of the ALiBaVa System described in Section 3.5.4.

A voltage bias is put across the sensor, which is then exposed to ^{90}Sr, which beta decays and produces electrons which are then detected. The sensor's capacity to act as a detector is then assessed based on how much charge is collected by the sensor for a varying applied voltage bias. Plotting the collected charge and analysing the shape of the curve can tell us something about the damage done to the system. A sensor that has suffered from radiation damage will collect less charge and therefore will not be as sensitive to detecting radiation.

3.6 Early Studies

A set of mini-sensors had been irradiated at the University of Birmingham irradiation facility to a fluence of $1\times10^{15}\text{cm}^{-2}$ prior to my involvement in the irradiation project.

The sensors were then tested as outlined in Section 3.5.4. The sensors were exposed to a ^{90}Sr source at various voltage biases and the collected charge was measured. This data was then compared to similar data taken at KEK in Tsukuba, Japan and Los Alamos in New Mexico, USA. Each sensor had received the same nominal radiation dose and had been exposed to ^{90}Sr at the same bias voltages. The results are seen plotted together in Figure 3.6.

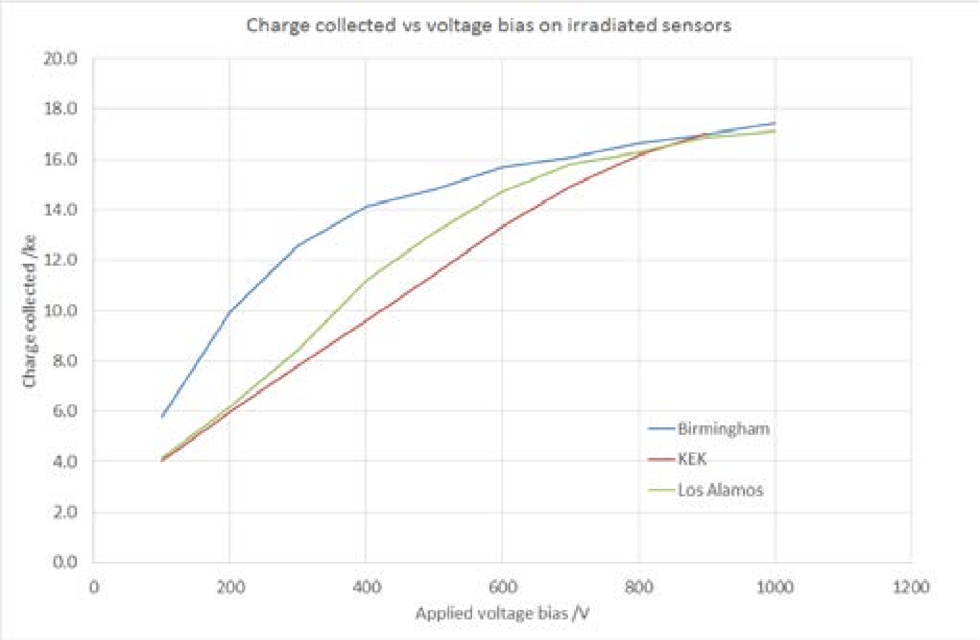

Figure 3.6: Plot showing the charge collection for a sensor irradiated in Birmingham and tested at Liverpool compared to sensors irradiated and tested at KEK and Los Alamos.

As can be seen, the Birmingham sensor is collecting more charge than the KEK or Los Alamos sensors. This would imply that it was not as damaged as the others. The sensors a KEK and Los Alamos were then deliberately annealed. They were kept at 80°C for 60 minutes, allowing some of the damage to repair itself. Plotting the Birmingham data against the annealed data from the other two facilities gives the plot in Figure 3.7.

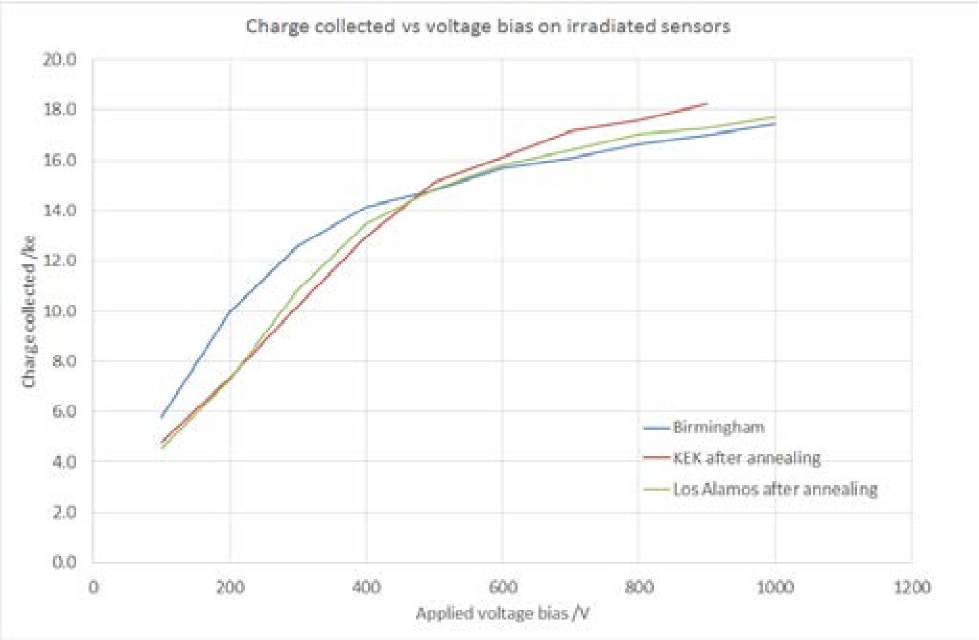

Figure 3.7: Plot showing the charge collection for a sensor irradiated in Birmingham and tested at Liverpool compared to sensors irradiated, tested and then annealed for 60 minutes at 80°C at KEK and Los Alamos.

As can be seen, the shape of the Birmingham data seems to fit to the annealed data of the other two facilities closer than in the first plot. The implication of this information is that somehow, the Birmingham sensor must have been annealed. This could only have been done through prolonged heat exposure. It was decided that the most likely cause of this was a large temperature spike during irradiation, despite the presence of the dedicated cold box. To this end, the temperatures of the sensors inside the box during irradiation needed to be measured and monitored. If tests confirmed that the temperature was high enough to encourage annealing, a new system would be needed to keep the temperature low during runs.

In order to understand why the sensors were being annealed, the temperatures needed to be measured and recorded. It was already clear that the temperatures are too high for the tests to run successfully. By gaining a better understanding of exactly how hot the sensor gets, appropriate measures could be taken to reduce the temperature.

3.6.1 The Temperature Sensor

The Pt-1000 is a type of resistance temperature detector. The name is derived from the fact that it is primarily made of platinum and that it is calibrated in such a way as to have a resistance of 1000Ω at 0°C. It can comfortably operate in temperatures ranging from -200°C to 600°C with an accuracy of ±0.05°C. It is approximately 2.5mm by 3.5mm in size and weighs 1g [67].

The Pt-1000 is connected to a data logger which sends the information to a computer to be stored for analysis. Two types of data loggers have been used during the tests included in this chapter. The one used at the time shall be specified in each test's section. The 'Keithley' data logger can record one input stream, where as the 'Agilent' can record many simultaneously. When required, the Pt-1000s are attached to the sensors using a two-part resin glue.

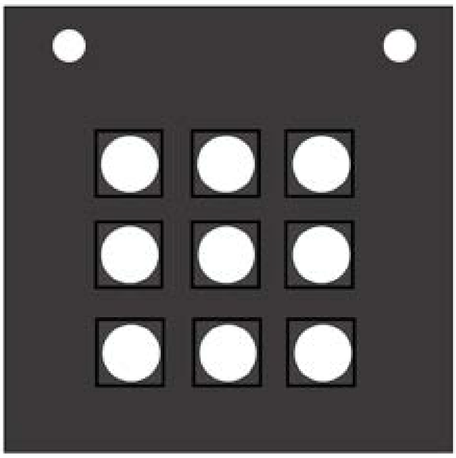

Figure 3.8: Diagram of the 3x3 frames, featuring a lip around the inside of the openings to hold sensors in place at the corners.

In order to reduce the amount of material surrounding the sensors which may act as insulation, a new frame was designed with a partial lip to hold sensors in place, as in Figure 3.8. Many tests were carried out, but in order to demonstrate the issues that came about, only one such experiment will be outlined in detail here.

Three mini-sensors were attached to an improved 3x3 frame in a diagonal formation. A Pt-1000 was attached to the centre of each sensor and wired up to an Agilent device, allowing the data from all three to be logged simultaneously. With beam current set to 1μA, the beam took a path over the sensor as shown in Figure 3.9.

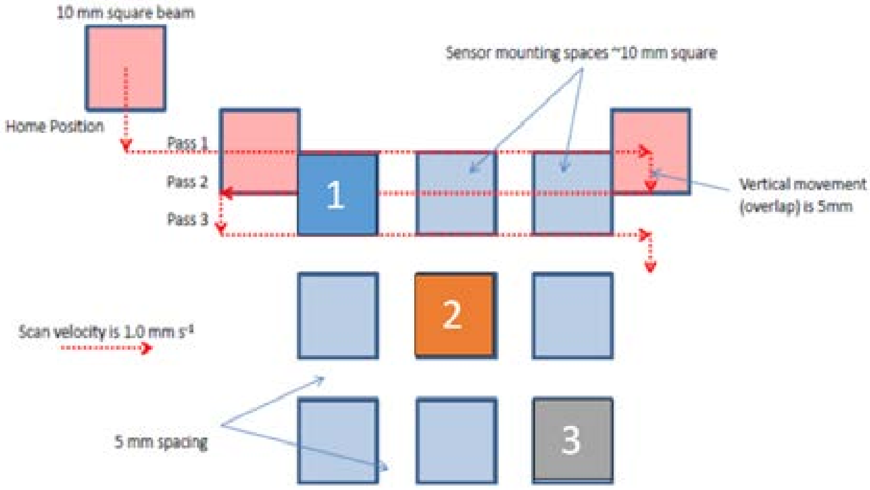

Figure 3.9: Diagram of the path taken by the beam. The path continued in a similar fashion downward until the entire frame had been irradiated. The colours of the sensors in this diagram are consistent with the colours of the plots in Figure 3.10 for each respective sensor.

The blue line (Sensor 1) in Figure 3.10, corresponds to the blue sensor in Figure 3.9, the orange line (Sensor 2) corresponds to the orange sensor and the grey line (Sensor 3) corresponds to the grey sensor. The peaks and troughs in the temperature plot follows the path made by the beam. The full height peaks correspond to the beam passing over the sensor completely, the half height peaks correspond to half the beam passing over the sensor.

The redesigned frames made very little difference. The temperatures were still getting too high, reaching a maximum of approximately 150°C. The next suggestion to address this problem was not based on improving cooling to the sensor, but instead to re-evaluate how the temperatures were being measured.

In all of the tests that had given very high temperatures (greater than 100°C), the Pt-1000 has passed through the beam as well as the sensor. A thorough investigation of the Pt-1000's properties under radiation was required to understand why. It was

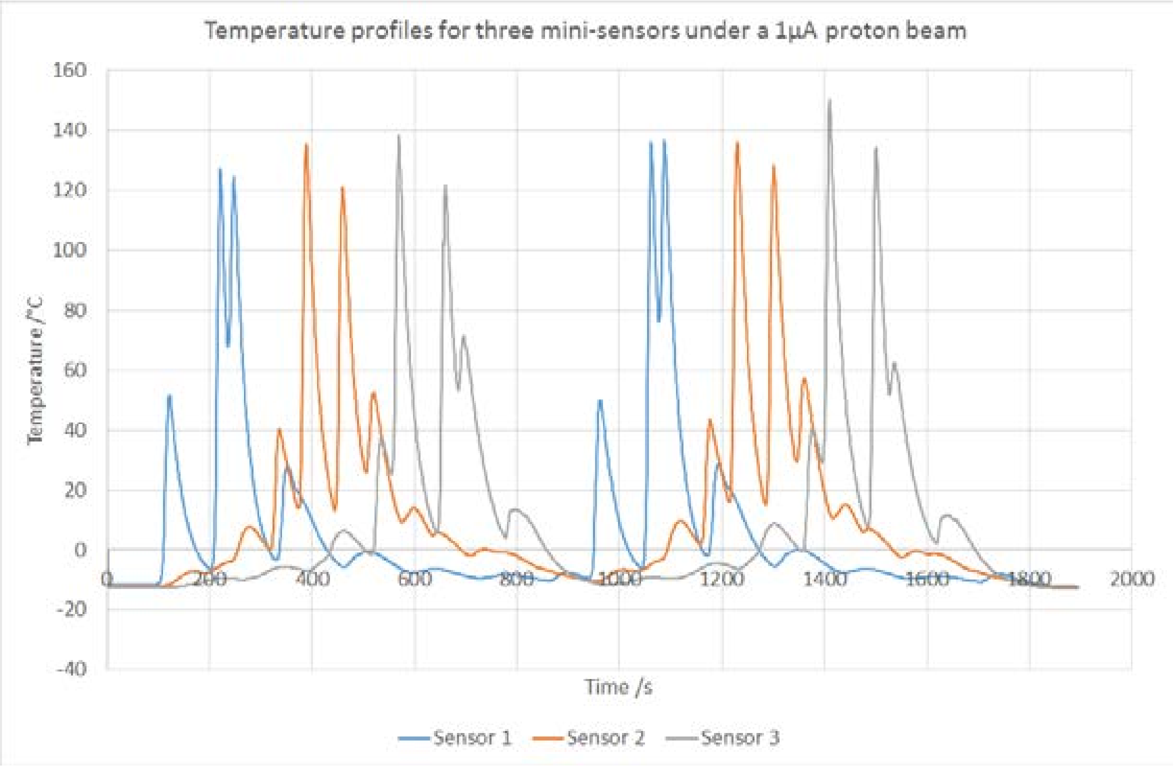

Figure 3.10: Plot showing the temperatures of the three sensors as recorded by the Pt-1000s attached to each as a 1μA proton beam passes multiple times.

found that a significant portion of the Pt-1000's internal wiring used platinum. The thermal properties of platinum are very different from that of silicon. Consider the energy deposited by a beam into a sensor:

$$\Delta E = FA\left(\frac{dE}{dx}\right)\rho l = F\left(\frac{dE}{dx}\right)m \tag{3.4}$$

where ΔE is the energy deposited, F is the paricle flux per unit area, A is the area of the sensor being irradiated, $\left(\frac{dE}{dx}\right)$ is the energy loss by the beam as it penetrates the sensor, ρ is the density of the sensor, l is its thickness and m is its mass. The resulting temperature change from the energy increase is described by $\Delta E = mC\Delta T$. Therefore:

$$\Delta T = \frac{\Delta E}{mC} = \frac{1}{C}F\frac{dE}{dx} \tag{3.5}$$

At constant flux, the temperature is directly, linearly dependent on $\frac{1}{C}\frac{dE}{dx}$. Specific heat capacity and energy lost in the material depend on the material. In Section 3.5.1, it was quoted that a fluence of 10^{15} cm^{-2} is achievable in 80 seconds with a beam with a cross section of 1 cm^2. This gives an approximate flux value of 1.25×10^{13} s^{-1} cm^{-2}. Table 3.2 shows these properties for carbon, silicon and platinum to demonstrate the heating in the frame, the sensor and the Pt-1000 respectively.

	Carbon	Silicon	Platinum
Specific Heat Capacity (J g^{-1} K^{-1})	0.71	0.70	0.13
$\frac{dE}{dx}$ (MeV g^{-1} cm^2)	17.9	15.7	9.0
$\frac{1}{C}\frac{dE}{dx}$ (1.6×10^{-13} cm^2 K)	25.2	22.4	69.2
ΔT (K s^{-1})	50.4	44.8	138.4

Table 3.2: Table showing some properties of various elements and how this relates to temperature gain in the beam.

As can be seen here, the temperature gain in the platinum is approximately 3 times greater than the gain in the sensor or the frame. The conclusion that was drawn from this is that when the frame is irradiated, the Pt-1000 heats up more than the sensor. The temperatures being recorded are not that of the sensor, but of the Pt-1000 itself.

Identifying this source of discrepancy did not dismiss all the heating issues. However it indicated that a better method of temperature measuring was required before any statements could be made about how hot the sensors got during irradiation.

A solution was devised to allow for temperatures to be measured without the Pt-1000 having to enter the beam. A ‘finger’ of silicon measuring 2mm x 20mm was attached to one corner of the mini-sensor. The Pt-1000 was then attached to the end of the finger. The finger was enclosed in a thermally insulating jacket of foam. When the mini-sensor is irradiated, the heat will travel down the finger toward the Pt-1000, where the temperature is recorded. For an image of how this looks, see Figures 3.19 and 3.20.

3.7 Temperature Tests Without Beam

A method is required to be able to understand the temperatures that the sensors can reach in the beam. In Section 3.6.1, it was shown that putting a resistance thermometer in the beam gave inaccurate readings. The solution to investigating the temperature profiles was to find a way to supply the equivalent amount of heat energy to the sensor without irradiating any components.

3.7.1 The Heating Element

The heat transferred by the beam was simulated by the creation of an electrical heating element. A small array of five 10Ω resistors in series, resulting in a net resistance of 50Ω, was mounted on a chip less than 1cm^2 (referred to from here on as the heating element). A 27MeV proton deposits 1.1MeV of energy into 300 microns of silicon. At a beam current of 1μA, this corresponds to a power transfer of 1.1W (1.1×10^6 joules per coulomb with 1×10^{-6} coulombs per second). Putting 1.1W across the heating element will result in all energy in the circuit being lost through the heat loss of the resistor array, therefore delivering 1.1W of heating energy to the sensor.

This however, assumes perfect energy transfer efficiency between the heating element and the sensor. Realistically, heat will be lost from the sides and the back of the array resulting in less energy being deposited in the sensor.

The advantage of this set up is that is avoids the accidental heating caused by irradiating the Pt-1000. The amount of energy transferred is exactly that which should be delivered to the sensor and is done so directly, avoiding the Pt-1000 heating up on its own, but as a result of being in thermal contact with the silicon. The heating element is connected via a series of long cables to a power supply in the control room, meaning that all aspects of any experiment can be conducted from the one desk.

As the element needs to remain in good thermal contact with the sensor, it cannot be moved. Unlike the beam that sweeps over the sample, the heating element will be fixed in place. Gluing the element on to the sensor would be unfeasible as not only would it ruin both the element and the sensor for further tests, it would also require an investigation of the thermal properties of the layer of glue that would lie between the two components. Instead, the heating element needs to be held in place with pressure. Attempts using rubber bands were not always successful as during some experiments, the high temperatures would cause the rubber to perish. The best solution was to use a window of Kapton tape as in previous experiments (for example, see Figure 3.11).

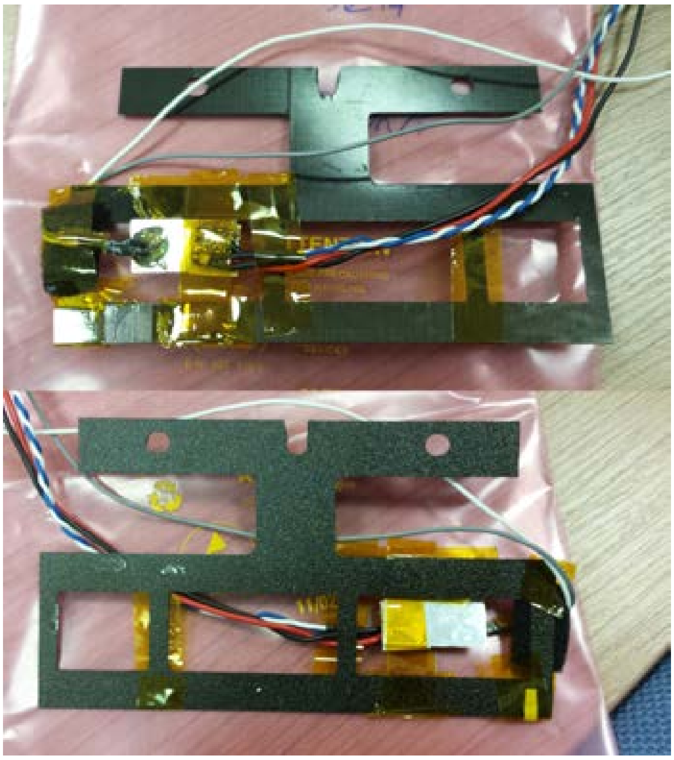

Figure 3.11: **Top:** Silver long sensor mounted on long frame. Pt-1000 glued to the left side of the sensor. Heating element pressed against the right side of the sensor by a window of Kapton tape. Red/Black wires power the heating element. Blue/white wires connect to second Pt-1000 stuck to the back of the heating element. **Bottom:** Reverse view of frame. Kapton window on other side helps hold heating element in place.

3.7.2 Extracting the Cooling Coefficient

The transfer of heat into a system can be modelled exponentially. The rate of energy flowing into the sensor is equal to that of the power transferred via the beam/heating element minus any energy lost through cooling. The cooling can be modelled by Newton's Law of Cooling (Equation 3.6).

$$\frac{dQ}{dt} = h\Delta T = h(T - T_A) \tag{3.6}$$

where Q is the heat energy, t is time, h is a cooling coefficient, T is temperature and T_A is ambient temperature (with ΔT defined as (T - T_A)). The differential describes heat lost over time. We can then define Q_{IN} ($= mC\Delta T$, where m = mass of sensor and C = specific heat capacity of silicon) as the over all energy entering the sensor. It follows that:

$$T = T_A + \frac{P}{h}\left(1 - e^{-t\frac{h}{mC}}\right) \tag{3.7}$$

where P is the power of the heating element. For full derivation, see Appendix A. As $t \to \infty$, $e^{-t\frac{h}{mC}} \to 0$ and $T \to T_F$ (where T_F is the final temperature at the plateau). If $T_F = T_A + \frac{P}{h}(1 - 0)$, then:

$$T_F - T_A = dT = \frac{P}{h} \tag{3.8}$$

If measurements have been taken of the temperature across a long period of time, values already exist for T_A, T_F and T for a given time. Power is 1.1W (see Section 3.7.1) and so h can be calculated. Different values of h can give us a quantitive way of determining the effectiveness of a cooling system.

3.7.3 The Cold Box - New Design

The case for an improved cooling sysem is already clear. Regardless of the accuracy of the Pt-1000 temperature measurements, there is evidence that the sensors are being annealed so the temperature must be brought down further. A new design was proposed by the University of Sheffield, the details of which will be outlined in this section.

The box is fundamentally very similar in design to its predecessor. Its outer dimenstions measure $60 \times 40 \times 50\text{cm}^3$ with two $15 \times 15\text{cm}^2$ windows and is made from insulating foam coated in plastic on the outside and metal on the inside. It is positioned upon the same mount and has the same method for attaching carbon fibre frames to the under side of the lid. The glycol chiller has been replaced with a liquid nitrogen based mechanism.

A large dewar of liquid nitrogen is positioned on the floor besides the mount. Attached to the top of the dewar is an electrical pump (specifically a Norhof 915 System [68]). The pump is connected to the same computer in the control room and is controlled from there. Liquid nitrogen that is pumped out, moves up a rubber tube toward a feed in through the top of the lid of the new box. It then precipitates through the box and lands on a metal heat sink - an array of metal teeth or prongs that are rapidly cooled by this processes. Then, as previously, a set of electrical fans (still controlled from the computer) blows air between the teeth of the heat sink, its increased surface area rapidly cooling the air (see Figure 3.13). This is all arranged in such a way the fan blows the cold air directly on to the sample area. Once again, the box is purged with dry nitrogen to prevent condensation of atmospheric water vapour.

This new system can comfortably set the cold box to -50°C in under 10 minutes. Not only is the temperature much lower, but the set up time for each experiment has now been drastically reduced. The Norhof 915 System regulates the temperature in the box by restricting and controlling the liquid nitrogen flow through the pump. It

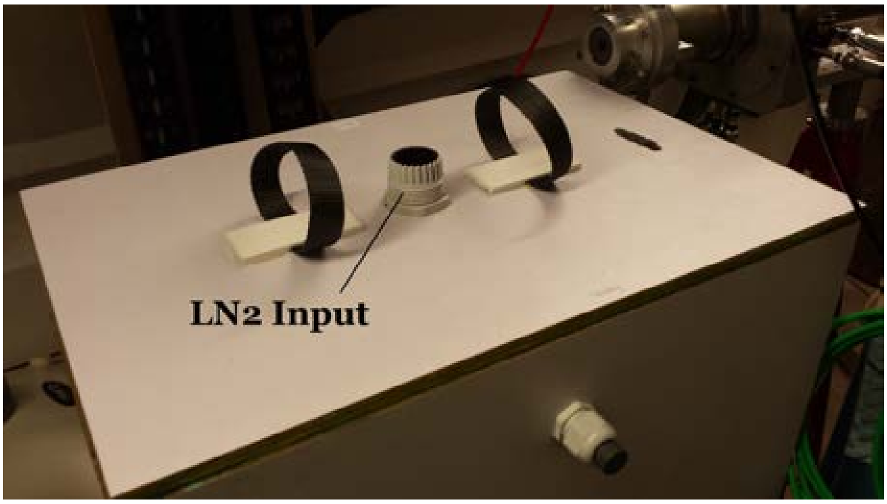

Figure 3.12: Photo of the lid of the new cold box. The the delivery tube connects to the pictured opening, which is positioned above the heat sink. Seen on the side of the box is a valve that allows air to flow out of the box whilst it is being purged with dry nitrogen.

Figure 3.13: Interior photo of the new cold box. Electric fan seen to the left. Heat sink to the right, placed directly underneath liquid nitrogen input. Edges of the box have been packed with silica gel bags to further reduce humidity inside the box.

has the capability to pump enough nitrogen to lower the temperature beyond -50°C, however this would be outside of the safe operating range for the electric fans inside the box.

Figure 3.14: The current state of the University of Birmingham irradiation facility after the installation. The dewar containing the liquid nitrogen used in the process can be seen to the left.

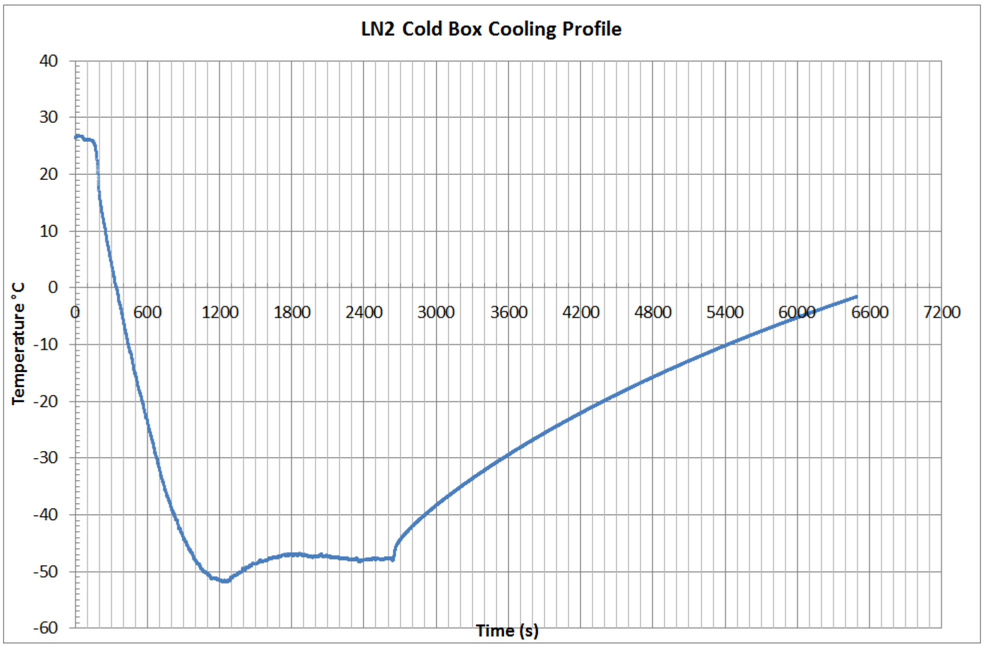

Figure 3.15: First test of the new cold box at the University of Birmingham. Rapid cooling for 20 minutes, followed by 10 minutes to reach stability. At approximately t = 2600s, the cold box was turned off.

3.7.4 Testing and Comparing the Finger Method

The first irradiation to take place following the installation of the new cooling system hoped to prove that attaching a finger to a mini-sensor would give an accurate temperature measurement as opposed to placing the Pt-1000 in the beam line. A 3x3 frame was set up and mounted upon it were three temperature recording methods to be compared. First was a long-sensor, mounted vertically. A Pt-1000 was placed at the top, in line with one of the windows on the first row of the frame. A second was placed at the other end of the sensor. The entire bottom half was surrounded in a thermally insulating jacket of foam. The second method was a 10mm by 10mm mini-sensor with a finger attached. A Pt-1000 was attached to the end of the finger. The final method was a simple mini-sensor with a Pt-1000 placed in the centre.

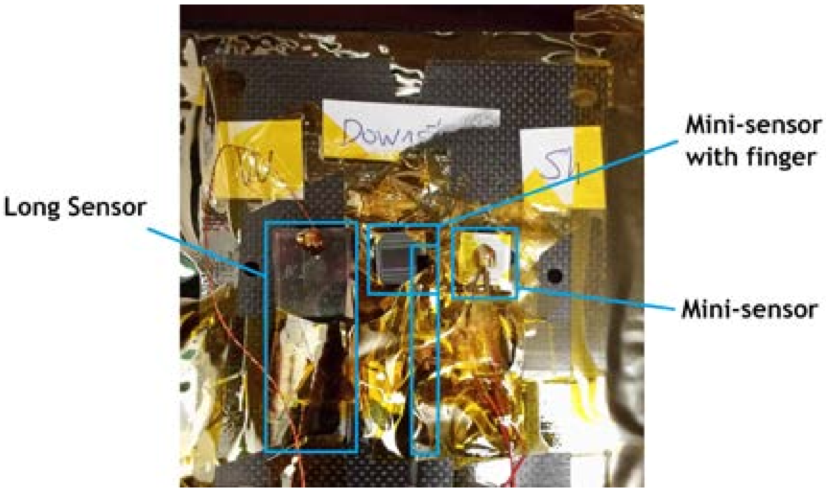

Figure 3.16: Photograph of the three tests mounted on the 3x3 frame as described above. Long with two Pt-1000s on the left. Mini-sensor with finger with one Pt-1000 in centre. Mini-sensor with central Pt-1000 on the right.

Each Pt-1000 was connected to an Agilent data logger. The cooling system was set to -50°C and given time to reach equilibrium. A 1μA beam was used for this experiment. The path taken by the beam was the same as in Figure 3.9, except with the sensors as placed in Figure 3.16 instead of the three mini-sensors. The resulting data is shown in Figure 3.17.

Pt-1000 Position	Initial T /°C	Maximum T /°C	ΔT /°C
Long (Top)	-56.28	27.92	84.19
Long (Bottom)	-54.99	-9.78	45.21
Finger	-56.58	-7.52	49.06
Mini-Sensor	-56.37	105.40	161.76

Table 3.3: Results of irradiating the three methods with a 1μA proton beam.

These results are very encouraging. As seen in Figure 3.18, the Pt-1000 on the

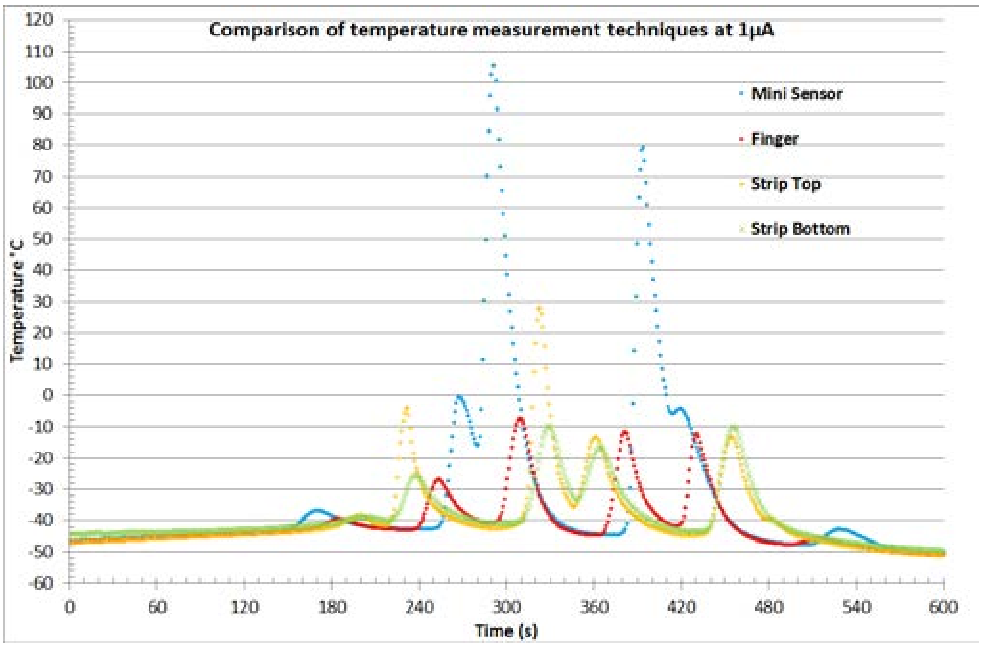

Figure 3.17: Plot of the temperatures recorded by the four Pt-1000s.

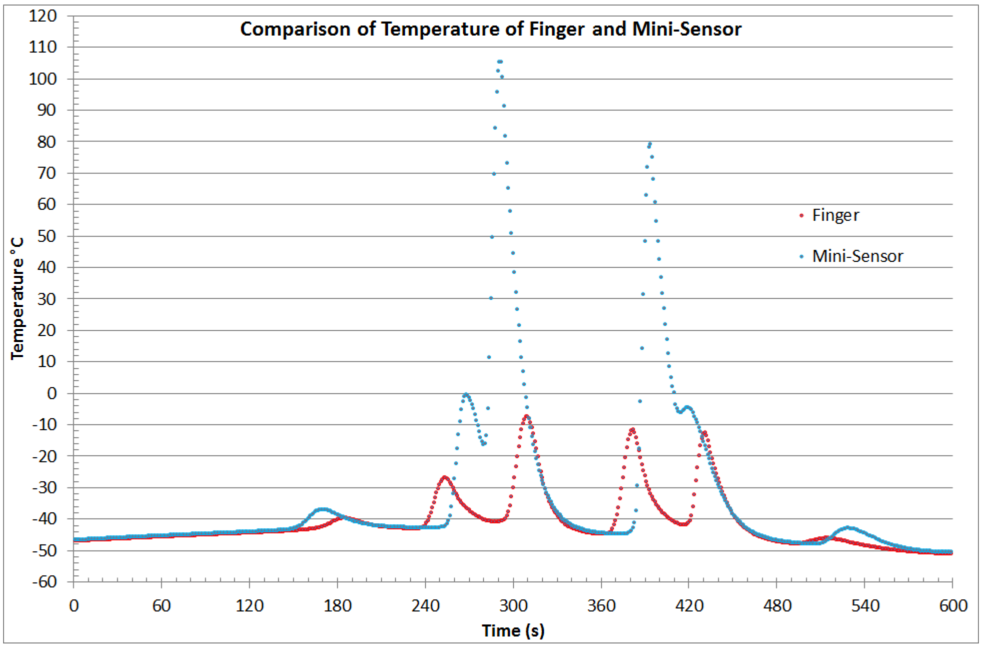

Figure 3.18: As Figure 3.17, but isolating the finger and the mini-sensor.

finger is not irradiated and therefore gives a more realistic reading. It is important to note that as Long (Top) and Mini-sensor results are the result of an irradiated Pt-1000, there is as of yet no evidence that the temperatures being recorded by the Finger and Long (Bottom) Pt-1000s accurately represent what the temperature in the beam line should be (this is explored in Section 3.7.5).

It is interesting to note that Mini-Sensor is hotter than Long (Top) by about 77.5°C. The current working theory to explain this difference is the difference in surface area of the two sensors. The mini-sensor has an area of 100mm^2 where the long sensor has an area of 450mm^2 (of which half is exposed to the air). The increased surface area means more contact with the cold air, resulting in more efficient cooling. The difference between Long Top and Bottom is 37.7°C and the difference between the Mini-Sensor and the Finger is 112.92°C. Again, this is explained by the difference in surface area.

3.7.5 Thermal Conductivity of the Finger

The experiment outlined in Section 3.7.4 cannot alone determine that the temperature recorded on the finger is an accurate representation of the temperature of the sensor. As the in-beam temperature measurements were recorded by directly irradiated Pt-1000s, they cannot be trusted. There is still no true value to compare the finger measurement to.

Using the heating element from Section 3.7.1 temperature profiles can be looked at without irradiating the Pt-1000. Two Pt-1000s were attached to a mini-sensor/finger system. One on the end of the finger, the other in the centre of the sensor. In order to conserve resources, a mini sensor and finger system that was incorrectly constructed was used (for details, see Figure 3.19).

The heating element was then pressed against the opposite side of the sensor and 1.1W applied to it. By recording the two temperature readings, the accuracy of the finger measurement can be determined. A third Pt-1000 was attached to the back of the heating element to monitor the temperature it was outputting. Test was conducted in the new cold box but at room temperature. The following variables were adjusted for different measurements; the fan turned on or off and the finger was insulated or exposed. Results of each test are shown in Figures 3.22-3.25 and in Table 3.4.

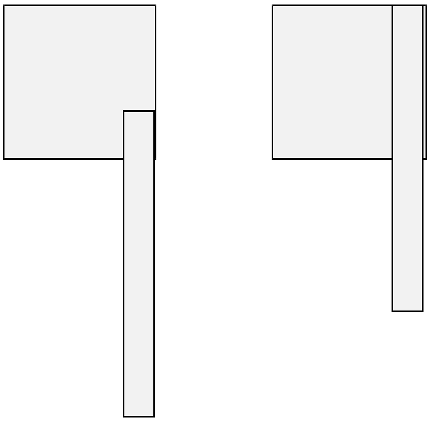

Figure 3.19: Diagram showing the difference between the correctly (left) and incorrectly (right) constructed mini/finger sensors.

Figure 3.20: Photograph of the mini/finger set up. Finger uninsulated. Two white Pt-1000s can be seen in the centre of the mini-sensor and on the end of the finger.

As can be seen, there is a significant ΔT between the finger and the sensor in all cases. It is also interesting to note that the temperature recorded by the Pt-1000 mounted on the heater is lower than the temperature recorded on the sensor. This could be for many reasons. The heat is generated at the point between the heater and the sensor. For the energy to reach the sensor Pt-1000, it only had to pass through 0.3mm of silicon. The other Pt-1000 was mounted on to one of the metal

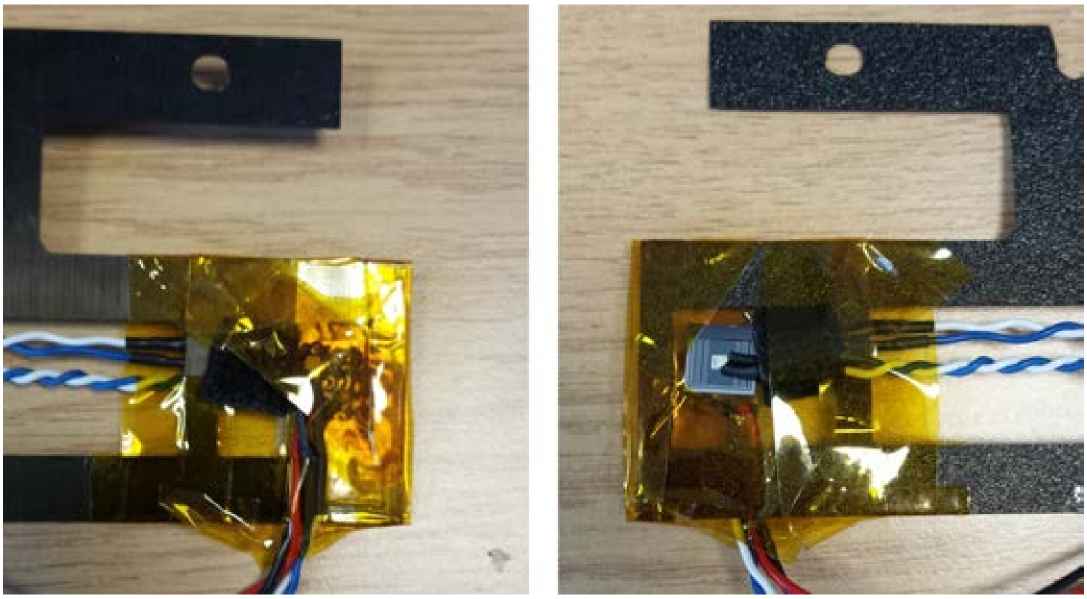

Figure 3.21: As Figure 3.20 but with finger insulated. Front and back views. On left image, the heating element can be seen underneath the kapton window. White Pt-1000 can be seen mounted on the left side of the back of the heater (again, under kapton window). Note that in this set up and in Figure 3.20, the mini-sensor always has one side exposed to the air.

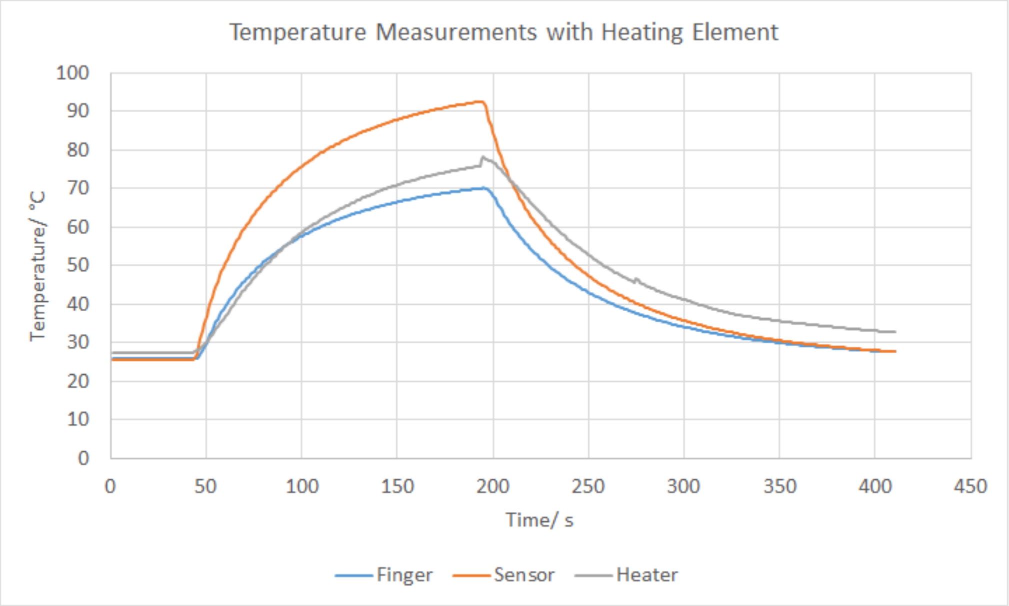

Figure 3.22: Plot of the temperatures of the sensor and the finger. Fan turned off.

contacts on the back of the heater. The board fragment that the heater is assembled on is 2-3mm thick. The contact is made of solder. The comparative difference in heat loss across 0.3mm of silicon compared to 2-3mm of solder and the other metals

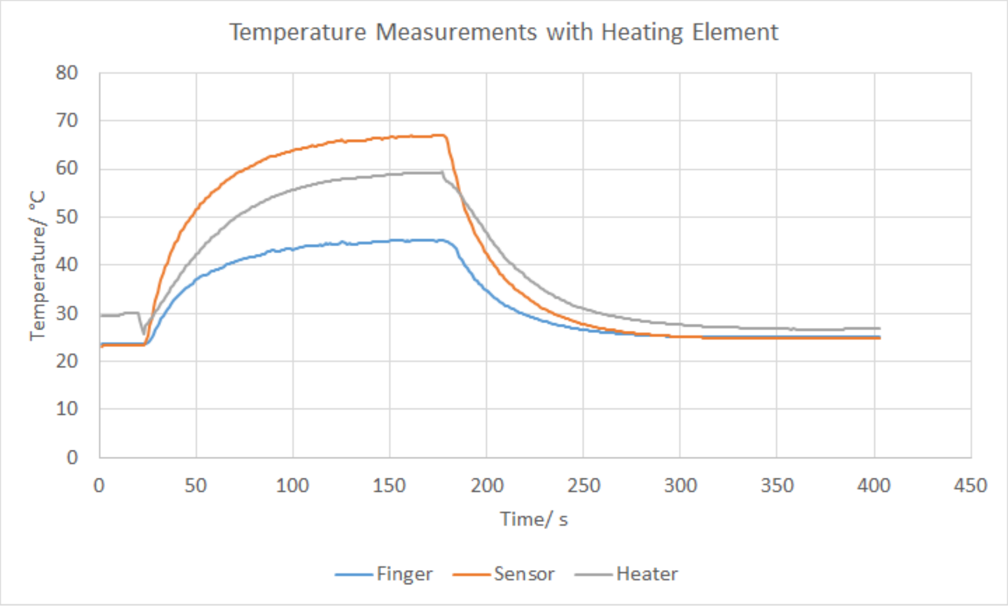

Figure 3.23: Plot of the temperatures of the sensor and the finger. Fan turned on.

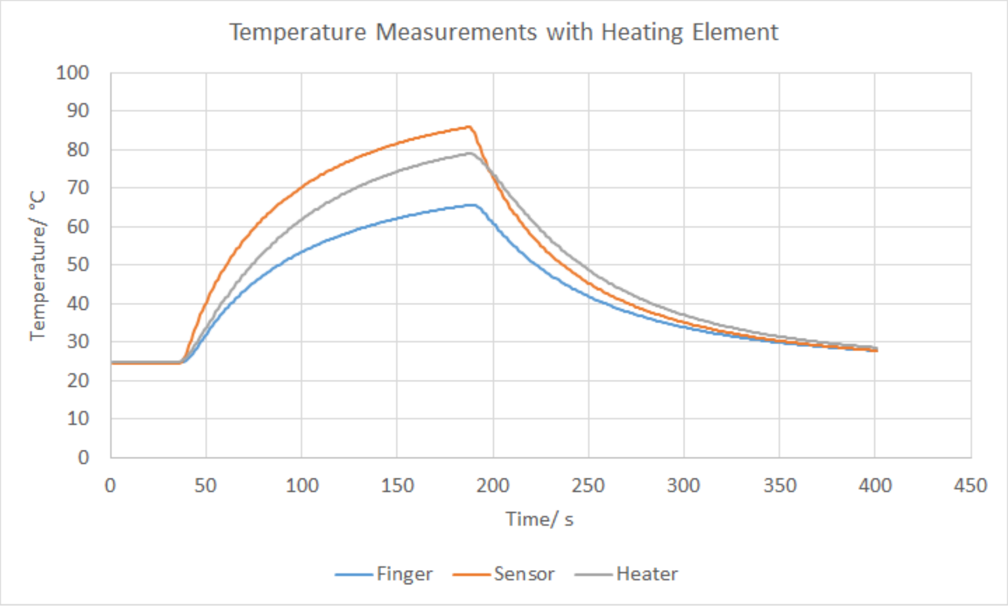

Figure 3.24: Plot of the temperatures of the sensor and the finger (insulated). Fan turned off.

involved in the path between the resistor and the contact is likely enough to cause this sort of temperature variation.

The cooling curves for the finger and the sensor follow very similar shapes. The heater is held in place with a kapton tape window, as insulation of the heater itself is not important in this experiment. This window covered the Pt-1000 attached to

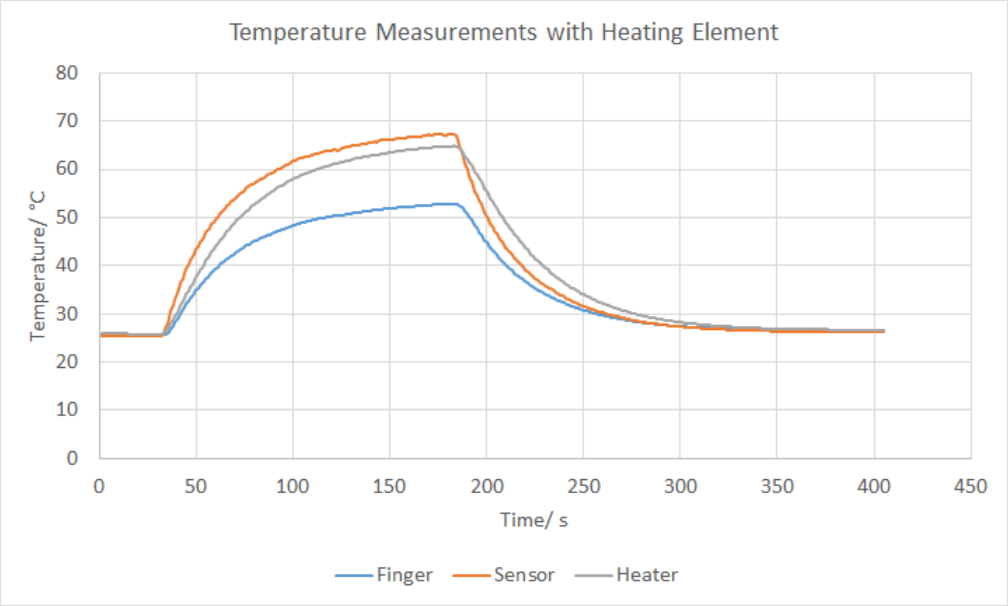

Figure 3.25: Plot of the temperatures of the sensor and the finger (insulated). Fan turned on.

the heater. This shielding can explain why the heater temperature drops at a slower rate.

In each of their respective cases (insulated and not insulated), the data follows the expectation that the temperatures are lower when the fan is on. It is illogical that the temperatures should be lower after the introduction of thermal insulation around the finger, however this is what is seen. Adding the insulation required direct contact with the frame. As the heating element is being held in place by pressure, it is very possible that a slight movement caused the contact between the sensor and the heater to change. This would explain the difference in temperature. This however does not really affect the experiment, as the measurement that matters is the temperature of one Pt-1000 in respect to the other.

As is logically expected, the smallest ΔT comes from having the fan on and the finger insulated. The fact that the ‘fan off’ experiments barely changed ΔT with the introduction of the insulation leads to the conclusion that it is less about insulating the finger and more about shielding it from the air flow.

3.8 Simulating an Irradiation Run

The final plan was to construct a model that would return estimations of the temperature changes experienced by sensors during irradiations based on a set of initial conditions. To reach this final result, there are two steps. First, the motion of the beam spot relative to the sensor needs to be modelled. Secondly, the sensor's reaction to the beam passing over it needs to be understood.

3.8.1 Modelling the Beam

As described previously in Figure 3.9, the beam follows a specific path, relative to the sensor. A program was created where users can input a path by specifying maximum distance traveled in x and y and then entering the speed in the x direction (speed in y direction is fixed at 20 mm/s). The coordinates and dimensions of the sensor are also input. The beam is modelled as 1 cm x 1 cm, with a slight Gaussian distribution.

An assumption is made that when the beam is entirely centred on the sensor 100% of the beam's power is transferred. The percentage of the beam spot area that overlaps the sensor can be used as an approximation as to the fraction of power transferred. The output of all of the above is a histogram that plots time against percentage area overlap. Multiplying this by the total power of the beam, one can model the irradiation as a solitary beam of varying power rather than a moving beam of constant power.

The option also exists to mount a finger on the sensor as previously described. Again, the location and dimensions are entered and a separate histogram is produced describing the percentage overlap of the finger and the beam.

3.8.2 Modelling Sensor Heating

There are multiple channels of heat transfer that need to be considered.

- Heat in to the sensor from the beam
- Heat out of the sensor to the air
- Optional:
  - Heat from sensor to the finger
  - Heat in to finger from the beam
  - Heat from the finger to the air

Three time dependent temperature profiles are created: the sensor, the finger and ambient. The ambient temperature is modelled as a straight line taken from the first and last data points before and after the irradiation respectively. No attempt is made to model changes in the ambient temperature based on heat transferred from the sensor and finger as this change would be negligible.

Initial conditions for the temperatures of the sensor and finger are based on the ambient air temperature at the start. The value for specific heat capacity for the sensor and finger is derived from fits performed during the heating element tests. Sensors and fingers were weighed accurately to return a mass value required for the calculation.

The model temperatures for finger, sensor and ambient are plotted along with data for the finger. Very good agreement is shown between the finger data and model.

3.8.3 Results

Different speeds were entered to produce different coverage percentage profiles. Different beam current values are entered, implemented as a different maximum power

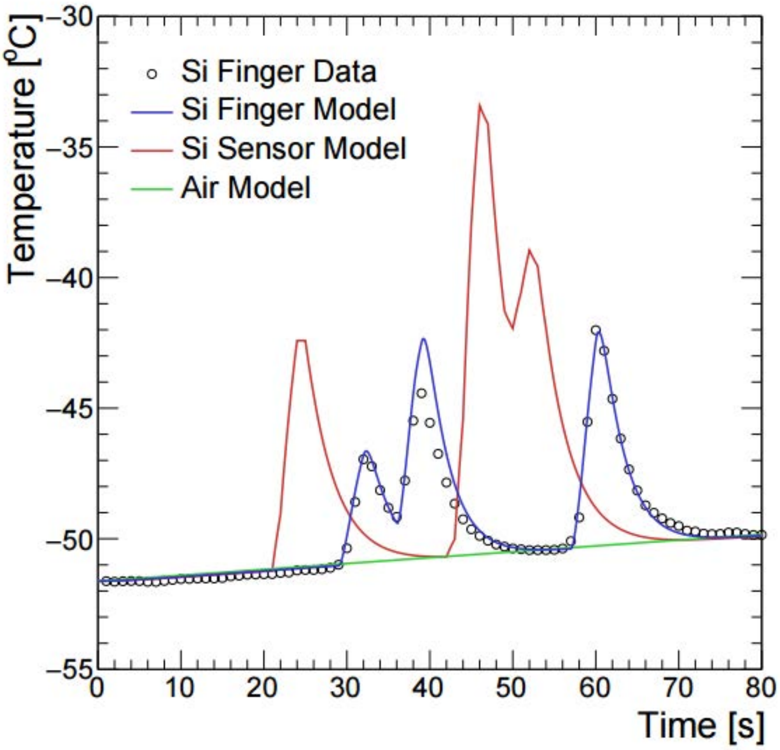

Figure 3.26: Model temperatures for a sensor, finger and air compared to data for the finger. Model and data shown here for beam speed of 4 mm/s with beam current of 0.5 μA.

delivered at 100% beam coverage. The change in temperature experienced by the sensor can then be seen for each configuration.

From this plot, the decision was made to run irradiations at a beam current of 0.5 μA with a beam spot speed of 4 mm/s, which results in a temperature change of 18°C when starting at initial conditions of approximately -30°C.

3.9 Summary

The primary problem faced in this work was the heating. Not only were the sensors being annealed, repairing the deliberate damage that had been caused to them, but the Pt-1000 thermometers gave inaccurate temperature readings during irradiations because of the effect of the radiation on the internal wiring of the device.

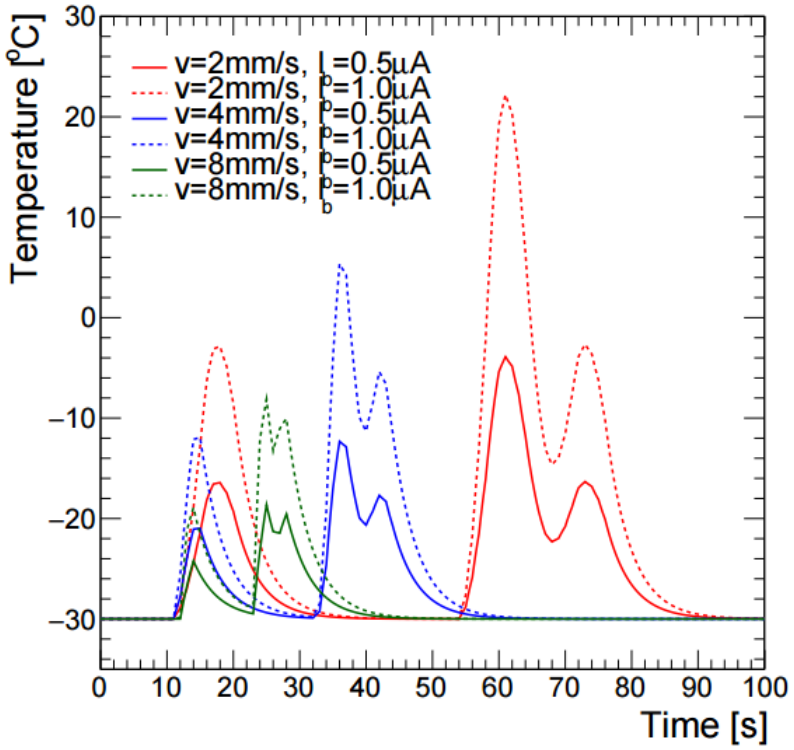

Figure 3.27: Sensor temperature simulations for all configurations of speeds at 2, 4 and 8 mm/s and beam currents of 0.5 and 1.0 μA.

Tests and suggestions where put in place to bring the temperature down by reducing the amount of material surrounding the sensor but the difference caused would not be enough to solve the problem alone.

Eventually a new cold box was designed, built and installed that used liquid nitrogen to bring the temperatures down to as low as -50°C. In order to be able to record temperature data, a system was devised whereby a finger of silicon was attached to the sensors to which the Pt-1000 was attached. The end of this finger would remain out of the beamline during irradiations.

The finger proved to be able to prevent the Pt-1000 from being irradiated, but a significant temperature difference was recorded between the sensor and the finger during non-irradation tests.

A model was developed which allows the user to enter initial conditions, irradiation path and sensor size. From this, accurate predictions of sensor temperature change could be derived. From this information, it was agreed upon that the best conditions to run irradiations under was at a beam current of 0.5 μA with a beam movement speed of 4 mm/s.

Running the irradiations with these lower temperatures did not result in a change in the charge collected. Annealing was ruled out as the cause. The cause of the anomalous charge collection was eventually identified as being the result of low energy protons hitting the target, which caused more ionisation damage than higher energy protons. This problem was eliminated by adding a thin shield of aluminium before the sample to filter out lower energy protons.

Parameters	Initial T_{Finger} /°C	Max T_{Finger} /°C	Initial T_{Sensor} /°C	Max T_{Sensor} /°C	Max ΔT (T_{Sensor}-T_{Finger}) /°C
Fan Off	25.75	70.14	25.47	92.65	22.56
Fan On	23.57	45.32	23.21	67.13	21.93
Fan Off, Insulated	24.84	65.73	24.57	85.878	20.72
Fan On, Insulated	25.55	52.27	25.27	67.35	14.63

Table 3.4: Table of results of the temperatures measured on the finger and the sensor of a mini-sensor/finger system under application of heat from the electric heating element.

CHAPTER 4

DATA AND MONTE CARLO SIMULATIONS

4.1 Software

Data and simulations need to be stripped of information that is not essential before they can be used in any physics analysis. Without this, the input files would be much too big to computationally process in a practical amount of time. The output of the ATLAS reconstruction software are data files in the xAOD format which contain summary information of the reconstructed and calibrated physics objects such as electrons, muons, taus, jets, track and event summary information such as which triggers were fired by the event. The 'x' in xAOD distinguishes the ATLAS Run 2 data event model from Run 1 which improves access speed and reduces file size. Further details on xAODs can be found at Reference [69], the documentation of the implementation of the ATLAS Run 2 event data model.

4.1.1 Detector Simulation

For both data and Monte Carlo (MC) the input to the reconstruction is the 'raw' data made up of hits. The MC hits are output from a simulation of the ATLAS detector which is based on GEANT4. It simulates the paths of particles through the detector material and the magnetic field.

4.1.2 Derivation Framework

The input to the derivation framework is xAOD. The events are further reduced in size (thinning) and selections for specific final states are made (skimming) to produce physics derivations. It applies the structures and tools required for specific user requirements and returns a DxAOD (Derived xAOD), which is designed to be smaller than the xAOD, eliminating data that is not useful for the analysis the derivation is intended for.

This analysis required the use of three different derivations based on the number of leptons in the event. HIGG5D1 is the derivation that selects only events with no isolated leptons, HIGG5D2 for one lepton events and HIGG2D4 for two lepton events. Analysis groups contact the central production team with requests for the derivations.

4.1.3 CxAOD Framework

The CxAOD (Calibrated xAOD) Framework is the framework used to process the DxAOD and produce the final 'ntuples' for the analysis. DxAOD files (from Section 4.1.2) are processed by the CxAOD Framework and the five packages that make it up (listed below). Auxiliary data is also generated at this stage. 'Shallow copies' of the data are created where only the 4-vector values that change during systematic shifts are written. The unchanged information points back to the nominal container.

Inputs and outputs remain separated by lepton number, as the original DxAODs were. The output file is referred to as a CxAOD. The five packages in this framework are outlined below.

- **CxAODMaker** - Main code that applies final calibration tools to the physics objects in the DxAOD files. The package also applies selections on the objects before outputting the CxAOD.
- **FrameworkExe** - The code for the executable files required to run the CxAODMaker jobs are contained here along with the associated configuration files.
- **FrameworkSub** - This package defines the input datasets used and contains scripts for tracking the progress of the processing.
- **CxAODReader** - Contains code to read CxAOD files. The other packages are used in creating the CxAOD. This package exists to read back the information. The reader package ensures consistency in the removal of overlapping objects for the nominal selection and systematically shifted objects. The final selections and calibrations that often change are made at this stage to avoid having to rerun the whole production process each time. These include the selection of event triggers and b-tagging selection and calibration.
- **CxAODTools** - This contains the general tools that do not depend directly on CxAODMaker or CxAODReader and includes event selection.

In addition to the core packages above, derived copies are used to implement selections specific to the analysis.

4.2 Object Reconstruction

In this section the object reconstruction parameters will be described. They were chosen with a view to maximise the acceptance of the objects we anticipate from the signal events. Efforts were also made during object reconstruction to reduce backgrounds coming from both electroweak and multijet events.

Rigorous reconstruction rules are required for leptons (both muons and electrons), small-R jets, large-R jets and the missing transverse energy. Leptons are important for the lepton veto in the control region and the one and two lepton requirements needed in the W+jets and Z+jets control regions respectively. The signal and control regions are further split up into resolved jets and fat jet regions. To this end, it is important to have clear rules for reconstruction of small-R (Section 4.2.3), large-R jets (Section 4.2.5), and the track jets associated with the latter (Section 4.2.6). Lastly, reconstructing the missing transverse energy is very important due to the expected high amount of E_T^{miss} in the signal events.

This section will only focus on the reconstruction of objects which are used in this analysis.

4.2.1 Muons

Muon objects are reconstructed based on information coming from the inner tracker and the muon spectrometer [70]. The selections used are those which are recommended by the ATLAS Muon Combined Performance Group.[1]

To select the desired number of leptons in the signal region (0 leptons, see Section 5.2), the W+jets control region (1 lepton, see Section 5.3.1) and the Z+jets control region (2 leptons, see Section 5.3.2), 'LooseMuons' selected. LooseMuons are defined as having passed the 'LooseID' identification criteria[71] to a working point of $\geq 99\%$ efficiency (this is referred to as the 'LooseTrackOnly' working point). As well as passing the isolation criteria, LooseMuons are defined as having $p_T > 7$ GeV, impact parameter ($d0$) significance < 3 and $|z_0 \sin\theta| < 0.5$. Here, the impact parameter significance is defined as $d0/\sigma(d0)$, where $d0$ is the impact parameter (the closest point on a track to the primary vertex) and $\sigma(d0)$ is the error on the impact

---

[1] https://twiki.cern.ch/twiki/bin/view/AtlasPublic/MuonPerformancePublicPlots

parameter. z_0 is the z-axis component of the vector connecting d_0 and the primary vertex and θ is the angle between the track and the z-axis (where the z-axis here is the beamline).

4.2.2 Electrons

Electrons are identified by matching energy clusters in the Electromagnetic (EM) calorimeter to tracks from the Inner Detector (ID). Background discrimination is supplied by the shower shape information from the calorimeter, the presence of high energy hits in the Transition Radiation Tracker (TRT) and compatibility criteria between the hits registered in the tracker and calorimeter.

Electron selections are based on the recommendations from the ATLAS Egamma group[2]. Selections are made on 'Loose' electrons which are defined as satisfying the 'LooseLH' identification criteria[72, 73]. The isolation requirements use the LooseTrackOnly working point. Electrons need to have $p_T > 7$ GeV, d0 significance < 5, $|z_0 sin\theta| < 0.5$ and must be central, where central is defined as electrons with $|\eta| < 2.47$.

4.2.3 Small-R Jets

The analysis is done in two parts: a resolved region using small-R jets and a merged region using large-R jets. In the resolved region, two b-tagged, small-R jets are used to reconstruct the Higgs boson. The individual small-R jets themselves are reconstructed using topoclusters taken from the energy deposits in the calorimeter cells. They are defined using the anti-k$_T$ algorithm [19]. The radius parameter in the algorithm is set to R = 0.4.

The anti-k$_T$ algorithm first looks for hard particles. Hard particles are defined as having p$_T > 20$ GeV. Particles with 7 GeV $< p_T <$ 20 GeV are referred to as soft

---

[2] https://twiki.cern.ch/twiki/bin/view/AtlasPublic/ElectronGammaPublicCollisionResults

particles. Soft particles within a predetermined radius R are clustered with the hard particle. Provided that there are no other hard particles within $2R$, all soft particles within radius R will cluster to the primary particle forming a cone. If a second hard particle is found within the range $R < x < 2R$, in order to prevent the two cones from overlapping, a straight line is drawn down the locus where the radii overlap, dictating which soft particles cluster to which jets.

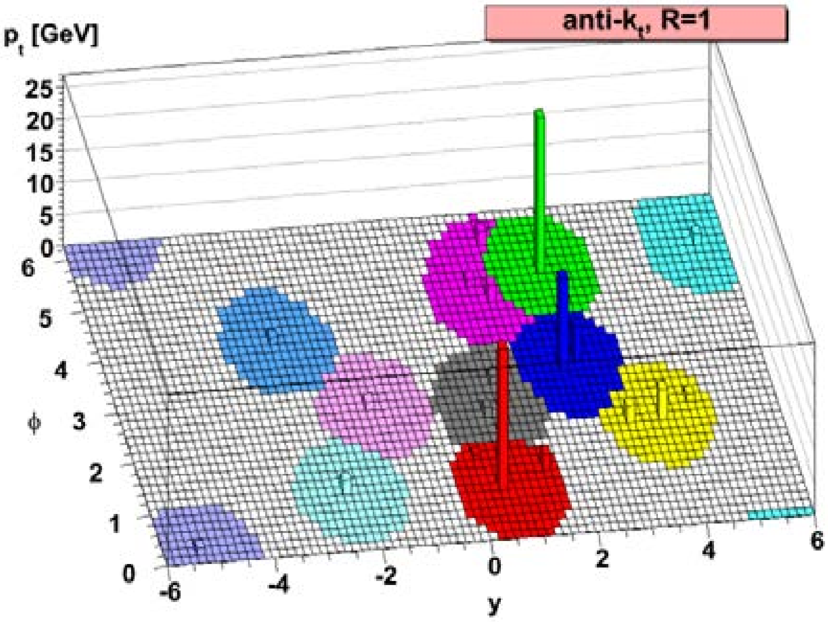

Figure 4.1: A sample of an event generated in Herwig with random soft “ghost” particles. Demonstrates how the anti-k$_T$ algorithm clusters particles.[19]

The energy scale of the jets needs to be corrected for effects coming from the detector. These include the difference in location between the primary vertex and the origin point of the detector, the lack of compensation from the calorimetry and the effect of dead material within the detector. The correction[74] scales the jets to the energies of the stable truth hadrons. Here, the definition of a stable hadron in the simulation is one with a lifetime (τ) where $c\tau > 10$ mm.

Jets have varying cuts on p_T based on the region of the detector within which they are found. Jets with $|\eta| < 4.5$ must have $p_T > 20$ GeV and jets with $|\eta| < 2.4$ must have $p_T < 50$ GeV. Rather than acting as a veto, jets within this population are submitted to another cut made on the observable output from the jet vertex tagger

(JVT)[75] at JVT > 0.64. The aim of this is to reduce the amount of jets that come from pileup.

To prevent overlap with electron tracks, a standard overlap removal procedure is applied as outlined in [76]. Jets located in $|\eta| < 2.5$ are referred to as ‘central jets’. Reconstruction of the Higgs boson is restricted to using central jets only in this analysis due to the selection requiring that b-quark decay products are detected in the silicon tracker. Jets outside of this region are ‘forward jets’.

4.2.4 MV2c20 b-Tagging Algorithm

It is important to distinguish which jets represent the b hadrons (b-jets), as these are specifically selected for Higgs boson reconstruction. The MV2c20 b-tagging algorithm is applied with a 70% signal efficiency working point. The algorithm uses multivariate techniques, namely a boosted decision tree which determines the discriminant based on track based observables[8, 77, 78].

The algorithm name indicates what fraction of the background training sample was made up of c-jets. It is harder to distinguish b-jets from c-jets than light jets. As such it is important to train over a reasonable c-jet sample size. In the 2015 configuration, MV2c20 means 20% of the training sample was c-jets, with 80% light jets. Figure 4.2 shows the output variable for the algorithm. To work at 70% operating efficiency, a cut on this output is placed at -0.0436. This value is taken from Table 4.1 which was taken from [8]. The high level of precision on this number is unnecessary, as the cut lies within a stable region, as seen in Figure 4.2. B-tagging efficiencies and rejection factors for c-, τ- and light-jets based on different cut values can be found in Table 4.1. The effect of increasing the fraction c-jets in the training population can be seen in Figure 4.3 where MV2c20 and MV2c00 algorithms are compared for c- and light-jet rejection (as suggested by the name, MV2c00 uses 0% c-jets and 100% light-jets in training). As can be seen, rejection of c-jets is much larger for MV2c20. The efficiencies for b-, c- and light-jets are shown as functions of jet p_T, $|\eta|$ and average number of interactions per bunch crossing are shown in Figure 4.4 for MV2c20 at 70% operating point.

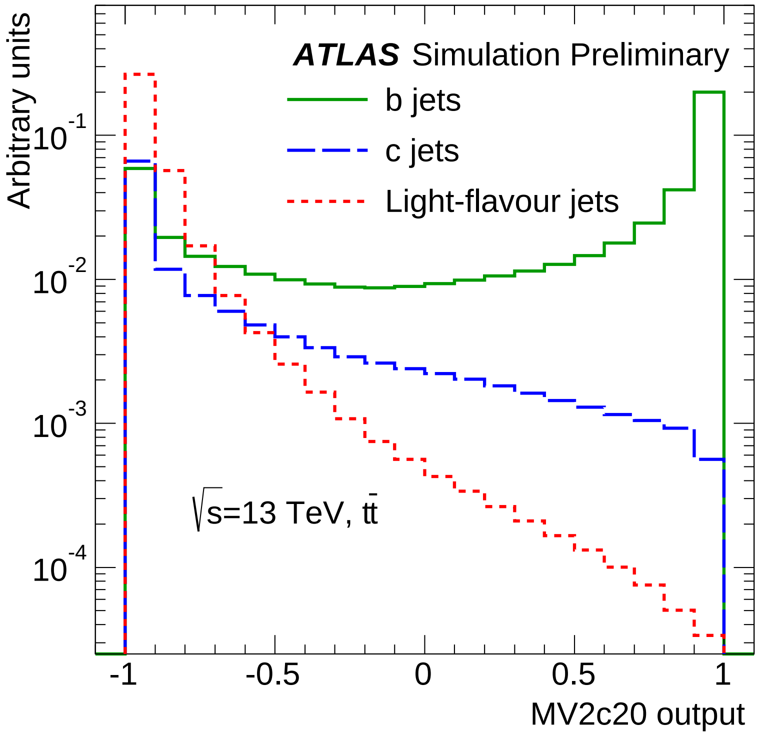

Figure 4.2: Output variable for the MV2c20 algorithm for b-, c- and light jets in $t\bar{t}$ events.[8]

Cut Value	b-jet Efficiency	c-jet Rejection	*tau*-jet Rejection	Light-jet Rejection
0.4496	60	21	93	1900
-0.0436	70	8.1	26	440
-0.4434	77	4.5	10	140
-0.7887	85	2.6	3.8	28

Table 4.1: B-tagging efficiency and c-, *tau*- and light-jet rejection factors for various MV2c20 output cuts.[8]

4.2.5 Large-R Jets

As well as considering Higgs boson reconstruction via two resolved small-R jets, the H→bb signal is also looked for in the 'merged' region. The merged region is so called as it is populated with highly boosted large-R jets, also known as fat jets. A pair of jets from a boosted vector boson will merge into a single fat jet. The mass of this

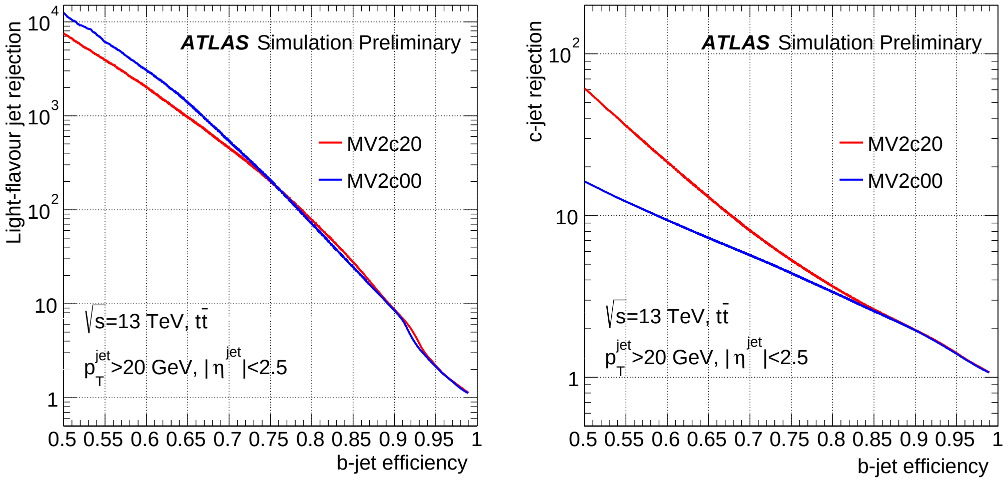

Figure 4.3: Light and c-jet rejection of the MV2c20 and MV2c00 algorithms for $t\bar{t}$ events.[8]

fat jet is calculated by combining the 4-vectors of the constituent ‘track jets’ (see Section 4.2.6). If one is able to discern the presence of two b-jets within this fat jet, it can be used to reconstruct the Higgs boson.

Fat jets are built up from topological clusters. These clusters are calibrated using the local calibration weighting scheme[79]. The anti-kt algorithm[80] used to reconstruct these fat jets operates with the distance parameter R = 1.0. The jets are then put through a trimming procedure which reclusters the components of the fat jet into a series of track jets[81]. The aim of this trimming procedure is to reduce the effects of pileup by excluding track jets which fail to meet certain criteria. The anti-kt algorithm is applied to reconstruct each track jet with a set radius R_{sub}. The trimming procedure then excludes any track jets with transverse momentum that is less than a given fraction of the fat jet. This fraction is referred to as f_{cut}. The values for these parameters used here are $R_{sub} = 0.2$ and $f_{cut} = 5\%$ (track jets are smaller than the small-R jets with R = 0.4). The remaining jets after the veto are summed to get the four-vector for the fat jet. The jet is then calibrated to the truth level jet energy scale and jet mass scale, supplied by the JetEtMiss group.

To select the most likely candidates for the signal process, the fat jet needs to be central and have high p_T. The jets must be within $|\eta| < 2$ and have $p_T > 200$ GeV,

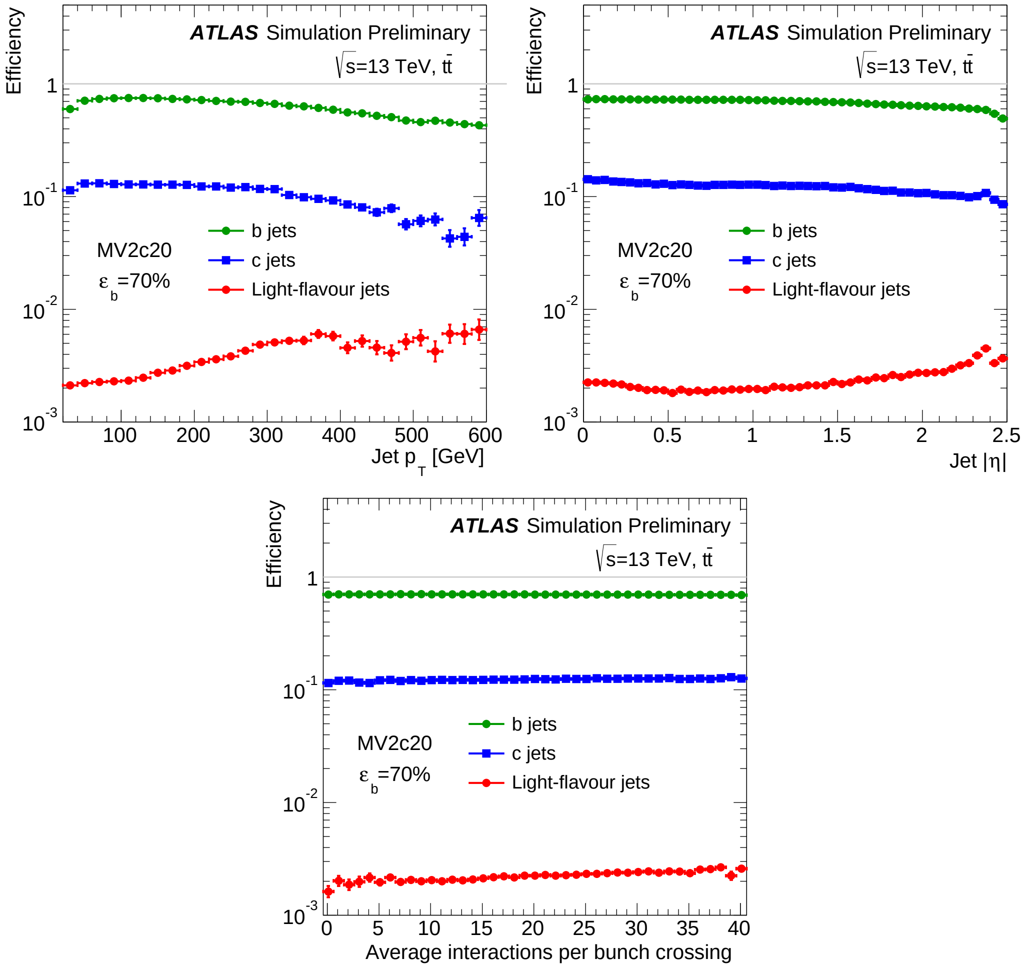

Figure 4.4: Efficiencies of tagging b-, c- and light-jets for the MV2c20 algorithm at 70% operating efficiency. Shown as a function of jet p_T, $|\eta|$ and average number of interactions per bunch crossing.[8]

which also selects tracks that have good agreement between the calorimeter and the ID.

Mono-Higgs signal fat jets have a particular topology and particular features which set them aside from QCD background jets.

B-jet taggers look at the mass of the jet and the topology to identify the flavour. The algorithm is modified to work with the boosted topology expected in fat jets. A signal fat jet is expected to contain two b-jets. The two highest p_T track jets contained within the fat jet are the ones considered for b-tagging. A 70% signal efficiency working point is applied. For more information on the track jets used in b-tagging of fat jets, see Section 4.2.6.

If a muon is found within dR < 0.2 of either of the track jets used in b-tagging, a correction is applied to the fat jet's 4-vector. This correction can be applied a maximum of two times for two muons.

Energy deposits in the topoclusters are assumed massless with their energy coming entirely from momentum. Recombining these objects, a reconstructed jet mass can be determined and then corrected using a MC-based calibration.

4.2.6 Track Jets

To pick out the constituent components of the fat jets, jet identification is repeated over the ID tracks with a smaller R parameter of 0.2 in the anti-kt algorithm (compared to 0.4 used for finding small-R jets). ID tracks have much better granularity and give a greater sense of the direction of the jet. This is useful as the more boosted the Higgs jet is, the greater the risk of objects merging together.

Once the list of identified track jets are compiled, they are then cross-referenced with the identified fat jets, to see whether they are associated or not. This process is known as 'ghost association'. The track jets are clustered within the fat jets and associations are drawn up between the them. In order for the track jets to be used in the b-tagging method mentioned in Section 4.2.5, track jets must have $\mathrm{p}_T > 10$ GeV, $|\eta| < 2.5$ and consist of at least two ID tracks.

4.2.7 MET

The MET is vital in the identification of the signal in this analysis as this is how the dark matter candidates will appear as they pass through the detector. Energy unaccounted for by reconstructed objects (as defined in Sections 4.2.1-4.2.6) is evaluated as MET[82]. This is done by the METMaker tool. A p_T^{miss} is calculated from the sum of the p_T from the reconstructed tracks with $|\eta| < 2.5$ originating from the primary vertex. Aside from use in identifying the signal, this is also used to remove beam induced backgrounds.

4.2.8 Combined Performance Plots

The combined performance plots summarise the detectors competence at reconstructing physics objects accurately and efficiently.

4.2.8.1 Muons

This section presents a summary of the combined performance plots for reconstructing muons during Run 2. The specific definition of which muons are used in this analysis is outlined in Section 4.2.1. All work in this section is taken from Reference [20]. Comparisons are made between 3.2 fb^{-1} of Run 2 data with $\sqrt{s} = 13$ TeV and $Z \rightarrow \mu\mu$ Monte Carlo simulations. Figure 4.5 shows reconstruction efficiency of Medium and Loose muons as a function of η. The efficiency for loose muons is only plotted for the region $|\eta| < 0.1$. In this region, the reconstruction efficiency between Medium and Loose muons varies dramatically, hence the Loose muons being explicitly plotted. Figure 4.6 shows the same for Tight muons. Muons used in both plots passed a selection for this study of $p_T > 10$ GeV.

Figures 4.7 and 4.8 show 2D maps in $\eta - \phi$ of the Medium muon reconstruction efficiency and Data/Monte Carlo scale factor respectively. As can be seen, the efficiency decreases the tighter the selections are. The analysis uses Loose muons, which have approximately 100% efficiency.

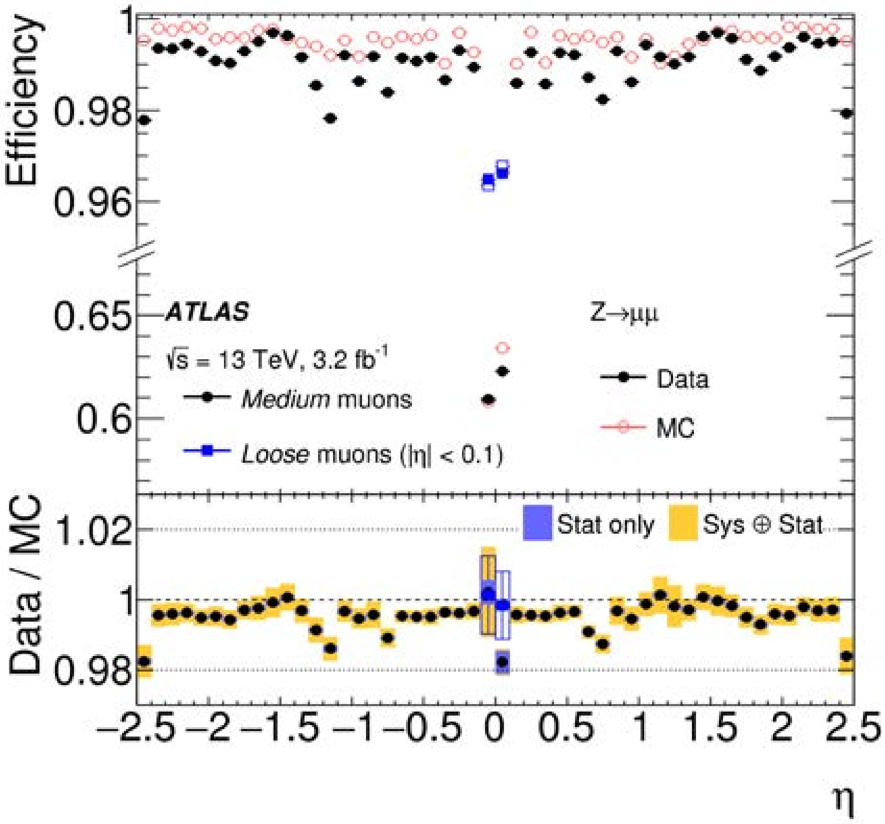

Figure 4.5: Reconstruction efficiency of Medium and Loose muons in Run 2 Data and Monte Carlo $Z \rightarrow \mu\mu$ samples shown in bins of η. A requirement that muons must have $p_T > 10$ GeV is made. [20]

4.2.8.2 Jet Reconstruction

Figure 4.9 shows the JES fractional systematic uncertainty as a function of jet momentum. Used in this plot was the complete 2015 $\sqrt{s}$ = 13TeV dataset. Jets displayed here are defined as anti-k$_T$ jets with distance parameter R = 0.4 and $\eta = 0$. Jet calibration is performed using the standard EM+JES calibration scheme. Pileup conditions for this test were based on the average experienced throughout the 2015 run. The calibration is done via a set of simulation based corrections and 'in situ' techniques. The latter uses the balance of transverse momentum between the jets and a reference object (a photon, vector boson, system of multijets). This is done within a range of $20 < p_T < 2000$ GeV[83].

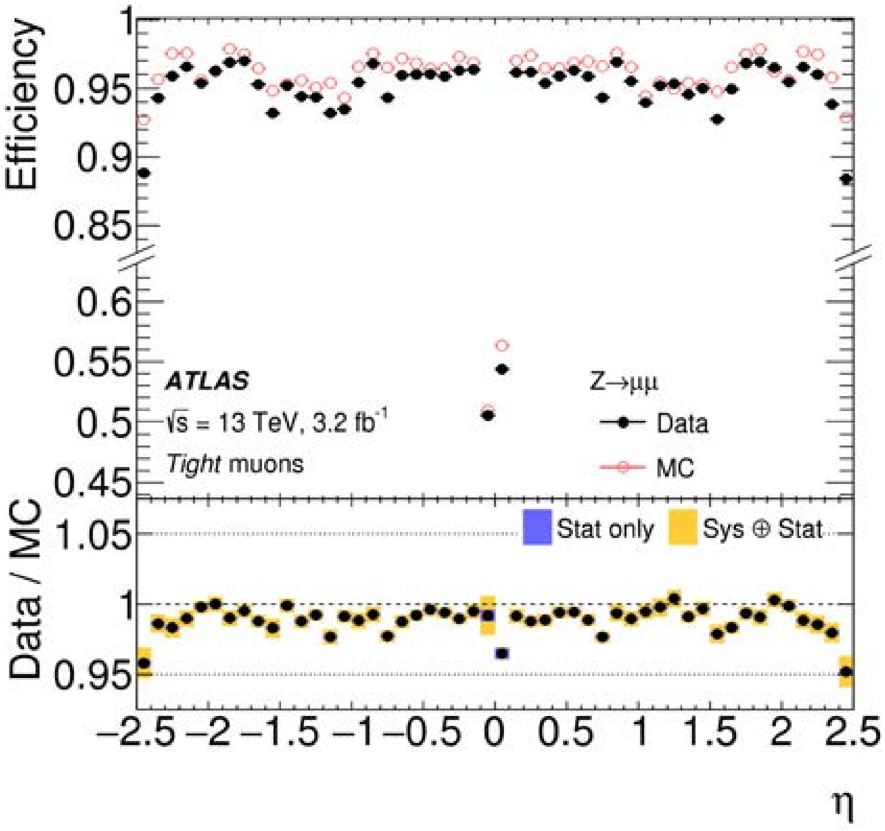

Figure 4.6: Reconstruction efficiency of Tight muons in Run 2 Data and Monte Carlo $Z \to \mu\mu$ samples shown in bins of η. A requirement that muons must have $p_T > 10$ GeV is made. [20]

The JES uncertainty decreases with increasing p_T as expected. From 200 GeV, a slow increase is observed due to statistical uncertainties from the 'in situ' calibrations. There is a sharp increase at 2000 GeV. This is because the multijet balance calibration only operates between 300 GeV and 2000 GeV. Above this, larger uncertainties are used from the single particle response. At low p_T, the contribution to uncertainty from flavour composition is significant. The composition is the inclusive dijet selection used in PYTHIA.

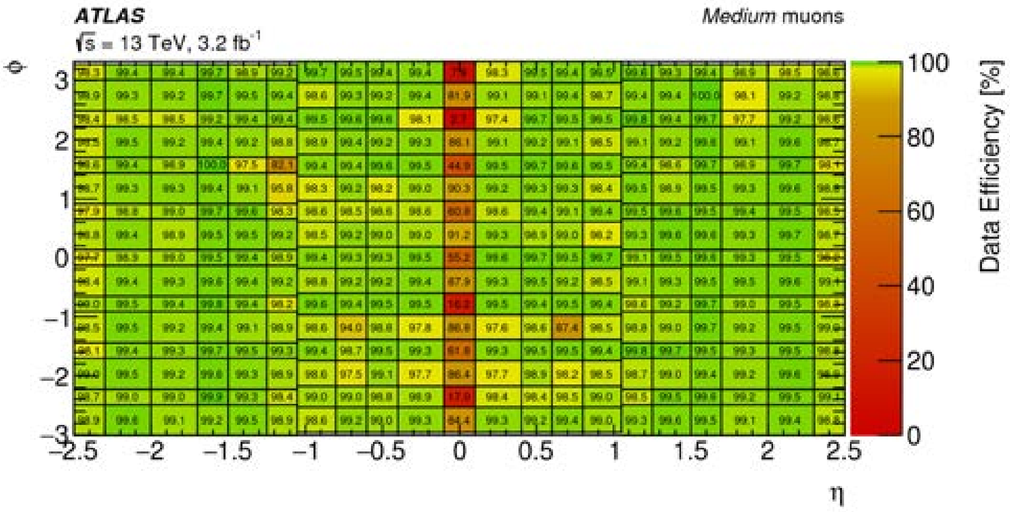

Figure 4.7: Reconstruction efficiency of Medium muons with $p_T > 10$ GeV in $Z \rightarrow \mu\mu$ events. Represented in bins of η and ϕ. Irregularity in bin sizes reflects the different bin boundaries in the barrel and endcap regions.[20]

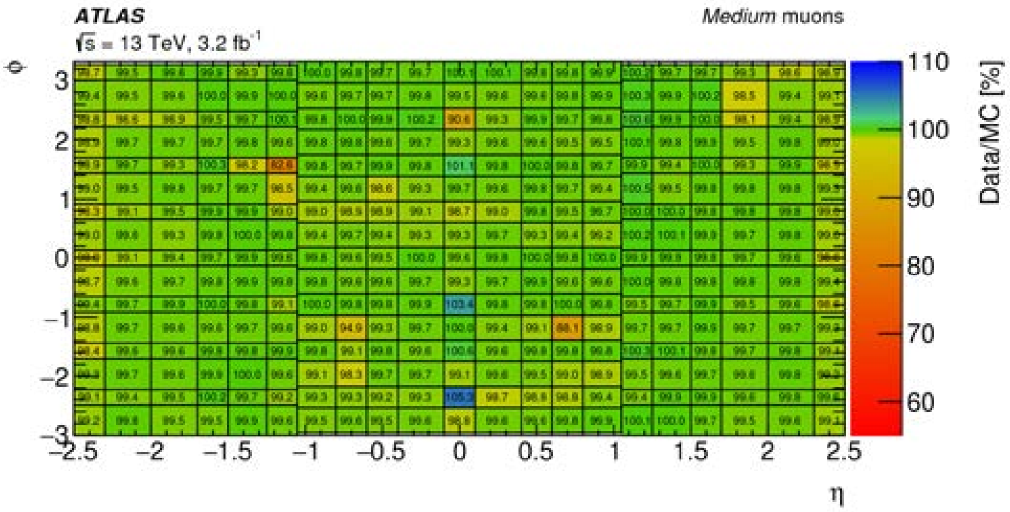

Figure 4.8: Data/MC scale factor of Medium muons with $p_T > 10$ GeV in $Z \rightarrow \mu\mu$ events. Represented in bins of η and ϕ. Irregularity in bin sizes reflects the different bin boundaries in the barrel and endcap regions.[20]

4.2.8.3 Missing Transverse Energy

The missing transverse energy is calculated by summing the combined transverse momenta of electrons, muons, taus, photons, jets and 'soft terms'. Soft terms are calorimeter clusters that are not associated with any objects.

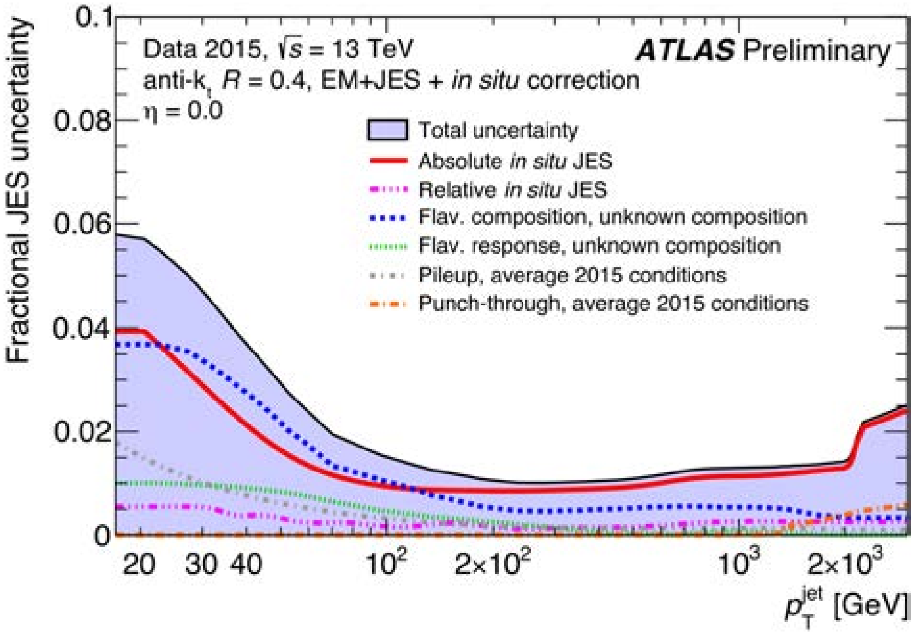

Figure 4.9: Fractional JES systematic uncertainty shown as a function of jet p_T for anti-k$_T$ jets with R = 0.4 and $\eta = 0.0$. Uses full 2015 dataset with $\sqrt{s} = 13$TeV.

During Run 1, different types of pile-up correction were tested on the soft term. Three of these methods used the jet area to calculate a track density value to be used in the pile up corrections. The leading method used an area called the Extrapolated Jet Area (EJA). A full list of area based methods can be found in Reference [21]. The main method which was approved and used in Run 1 was the Soft-Term Vertex-Fraction method (STVF). This involves scaling the soft-terms in the MET calculation by the ratio of the sum of soft-term track p_T from the hard-scatter vertex to the same sum over all primary vertices (including hard-scatter).

Figure 4.10, shows the missing transverse energy of the soft terms in a sample made up of $Z \rightarrow \mu\mu$ Monte Carlo with no pileup suppression applied. The MET distribution is generally peaked at low values (MET$<$ 20 GeV) as there is no expected MET in $Z \rightarrow \mu\mu$. Backgrounds used were $t\bar{t}$, WZ, ZZ and WW. 20fb^{-1} of 8 TeV Run 1 data is plotted alongside the simulations. Selection was made on MC and data that no jets should have $p_T > 20$ GeV. Figures 4.11-4.12 show the effects of the different suppression methods.

Figures 4.11 and 4.12 appear much more suppressed than in Figure 4.10. This

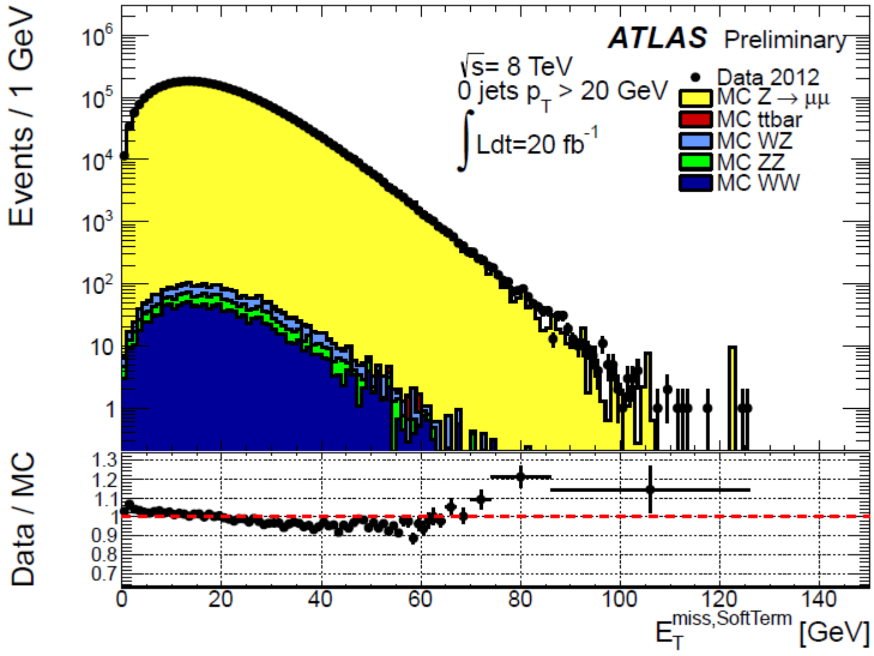

Figure 4.10: Distribution of the soft-term contribution to missing transverse energy with no pileup suppression applied.[21]

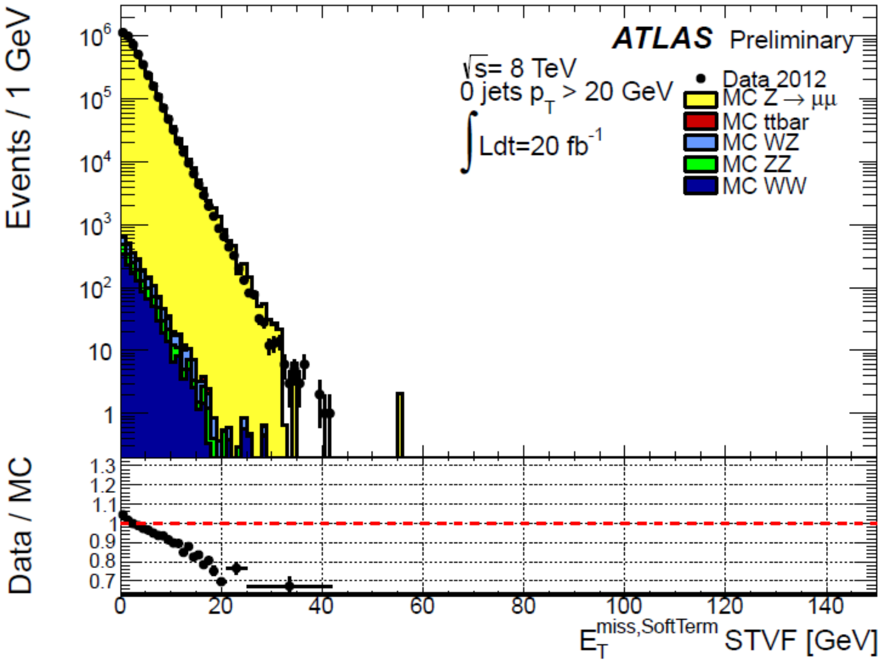

Figure 4.11: Distribution of the soft-term contribution to missing transverse energy with STVF pileup suppression applied.[21]

suppression is the weighting down of the soft terms from pileup. The STVF method is chosen because it achieves a high level of suppression. The poor modelling of this

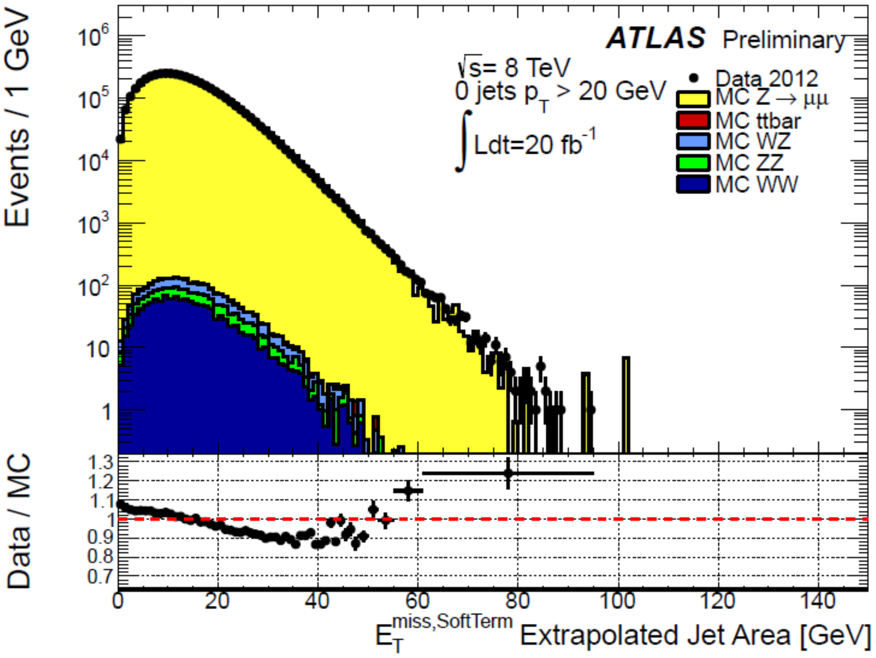

Figure 4.12: Distribution of the soft-term contribution to missing transverse energy with EJA pileup suppression applied.[21]

by the simulation is not a significant concern as the residual soft term contribution itself is small. For Run 2, plots were made showing E_x^{miss} and E_y^{miss} for the track soft terms of the total missing transverse energy, plotted against ΣE_T and the number of primary vertices. $Z \to \mu\mu$ Monte Carlo simulations were used once again and compared with 6pb^{-1} of 13 TeV 2015 data. These are shown in Figures 4.13 and 4.14, which demonstrate that the data is described well by the MC.

4.3 Data Sample

The data used in this analysis is Run 2 data taken from the ATLAS detector during 2015. Combined performance calculations and efficiency corrections are introduced to the data after it is processed through the CxAOD framework in Section 4.1.3. The specific production run used in this analysis is CxAOD_00-18-00 which contains 3.2 fb^{-1} of 25 ns data. A Good Runs List (GRL) removes periods of data taking where the detectors were faulty or inefficient to better improve the quality of the

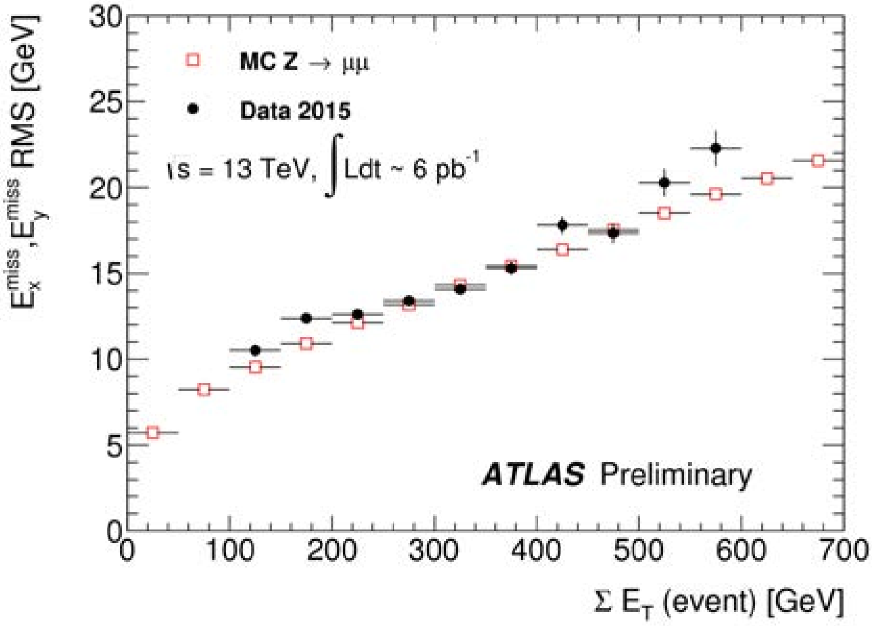

Figure 4.13: Missing transverse energy track soft-term resolution in x and y for 13 TeV 2015 data as a function of total transverse energy in the event.

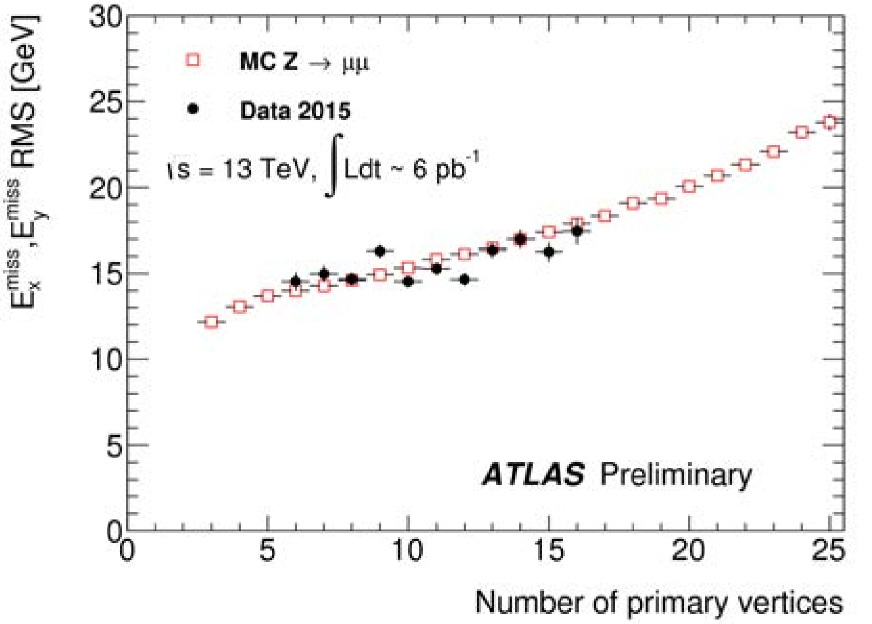

Figure 4.14: Missing transverse energy track soft-term resolution in x and y for 13 TeV 2015 data as a function of number of primary vertices in the event.

data. The GRL used for this production is data15_13 TeV.periodAllYear_DetStatus-v73-pro19-08_DQDefects-00-01-02_PHYS_StandardGRL_All_Good_25ns.xml.

4.4 Background Simulation

Simulations of all the significant backgrounds had to be generated for this analysis. The backgrounds have a preliminary scaling in order to set the ratios of the backgrounds based on the cross-sections. The control regions and the signal sideband regions are scaled to match the corresponding regions of data to account for deficiencies in the modelling. These normalisations are determined by a profile likelihood fit, which is described in Section 6.1. Simulations are also required for all the signal models discussed in Sections 1.5-1.6.3, each model being simulated multiple times for varying Dark Matter mass and intermediate state mass.

Table 4.2 shows a summary of the production methods used to generate the various simulations required for this analysis. The table shows the order of the calculation, the Parton Density Function (PDF) set used in the matrix element and the theory cross section to which they are normalised.

4.4.1 W/Z + jets Background

V + jets events make up a very significant portion of the background, where V corresponds to the vector bosons W and Z.

These events are generated in Sherpa 2.1.1[85]. Cross sections for these backgrounds are calculated up Next to Next to Leading Order (NNLO)[86]. These theoretical cross sections are used to initially normalise the backgrounds pre-fitting. The total cross sections are normalised to NNLO calculations within certain m_{ll} ranges.

4.4.2 $t\bar{t}$ Background

$t\bar{t}$ events also make up significant portions of the control regions used in the fit. $t\bar{t}$ events are generated in Powheg plus the Pythia6 interface[87]. Cross sections for the $t\bar{t}$ events are calculated using NNLO as well as next-to-next-to-leadinglogarithms (NNLL) which are also used for normalising the pre-fit distributions[88].

4.4.3 Other Background Processes

The main other backgrounds are diboson and single top quark events. Diboson events such as WW, WZ and ZZ are simulated in Sherpa 2.1.1. As in $t\bar{t}$ event production, POWHEG is also used to simulate the single top quark events. Cross sections used for the different types of single top quark events can be found at [89, 90, 91].

4.4.4 QCD Background

The QCD background events are not Monte Carlo simulated. Data driven QCD background estimates are used. For more details on how this is done, see Section 5.3.3.

4.4.5 Fragmentation and Hadronisation Modelling

All of the MC simulations listed in Sections 4.4.1-4.4.4 have a parton shower and fragmentation model. They all use a common tune to implement Initial State Radiation (ISR) and Final State Radiation (FSR) in order to simulate higher order QCD processes. The Multi Parton Interactions (MPI) processes are also included. The hadronisation of the partons from these processes is performed by EvtGen[92].

4.5 Signal Simulation

Mono-Higgs to b-jets in association with Dark Matter signal events are created using the MadGraph generator interfaced to PYTHIA8. For details of which mass combinations were generated, see Tables 1.4 and 1.5. The PDF used for the signal events was NNPDF30_lo_as_0130. For determining the uncertainty of the signal on the model parameters, the A14 eigentune [93] contains a set of Hessian systematic variations. These variations include those associated with FSR, ISR and MPI (Final State Radiation, Initial State Radiation and Multi-Parton Interactions). The tuning uses observables which are sensitive to the underlying event (transverse activity with leading track and calorimeter jets), jet structure (jet masses, jet shapes) and additional jet emissions (dijet azimuthal decorrelation, $t\bar{t}$ gap fraction and Z-boson p_T). More information on signal acceptance uncertainties can be found in Section 5.5.

4.6 Pileup Simulation

The mean number of interactions per bunch crossing, $< \mu >$, for the 2015 dataset is $< \mu >$=13.7 for proton-proton collisions at $\sqrt{s}$ =13 TeV. $< \mu >$ is measured by the LHC beam parameterised and normalised to the total σ_{inel} cross section at 13 TeV as measured by ATLAS[22]. The distribution of the number of collisions is shown in Figure 4.15.

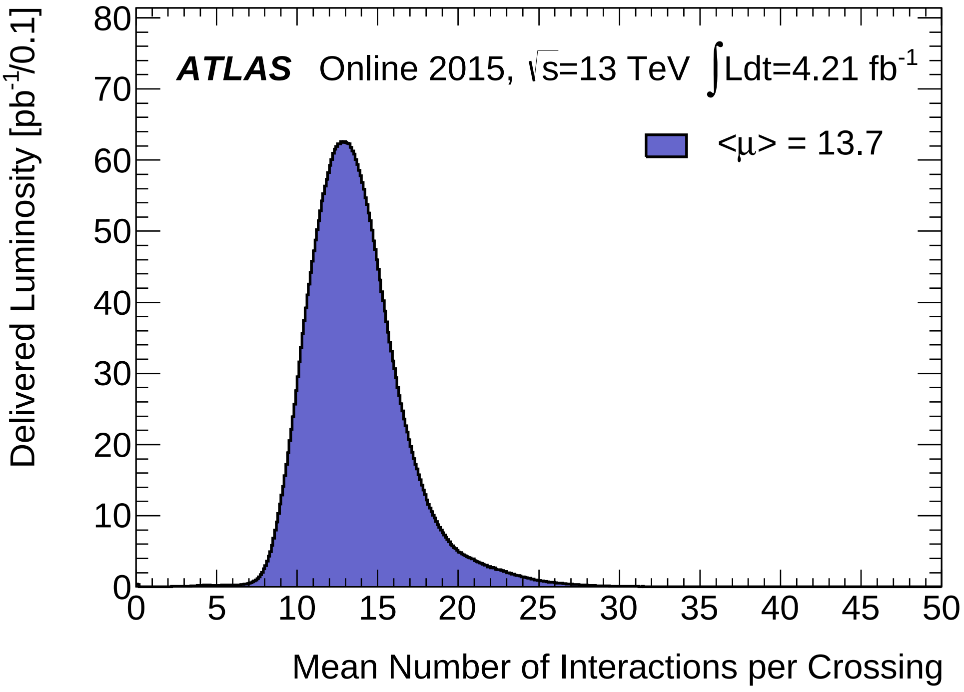

Figure 4.15: Distribution of the number of interactions per bunch crossing for 2015 proton-proton events within the ATLAS detector during stable beams with $\sqrt{s}$ = 13 TeV. Integrated luminosity over this period is 4.21 fb^{-1}[22].

Process	Generator	PDFs	σ_{norm}(pb)
$t\bar{t}$	POWHEG + PYTHIA6 (NLO)	CT10 [84]	831.76
$W \to \ell\nu$**+jets**	SHERPA (NLO)	CT10	20080
$Z \to \ell\ell, \nu\nu$**+jets**	SHERPA (NLO)	CT10	1906(66 $< m_{ll} <$116 GeV)
Single top			
t-channel	POWHEG + PYTHIA6 (NLO)	CT10	136.02+80.95
s-channel	POWHEG + PYTHIA6 (NLO)	CT10	6.35+3.97
Wt	POWHEG + PYTHIA6 (NLO)	CT10	71.7
Diboson			
$Wl\nu Wqq$	SHERPA (NLO)	CT10	23.65
$Wl\nu Zqq$	SHERPA (NLO)	CT10	11.41
$WqqZll$	SHERPA (NLO)	CT10	3.42
$WqqZ\nu\nu$	SHERPA (NLO)	CT10	6.75
ZZ	SHERPA (NLO)	CT10	15.03
SM $qq \to VH(\to bb)$	PYTHIA8 (LO)	NNPDF2.3LO	0.7639
SM $gg \to VH(\to bb)$	POWHEG +PYTHIA8 (LO)	CT10	0.1057
mono-H signals	MadGraph + PYTHIA8	NNPDF30_lo_as_0130	

Table 4.2: List of MC generators and parton distribution functions (PDFs) used for the signal and background processes. Details are given in the text.

CHAPTER 5

EVENT SELECTION

5.1 Analysis Strategy

All generated signal samples for this analysis will contain dark matter candidates back to back with a hadronically decaying Higgs boson. A common feature of the models is that the Higgs boson is produced with very high transverse momentum. In the opposing direction, the dark matter candidates will fail to be picked up by the detector, resulting in a large amount of E_T^{miss}. These objects give us two distinctive features to look for in the analysis. The first being the large missing transverse energy from the dark matter candidates. The second, being the decay of the high p_T Higgs boson to a pair of bottom quarks. Depending on the transverse momentum of the Higgs boson, the b-quark jets can appear differently in the detector, giving two categories to consider. The first is when the Higgs boson decays into two b-quark jets which are separated and easily resolved. This we refer to as the "resolved" region. As well as this, in the event of a highly boosted Higgs boson, the two b-quark jets are much less separated and are often interpreted as a single large radius jet (or “fat jet”). This is referred to as the “merged” region.

These two features go a long way toward singling out new physics, but much more work is required to diminish background processes. These are outlined below.

- Require events with large missing transverse momentum
- Use a missing transverse energy threshold to decide whether or not an event should be considered in the resolved or the merged region. The correlation between the value of E_T^{miss} and the transverse momentum of the Higgs boson allows for this to be a suitable discriminator. This is further discussed in Section 5.2.1.
- Resolved Region (Low E_T^{miss}):
  - Identify the two central jets to be used in Higgs boson reconstruction. Follow this selection process up with a series of cuts designed to reduce the background processes
  - Split the selected events up into populations based on the number of b-tagged jets contained in the event (0, 1 or 2)
  - Reconstruct the Higgs boson and use its invariant mass as the final discriminant
- Merged Region (High E_T^{miss}):
  - Select large radius jet
  - Split events up into populations based on number of b-tagged track jets associated with the fat jet
  - Calculate large radius jet invariant mass for use as the final discriminant
- Create control regions, each defined and selected to focus on a specific major background process. This is achieved by classifying according to the number of leptons in the event and the number of b-tagged jets.

- Calculate and create a spectrum for $E_{T,nomu}^{miss}$. This is defined as the vector sum of the missing transverse energy and the muons in the event. This is done for the 1 lepton control region as it creates a proxy for the dijet system to recoil against.
- Look for an excess of events in the dijet (resolved region) or single jet (merged region) mass for the signal region, around the Higgs boson mass, where one would expect to see the reconstructed Higgs boson from the signal process.
- If there is no significant excess in the data, set a 95% confidence level upper limit on the cross section for the signal.

As mentioned above, control regions pertaining to the major background processes will need to be defined. These backgrounds are ones that exhibit similar characteristics to the signal - background events with large missing transverse energy and either a pair of b-tagged small-R jets or a fat jet with b-tagging in its substructure. The three primary backgrounds are Z + jets (where the Z decays into neutrinos), W + jets (where the charged lepton from W decay fails to be detected) and $t\bar{t}$ events (where both W-bosons produced during top decay go to leptons and the charged leptons are not reconstructed).

Regarding the Z + jets background control region, it is most important to isolate events which contain a Z boson and two jets. The branching fractions for the decays of the Z boson are well known. As such, it doesn't matter which Z boson decays are used to identify these events. For this control region, a requirement will be set that events contain two leptons. It will identify events where the Z boson decays into a pair of charged leptons. A requirement of charged leptons reduces all other backgrounds. The combined transverse momentum of these charged leptons can be used as a proxy for the missing transverse energy in the signal - requirements imposed in the signal region on missing transverse energy are replaced in this control region by the invariant mass of the two charged leptons.

The W + jets and $t\bar{t}$ control regions will have a requirement that a single muon be present in the event. The assumption is made that the identification of the lepton has no bearing on the characteristics of the rest of the event when generated. As such, the matrix element properties of an event where there is a lepton identified, should be the same as events where one is missed. This means one can look at events with a single muon as a reliable representation of background topology. The combination of the missing transverse momentum and the transverse momentum of the muon can be combined (as briefly mentioned above) to create a so called $E_{T,nomu}^{miss}$, a proxy to recoil against the dijet system. Beyond this, the control region can be split based on the number of b-tagged jets/track jets which is effective at separating the W + jets and the $t\bar{t}$ events.

5.2 Signal Region

The signal region is defined as the phase space within which we expect to find the signal events. The selections designed to single out this phase space are based on the topology of the signal event, in this case, $H \to bb$. There are two distinct types of region where signal events can be found, based on the kinematics of the Higgs boson. Signal events with a Higgs boson of low to medium range kinetic energy allow for the two b-jets to be resolved independently as two small-R jets (details of such objects can be found in Section 4.2.3). Higgs bosons with very high momentum result in jets that are largely boosted in the detector, often causing them to merge into one fat jet (for details see Section 4.2.5). As such, the analysis is split into two signal regions, one where signal contains two resolved b-jets and one where it contains one fat jet which the b-tagging algorithm identifies as containing two b-tagged track jets. How events are sorted into the two categories is outlined in Section 5.2.1.

The cuts applied to select the signal region are were chosen to optimise $S/\sqrt{B}$. The cuts vary slightly for the resolved and merged regions, however both share the following common selections:

- Must pass E_T^{miss} trigger (HLT_xe70). For details about trigger efficiency, see Section 2.3.

- Required to have at least one reconstructed vertex (with at least 3 associated tracks).

- Event is excluded if it contains any bad jets. A bad jet is an energy deposit in the calorimeters which does not originate from a hard collision process but is identified as one. Sources of bad jets include sporadic noise bursts in the hadronic calorimeter, coherent noise or isolated pathological cells in the EM calorimeter, hardware problems, beam induced backgrounds and cosmic radiation. Jets are excluded if they fail the LooseBadJet cleaning requirements, which are described in further detail at [94]. This ensures an accurate representation of the event's E_T^{miss}.

- No loose electrons or muons (where electron and muon objects are defined in Sections 4.2.2 and 4.2.1 respectively).

- $E_T^{miss} > 150$ GeV to ensure events pass the trigger turn on curve as shown in Section 2.3

- $p_T^{miss} > 30$ GeV to reduce the amount of non-collision background (p_T^{miss} is the missing transverse momentum calculated using the inner tracker)

Whilst the above are applied to both the MC simulations and the data, the following two conditions are data specific:

- Dataset must be present on the GRL, to exclude luminosity blocks where the detector was not fully efficient

- Exclude events with errors due to noise bursts or corruption of data

5.2.1 Separation of Resolved and Merged Region

Before selection cuts are applied, the events must be sorted into those with resolved or merged jets from the Higgs boson. The two exclusive populations are separated by a E_T^{miss} cut at 500 GeV. Events with $\mathrm{E}_T^{miss} < 500$ GeV are considered resolved events and events with $\mathrm{E}_T^{miss} > 500$ GeV are considered merged events. Large E_T^{miss} implies higher energy Dark Matter candidates (or similarly backgrounds with neutrinos). As this is produced in association with the Higgs boson, it can be implied that the Higgs boson would be boosted, as the mutual parent must also have been high energy. The threshold at 500 GeV is the result of studies in the $A \rightarrow Zh \rightarrow \nu\nu bb$ analysis which has the same final state as the analysis here. The studies have shown it to be an efficient way of dividing the events[95].

The cut at $\mathrm{E}_T^{miss} = 500$ GeV does not separate resolved and merged events with 100% efficiency, and therefore will reduce the accepted sample size. A test was performed to quantify the potential improvement from the recovery of such events, as described below.

The default analysis was carried out with the split in place as described above on $A \rightarrow Zh \rightarrow \nu\nu bb$ samples. If a Higgs boson candidate was not found in an event (where the Higgs boson candidate is required to have a mass within the range of 50-200 GeV), the code would then look for jets of the opposing types in both categories (i.e. resolved in $\mathrm{E}_T^{miss} > 500$ GeV and merged in $\mathrm{E}_T^{miss} < 500$ GeV). The gain in signal events is shown in Figure 5.1. The increase in number of signal events was less than 5% so it was decided that this is not enough of an impact to require a change in strategy.

5.2.2 Resolved Region

Small-R jets (defined in Section 4.2.3) are among some of the more common objects present in events. In the resolved region, this can present a problem, as it makes

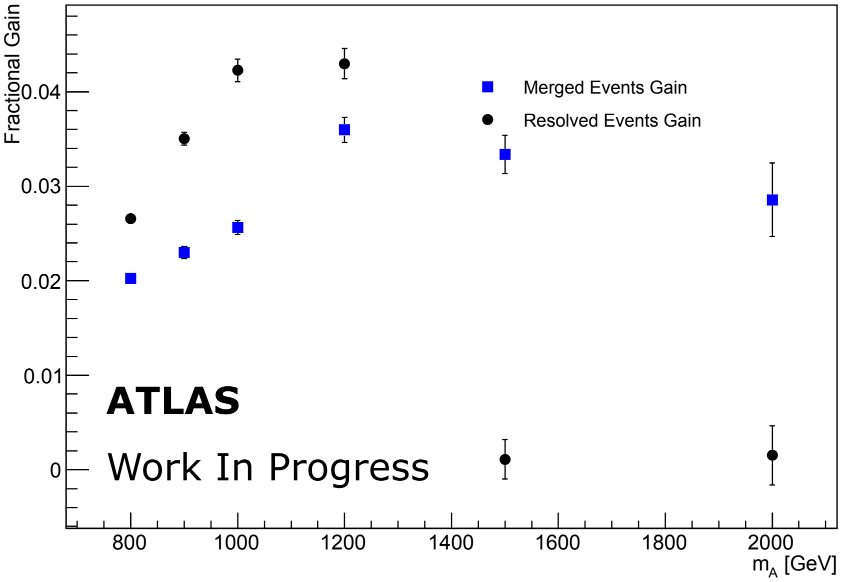

Figure 5.1: The fractional gain in 2 tag signal events if we include merged events with $E_T^{miss} < 500$ GeV that fail the resolved selection and resolved events with $E_T^{miss} > 500$ GeV that fail the merged selection. The signal is an $A \to Zh$ MC, which is shown for various A masses.

it harder to distinguish which jets should be used to reconstruct the Higgs boson. However the topologies of these additional jets can be used to distinguish which events are signal and not, through a series of trained cuts.

All small-R jets are sorted into the following three categories: b-tagged central jets, central jets and forward jets. Central jets are defined as small-R jets within $|\eta| < 2.5$, with jets outside this being considered as forward jets. Central jets which have passed the b-tagging algorithm are prioritised. Within each of the three populations, jets are ordered by transverse momentum. The first two jets from this ordered list are then used to reconstruct the Higgs boson, giving priority to central b-tagged jets for this purpose. This can lead to the Higgs boson being comprised of bb, bj or jj depending on whether the event has 2, 1 or 0 b-tagged jets respectively, where j represents a non b-tagged central jet. Events are also filtered by number of central jets. Events are separated into two categories, events consisting of exactly 2 jets or events containing more than 2 jets. These are labeled as ‘2jet’ and ‘3pjet’ populations respectively. It is expected that the signal events would be those located in the ‘2jet’ region with 2 b-tagged jets.

Jets outside the reconstruction can still have an impact on whether an event is successfully identified or not. In an event with a large amount of background jets, there is a high chance that a subset of these jets have been incorrectly measured or reconstructed. This unaccounted for energy can result in an inaccurate measurement of the missing transverse energy, increasing it beyond what it should be. As E_T^{miss} is a very important observable in the analysis, such events where this is a significant problem must be removed. This is done through a series of so-called ‘anti-QCD’ cuts. These are tailored to reduce the number of multi-jet background events. The cuts themselves are inspired by work on the Standard Model VH($\nu\nu bb$) analysis and the VH($\nu\nu bb$) resonance search. The anti-QCD cuts need only be applied to the resolved region, because the $E_T^{miss} > 500$ GeV cut eliminated almost all of the multi-jet background events in the merged region.

The requirements imposed on signal events to reduce multi-jet background are:

- **min($\Delta\Phi$(E_T^{miss},Central/Forward jets))** $> 20°$ - It is expected that the jets and the missing transverse energy will be back to back in the detector. If misread energy from a jet is contributing to the E_T^{miss}, then the E_T^{miss} four vector will be pulled towards the jet. To avoid this, the minimum distance in the event between the E_T^{miss} and any central/forward jet is required to be greater than 20°.

- $\Delta\Phi$ (E_T^{miss} , p_T^{miss}) $< 90°$ - Where as E_T^{miss} is calculated from the data taken from the calorimeter, p_T^{miss} (also referred to often as MPT) is missing transverse momentum according to the tracker. If the E_T^{miss} measured truly is the missing transverse energy of the event, one would expect it to be colinear with MPT in the detector. A poorly measured event in the calorimeter will affect the E_T^{miss} but not the MPT, resulting in a misalignment.

- $\Delta\Phi$ (E_T^{miss} , H_{reco}) $> 120°$ - It is expected that in the signal, the E_T^{miss} and the reconstructed Higgs boson should be produced back to back.

- $\Delta\Phi$ ($j^1_{H_{reco}}$,$j^2_{H_{reco}}$) $< 140°$ - Here $j^1_{H_{reco}}$ and $j^2_{H_{reco}}$ are the two jets from the list outlined above which are used to reconstruct the Higgs boson. We expect these to be relatively close to each other in the detector due to the high energy of the Higgs boson. Background QCD jets are often produced back to back.

As multi-jet backgrounds are not simulated in Monte Carlo, one instead looks for an excess in the data above the known and simulated background. Any excess in data above the backgrounds already modelled in a region outside of where the signal is assumed to be due to these background QCD events. Figure 5.2 shows the background simulations compared to data before any of the anti-multijet cuts are applied. The motivation for the placement of the above cuts can be clearly seen with the multijet contributing at low min($\Delta\Phi(E_T^{miss}$,Central Forward jets)). The multijet background contributes more at low E_T^{miss}. Figure 5.2(d) shows that the multijet background has a large fraction of events with 1 or 2 jets containing a μ. This suggests that the E_T^{miss} contributions from QCD backgrounds is the result of semi-leptonic decays.

Figure 5.3 shows how some of the key variable plots look after the $\Delta\Phi(\mathrm{E}_T^{miss}$,small-R jets) $<$ 20 degrees region has been excluded. A significant amount of QCD background has been reduced following this cut. Figure 5.4 shows the same key variable plots after all anti-multijet background cuts have been applied. For details on how this was approximated, see Section 5.3.3. In general the data is well described by the MC.

Lastly, the events that survive are divided into nine populations. The motivation behind this is explained when it comes to fitting the simulation to the data based on the control regions. By dividing the regions into sub-regions based on number of b-tagged jets and E_T^{miss} intervals, you can allow for different background processes to dominate in each population. This allows for a more accurate and representative way of fitting the MC to data, rather than a single fit to the sum of all backgrounds. This optimizes signal sensitivity and helps to constrain the backgrounds. The populations are separated in two observables: number of b-tags (0, 1 or 2) and E_T^{miss} interval

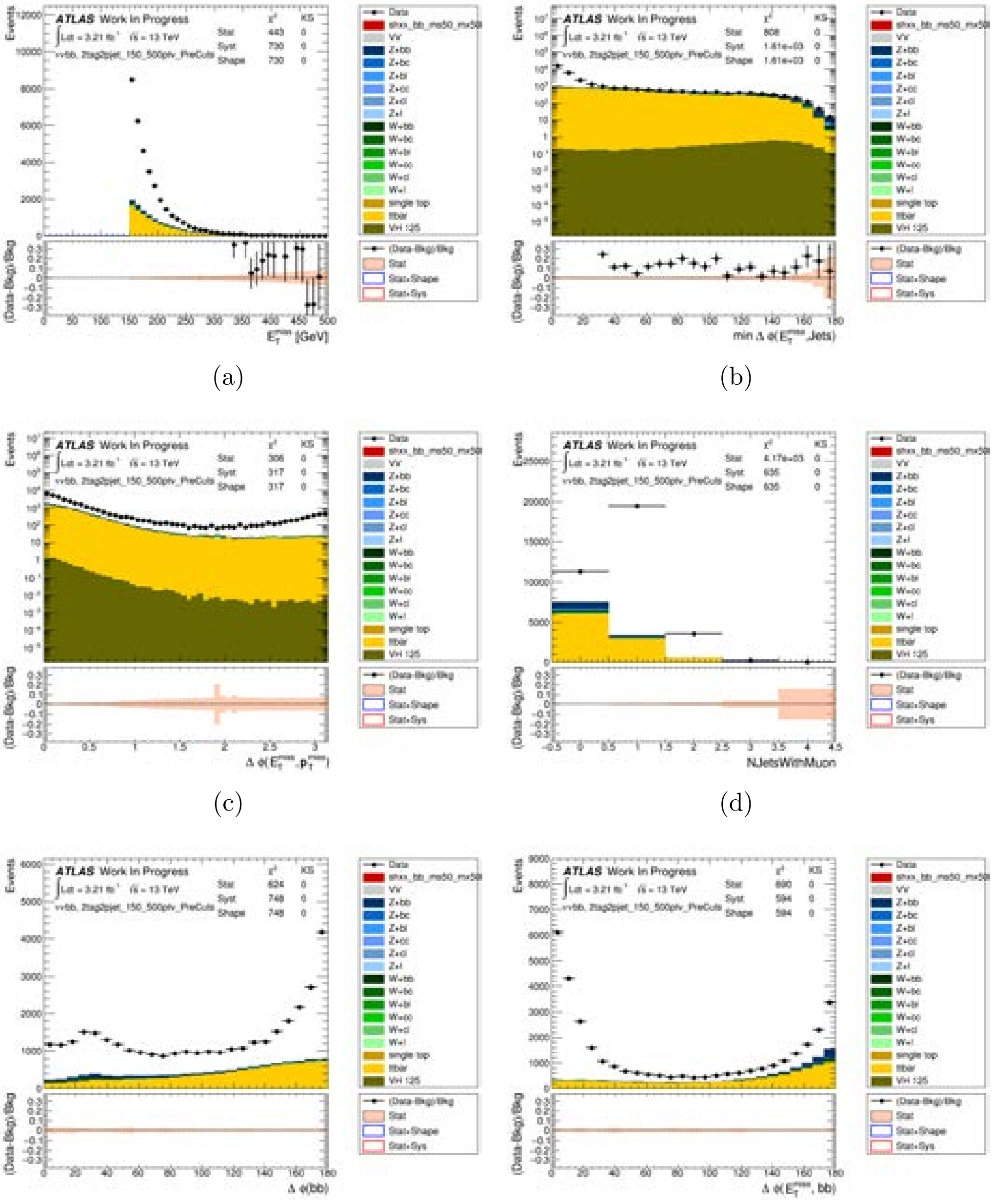

(a) (b)

(c) (d)

(e) (f)

Figure 5.2: Key distributions comparing 2 tag resolved analysis data and the MC backgrounds before anti-QCD cuts: (a) E_T^{miss}, (b) min($\Delta\Phi$(E_T^{miss}, jets)), (c) $\Delta\Phi$ (E_T^{miss}, p_T^{miss}), (d) the number of jets that contain a muon, (e) the azimuthal difference between the jets and (f) the azimuthal difference between the E_T^{miss} and the jet pair.

([150-200] GeV, [200-350] GeV, [350-500] GeV). Splitting the analysis up in this way will increase sensitivity. Figure 1.8 in Section 1.7 shows the E_T^{miss} distributions for the signal models. From these it is clear to see that the above bins are appropriate.

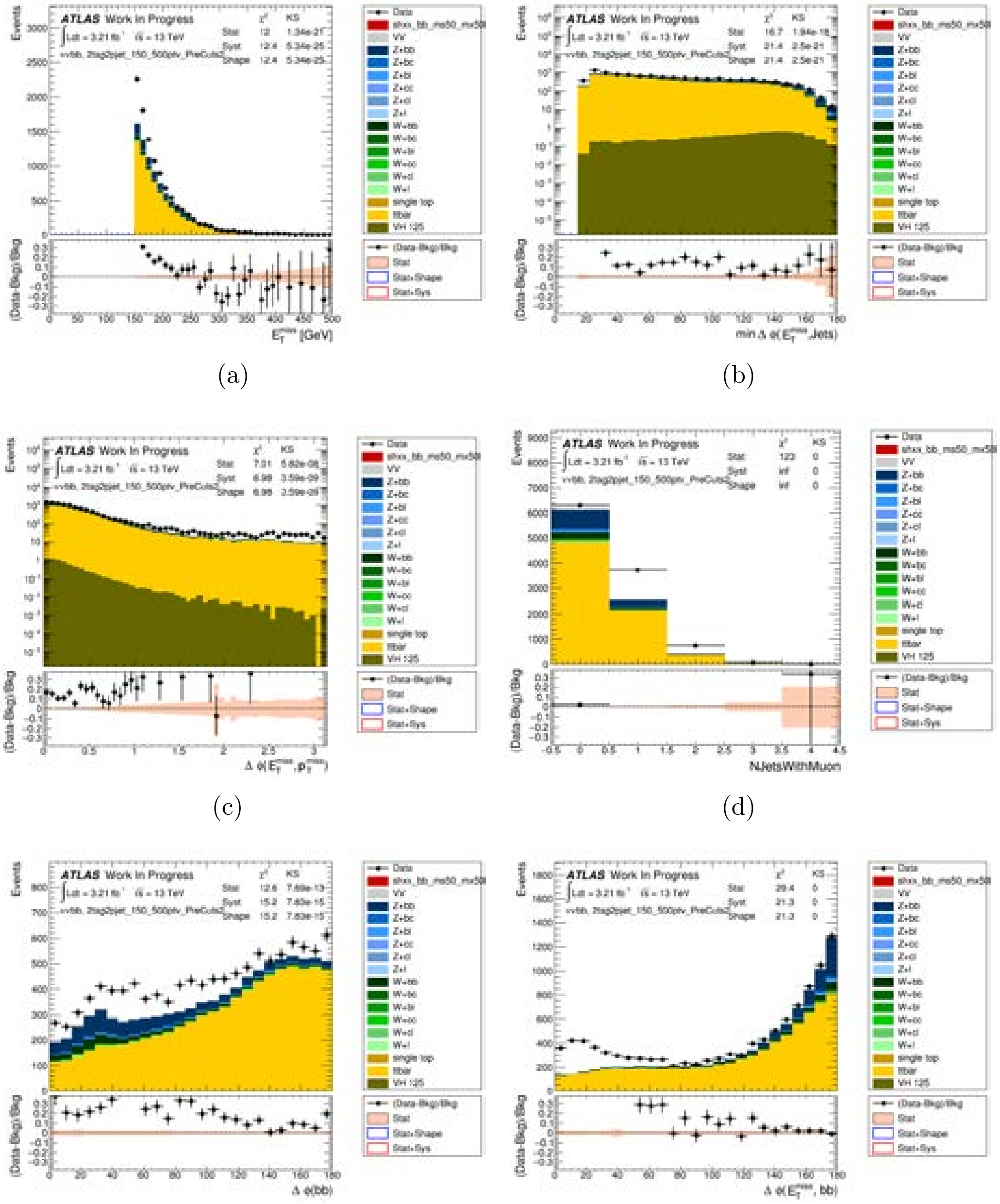

(a) (b)

(c) (d)

(e) (f)

Figure 5.3: Key distributions comparing 2 tag resolved analysis data and the MC backgrounds after the exclusion of the $\Delta\Phi(\mathrm{E}_T^{miss}$, small-R jets$) < 20$ degrees region: (a) E_T^{miss}, (b) min($\Delta\Phi(\mathrm{E}_T^{miss}$, jets)), (c) $\Delta\Phi$ (E_T^{miss}, p_T^{miss}), (d) the number of jets that contain a muon, (e) the azimuthal difference between the jets and (f) the azimuthal difference between the E_T^{miss} and the jet pair.

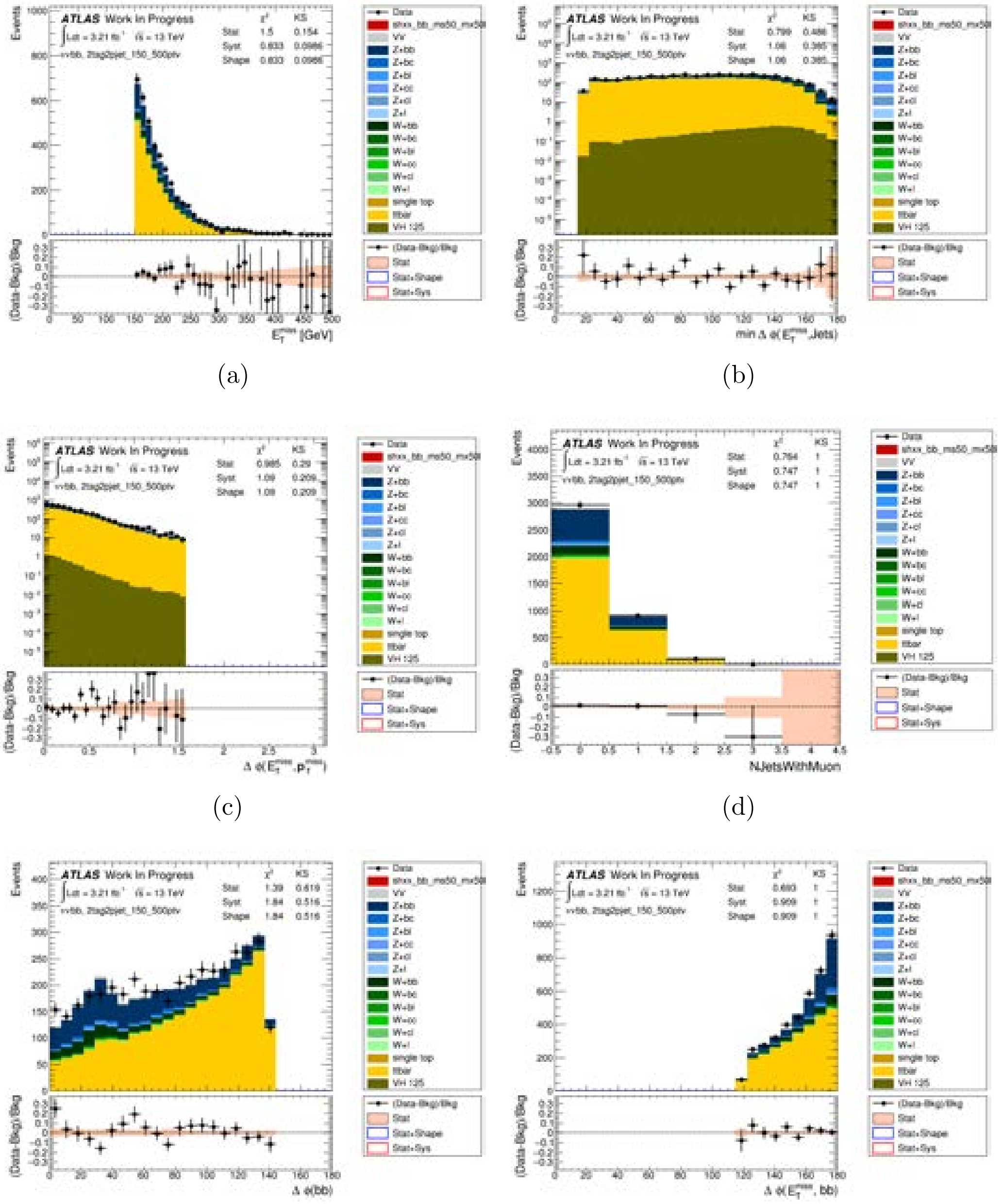

(a) (b)

(c) (d)

(e) (f)

Figure 5.4: Key distributions comparing 2 tag resolved analysis data and the MC backgrounds after the anti-QCD cuts: (a) E_T^{miss}, (b) min($\Delta\Phi$(E_T^{miss}, jets)), (c) $\Delta\Phi$ (E_T^{miss}, p_T^{miss}), (d) the number of jets that contain a muon, (e) the azimuthal difference between the jets and (f) the azimuthal difference between the E_T^{miss} and the jet pair.

5.2.3 Merged Region

As explained at the start of Section 5.2, this region is populated by events with $E_T^{miss} > 500$ GeV. This clean cut means there is no possibility of these events overlapping with those in the resolved region. As also mentioned in Section 5.2.2, this E_T^{miss} cut eliminates almost all of the multi-jet background events, removing the need for further anti-QCD cuts. No further cuts are required for this region.

It is worth noting that instead of small-R jets being used to reconstruct the Higgs boson, b-tagged track jets are searched for within the fat jet. For more details about fat jets and track jets, see Sections 4.2.5 and 4.2.6 respectively. Unlike in the resolved region where jets can be ordered by b-tagging, central/forward topology (described in Section 5.2.2), in the merged region, the two highest p_T track jets are used to reconstruct the Higgs boson.

As in the resolved region, the merged region is split into separate populations prior to fitting. It is split into three populations based on number of b-tagged track jets inside the fat jet (2, 1 or 0).

5.3 Control Regions

Aside from the signal region, a number of control regions are also defined. These control regions are designed to be orthogonal to the events contained in the signal region. This is largely done based on the required number of leptons in the event. Whereas the signal region requires 0 leptons, control regions designed to contain 1 and 2 leptons are created. It is found that in the 1 lepton control region, the W+jets background dominates, whilst in the 2 lepton control region, Z+jets dominates, with a strong contribution coming from $t\bar{t}$ in both. These are then treated in a similar manner to the 0 lepton population. They are divided into resolved and merged events in the same manner, the former then being subjected to similar anti-QCD cuts.

The data driven estimate of the multi-jet background is included here. Details of how this is made can be found in Section 5.3.3.

The likelihood fit in the analysis is performed on the reconstructed dijet mass in the resolved region and the single jet mass in the merged region. The expected signal has a peak on these two distributions at approximately the Higgs boson mass. This naturally leads to sideband regions which can also be used as control regions in the fit. These will not be discussed in this section. For more information, see Section 6.1.

5.3.1 W Control Region

The control region where it is required that all events must contain 1 lepton is referred to as the W Control Region, due to the dominance of the W+jets background. There is also a significant contribution from $t\bar{t}$. Fitting this control region will appropriately normalise the W+jets and $t\bar{t}$ backgrounds to the data.

This region uses the same E_T^{miss} trigger as the signal region (HLT_xe70). On top of this a selection is made requiring exactly one muon and zero electrons.

A very similar process is then applied to this control region as is applied to the signal region. It is split into resolved and merged regions based on the 500 GeV E_T^{miss} cut and the resolved region is then further subjected to the same anti-QCD cuts as the signal region. The only difference being that a modification needs to be made to the E_T^{miss} before the cuts are performed. Muons passing through the calorimeters leave only a trace amount of energy. As the E_T^{miss} is calculated from calorimeter deposits, this muon is not detected, leading to its momentum contributing to the E_T^{miss}. In order to cancel out this effect, the four vector of the muon is added to the four vector of the E_T^{miss}. This correction to the E_T^{miss} must be applied before any E_T^{miss} based selections are performed, including the separation into resolved and merged regions. Wherever E_T^{miss} is referred to in the context of the W Control Region, one must now assume that this correction has been made.

Plotted in Figures 5.5 and 5.6 are the dijet/single jet mass distributions for the resolved/merged regions respectively after the selection cuts. Plots here are shown prior to the likelihood fit that is ultimately performed, as described in Section 6.1. From these plots, it can be seen that the $t\bar{t}$ background dominates in the 1 and 2 b-tag regions compared to W+jets which dominates in the 0 b-tag region.

5.3.2 Z Control Region

The 2 lepton control region is dominated by the Z+jets background. As such the fitting of this control region will normalise the Z+jets background to the data.

The 2 lepton region does not use the HLT_xe70 E_T^{miss} trigger like the signal and W control regions because the sample size becomes too small if E_T^{miss} triggers are used. For list of triggers used in 2 lepton region, see Section 2.3.

After the triggers are applied, events are selected that have either exactly 2 electrons or exactly 2 muons. They are required to have $|\eta| < 2.47$ and $|\eta| < 2.7$ respectively. Out of the two leptons, one is required to pass LOOSEVH requirements and have $p_T > 7$ GeV. The other lepton must pass MEDIUMVH requirements and have

$p_T > 25$ GeV - this is the triggering lepton. If the pair are electrons, the di lepton invariant mass must satisfy $83 < m_{ll} < 99$ GeV. The mass range for muons is larger than electrons as muons have poorer momentum resolution at higher energy than electrons. If the leptons are muons, the invariant mass must be within $71 < m_{ll} < 106$ GeV. Following this, the jet-based cuts are the same as in the signal and W control regions.

As in the W Control region, the missing transverse energy needs to be modified before the E_T^{miss} based cuts can be applied. Instead of E_T^{miss}, we use $p_T^{\mu\mu}$, the momentum of the two leptons. It acts as a proxy for the E_T^{miss}, as the object that recoils against the di-jet system.

Figures 5.7 and 5.8 show the di-lepton mass for the resolved and merged regions of the Z control region respectively where the two leptons are electrons. Figures 5.9 and 5.10 are the same but for the case where the two leptons are muons.

The E_T^{miss} distribution for the electron and muon channels are shown in Figures 5.11 and 5.12. Figures 5.13 and 5.14 show the di-lepton distributions for the resolved and merged regions respectively (includes both electrons and muons). In these early stages, the agreement seems poor.

5.3.3 Multijet Estimation

Unlike the other backgrounds which are simulated in Monte Carlo, the multijet background is simulated via a data driven method. Events that pass pre-selection (see Section 5.2) are then subjected to an inverted version of one of the anti-QCD cuts. The region that satisfies min($\Delta\Phi(E_T^{miss}$,Central/Forward Jets)) $< 20°$ is largely populated by multijet background events, as seen in Figure 5.2. Distributions such as the E_T^{miss} and the dijet mass taken from the population that pass this selection are used as a template for the simulated multijet background in the signal region.

As with all backgrounds, there needs to be some form of normalisation. The scale factor used here is taken as the ratio of events above the min($\Delta\Phi(E_T^{miss}$,Central Forward Jets)) $= 20°$ threshold to those below it. The fitting for this background is performed on the distribution of the number of small-R jets that contain a muon. This is because this distribution is sensitive to QCD background processes which is dominated by jets with real muons from semi-leptonic decays. The only jets considered in this fit are those that pass the pre-selection criteria and have min($\Delta\Phi(E_T^{miss}$,Central/Forward Jets)) $> 20°$.

This scaled multijet distribution plus the combined contribution of all the MC backgrounds is used to fit to data. As done in the signal and control region fitting, it is split into three regions before splitting based on number of b-tags (2, 1 and 0). Figure 5.15 shows that post-fit there is good agreement between the combined MC backgrounds and multijet estimate and the data. The scale factors across all b-tags agree within errors. The scale factors average to give a scale factor of 0.055 with 100% uncertainty applied. In the 2 b-tag signal region, the multijet is expected to make up $3 \pm 3\%$ of the background.

5.4 Systematic Uncertainties

Systematic Uncertainties are unavoidable as products of objection reconstruction methods and from the limitations and uncertainties of the theoretical models used to describe the backgrounds and the signals. They follow through the analysis, compounding with each other resulting in an over all uncertainty that affects the distribution of dijet masses, the key observable used in the fit.

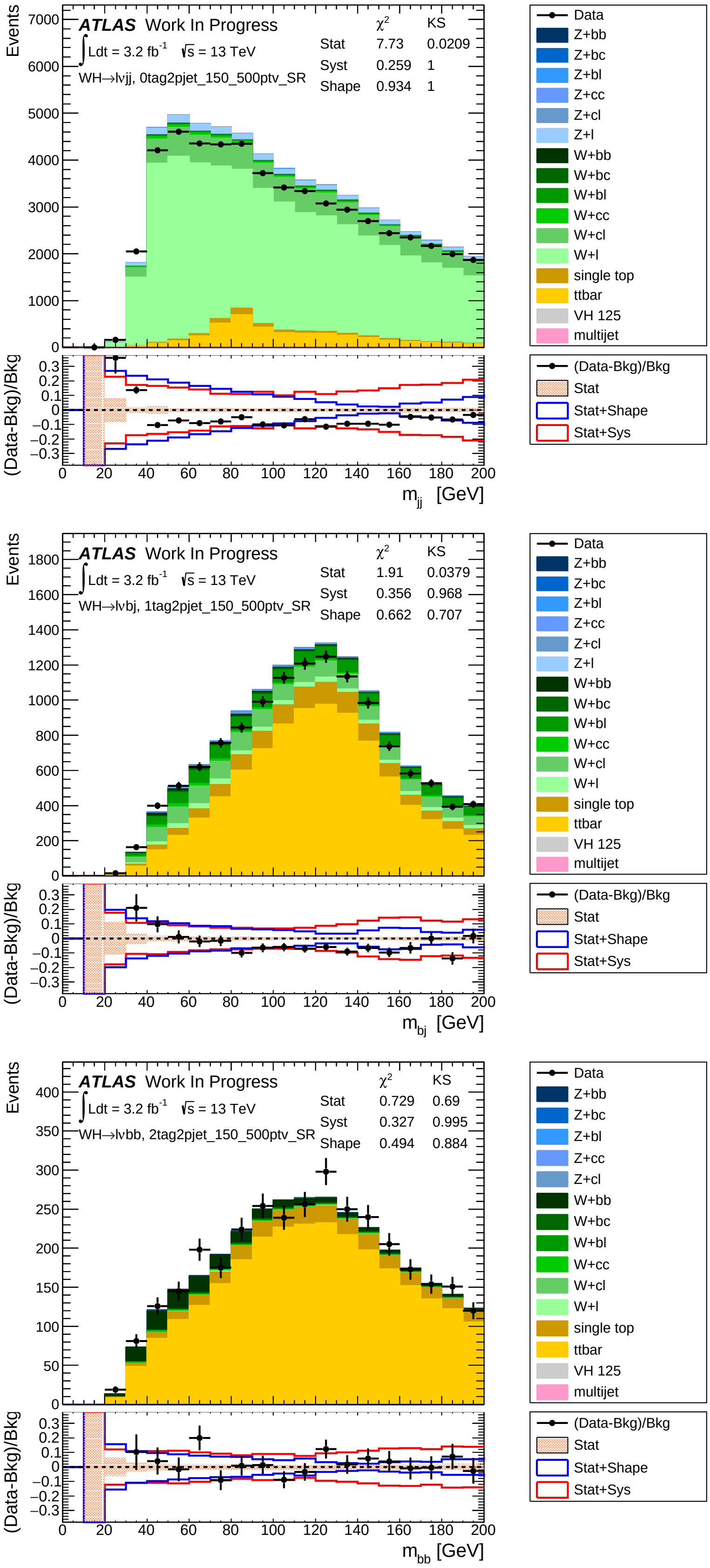

Figure 5.5: The invariant mass of the two signal jets for the 1 lepton resolved analysis control region for 0, 1 and 2 tag events respectively.

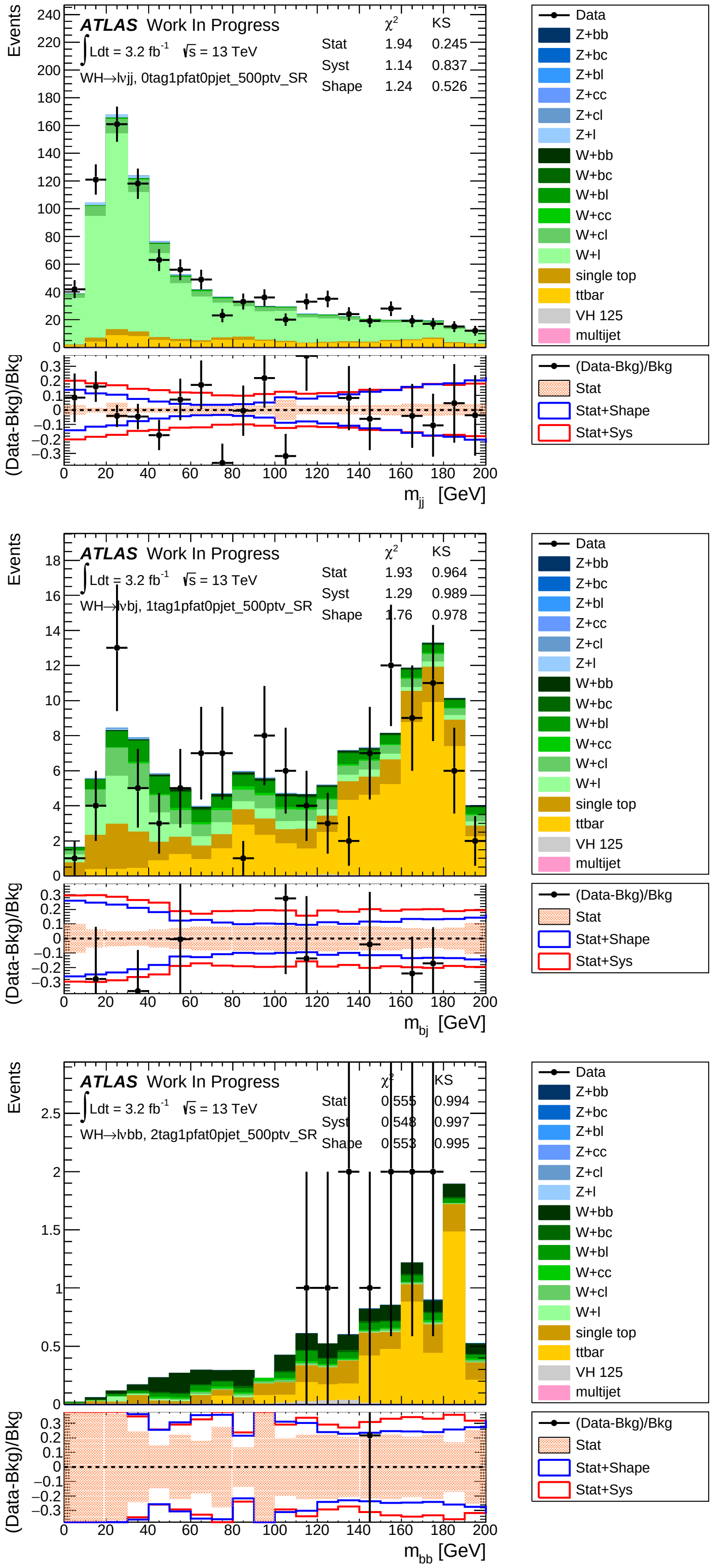

Figure 5.6: The invariant mass of the two signal jets for the 1 lepton merged analysis control region for (a) 0, (b) 1 and (c) 2 tag events respectively.

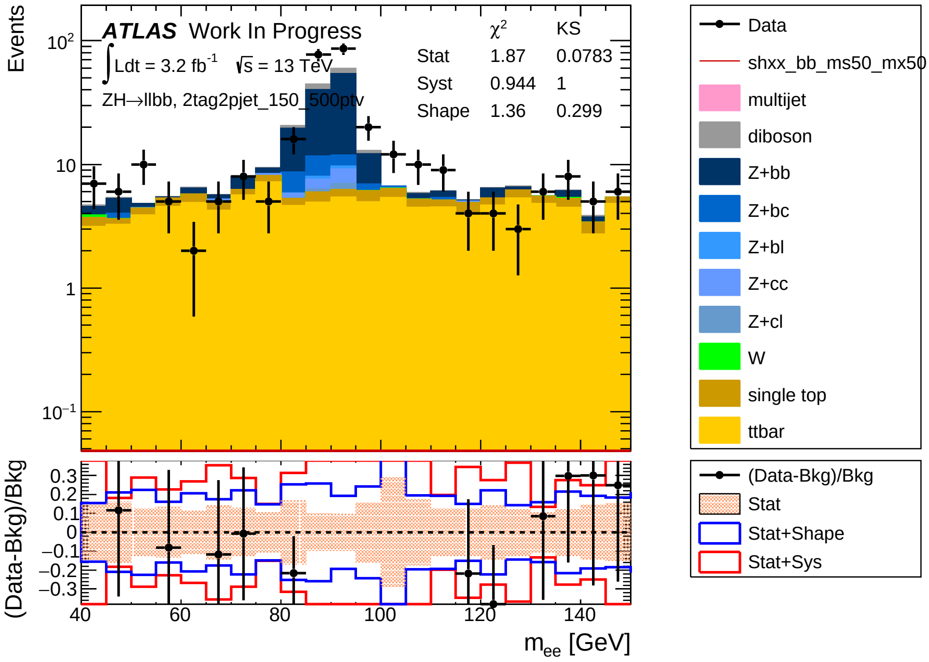

Figure 5.7: The invariant mass of the two electrons for the 2 lepton resolved analysis control region for 2 tag events respectively.

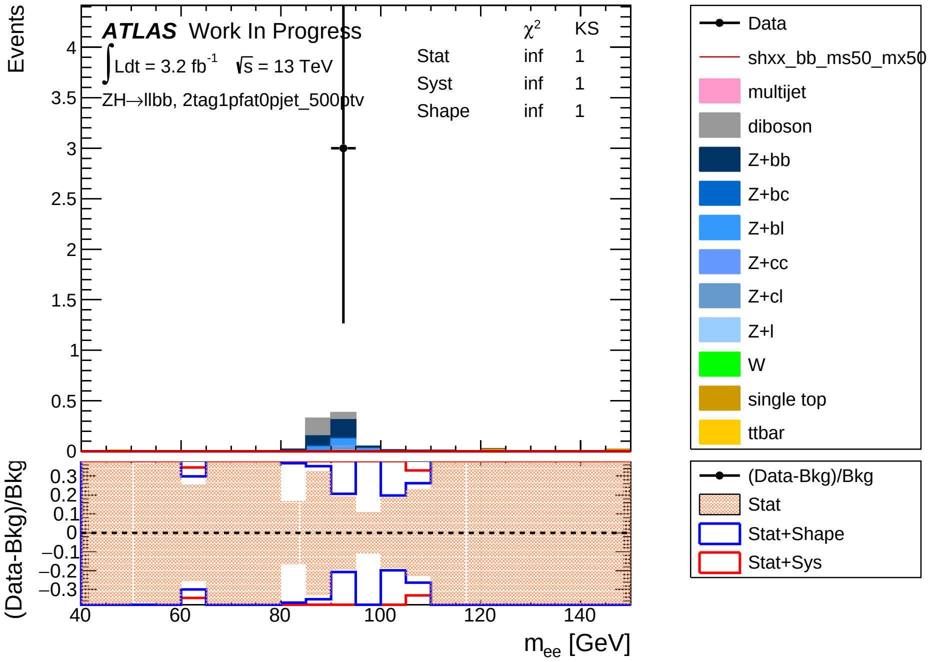

Figure 5.8: The invariant mass of the two electrons for the 2 lepton merged analysis control region for 2 tag events respectively.

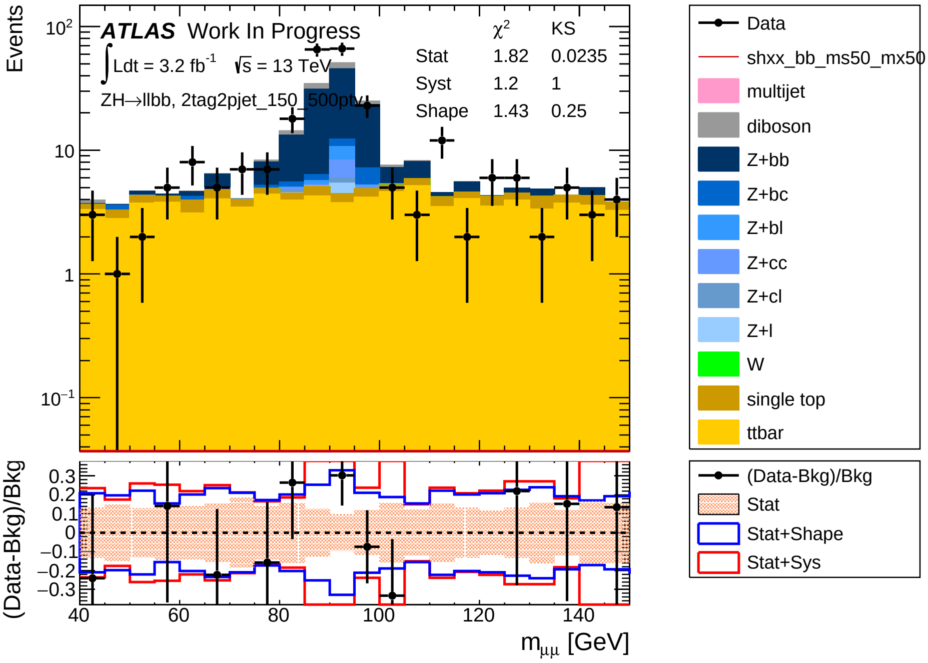

Figure 5.9: The invariant mass of the two muons for the 2 lepton resolved analysis control region for 2 tag events respectively.

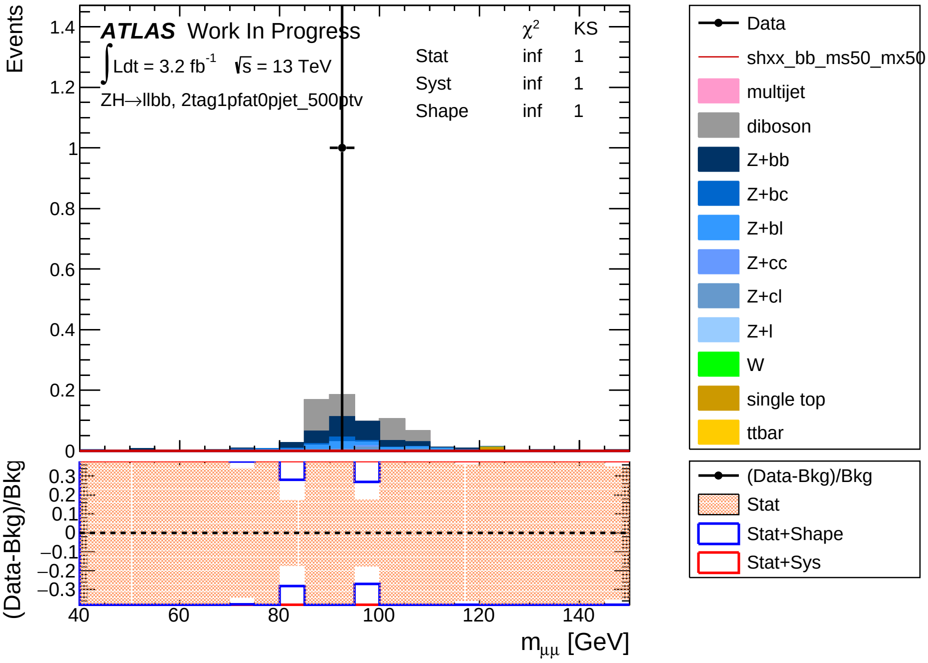

Figure 5.10: The invariant mass of the two muons for the 2 lepton merged analysis control region for 2 tag events respectively.

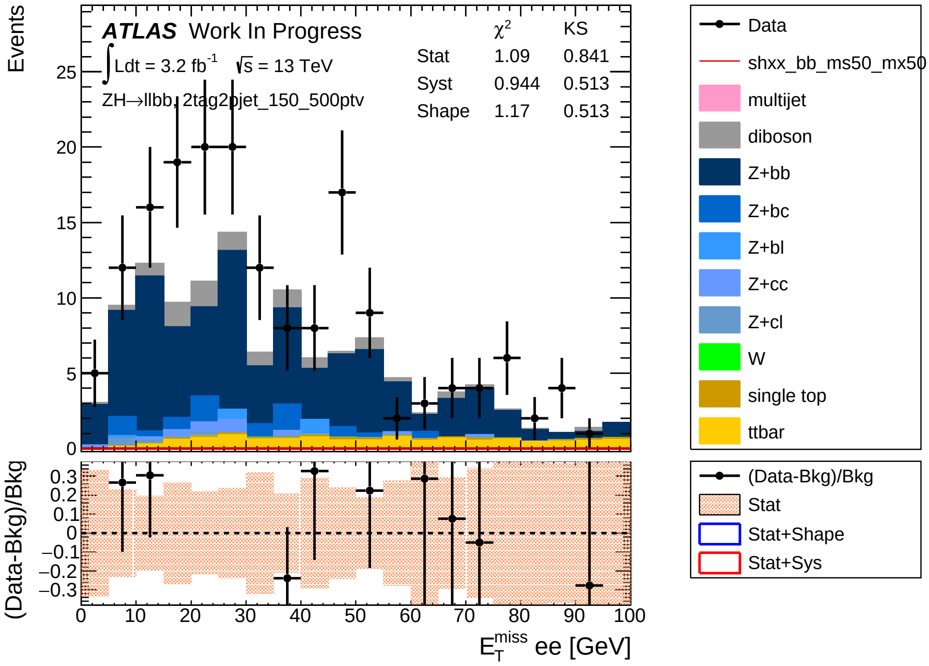

Figure 5.11: The E_T^{miss} for the 2 lepton resolved electron analysis control region for 2 tag events respectively.

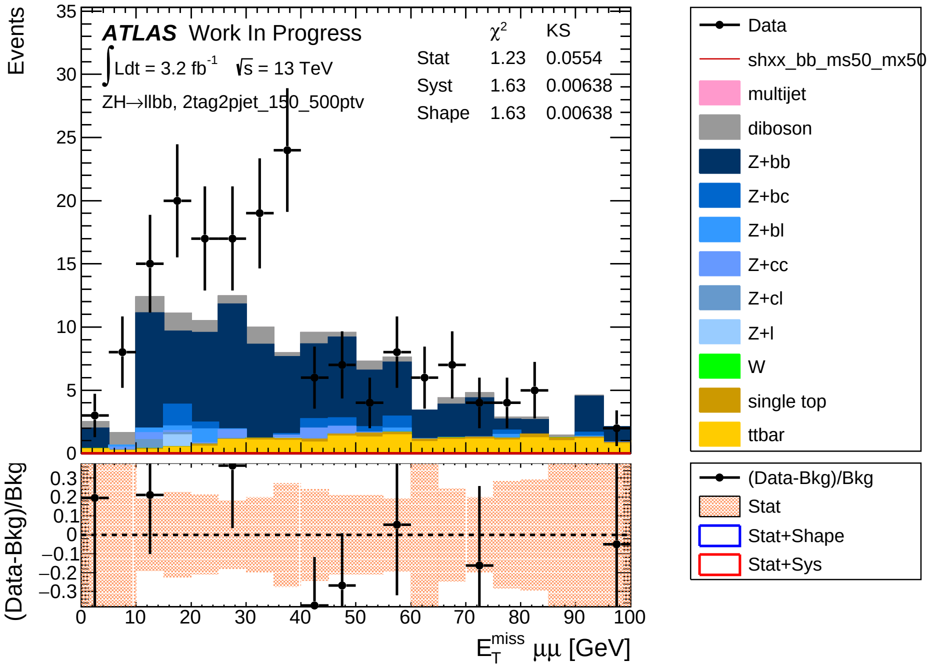

Figure 5.12: The E_T^{miss} for the 2 lepton resolved muon analysis control region for 2 tag events respectively.

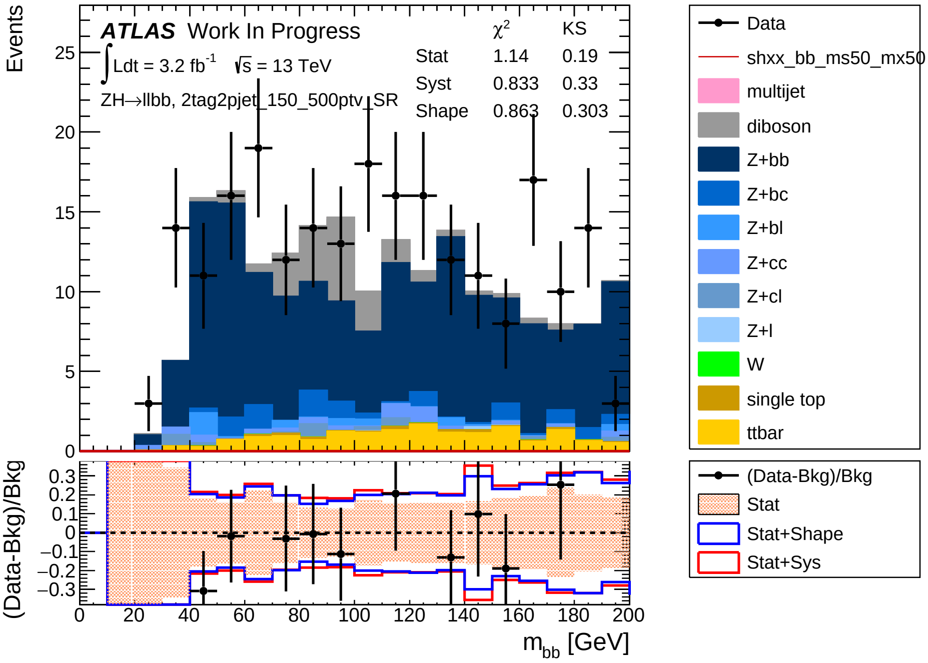

Figure 5.13: The invariant mass of the two signal jets for the 2 lepton resolved analysis control region for 2 tag events respectively.

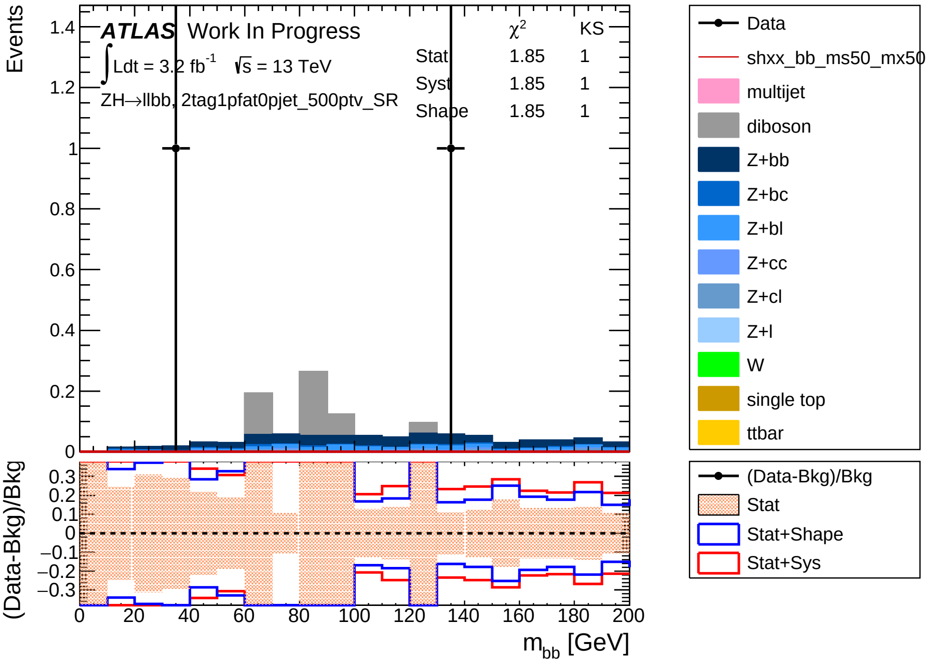

Figure 5.14: The invariant mass of the two signal jets for the 2 lepton merged analysis control region for 2 tag events respectively.

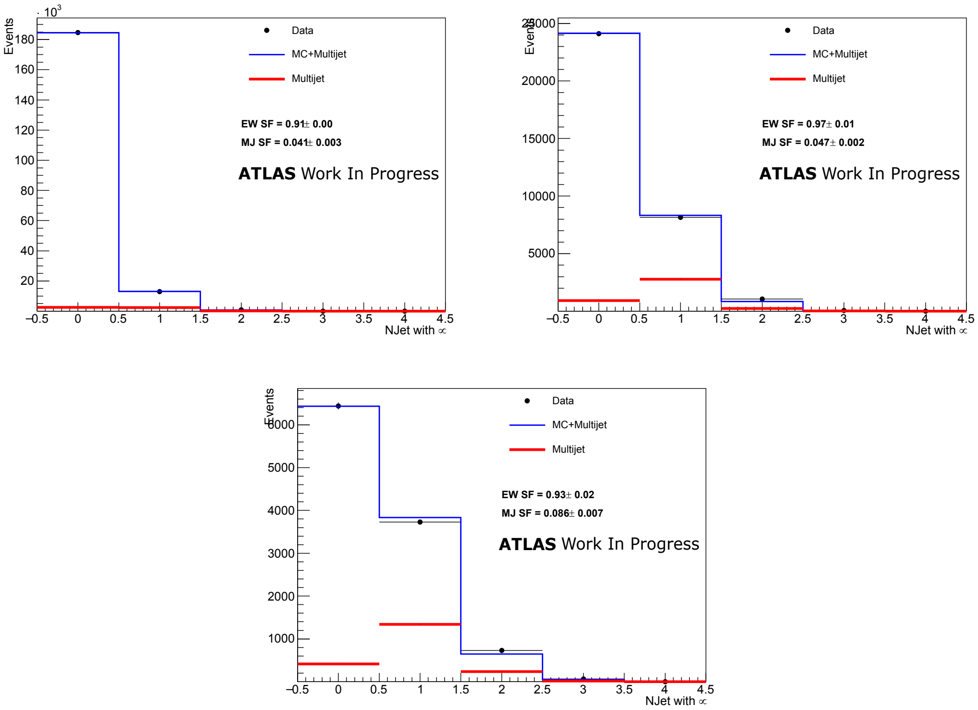

Figure 5.15: Distributions of the number of small-R jets that contain a muon for 0,1,2 tag small R jets. The small-R data is fit with templates of the multijet and MC.

Source	Description	Analysis Name
Trigger	E_T^{miss} Trigger	SysMETTrig
Trigger	Electron Trigger	SysEL_EFF_Trigger_TotalCorrUncertainty
Trigger	Muon Trigger	SysMUON_EFF_TrigSystUncertainty
Trigger	Muon Trigger	SysMUON_EFF_TrigStatUncertainty
Electrons	Energy scale	SysEG_SCALE_ALL
Electrons	Energy resolution	SysEG_RESOLUTION_ALL
Electrons	ID efficiency	SysEL_EFF_ID_TotalCorrUncertainty
Electrons	Isolation efficiency	SysEL_EFF_Iso_TotalCorrUncertainty
Electrons	Isolation efficiency	SysEL_EFF_Reco_TotalCorrUncertainty
Muons	p_T resolution MS	SysMUONS_MS
Muons	p_T resolution ID	SysMUONS_ID
Muons	p_T scale	SysMUONS_SCALE
Muons	Efficiency	SysMUON_EFF_Sys
Muons	Efficiency	SysMUON_EFF_Stat
E_T^{miss}	Soft term	SysMET_SoftTrk_ResoPerp
E_T^{miss}	Soft term	SysMET_SoftTrk_ResoPara
E_T^{miss}	Soft term	SysMET_SoftTrk_Scale
Small-R Jets	JES	SysJET_GroupedNP_(1,2,3)
Small-R Jets	Energy resolution	SysJET_JER_SINGLE_NP
Large-R Jets	p_T resolution	SysFATJET_JER
Large-R Jets	Mass resolution	SysFATJET_JMR
B-tagging	b tagging systematics - Split into 3	SysFT_EFF_Eigen_B
B-tagging	for B, 4 for C and 5 for L	SysFT_EFF_Eigen_C
B-tagging	The systematics are assumed to be fully correlated	SysFT_EFF_Eigen_L
B-tagging	for small-R calo jets and small-R track jets	
Background Modelling	W+jets MC modelling uncertainty on	SysWDPhi
Background Modelling	$\Delta\Phi$ (jet ,jet), m_{JJ}, and p_T^W	SysWMbb
Background Modelling	distribution.	SysWPtV
Background Modelling	W+jets MC modelling uncertainty on	SysZDPhi
Background Modelling	$\Delta\Phi$ (jet ,jet), m_{JJ}, and p_T^W	SysZMbb
Background Modelling	distribution.	SysZPtV
Background Modelling	The top modelling uncertainty on m_{JJ}	SysTtbarMbb
Background Modelling	The top modelling uncertainty on p_T^{bb}	SysTtbarPtbb
Background Modelling	The diboson modelling uncertainty on m_{JJ}	SysVVMbb

Table 5.1: Overview of the systematic uncertainties considered.

All of the systematic uncertainties which impacted upon this analysis in some way are listed in Table 5.1. Each systematic is briefly described below.

- **Trigger** - For the E_T^{miss} trigger, the uncertainty used is the full difference between Monte Carlo and data, as seen in Section 2.3.
- **Electron Reconstruction** - The systematic uncertainties related to the use of electrons have already been documented in detail by the E/gamma combined performance group. This includes uncertainties from the reconstruction of the electron. This is only used in the 2 lepton control region[96].
- **Muon Reconstruction** - Again, the systematics associated with muons have been understood and developed by the muon combined performance group. The three main sources of uncertainty when using muon objects are the efficiency, muon isolation and the energy scale[97]. Event yield is worked out after applying a 1σ variation over the smearing and efficiency scale factors.
- **MET Reconstruction** - The soft terms in the E_T^{miss} are given their uncertainties by the METSystematicsTool. Uncertainties associated with the hard objects are used in the calculation of the uncertainties associated with the E_T^{miss}.
- **Small-R Jet Reconstruction** - The jet energy scale and resolution (JES and JER respectively) are calculated by tools from the Jet/EtMiss group[83].There is one Nuisance Parameters (NP) for **JER!** (**JER!**) and three for JES.
- **Large-R Jet Reconstruction** - Same uncertainties as Small-R jets. Need to also consider jet mass scale and jet mass resolution (JMS and JMR respectively).
- **B-tagging** - Uncertainties on b-tagging efficiency are based upon techniques used in [78]. Further details are provided by the ATLAS flavour tagging group. The main sources of uncertainty are how well the simulation models the $t\bar{t}$

process, estimations of other background contaminants and uncertainties arising from imperfect knowledge of the JES and **JER!**. The dominant uncertainty comes from background subtraction. For full details, see [78].They are calculated for two regions, resolved small-R jets and the track jets that make up the fat jets in the merged region. They are parameterised for bottom, charm and light quarks. For more information on b-tagging, see Section 4.2.4.

- **Theoretical Uncertainties on the Signal** - See Sections 5.5 and 5.6.

5.5 Signal Acceptance Uncertainties

Uncertainties on the signal acceptance are derived by varying the parameters when generating the MC samples in MadGraph and Pythia.

The nominal PDF used is NNPDF2.3LO [98]. This is compared to two other PDFs, MSTW2008lo68cl [99] and CTEQ6L1 [100]. The largest deviations from the two PDFs are used as uncertainties. The uncertainties associated with comparing different PDFs are usually larger than those within contained within the tune associated with the PDF.

The A14 eigentune [93] (the underlying event tune for nominal events) contains Hessian systematic variations for the Neural Network Parton Density Function (NNPDF) set which cover the total uncertainty. Variations as a result of ISR, FSR and MPI are covered by pairs of tune variations, each one providing full coverage of observables. The pairs can either be implemented separately or together in quadrature.

5.6 Background Modelling Systematics

In this section, the systematic uncertainties associated with the Monte Carlo simulations of the backgrounds are discussed. The primary backgrounds modelled in

Monte Carlo are W+jets, Z+jets and $t\bar{t}$ as discussed in Section 4.4. The end result of the analysis includes these background simulations being normalised to Run 2 data using a likelihood fit in specific control regions designed to enrich each background individually.

Also considered are uncertainties on the shape of the background simulations. These uncertainties are found by comparing with data in the control regions. If there is no such control region that supplies an adequately pure sample of background, the uncertainties on shape are derived by comparing simulations of the same background from different Monte Carlo Generators.

The strategy is outlined as such:

- Control regions defined to isolate high purity samples of the various background processes (W+jets, Z+jets and $t\bar{t}$).
- The background simulation is normalised to the data. Only the main background associated with the control region is allowed to vary. Small backgrounds remain fixed. After normalisation, the total number of background events (defined as the main background under scrutiny plus smaller components) is equal to the number of data events in the control region.
- Plots are made of the key kinematic variables, comparing data and Monte Carlo, along with the ratio of the two. This process is carried out in three separate bins based on number of b-tagged jets (0, 1 and 2). This is because the composition of main and impure backgrounds may be different for each of these bins.
- A mathematical function is derived to correct for the variations or calculate uncertainties in the ratio between data and Monte Carlo.

The following three sections describe this process for the three previously mentioned major backgrounds.

5.6.1 Z+jets Modelling

The control region for the Z + jets background is described in Section 5.3.2. Figure 5.16 shows p_T^V for data and the default Monte Carlo model for Z + jets (Sherpa v2.1) before selection cuts are applied. As described in the strategy, the plots show the distribution split up into bins based on number of b-tagged jets in the event. The benefit of this is immediately obvious, but noticing the variation in the impurity backgrounds (shown in red) based on number of b-tagged jets. These impurities (which here largely are associated with $t\bar{t}$) are minimal for 0 tag events and increase with number of tags. Even at highest contribution from impure backgrounds (2 b-tags), the control region is still pure enough in Z + jets to be used to analyse the shape of the distribution and to be used as a control region for this background. In order to reduce contamination from $t\bar{t}$ and single top events, a cut is placed on the E_T^{miss} significance which must be less than 3.5. The E_T^{miss} significance is defined as the ratio between the E_T^{miss} and the square root of the sum of the momenta from the leptons and the jets.

As can be seen, there is good agreement between data and Monte Carlo in the 2 b-tag bin. No correction needs to be made to the shape. For a given bin in the p_T^V distribution, the associated uncertainty is modelled as $\pm 0.1 \log 10(p_T^V/50)$ GeV. This uncertainty is depicted on the plots through the dotted blue line. In all three bins, the minimal data/MC disagreement lies within this uncertainty. The functional forms for these uncertainties are taken from the Run 1 VHbb analysis paper [101]. The agreement between data and MC is significantly improved across the two runs due to improvements to the Sherpa model. Seeing good modelling of the 0-tag region, gives confidence that 1 and 2 tag regions would be modelled well. This however cannot be directly tested as it is impossible to get a pure sample for these regions. The shape information from the 0-tag plots are not used (see Section 6.1.2).

Figure 5.17 shows the distribution of $\Delta\phi_{jj}$ in bins of 0, 1 and 2 b-tags per event, where $\Delta\phi_{jj}$ is defined as the angle measured between the two signal jets in the event.

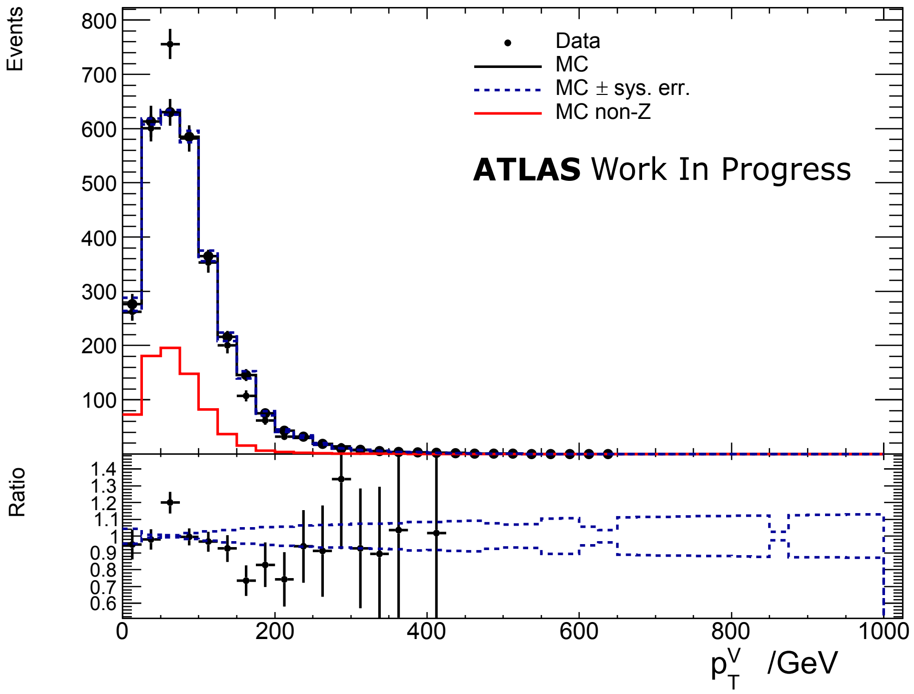

Figure 5.16: The transverse momentum of the Z p_T^Z for the 2 lepton control region for 2 tags before selection cuts.

Again, it is shown for both data and Monte Carlo and there is good agreement. No corrections are made to the shape. The uncertainty on the Monte Carlo shape is modelled as $\pm 0.05 \times (\Delta\phi_{jj} - \pi/2)/\pi/2)$ (again, represented by the dotted blue line on the plot).

The last kinematic variable studied is the distribution of m_{jj}, the combined mass of the two signal jets, split up into events with 0, 1 and 2 b-tags for both data and Monte Carlo. This is shown in Figure 5.18 for 2 b-tags. Note that there is a 'blinded' region in the 2 b-tagged jets bin at approximately 125 GeV. Consistent with the previous kinematic variables in these control regions, there is strong agreement between data and Monte Carlo. The uncertainty on this shape is modelled as $\pm 0.0005 \times (m_{jj} - 100\text{ GeV})$ which is again represented by the dotted blue line.

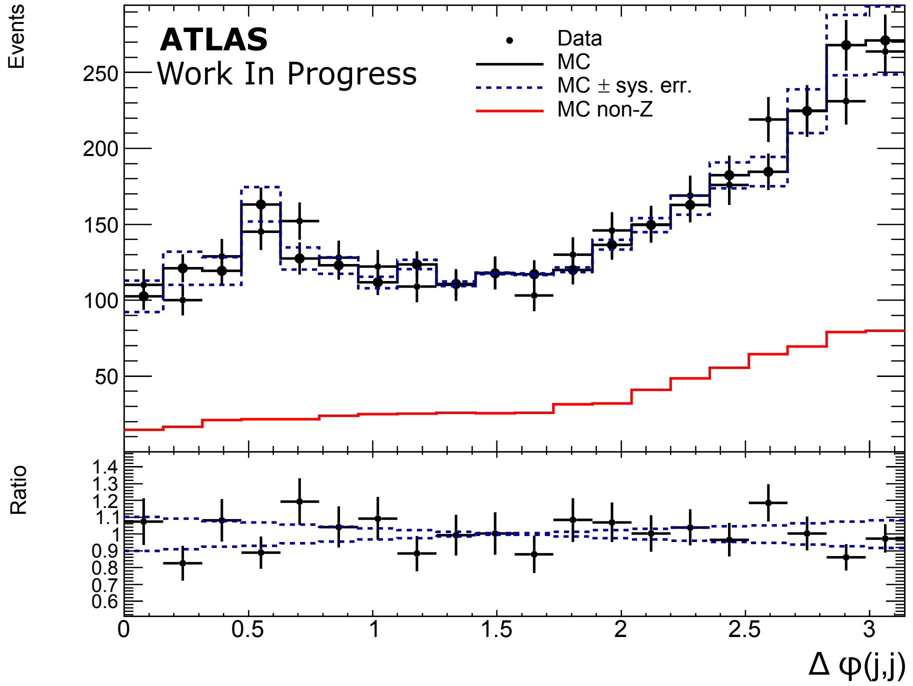

Figure 5.17: The $\Delta\phi_{jj}$ between the two signal jets for the 2 lepton control region for 2 tags before selection cuts.

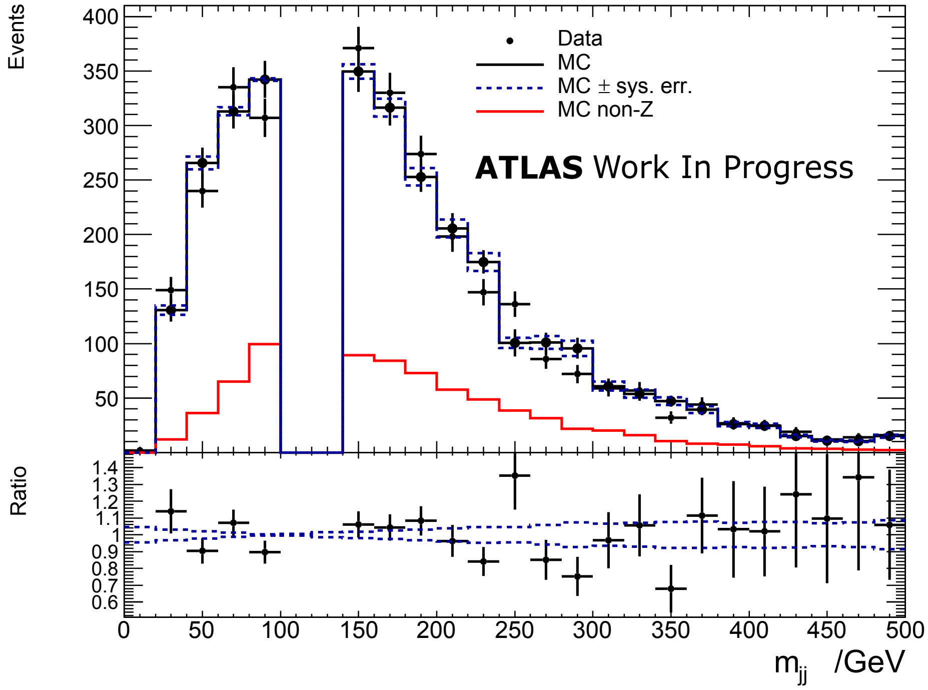

Figure 5.18: The m_{jj} distribution for the 2 lepton control region for 2 tags before selection cuts.

5.6.2 W+jets Modelling

The W+jets control region is defined in Section 5.3.1. Figure 5.19 shows the distribution of p_T^W in the 0 b-tagged jets bin. Only this bin is shown as the background event impurities are small. In the 1 and 2 b-tagged jet bins, the contribution is significantly higher, and as such, these plots cannot be reliably used to describe the shape of the W+jets background.

The function describing the uncertainty on this kinematic variable is the same as the one used for Z+jets, $\pm 0.1 \times \log 10(p_T^V/50\text{ GeV})$, again shown by the dotted blue line. The uncertainties of both the W and Z backgrounds are similar. This 0 b-tagged jet bin describes, by definition, events with W + light jets.

The W + heavy jet events (with 1 or 2 b-tagged jets) are dominated by the $t\bar{t}$ background. As such, data cannot be used in these bins to evaluate the uncertainty. To calculate the uncertainty, the shape of W + heavy jets is compared between models. The standard Sherpa prediction used in this analysis is compared with the same simulation from MadGraph. This is shown in Figures 5.20 split into two b-tag bins.

The 0 b-tag bin (found in Appendix C, Figure C.4) shows some disagreement between the two models, with some MadGraph points lying outside of the Sherpa uncertainty. However this hard distribution of p_T^W has been previously documented and is a known issue. Comparing it to Figure 5.19 shows that the Sherpa prediction better matches the data. The 1 and 2 b-tag regions show better agreement with more of the MadGraph points falling within the Sherpa uncertainty.

As with Z+jets, the next kinematic variable studied was the angle between signal jets, $\Delta\phi_{jj}$. And as with the p_T^W distribution the strategy is split for 0 b-tag and the 1 and 2 b-tag bins, again due to the high contribution of $t\bar{t}$ in the latter.

The 0 b-tag data comparison plot can be seen in Figure 5.21. There is good agreement, so no correction is needed. Again, the function describing the uncertainty

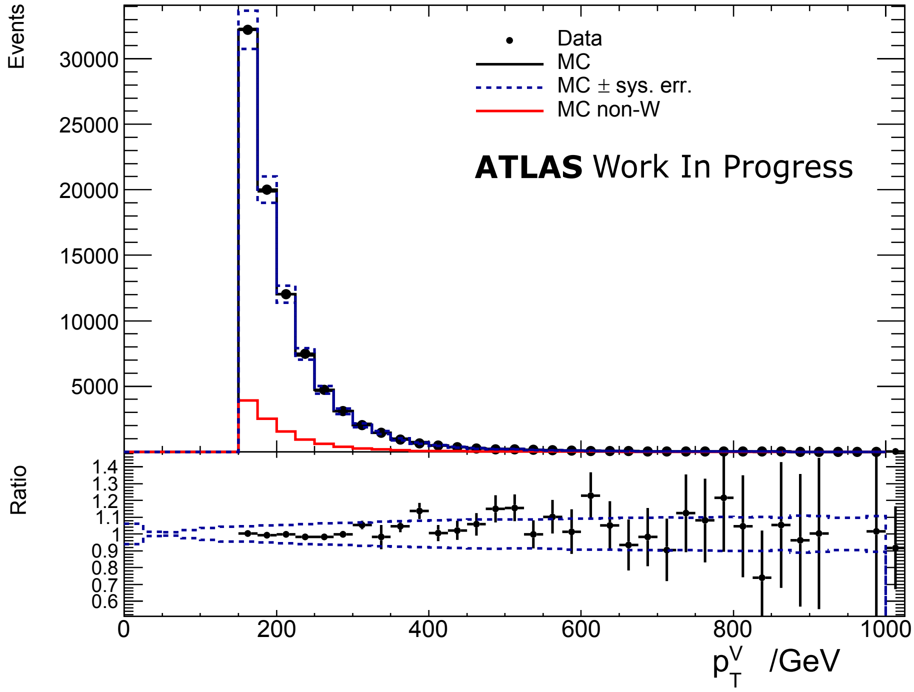

Figure 5.19: The transverse momentum of the W p_T^W for the 1 lepton control region for 0 tags.

is the same one used for the corresponding variable in Z+jets. It is modelled as $\pm 0.05 \times (\Delta\Phi_{jj} - \pi/2)/\pi/2)$.

Comparisons between Sherpa and MadGraph are shown for the 1 and 2 b-tag bins (and in 0 b-tag in Appendix Figure C.5). This can be found in Figure 5.22. Here it is seen that the MadGraph estimation falls within the described uncertainty on the Sherpa estimation in all bins.

Lastly, the m_{jj} distribution is shown for W+jets. The 0 b-tag bin is shown as a comparison between data and Monte Carlo in Figure 5.23. The agreement is good and the uncertainty is modelled as $\pm 0.0005 \times (m_{jj} - 100$ GeV) for $m_{jj} < 300$ GeV and is constant above 300 GeV. This is the same as in Run 1, which continues to describe the uncertainty on the shape well.

As before, comparisons between the Sherpa and MadGraph simulations are shown for 1 and 2 b-tag bins in Figure 5.24 (0 b-tag found in Appendix Figure C.6). There is good agreement between MadGraph and data in both bins and the Sherpa

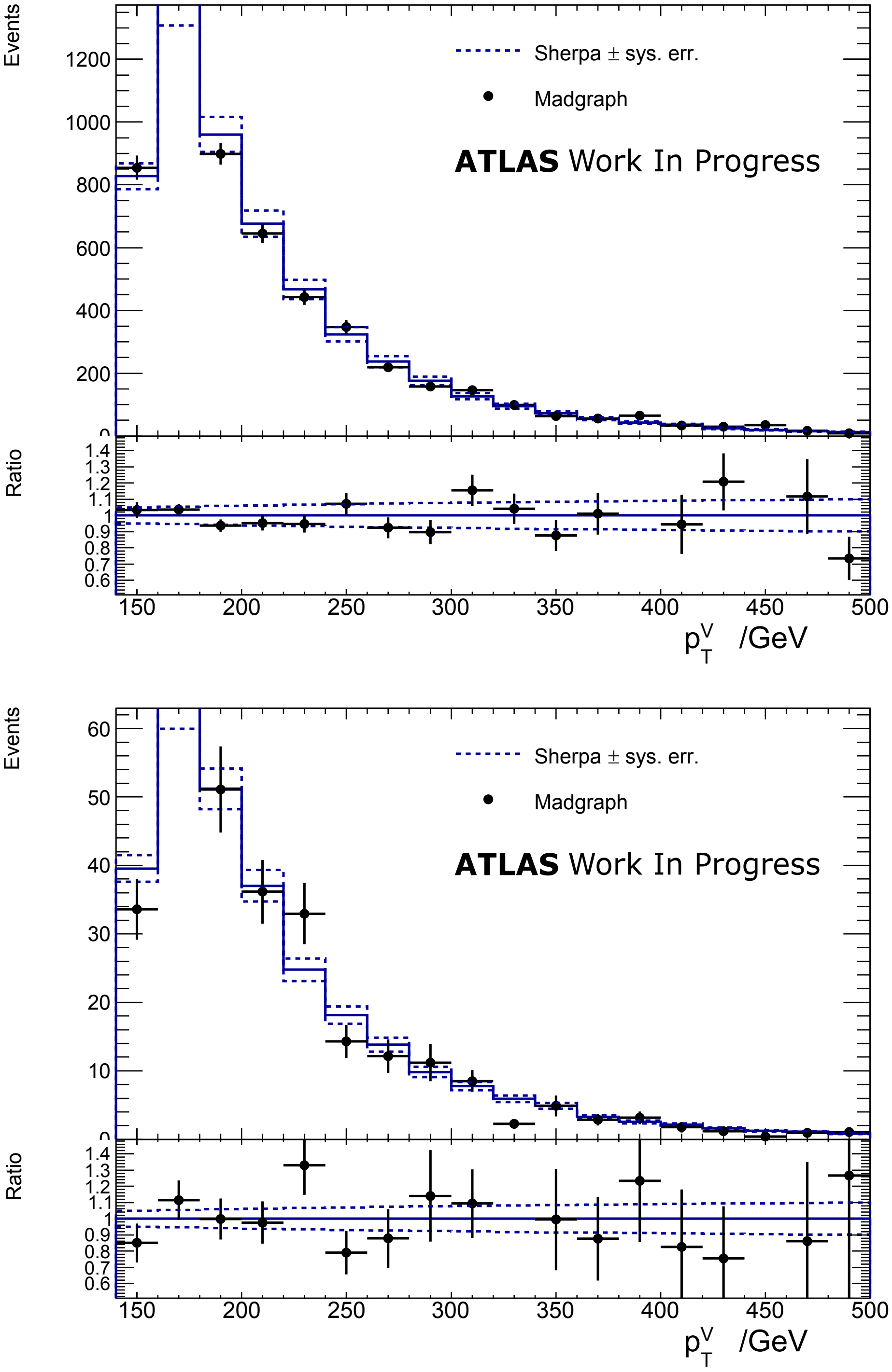

Figure 5.20: Comparison of the W+jets prediction from MadGraph with that from Sherpa as a function of the transverse momentum of the W (p_T^W) for the 1 lepton control region for 1 (top) and 2 (bottom) tags.

uncertainty remains reasonable, covering most of the MadGraph points.

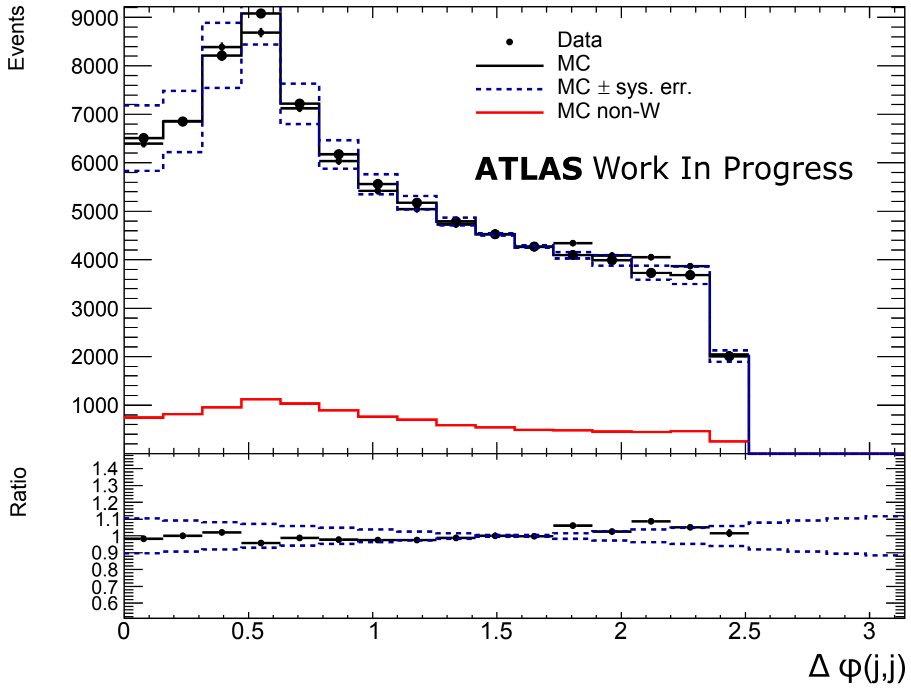

Figure 5.21: The $\Delta\phi_{jj}$ between the two signal jets for the 1 lepton control region for 0 tags.

5.6.3 $t\bar{t}$ Modelling

The $t\bar{t}$ background does not have its own dedicated control region but can be found predominantly in the W control region as described in Section 5.3.1, especially in the events in this region with 2 b-tag jets. This background can also be found in the Z control region (see Section 5.3.2), if a selection is made to look exclusively at e-μ lepton pairs.

Figure 5.25 shows the p_T^{bb} and m_{bb} distributions for the $t\bar{t}$ backgrounds in the cases of having 1 lepton (W control region) and 2 leptons (e-μ lepton pairs in Z control region). Where as previously p_T^V was used for the comparison, p_T^{bb} is used in both the 1 and 2 lepton events. This is because the p_T^{bb} distributions between the two are more comparable to each other than the p_T^V distributions of both because of the different ways the V would decay.

At low values of p_T^{bb}, there is good agreement, but at higher p_T^{bb} the simulation under-

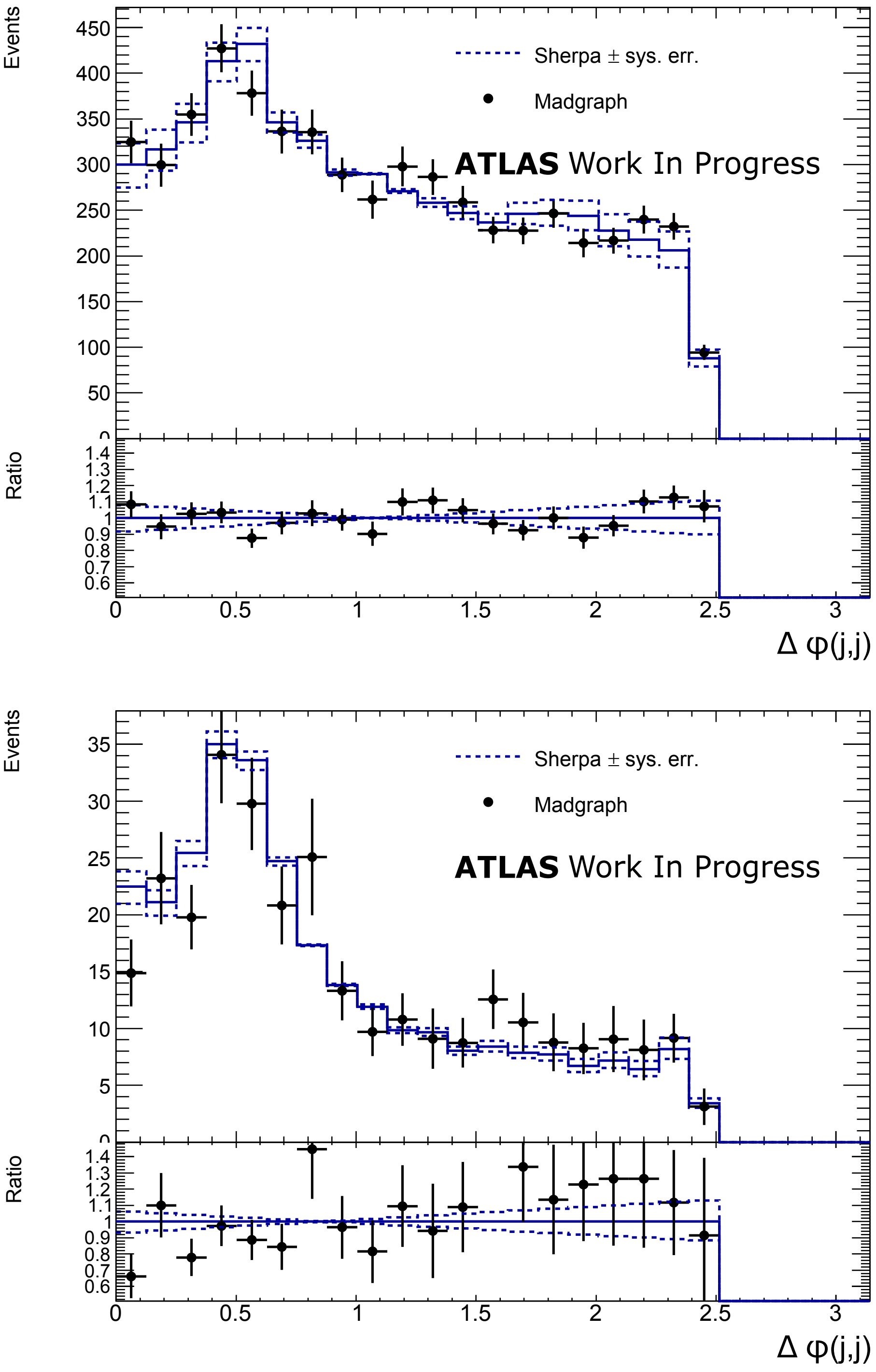

Figure 5.22: Comparison of the W+jets prediction from MadGraph with that from Sherpa as a function of the $\Delta\phi_{jj}$ between the two signal jets for the 1 lepton control region for 1 (top) and 2 (bottom) tags.

estimates the number of events compared to data. Two models for the uncertainty on this kinematic variable are used. For events with $p_T^{bb} < 100$ GeV, the uncer-

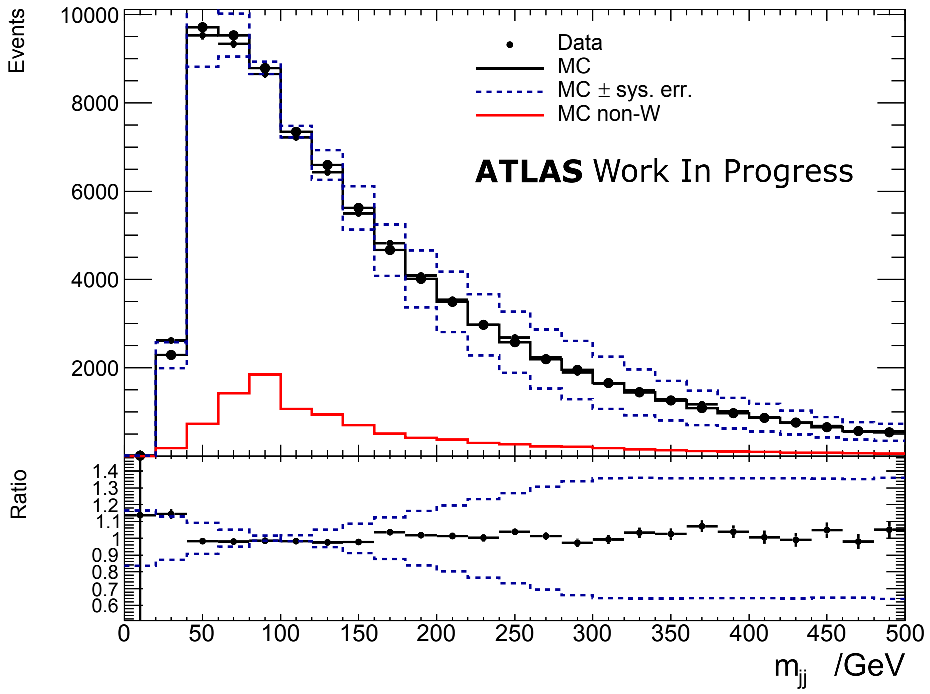

Figure 5.23: The m_{jj} distribution for the 1 lepton control region for 0 tags.

tainty is modelled as $\pm 0.1 \log 10(p_T^V/50\text{GeV})$. For events with $p_T^{bb} > 100$ GeV, the uncertainty is $\pm 0.4 \log 10(p_T^V/100\text{GeV})$.

There is good agreement in the m_{bb} plots, but not as good as in the previous two background cases. As such, a slightly modified function is used to describe the uncertainties, $\pm 0.001 \times (m_{jj} - 100 \text{ GeV})$.

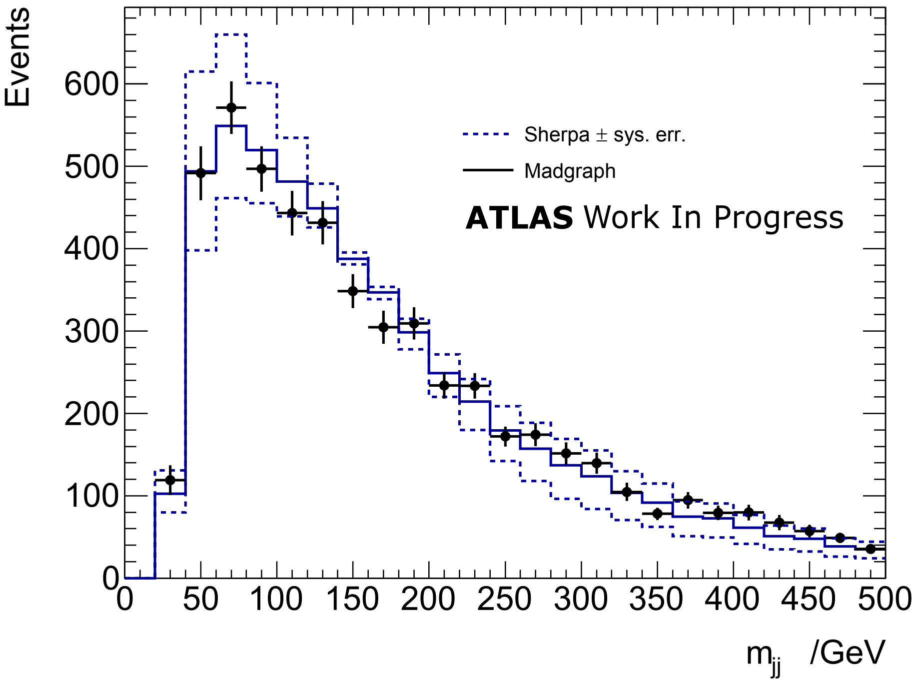

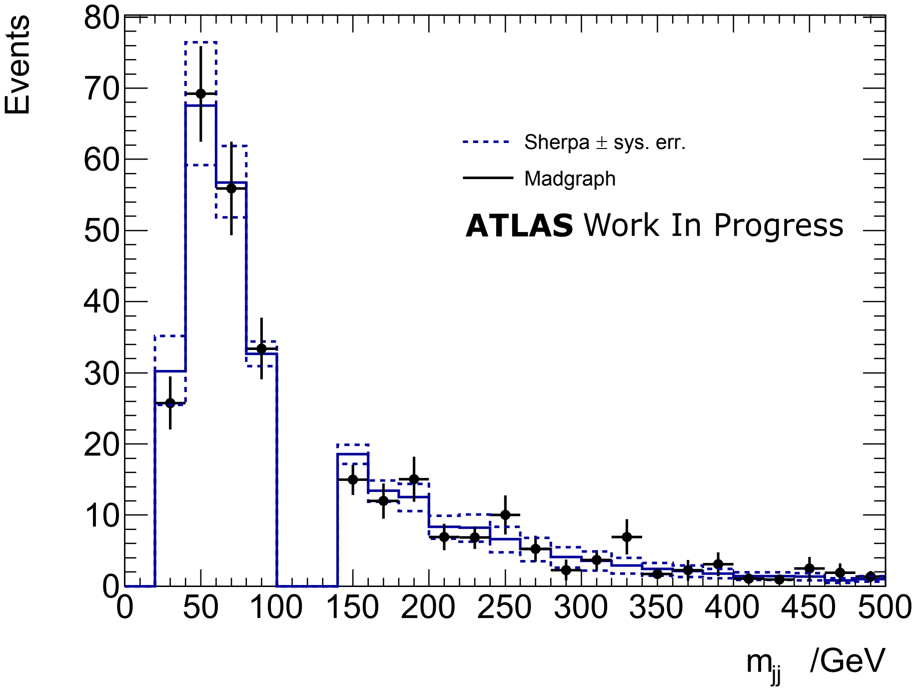

Figure 5.24: Comparison of the W+jets prediction from MadGraph with that from Sherpa as a function of m_{jj} for the 1 lepton control region for 1 (top) and 2 (bottom) tags.

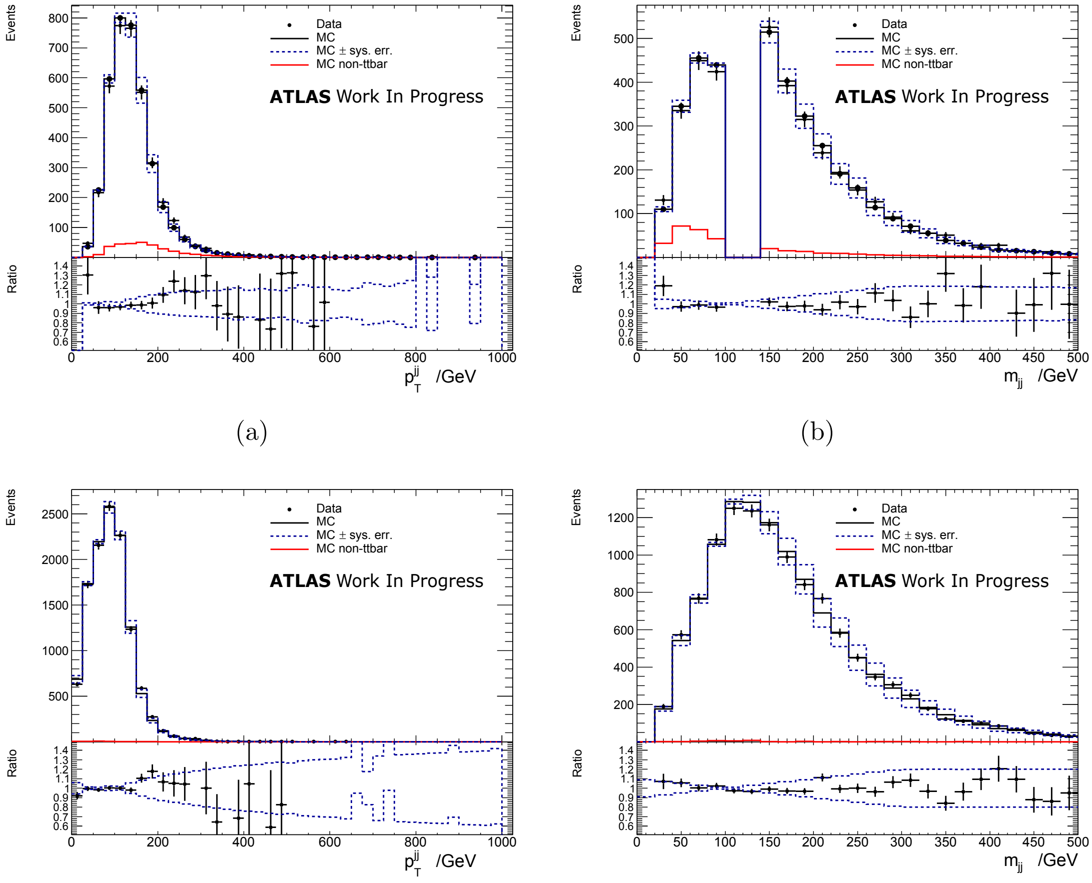

(a)

(b)

(c)

(d)

Figure 5.25: The p_T^{bb} and m_{bb} distributions in the top control regions of the 1 lepton selection ((a) and (b)), and for the 2 lepton e-μ selection ((c) and (d)).

5.6.4 Other Background Modelling

The other lesser backgrounds are not allowed to float or be normalised. Instead, these are fixed at the expected yield from the Monte Carlo simulations, but each comes with their own associated uncertainty.

The uncertainties for light jet events are derived from comparisons between MC and data events with 0 b-tagged jets. Uncertainties for heavy flavour jets are estimated by comparing the ratios in Sherpa with Madgraph and taking the largest difference between them.

CHAPTER 6

STATISTICAL ANALYSIS

6.1 Fitting framework

After selections have been made on the data and the simulations the final stage of processing is a combined profile likelihood fit. Known and unknown parameters describing the simulations are compared to the data, with certain backgrounds given the freedom to float and be rescaled to match the data distributions in control regions. This process is outlined in this section.

The W+jets, Z+jets and $t\bar{t}$ backgrounds are allowed to have a floating normalisation in the fitting process. The process is a profile likelihood fit (for further details see Section 6.1). The other backgrounds such as diboson, VH and single top quark events are not allowed to float and instead use the suggested normalisation from Monte Carlo with an associated error. They may however be subjected to profiling allowing them to be altered by the fit.

6.1.1 Likelihood definition

The primary analysis performed to compare simulation and data is a binned likelihood function. This function is described below as a product of Poisson probability terms.

$$\mathrm{Pois}\left(n|\mu S + B\right)\left[\prod_{b\in\mathrm{bins}}^{n} \frac{\mu\nu_b^{\mathrm{sig}} + \nu_b^{\mathrm{bkg}}}{\mu S + B}\right], \tag{6.1}$$

In this equation, ν_b^{sig} and ν_b^{bkg} are the expected signal and background yields in bin b respectively. Here, μ is defined as the signal strength parameter, which acts to scale the signal yield.

The relationship between the predictions and the systematic uncertainties is described by NP, which are denoted as θ. NPs are parameterised by one of two types of prior: Gaussian or log-normal. Log-normal priors are used in calculating normalisation uncertainties, as this way a positive likelihood value is obtained.

The contents of each background and signal bin is calculated via a function in terms of θ. For normally distributed θ functions, the bins are parameterised in such a way that the rates are log-normally distributed.

The main function of priors is to constrain the possible values of NPs to keep them within the uncertainties around their nominal values. Penalty measurements are added into the likelihood calculation which enforce these constraints. They are designed to increase in value as the NP deviates from its nominal value. Therefore the likelihood function $(\mathcal{L}(\mu, \theta))$ can be described as a function of θ and μ.

To find the nominal fit, the likelihood function must be maximised with respect to all parameters. This value is known as the Maximised Log-Likelihood value (MLL). One defines a test statistic q_μ as $q_\mu = 2\ln(\mathcal{L}(\mu, \hat{\hat{\theta}}_\mu)/\mathcal{L}(\hat{\mu}, \hat{\theta}))$. Here, $\hat{\theta}$ and $\hat{\mu}$ are the parameters which give the MLL where $0 \leq \hat{\mu} \leq \mu$. Also $\hat{\hat{\theta}}_\mu$ are the values of the NPs which will maximise the likelihood for each μ. The aim of this test statistic is to measure agreement between the data and the background model. It also tests exclusion intervals which are derived with the CL_s method[102].

6.1.2 Fit inputs and variables

A summary of the input regions for fitting are outlined below:

- **Signal Region** - The signal region is defined as being 0 lepton events with either 1 or 2 b-tagged jets. The distribution used in fitting is m_{jj}.
- **Z+jets** - 2 lepton region, split into 0, 1 and 2 b-tag bins. Also included for this background is 0 lepton, 0 b-tag events.
- **W+jets and** $t\bar{t}$ - 1 lepton region split into 0, 1 and 2 b-tag bins.

Each of these is further split up into four bins based on MET or the MET proxy associated with that region, such as p_T^V. In order to simplify the fitting process, shape information is not taken into account in any distributions with 0 b-tagged jets.

6.1.3 Nuisance parameters: normalisation and systematic uncertainties

The systematic uncertainties associated with this analysis are represented in the fitting process as nuisance parameters. This process sorts these uncertainties into one of two different types of nuisance parameter.

6.1.3.1 Floating parameters

Floating parameters can be normalised and are usually used for fitting quantities such as cross-section or detector acceptance. Typically, these values have theory normalisations which may not be completely correct and are allowed to be dictated entirely by the data in control regions.

This analysis has four freely floating parameters to be normalised during fitting. These are:

- Signal: Signal strength [μ]
- Wbb: $W + bb$ normalisation [`norm_Wbb`].
- Zbb: $Z + bb$ normalisation [`norm_Zbb`].
- Top: $t\bar{t}$ quark production normalisation [`norm_ttbar`].

The lesser backgrounds are fixed at the expected yield from the MC simulations, each with their own associated uncertainty (for full list, see Section 5.6.4). These uncertainties on the backgrounds are described in detail in Section 5.6.

6.1.3.2 Nuisance parameters with priors

If the value of a systematic uncertainty has already been constrained, it is known as a nuisance parameter with a prior. As well as the previously mentioned free floating parameters, the fit has nuisance parameters associated with Monte Carlo modelling and experimental uncertainties.

6.1.4 Nuisance parameters: statistical uncertainties

All above uncertainties have been systematic, but the analysis also needs to address its own limitations in terms of how the data is stored and represented, the systematic uncertainties. Distributions are stored in histograms. A histogram with an infinite number of bins is a physical impossibility, therefore there must be some statistical uncertainty associated with how the data has been binned.

The method for calculating these uncertainties is known as the Barlow-Beeston method, which is implemented as default in HistFactory[103], a tool that creates workspaces for analyses based on template histograms which bypasses the need to understand the modelling language. It introduces a new nuisance parameter (per bin) associated with the statistical uncertainty on the number of background events in each bin. There is no bin-to-bin correlation for this nuisance parameter. Instead of choosing to implement this uncertainty in every bin, it is only applied to the bins where the statistical uncertainly is of a predetermined significant size. The threshold for determining whether the uncertainty is large enough to be considered is set at 1%.

6.1.5 Pruning of the Systematic Uncertainties

Some of the systematic uncertainties described in Section 5.4 have such a small effect on the overall distributions, that it would be simpler to omit them than attempt to include them in the process. As well as this, simulations with very low statistics but with associated systematics can register as very large fluctuations, resulting in artificial variations entering into the fitting process. Checks were made to compare the pruned vs non-pruned analysis. Pruning these systematics provided improved speed, greater stability and didn't affect the overall sensitivity. Without pruning, small backgrounds with large errors resulted in large pulls after the fit.

A series of checks were performed to ensure stability of fits to noise fluctuations; details justifying the specific variations made are described in the VHbb Run 1 analysis [101].

- Statistical fluctuations associated with systematics that require a re-sampling of the events (such as JES) can be reduced using the smoothing method outlined in Section 6.1.5.1.
- Normalisation uncertainty can be omitted for a given background within a region if one of the following is true:

  - The variation as a result of the uncertainty is less than 0.5%
  - The up and the down variations in the distributions both have the same sign uncertainty

- Shape uncertainty can be omitted for a given background in a region if one of the following is true:
  - After normalisation is removed, no bins have deviation $> 0.5\%$
  - If either the up or down variation (but not both) are non-zero and all previous conditions are passed
- Shape and normalisation uncertainties can be omitted for a background in a region if:
  - the background in question makes up less than 2% of the overall background
  - Signal is $< 2\%$ of total background and the errors associated with normalisation and shape are both $< 0.5\%$ of total background
  - If a bin has signal contribution $> 2\%$ of total background and shape and normalisation error $< 2\%$ of signal yield

- Neglect the shape and normalisation uncertainty for a given sample in a given region if the sample is less than 2% of the total background:
  - if the signal $< 2\%$ of the total background in all bins and the shape and normalisation error are each $< 0.5\%$ of the total background
  - if at least one bin has a signal contribution $> 2\%$ of the total background, only in those bins where the shape and normalisation error are each $< 2\%$ of the signal yield

6.1.5.1 Smoothing

To evaluate the uncertainties associated with reconstructed objects in the analysis, two methods are employed. In instances where the simulation is corrected via a scale factor (such as in flavour tagging or to account for JES uncertainties) the weight is moved up and down. The effect this has on the final distribution is described as a +1 or -1 σ shift. In the specific case of JES uncertainties, this can result in some events falling outside of acceptance.

To address these issues, smoothing algorithms are used which were developed during the Run 1 analysis. Bins between extrema are merged until there is only one local extremum in m_{bb}. Then these bins are merged sequentially starting at the upper limit of the distribution working downwards. Merging continues until each bin has a statistical uncertainty $< 5\%$ (when calculated using the nominal template). Following this a comparison is drawn between the integral of the nominal distribution and the above shifted distribution. This gives the $\pm 1\sigma$ variation, which is used as the uncertainty for the nominal bins. For more details on the smoothing procedure, see Reference [104].

6.1.6 Understanding the fit configuration

This section contains the results of tests to evaluate the outcome of the fitting procedure.

6.1.6.1 Nuisance parameter pulls and constraints

Figure 6.1 shows the nuisance parameter pulls and constraints for the Asimov fit where $\mu = 1$ and for the data fit. Error bars for the Asimov fit and the data fit are largely consistent for all parameters. As such none are over-constrained. Almost all parameters have 0 pull in the Asimov fit, which is expected. The three normalisation parameters ‘norm_Wbb’, ‘norm_Zbb’ and ‘norm_ttbar’ are pulled to one standard deviation in both Asimov and data. The only other significant pulls are in the data fit, specifically 'WPtV_Wl', 'FT_EFF_Eigen_C_0_Y2015' and 'JET_GroupedNP_3_Y2015'.

6.1.6.2 Nuisance parameter ranking

Once the MLL value is calculated, the NPs are allowed to vary by $\pm 1\sigma$. At these extremes, the likelihood is maximised again. By observing how much the best fit value (μ) changes with respect to this gives a measure of how sensitive the fit is to the particular NP. The top 15 most influential NPs are shown in Figure 6.2 for the case where $m_\chi = 400$ GeV, $m_{Z'} = 2000$ GeV and $m_H = 125$ GeV with $\mu = 0$. The most significant parameter is associated with charm identification as an element of the b-tagging algorithm. As reliable b-tagging is crucial to the analysis, it makes sense that this pull would have a greater effect. Other notable parameters include the normalisation parameter on the $t\bar{t}$ background.

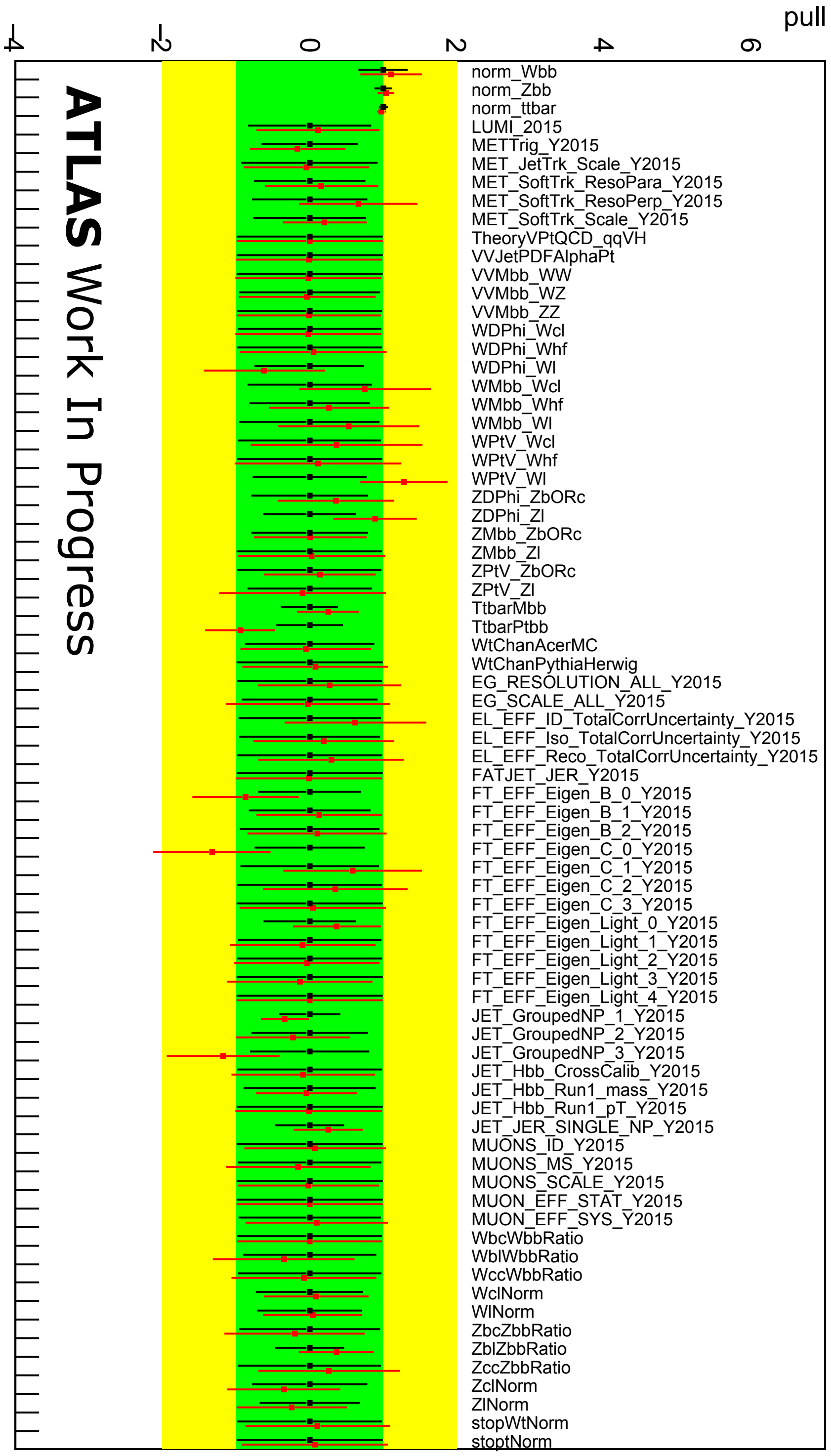

Figure 6.1: The nuisance parameter pulls for the Asimov fit with $\mu = 1$ (black) and data fit (red). Signal here is simplified vector model with $m_\chi = 400$ GeV and $m_{Z'} = 2000$ GeV.

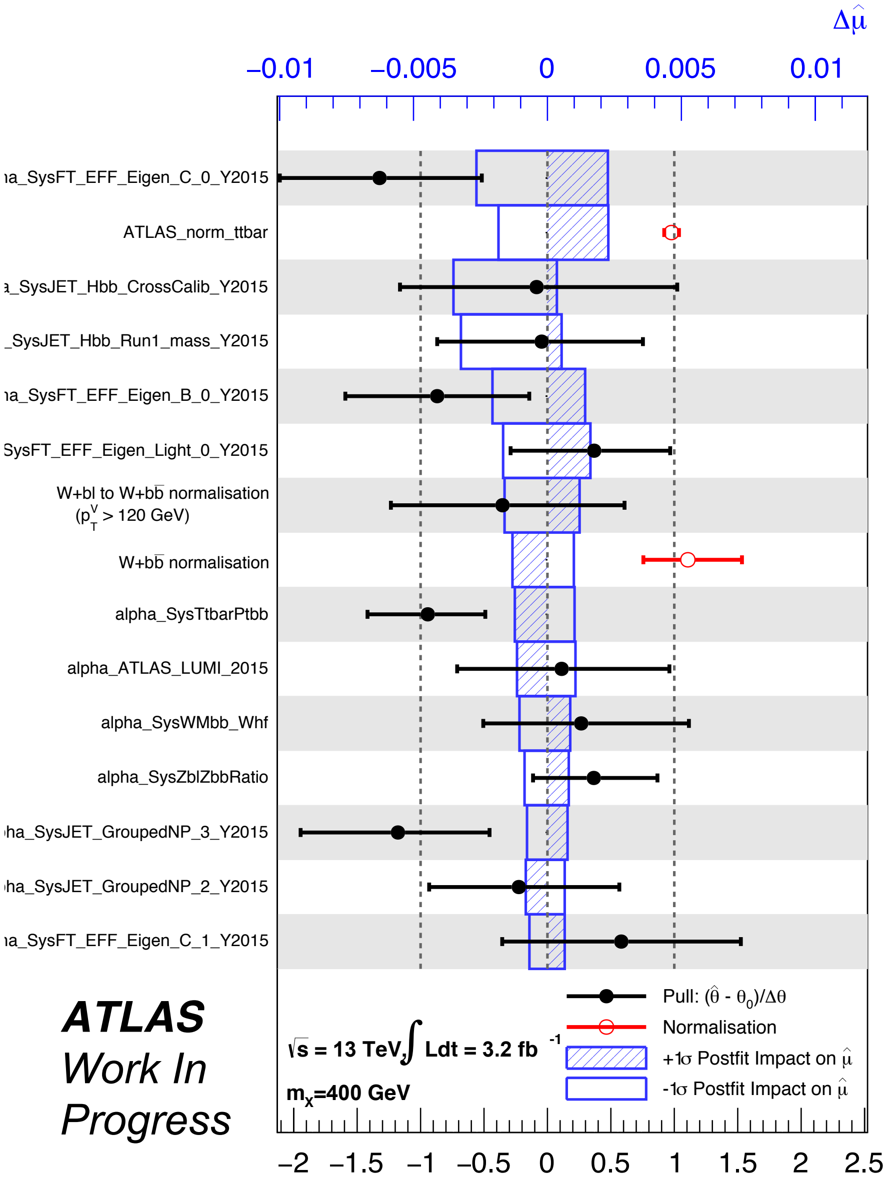

Figure 6.2: Ranking of the 15 most important nuisance parameters for the simplified vector model with $m_\chi = 400$ GeV and $m_{Z'} = 2000$ GeV.

6.2 Post-fit plots

The plots after the fit to data are shown here. Figures 6.2 - 6.11 show the m_{bb} distributions for the 0, 1 and 2 lepton regions. Each is represented twice, once for the 1 and 2 b-tagged jet regions respectively. These are then in turn split into the four MET (or proxy) bins. All show good agreement between background simulation and data. From these plots, there is no evidence of any signal. Note that the signal simulation has an arbitrary cross-section applied. The scaling is meaningless, but is included to demonstrate the expected shape if such a signal were found. These plots also show the 'pre-fit' normalisation for the total background (shown by the blue dashed line), to illustrate how the fitting affected the shape of the background distribution. The most notable difference between pre and post fit normalisation can be seen in the plots of events with 1 b-tagged jet, specifically for 0 and 1 lepton regions. The 'pre-fit' background estimation was more similar to the data in the 2 b-tagged jet bins.

As stated above, the post-fit plots show that the MC background only describes the data well. Therefore these plots can be used to extract limits on signal observation. These limits are shown and discussed in Section 7.1.

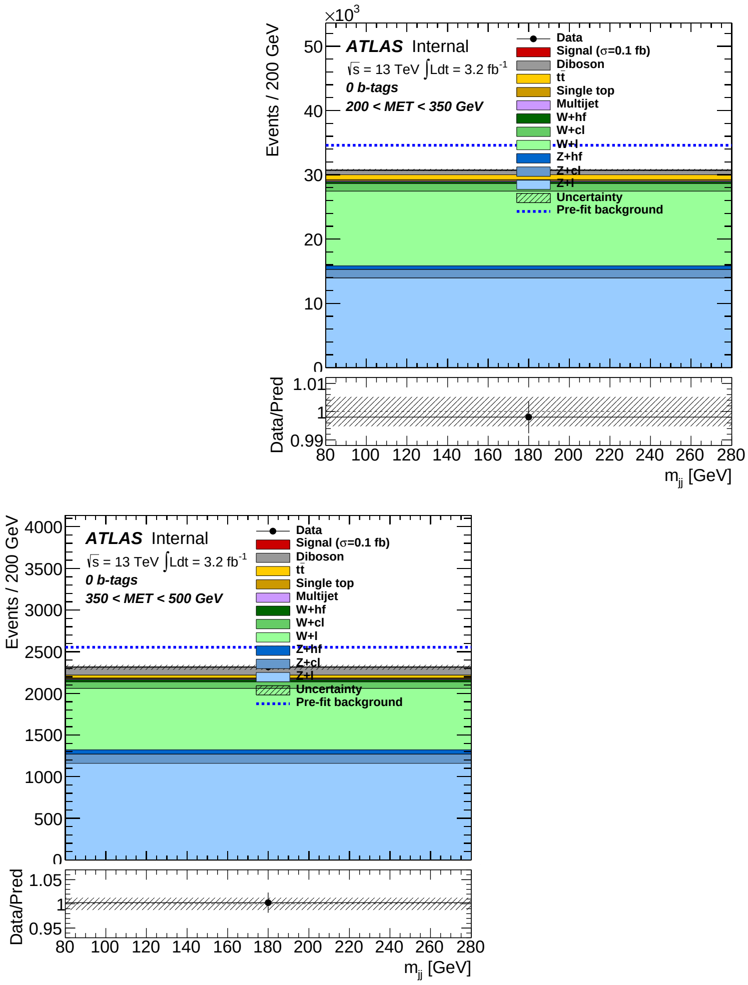

Figure 6.3: Post-fit plots of the invariant mass of the two signal jets for the 0 lepton control region for 0 tag events. The pre-fit background is also shown on the plot. Signal here is simplified vector model with $m_\chi = 400$ GeV and $m_{Z'} = 2000$ GeV.

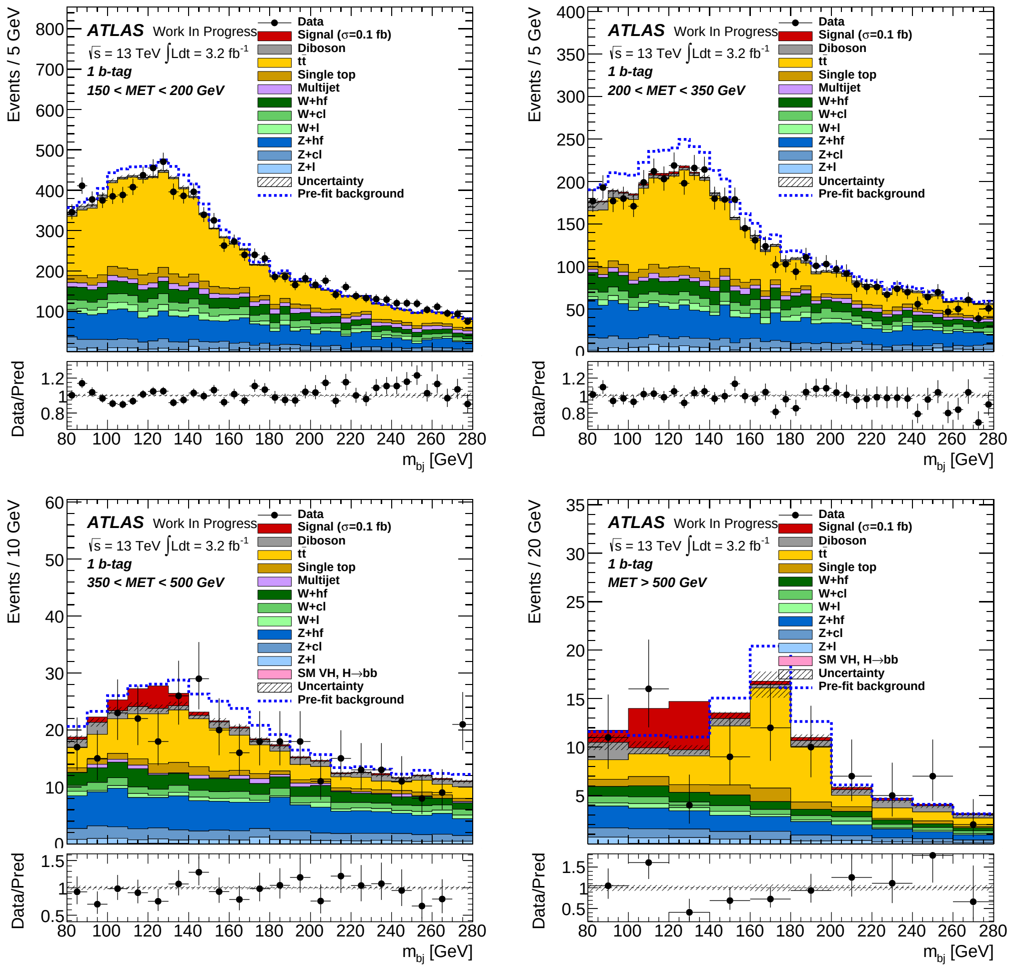

Figure 6.4: Post-fit plots of the invariant mass of the two signal jets for the 0 lepton control region for 1 tag events. The pre-fit background is also shown on the plot. Signal here is simplified vector model with $m_\chi = 400$ GeV and $m_{Z'} = 2000$ GeV.

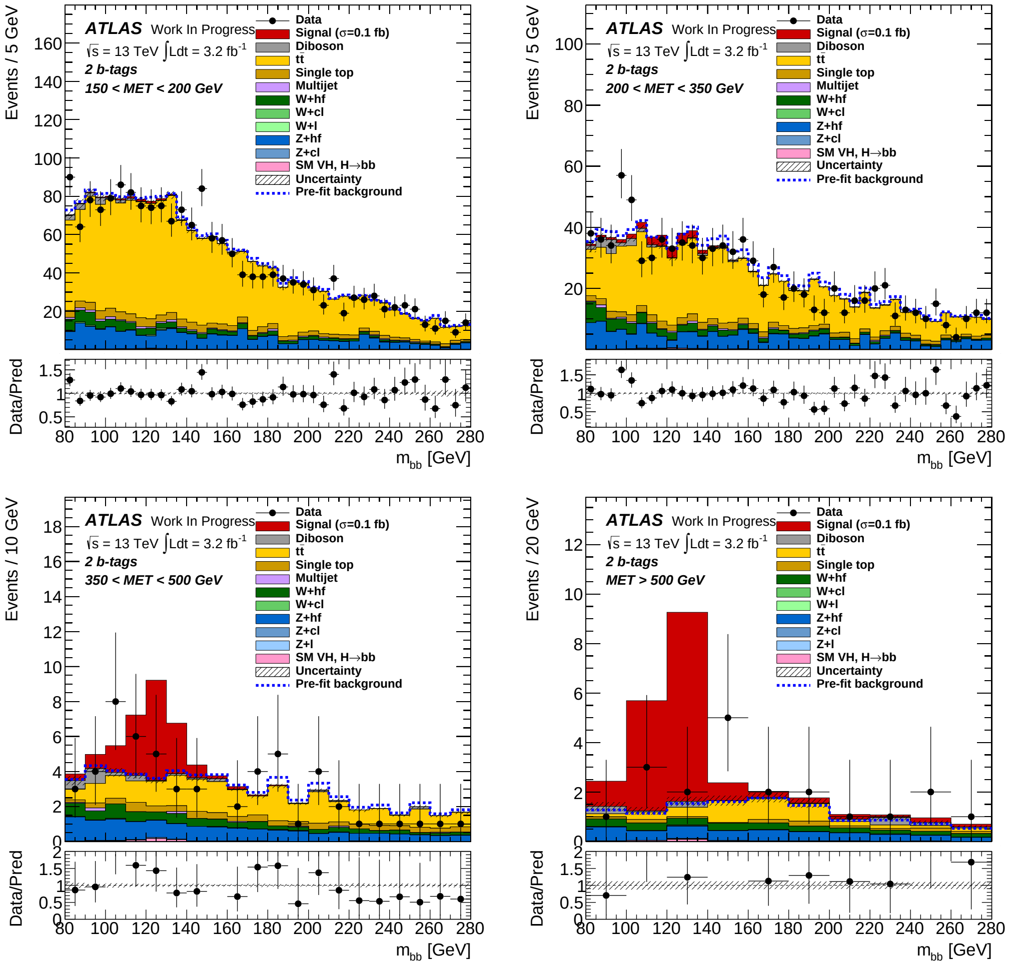

Figure 6.5: Post-fit plots of the invariant mass of the two signal jets for the 0 lepton signal region for 2 tag events. The pre-fit background is also shown on the plot. Signal here is simplified vector model with $m_\chi = 400$ GeV and $m_{Z'} = 2000$ GeV.

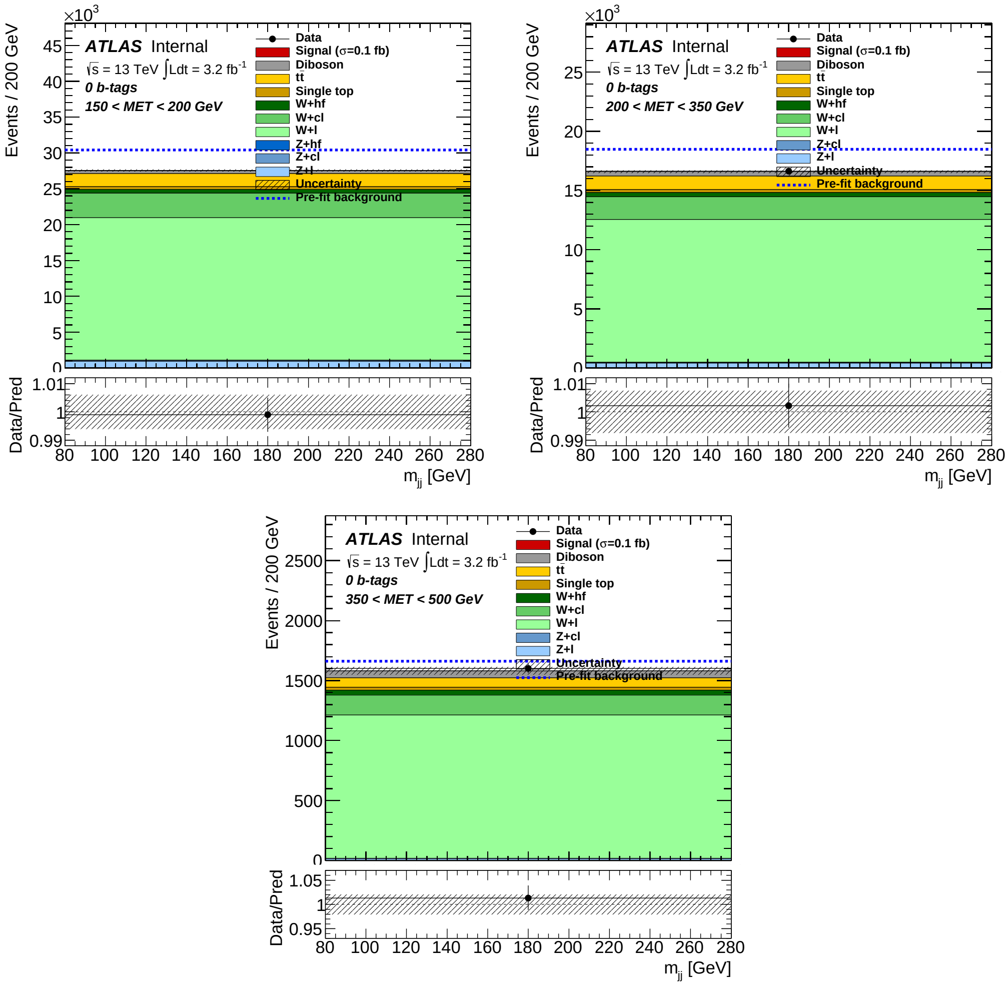

Figure 6.6: Post-fit plots of the invariant mass of the two signal jets for the 1 lepton control region for 0 tag events. The pre-fit background is also shown on the plot.

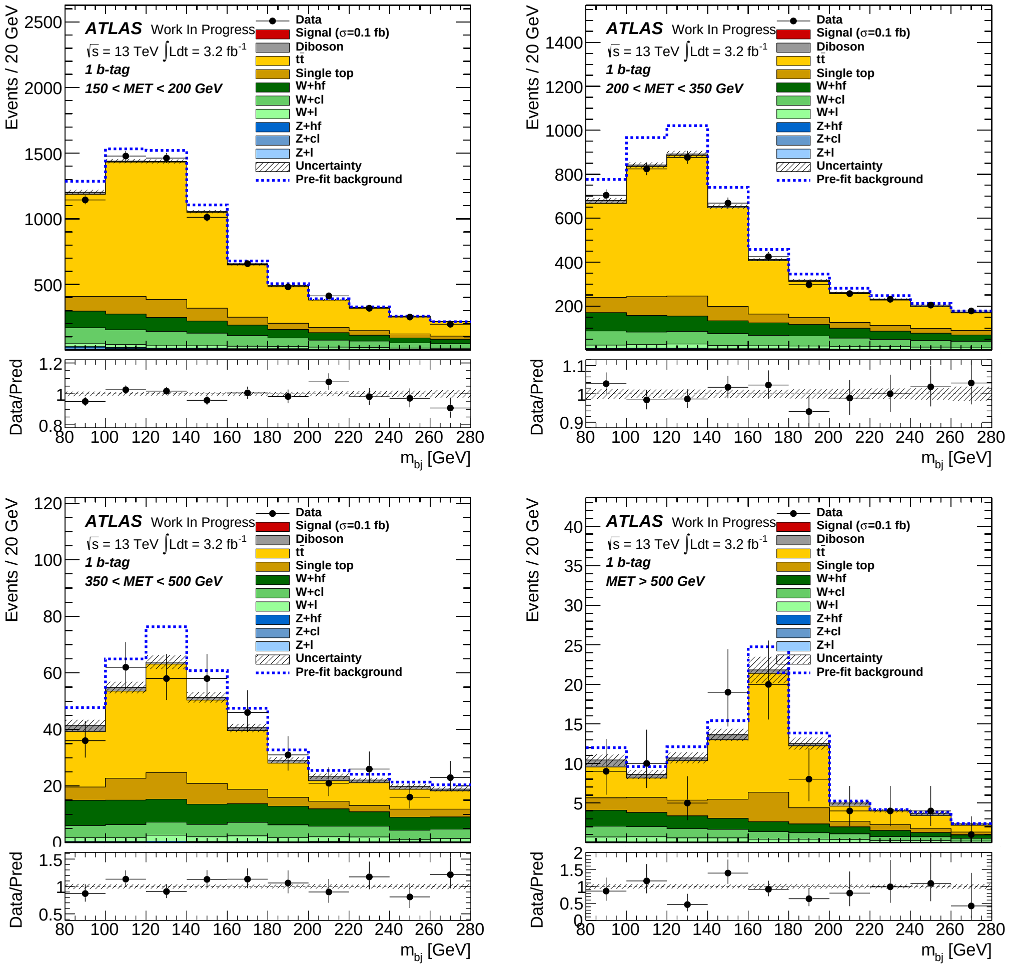

Figure 6.7: Post-fit plots of the invariant mass of the two signal jets for the 1 lepton control region for 1 tag events. The pre-fit background is also shown on the plot.

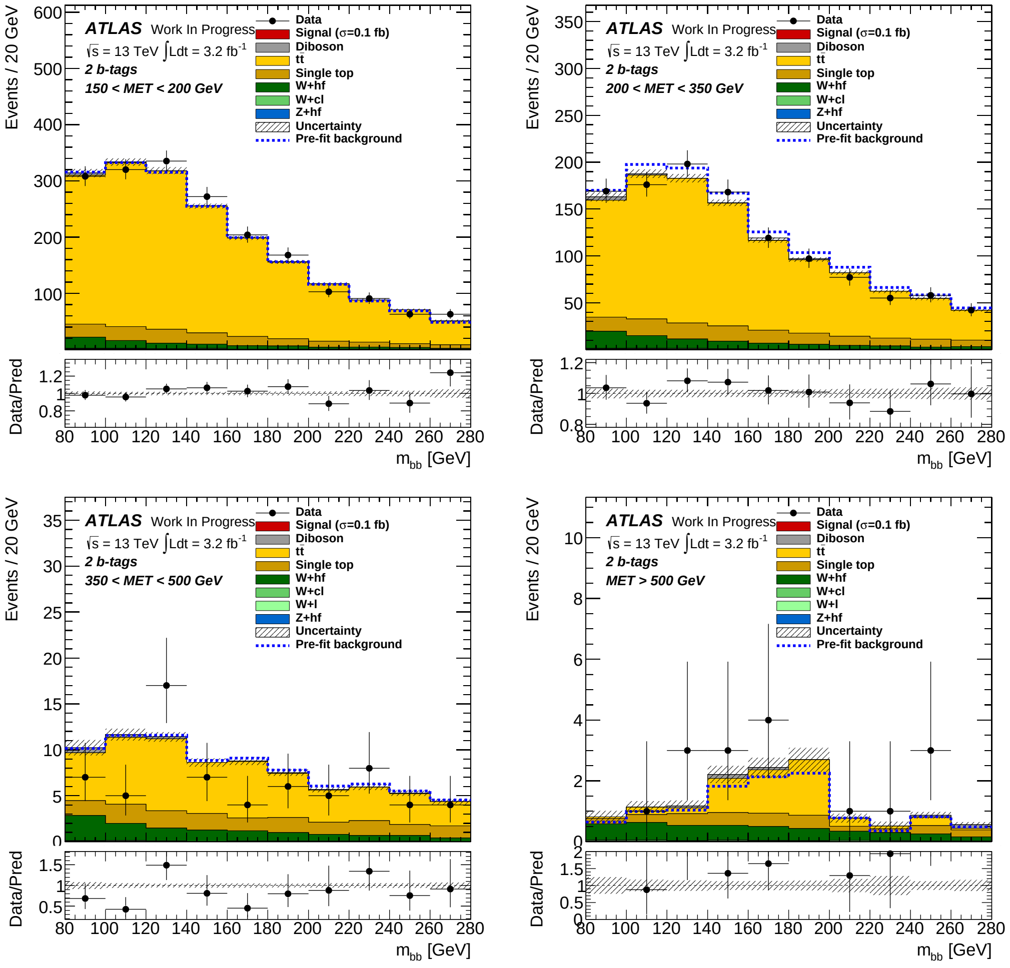

Figure 6.8: Post-fit plots of the invariant mass of the two signal jets for the 1 lepton control region for 2 tag events. The pre-fit background is also shown on the plot.

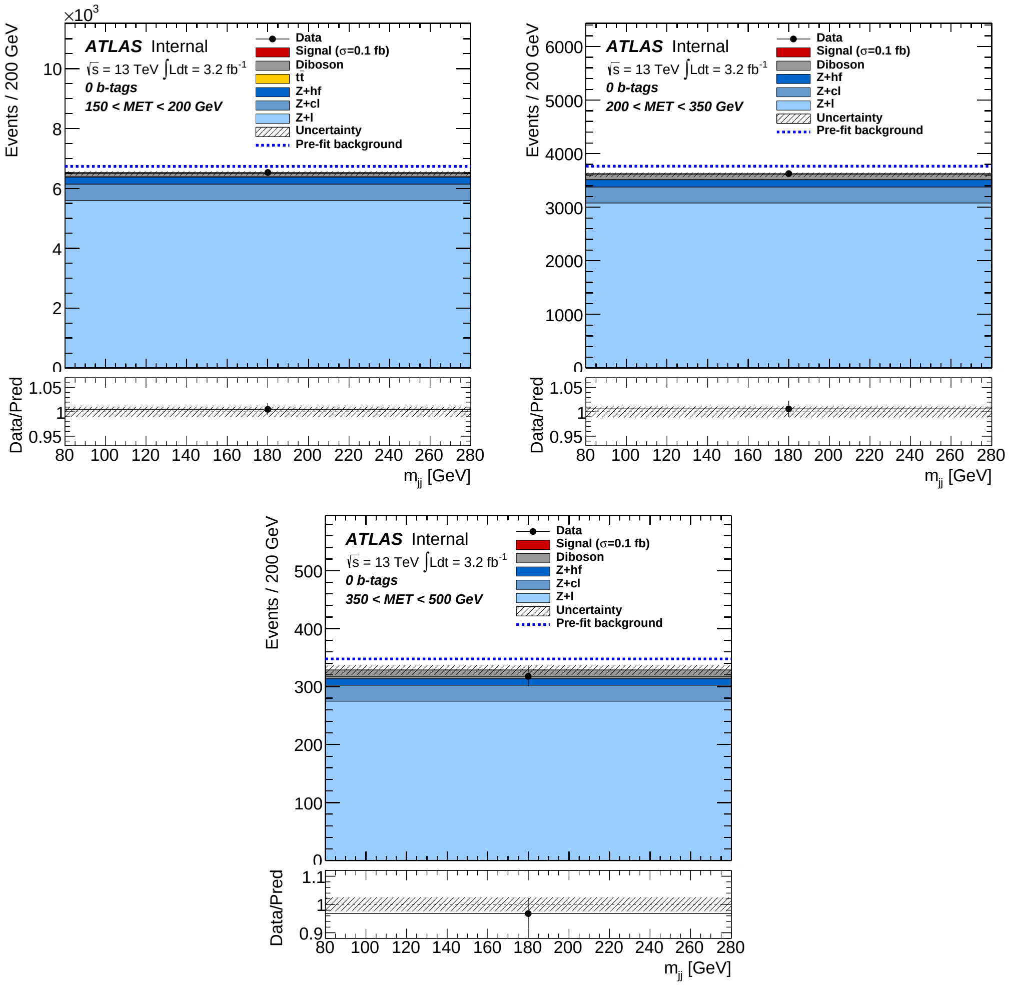

Figure 6.9: Post-fit plots of the invariant mass of the two signal jets for the 2 lepton control region for 0 tag events. The pre-fit background is also shown on the plot.

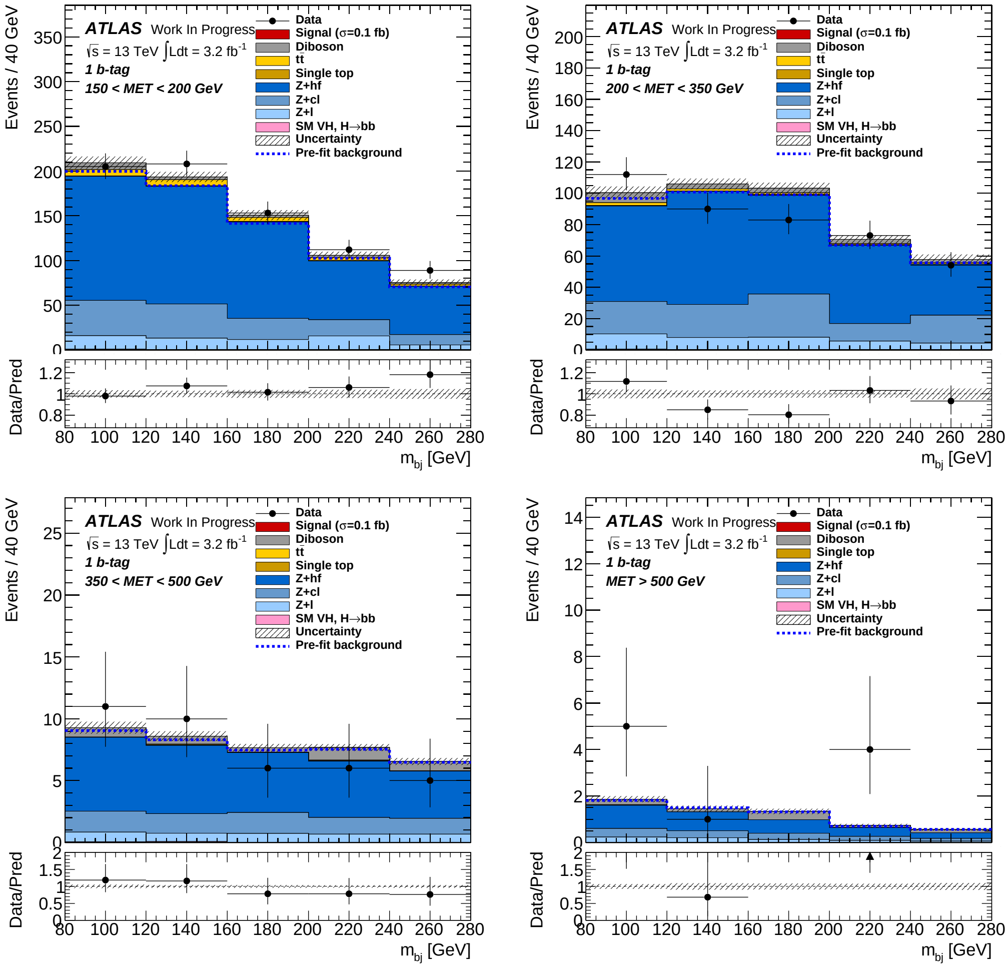

Figure 6.10: Post-fit plots of the invariant mass of the two signal jets for the 2 lepton control region for 1 tag events. The pre-fit background is also shown on the plot.

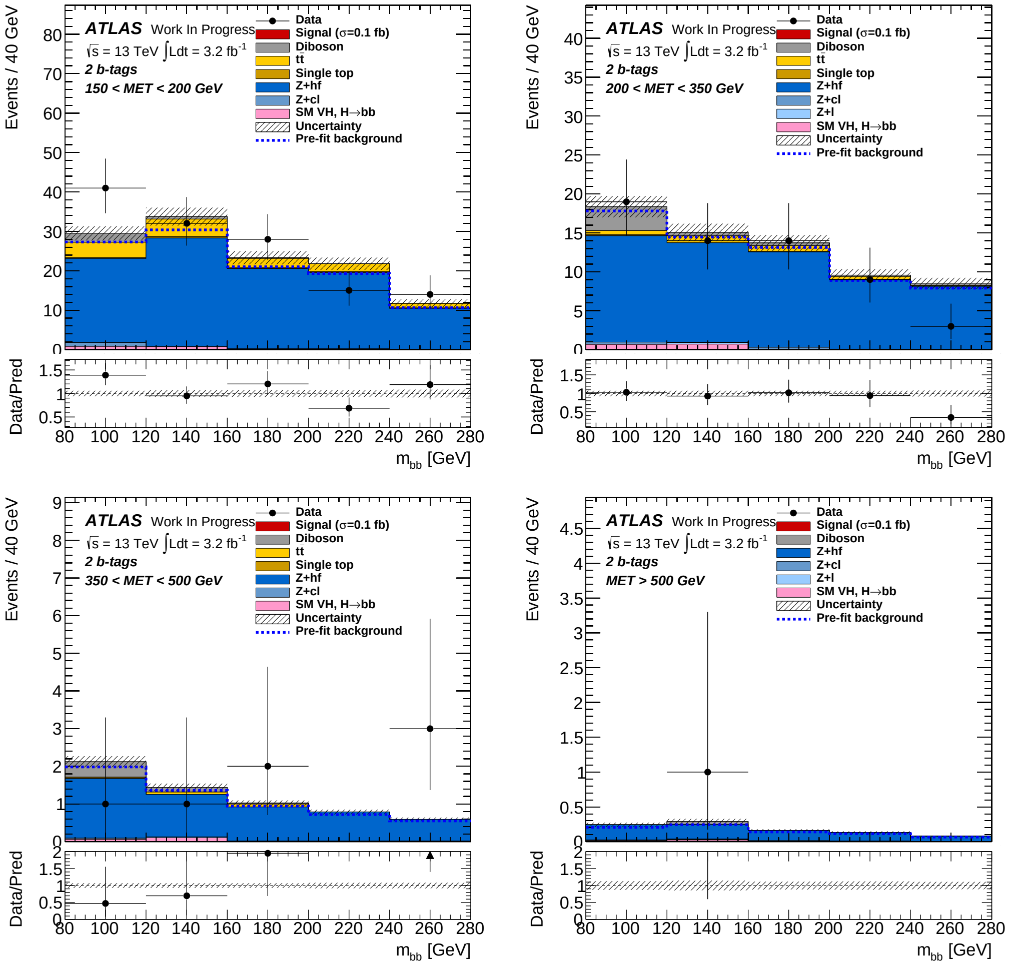

Figure 6.11: Post-fit plots of the invariant mass of the two signal jets for the 2 lepton control region for 2 tag events. The pre-fit background is also shown on the plot.

CHAPTER 7

RESULTS AND INTERPRETATION

7.1 Interpretation of Limits

The end goal of this analysis was to discover new physics. However, as seen in Section 6.2, the data is largely consistent with the background expectations. As such a discovery cannot be claimed, limits can be imposed on the production cross sections of the signal events. The results are presented below, split into three categories: simplified models, Z'-2HDM models and the EFT models. The theory behind these is discussed in Sections 1.5 - 1.6.3.

7.1.1 Simplified Models

Note that in this section, only the vector models will be used. There is currently poor theoretical understanding of mixing between the Higgs boson and scalar particles

Limit	m($_{Z'}$) [GeV]	m($_{\chi}$) [GeV]
Expected	200	126.58
+1 σ	200	109.10
-1 σ	200	135.33
Observed	200	111.60

Table 7.1: The single 95% confidence level exclusion point determined from the reference cross section.

and as such, these models are omitted from these results.

The interpretation of these simplified model results is based upon an agreed method from the LHC dark matter working group[105]. The signal simulation is scaled to the data during the fit and is converted into a limit on the cross section using the scale factor with the CL$_S$ frequentist formalism[106]. The associated scale factor μ, is used to scale the theoretical cross sections to extract upper limits at 95% confidence level. These are upper limits on $\sigma(pp \rightarrow h\chi\chi)Br(h \rightarrow bb)$. In order to extract a limit on just $\sigma(pp \rightarrow h\chi\chi)$, one only needs to divide by $Br(h \rightarrow bb)$, where the Standard Model branching ratio of $Br(h \rightarrow bb) = 0.571$. The result of this is shown for the vector simplified models in Figure 7.1 as a function of $m_{Z'}$ for fixed m_χ and vice versa. These plots are taken from an ATLAS internal document describing the analysis [23].

These limits are more conveniently represented when displayed in a ($m_{mediator}$,m_χ) space. To achieve this, a cross section vs m_χ plot is made for each $m_{mediator}$. The theoretical cross section is plotted on top, as in Figure 7.2. The point at which the theoretical cross section crosses with the expected limit, is considered as a lower limit on the m_χ. This information can then be represented as a single data point on a plot of $m_{mediator}$ vs m_χ. Information about where the theory crosses the observed and upper/lower limits can also be extracted and turned into data points in the same way, as seen in Table 7.1.

This is done for all values of m(Z'). These exclusion limits are shown for all Z' masses in Figures 7.3 and 7.4. A summary of the limit crossings can be found in Table 7.2. Due to the coarse selection of mass points used when creating the models and

$m_{Z'}$ [GeV]	Expected	+1 σ	-1 σ	Observed
10	5.40	3.73	6.65	4.15
50	31.26	21.33	37.34	22.60
200	126.58	109.10	135.33	111.60
500	448.28	379.91	471.03	400.35
1000	250.27	904.25	720.74	919.92

Table 7.2: 95% confidence level m_χ exclusion limits for the simplified vector models.

due to the absence of some $m_{Z'}$ and m_χ combinations, some points are connected continuously in order to cover the full range of masses. These points are plotted and connected in Figure 7.5.

7.1.2 Z'-2HDM Model

Treatment of the Z'-2HDM model is very similar to the simplified vector model. The major difference being the use of m_{A_0} instead of m_χ. The final exclusion plot will be presented in a $m_{Z'}$ vs m_{A^0} space.

Before the limits could be extracted, an important comparison was made with a similar test done during Run 1. Unlike the simplified model, there already exists a limit plot for Z'-2HDM. Some of the parameters used in generating the signal Monte Carlo files in this analysis differed from those that were used in Run 1. For a like-with-like comparison, this issue needed to be addressed. The models used during this analysis were generated using g_Z=0.1 and tan(β)=3.0. During Run 1, the values used in the simulation were g_Z=0.8 and tan(β)=1.0. The main impact these changes had were on the theoretical cross sections associated with the mass points for this model. These cross sections were recalculated using the previous model and parameters. These changes to cross section changed the normalisation of the signal samples, but did not affect the shape of any distributions. The corrected cross sections can be found in Table 7.3.

The expected and observed limits are then compared to the theoretical cross section in a similar manner as done for the simplified model. Plots for fixed m_A with varying

$m_{Z'}$ [GeV]	m_A [GeV]	σ [pb]
600	300	0.452
600	400	0.061
800	300	0.277
800	400	0.087
800	500	0.021
800	600	0.004
1000	300	0.144
1000	400	0.056
1000	500	0.020
1000	600	0.006
1000	700	0.002
1000	800	0.001
1200	300	0.075
1200	400	0.033
1200	500	0.013
1200	600	0.005
1200	700	0.002
1200	800	0.001
1400	300	0.041
1400	400	0.019
1400	500	0.008
1400	600	0.004
1400	700	0.002
1400	800	0.001

Table 7.3: Signal cross sections from the Z'-2HDM model.

$m_{Z'}$ and the inverse are plotted, and the intersection between expected and theory is given as the lower limit. Two assumptions are made here. Firstly that $m_\chi < \frac{1}{2}m_A$ and secondly that $BR(A \rightarrow \chi\chi) = 100\%$. This is shown in Figure 7.6. These are then represented on a m_A vs $m_{Z'}$ plot with the Run 1 results also shown in Figure 7.7. This analysis is significantly better than the one performed with Run 1 data. This is not only a product of the Run 2 data compared to the Run 1 data, but more a result of of the increased optimisation of this analysis compared to what was previously used, specifically the use of p_T^{miss} bins and the background control regions used during fitting.

7.2 Analysis Outlook

This analysis was performed using 2015 13 TeV Run 2 data. At the time of writing, the 2016 dataset has been completed and extensions to this analysis are underway. The addition of the 2016 data means increased statistics across the board, with a total integrated luminosity of 36.5 fb^{-1}. As well as increased statistics, new signal samples were generated for masses not included in this analysis. Details of these new models can be found in Table 7.4. Only the Z'-2HDM is being used in this analysis to derive model independent limits [107].

	A^0 Masses						
Z' Mass	200 GeV	300 GeV	400 GeV	500 GeV	600 GeV	700 GeV	800 GeV
200 GeV	🔴	🔴	🔴				
400 GeV	🔴	🔴	🔴	🔴			
600 GeV	🔴	🔴⚫	🔴⚫	🔴	🔴		
800 GeV	🔴	🔴⚫	🔴⚫	🔴⚫	🔴⚫	🔴	
1000 GeV		🔴⚫	🔴⚫	🔴⚫	🔴⚫	🔴⚫	🔴⚫
1200 GeV		🔴⚫	🔴⚫	🔴⚫	🔴⚫	🔴⚫	🔴⚫
1400 GeV		🔴⚫	🔴⚫	🔴⚫	🔴⚫	🔴⚫	🔴⚫
1600 GeV		🔴	🔴	🔴	🔴	🔴	🔴
1800 GeV		🔴	🔴	🔴	🔴	🔴	🔴
2000 GeV		🔴	🔴	🔴	🔴	🔴	🔴
2200 GeV		🔴	🔴	🔴	🔴	🔴	🔴
2400 GeV	🔴	🔴	🔴	🔴	🔴	🔴	🔴
2600 GeV	🔴	🔴	🔴	🔴	🔴	🔴	🔴
2800 GeV	🔴	🔴	🔴	🔴	🔴		
3000 GeV	🔴	🔴	🔴	🔴	🔴		

Table 7.4: Table showing the combinations of Z' and A^0 masses used when generating Z'-2HDM model in both the 2015 (black) and 2016 (red) analyses.

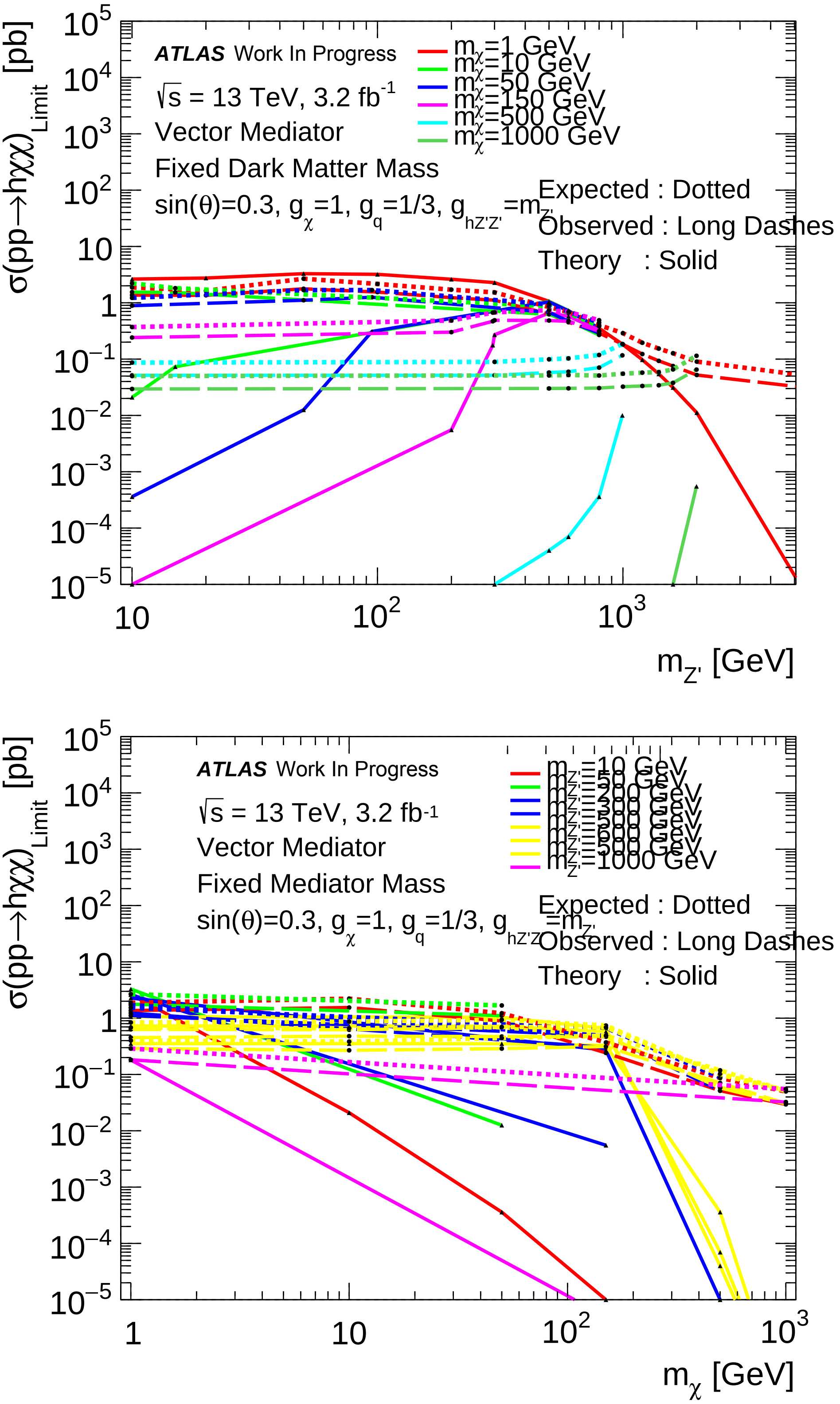

Figure 7.1: Expected and observed limits, along with the theoretical limits on the signal cross section for the various signal points in the vector model. Shown here are the limits presented as a function of mediator mass for a fixed dark matter mass (left) and as a function of dark matter mass for a fixed mediator mass (right). Plots from [23].

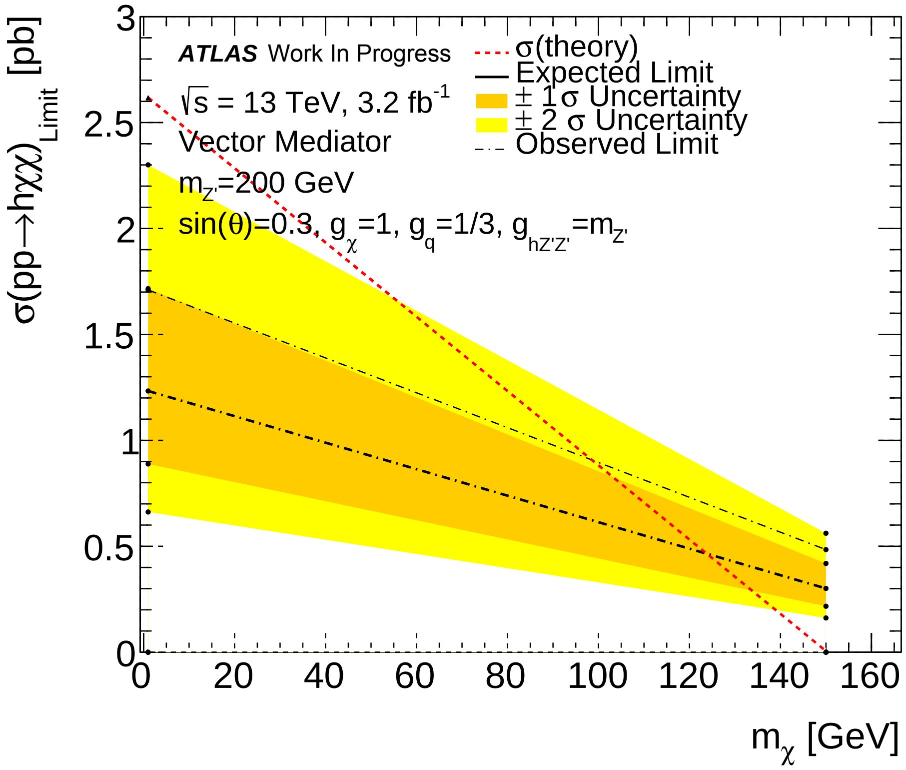

Figure 7.2: Demonstration of the determination of the expected, observed, and uncertainty band mass points for a single signal point. The point chosen is for a fixed mediator mass of 200 GeV.

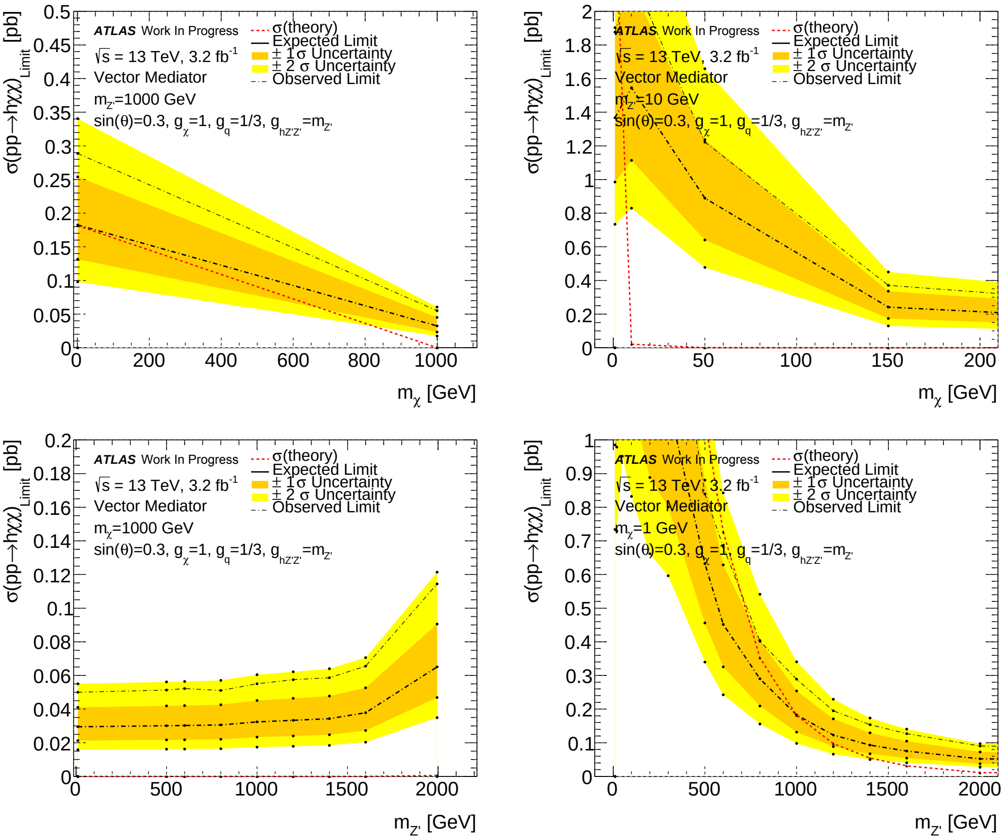

Figure 7.3: Cross section limits determined for the vector simplified model shown in linear scale for low and high mass examples.

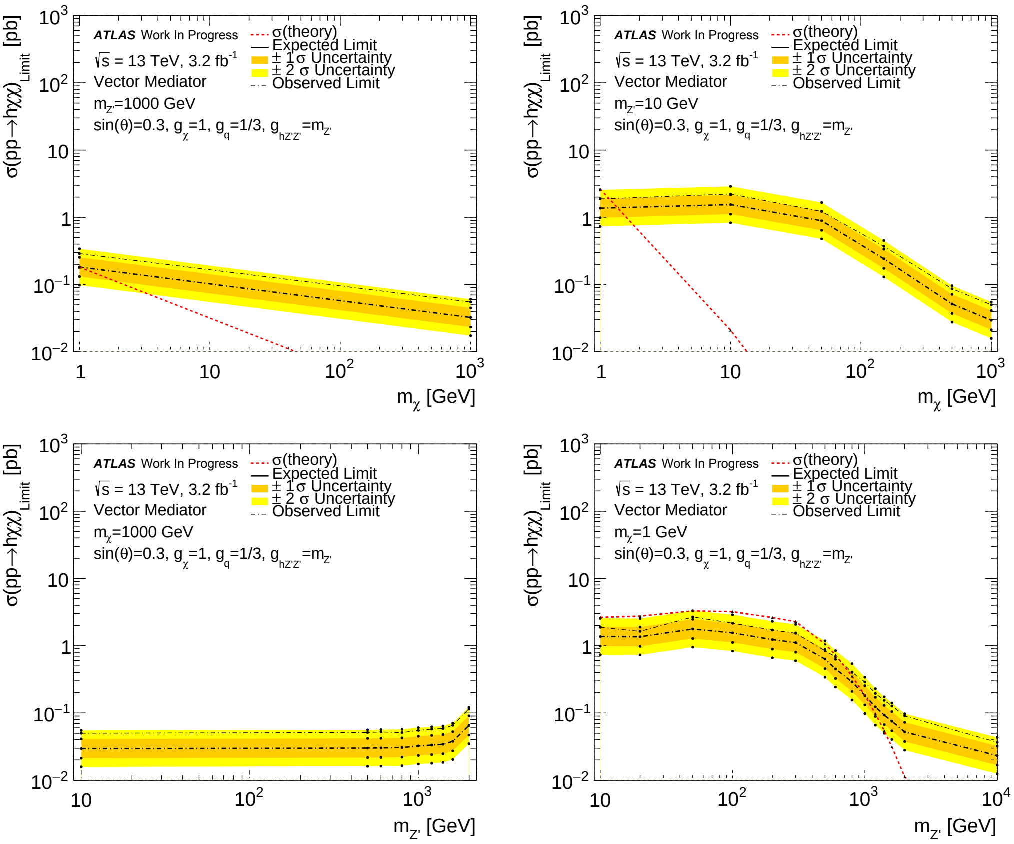

Figure 7.4: Cross section limits determined for the vector simplified model shown in logarithmic scale for low and high mass examples.

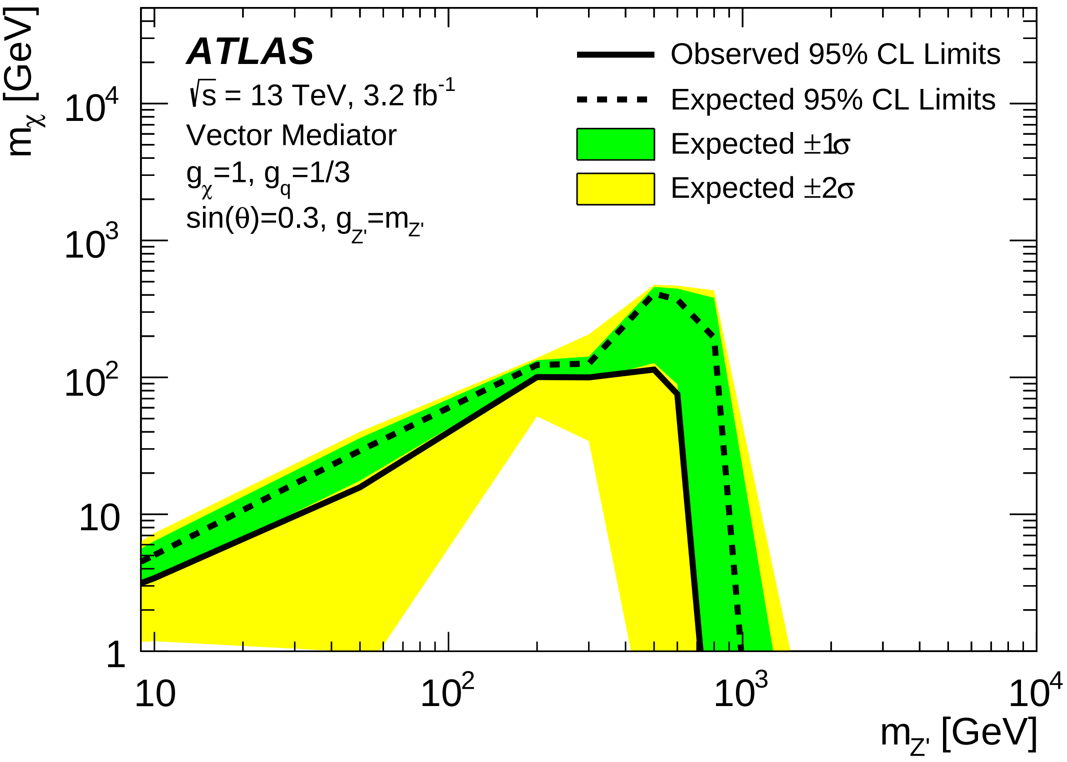

Figure 7.5: Mass exclusion for the vector simplified model.

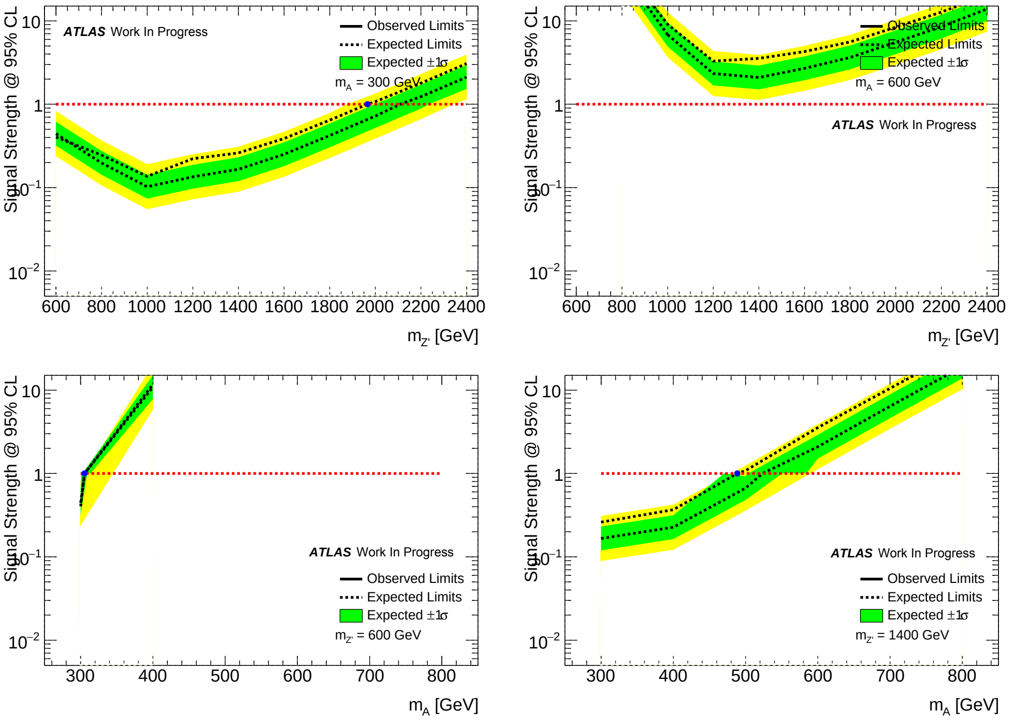

Figure 7.6: Cross section limits determined for the Z'-2HDM model shown in logarithmic scale, showing low and high mass examples.

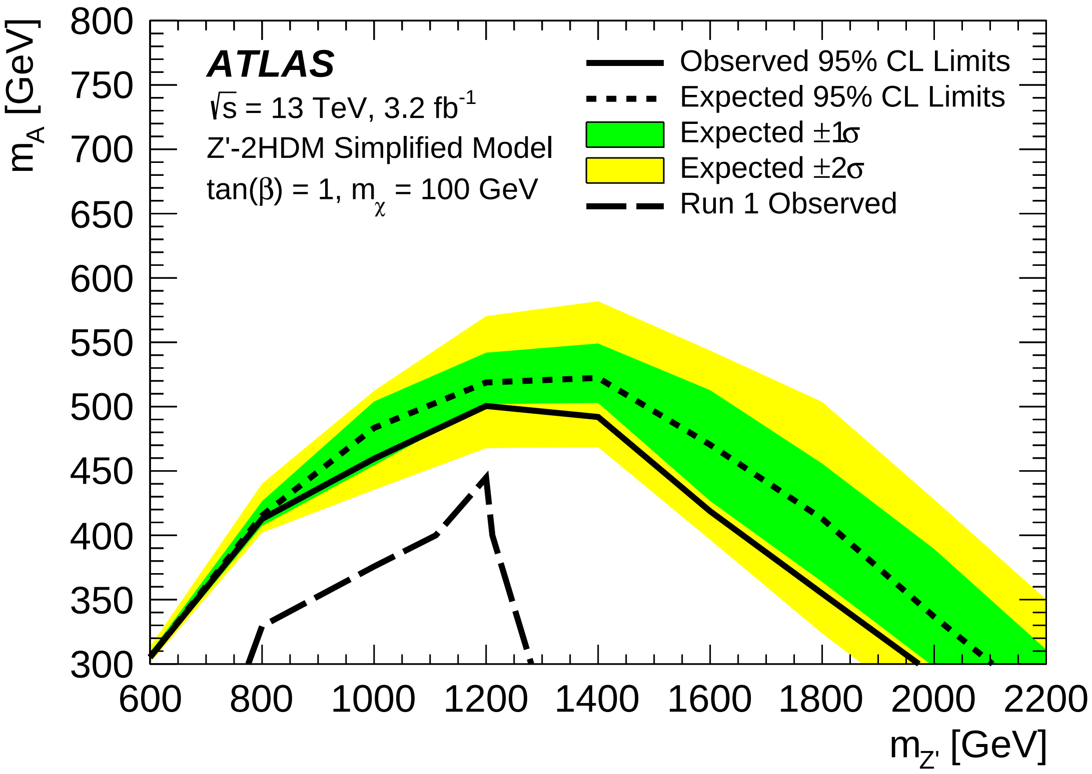

Figure 7.7: Mass exclusion for Z'-2HDM model.

REFERENCES

[1] M. Baca *et al.*, “Search for Dark Matter in association with a Higgs boson decaying to b-quarks in pp collisions at $\sqrt{s} = 13$ TeV with the ATLAS detector,” Tech. Rep. ATL-COM-PHYS-2016-100, CERN, Geneva, Feb 2016. (Unpublished).

[2] P. Allport *et al.*, “Recent results and experience with the Birmingham MC40 irradiation facility,” *JINST*, vol. 12, no. 03, p. C03075, 2017.

[3] P. Dervan *et al.*, “Upgrade to the Birmingham Irradiation Facility,” *Nucl. Instrum. Meth.*, vol. A796, pp. 80–84, 2015.

[4] R. French *et al.*, “Scanning facility to irradiate mechanical structures for the LHC upgrade programme,” *Proceedings of Science*, vol. 419, pp. 2–5, Jun 2014.

[5] L. B. A. Hommels *et al.*, “Detailed studies of full-size ATLAS12 sensors,” *Nucl. Instrum. Meth.*, vol. A831, pp. 167–173, 2016.

[6] K. A. Olive *et al.*, “The Review of Particle Physics,” *Chin. Phys. C*, vol. 38, p. 109, 2014.

[7] A. Djouadi and M. Grazzini, “The higgs boson in the standard model,” *Discovery of the Higgs Boson*, pp. 1–44, 2016. World Scientific.

[8] “Expected performance of the ATLAS b-tagging algorithms in Run-2,” Tech. Rep. ATL-PHYS-PUB-2015-022, CERN, Geneva, Jul 2015.

[9] ATLAS Collaboration, “Search for dark matter produced in association with a Higgs boson decaying to two bottom quarks in pp collisions at $\sqrt{s} = 8$ TeV with the ATLAS detector,” Tech. Rep. CERN-PH-EP-2015-247, 2015.

[10] C. Lefvre, “The CERN accelerator complex. Complexe des acclrateurs du CERN.” Dec 2008.

[11] J. Pequenao, “Computer generated image of the whole ATLAS detector,” Tech. Rep. CERN-GE-0803012, Mar 2008. https://cds.cern.ch/record/1095924.

[12] J. Pequenao, “Event Cross Section in a computer generated image of the ATLAS detector,” Tech. Rep. CERN-GE-0803022, Mar 2008. https://cds.cern.ch/record/1096081.

[13] M. Aaboud *et al.*, “Performance of the ATLAS Track Reconstruction Algorithms in Dense Environments in LHC Run 2,” *Eur. Phys. J.*, vol. C77, no. 10, p. 673, 2017.

[14] J. Pequenao, “Computer generated image of the ATLAS inner detector,” Tech. Rep. CERN-GE-0803014, Mar 2008. http://cds.cern.ch/record/1095926.

[15] F. Hugging, “The ATLAS Pixel Insertable B-Layer (IBL),” *Nucl. Instrum. Meth.*, vol. A650, pp. 45–49, 2011.

[16] “ATLAS Photos - TRT.” http://atlasexperiment.org/photos/inner-detector-trt.html.

[17] “ATLAS liquid argon calorimeter: Technical design report,” no. CERN-LHCC-96-41, 1996.

[18] ATLAS Collaboration, “Standalone Vertex Finding in the ATLAS Muon Spectrometer,” *JINST*, vol. 9, p. P02001. 22 p, Nov 2013.

[19] M. Cacciari, G. P. Salam, and G. Soyez, “The anti-k_T jet clustering algorithm,” *JHEP*, vol. 0804, no. LPTHE-07-03, p. 063, 2008.

[20] ATLAS Collaboration, “Muon reconstruction performance of the ATLAS detector in proton-proton collision data at $\sqrt{s} = 13$ TeV.” Eur. Phy. J. C. (2016) 76:292.

[21] ATLAS Collaboration, “Pile-up Correction in Missing Transverse Momentum Reconstruction in the ATLAS Experiment in Proton-Proton Collisions at $\sqrt{s}$ = 8TeV.” ATLAS-CONF-2014-019.

[22] ATLAS Collaboration, “Luminosity summary plots for 2015 data taking.” `https://twiki.cern.ch/twiki/bin/view/AtlasPublic/LuminosityPublicResultsRun2`.

[23] M. Baca *et al.*, “Search for Dark Matter in association with a Higgs boson decaying to b-quarks in pp collisions at $\sqrt{s} = 13$ TeV with the ATLAS detector,” Tech. Rep. ATL-COM-PHYS-2015-1399, CERN, Geneva, Nov 2015. (Unpublished).

[24] Ade, P. et al, “Planck 2013 results. I. Overview of products and scientific results,” *ASTRONOMY AND ASTROPHYSICS*, vol. 571, p. 37, 2014.

[25] ATLAS Collaboration, “Observation of a new particle in the search for the Standard Model Higgs boson with the ATLAS detector at the LHC,” *Phys. Lett. B*, vol. 716, no. CERN-PH-EP-2012-218, p. 1, 2012.

[26] CMS Collaboration, “Observation of a new boson at a mass of 125 GeV with the CMS experiment at the LHC,” *Phys. Lett. B*, vol. 716, no. CMS-HIG-12-028, CERN-PH-EP-2012-220, p. 30, 2012.

[27] D. Abercrombie *et al.*, “Dark Matter Benchmark Models for Early LHC Run-2 Searches: Report of the ATLAS/CMS Dark Matter Forum,” Tech. Rep. FERMILAB-PUB-15-282-CD, 2015.

[28] J. Abdallah *et al.*, “Simplified Models for Dark Matter Searches at the LHC,” *Phys. Dark Univ.*, vol. 9-10, no. FERMILAB-PUB-15-283-CD, CERN-PH-TH-2015-139, pp. 8–23, 2015.

[29] F. Englert and R. Brout, “Broken symmetry and the mass of the gauge vector mesons,” *Phys. Rev. Lett.*, vol. 13, pp. 321–323, 1964.

[30] P. Higgs, “Broken symmetries and the masses of gauge bosons,” *Phys. Rev. Lett.*, vol. 13, pp. 508–509, 1964.

[31] G. Guralnik, C. Hagen, and T. Kibble, “Global Conservation Laws and Massless Particles,” *Phys. Rev. Lett.* , vol. 13, p. 585, 1964.

[32] Y. Nambu and G. Jona-Lasinio, “Dynamical model of elementary particles based on an analogy with superconductivity. 1.,” *Phys. Rev.*, vol. 122, pp. 345–358, 1961.

[33] J. Goldstone, “Field theories with superconductor solutions,” *Nuovo Cim.*, vol. 19, pp. 154–164, 1961.

[34] J. Goldstone, A. Salam, and S. Weinberg, “Broken symmetries,” *Phys. Rev.*, vol. 127, pp. 965–970, 1962.

[35] H. Georgi, S. Glashow, M. Machacek, and D. V. Nanopoulos, “Higgs bosons from two gluon annihilation in proton proton collisions,” *Phys. Rev. Lett.*, vol. 40, p. 692, 1978.

[36] D. S. Akerib *et al.*, “The Large Underground Xenon (LUX) Experiment,” *Nucl. Instrum. Meth.*, vol. A704, pp. 111–126, 2013.

[37] J. McDonald, “Gauge singlet scalars as cold dark matter,” *Phys. Rev.*, vol. D50, no. IFM-13-93, pp. 3637–3649, 1994.

[38] C. P. Burgess, M. Pospelov, and T. ter Veldhuis, “The Minimal model of nonbaryonic dark matter: A Singlet scalar,” *Nucl. Phys.*, vol. B619, pp. 709–728, 2001.

[39] B. Patt and F. Wilczek, "Higgs-field portal into hidden sectors," Tech. Rep. MIT-CTP-3745, 2006.

[40] Y. G. Kim and K. Y. Lee, "The Minimal model of fermionic dark matter," *Phys. Rev.*, vol. D75, no. KAIST-TH-2006-04, p. 115012, 2007.

[41] J. March-Russell, S. M. West, D. Cumberbatch, and D. Hooper, "Heavy Dark Matter Through the Higgs Portal," *JHEP*, vol. 07, no. OUTP-07-20P, FERMILAB-PUB-08-014-A, p. 058, 2008.

[42] I. Low, P. Schwaller, G. Shaughnessy, and C. E. M. Wagner, "The dark side of the Higgs boson," *Phys. Rev.*, vol. D85, no. ANL-HEP-PR-11-64, MADPH-11-1576, p. 015009, 2012.

[43] L. Lopez-Honorez, T. Schwetz, and J. Zupan, "Higgs portal, fermionic dark matter, and a Standard Model like Higgs at 125 GeV," *Phys. Lett.*, vol. B716, no. UCHEP-12-01, pp. 179–185, 2012.

[44] G. Belanger, B. Dumont, U. Ellwanger, J. F. Gunion, and S. Kraml, "Status of invisible Higgs decays," *Phys. Lett.*, vol. B723, no. LAPTH-013-13, LPSC-13039, LPT-12-53, UCD-2013-2, pp. 340–347, 2013.

[45] M. Cirelli, E. Del Nobile, and P. Panci, "Tools for model-independent bounds in direct dark matter searches," *JCAP*, vol. 1310, no. CP3-ORIGINS-2013-014-DNRF90, DIAS-2013-14, SACLAY-T13-022, p. 019, 2013.

[46] L. Carpenter, A. DiFranzo, M. Mulhearn, C. Shimmin, S. Tulin, and D. Whiteson, "Mono-Higgs-boson: A new collider probe of dark matter," *Phys. Rev.*, vol. D89, no. 7, p. 3, 2014.

[47] ATLAS Collaboration, "Search for Dark Matter in Events with Missing Transverse Momentum and a Higgs Boson Decaying to Two Photons in pp Collisions at $\sqrt{s} = 8$ TeV with the ATLAS Detector," *Phys. Rev. Lett.*, vol. 115, no. 13, p. 131801, 2015.

[48] ATLAS Collaboration, "Search for new phenomena in final states with an energetic jet and large missing transverse momentum in pp collisions at $\sqrt{s} = 8$ TeV with the ATLAS detector," no. CERN-PH-EP-2014-299, 2015.

[49] CMS Collaboration, "Search for dark matter, extra dimensions, and unparticles in monojet events in proton-proton collisions at $\sqrt{s} = 8$ TeV," no. CMS-EXO-12-048, CERN-PH-EP-2014-164, 2014.

[50] ATLAS Collaboration, "Search for dark matter in events with heavy quarks and missing transverse momentum in pp collisions with the ATLAS detector," *Eur. Phys. J.*, vol. C75, no. 2, p. 92, 2015.

[51] ATLAS Collaboration, "Search for new phenomena in events with a photon and missing transverse momentum in pp collisions at $\sqrt{s} = 8$ TeV with the ATLAS detector," *Phys.Rev.*, vol. D91, no. 1, p. 012008, 2015.

[52] CMS Collaboration, “Search for new phenomena in monophoton final states in proton-proton collisions at $\sqrt{s} = 8$ TeV,” no. CMS-EXO-12-047, CERN-PH-EP-2014-253, 2014.

[53] ATLAS Collaboration, “Search for dark matter in events with a Z boson and missing transverse momentum in pp collisions at $\sqrt{s}$=8 TeV with the ATLAS detector,” *Phys.Rev.*, vol. D90, no. 1, p. 012004, 2014.

[54] ATLAS Collaboration, “Search for new particles in events with one lepton and missing transverse momentum in pp collisions at $\sqrt{s} = 8$ TeV with the ATLAS detector,” *JHEP*, vol. 1409, no. CERN-PH-EP-2014-139, p. 037, 2014.

[55] CMS Collaboration, “Search for physics beyond the standard model in final states with a lepton and missing transverse energy in proton-proton collisions at $\sqrt{s} = 8$ TeV,” no. CMS-EXO-12-060, CERN-PH-EP-2014-176, 2014.

[56] ATLAS Collaboration, “Search for dark matter in events with a hadronically decaying W or Z boson and missing transverse momentum in pp collisions at $\sqrt{s} = 8$ TeV with the ATLAS detector,” *Phys.Rev.Lett.*, vol. 112, no. 4, p. 041802, 2014.

[57] ATLAS Collaboration, “Search for invisible particles produced in association with single-top-quarks in proton-proton collisions at $\sqrt{s} = 8$ TeV with the ATLAS detector,” *Eur. Phys. J.*, vol. C75, no. 2, p. 79, 2015.

[58] ATLAS Collaboration, “The ATLAS Experiment at the CERN Large Hadron Collider,” *JINST*, vol. 3, pp. 1–5, 2008.

[59] CMS Collaboration, “The CMS Experiment at the CERN LHC,” *JINST*, vol. 3, pp. 1–5, 2008.

[60] LHCb Collaboration, “The LHCb Experiment at the LHC,” *JINST*, vol. 3, pp. 2–3, 2008.

[61] ALICE Collaboration, “The ALICE Experiment at the CERN LHC,” *JINST*, vol. 3, pp. 1–8, 2008.

[62] L. Evans and P. Bryant, “LHC Machine,” *JINST*, vol. 3, p. S08001, 2008.

[63] T. Barillari, “The atlas liquid argon hadronic end-cap calorimeter: construction and selected beam test results,” *Nucl.Phys.Proc.Suppl.*, vol. 150, pp. 102–105, 2006.

[64] “Letter of Intent for the Phase-I Upgrade of the ATLAS Experiment,” Tech. Rep. CERN-LHCC-2011-012. LHCC-I-020, CERN, Geneva, Nov 2011.

[65] ATLAS Collaboration, “Letter of Intent for the Phase-II Upgrade of the ATLAS Experiment,” Tech. Rep. CERN-LHCC-2012-022. LHCC-I-023, CERN, Geneva, Dec 2012.

[66] V. Cindro, "World Irradiation Facilities for Silicon Detectors," *PoS*, vol. Vertex2014, p. 026, 2014.

[67] "Innovative sensor technology - platinum temperature sensors." `http://www.farnell.com/datasheets/1728699.pdf`.

[68] "Norhof - ln2 microdosing system." `http://www.norhof.com/`.

[69] A. Buckley *et al.*, "Implementation of the ATLAS Run 2 event data model," Tech. Rep. ATL-SOFT-PROC-2015-003. 7, CERN, Geneva, May 2015.

[70] ATLAS Collaboration, "Measurement of the muon reconstruction performance of the ATLAS detector using 2011 and 2012 LHC proton-proton collision data," *Eur. Phys. J. C*, vol. 74, no. CERN-PH-EP-2014-151, p. 3130, 2014.

[71] G. Aad *et al.*, "Muon reconstruction performance of the ATLAS detector in proton-proton collision data at $\sqrt{s} = 13$ TeV," *The European Physical Journal C*, vol. 76, no. 5, p. 292, 2016.

[72] ATLAS Collaboration, "Electron efficiency measurements with the ATLAS detector using the 2012 LHC proton-proton collision data." ATLAS-CONF-2014-032.

[73] ATLAS Collaboration, "Electron reconstruction and identification efficiency measurements with the ATLAS detector using the 2011 LHC proton-proton collision data," *Eur.Phys.J.*, vol. C74, no. 7, p. 2941, 2014.

[74] ATLAS Collaboration, "Jet energy measurement and its systematic uncertainty in proton–proton collisions at $\sqrt{s} = 7$ TeV with the ATLAS detector," *Eur. Phys. J. C*, no. CERN-PH-EP-2013-222, p. 75:17, 2015.

[75] "Tagging and suppression of pileup jets with the ATLAS detector," Tech. Rep. ATLAS-CONF-2014-018, CERN, Geneva, May 2014.

[76] D. Adams *et al.*, "Recommendations of the Physics Objects and Analysis Harmonisation Study Groups 2014," no. ATL-COM-PHYS-2014-451, 2014. (Unpublished).

[77] "Commissioning of the ATLAS b-tagging algorithms using $t\bar{t}$ events in early Run-2 data," Tech. Rep. ATL-PHYS-PUB-2015-039, CERN, Geneva, Aug 2015.

[78] ATLAS Collaboration, "Performance of b-Jet Identification in the ATLAS Experiment," *JINST*, vol. 11, no. 04, p. P04008, 2016.

[79] ATLAS Collaboration, "Performance of jet substructure techniques for large-R jets in proton–proton collisions at $\sqrt{s} = 7$ TeV using the ATLAS detector," *JHEP*, vol. 1309, no. CERN-PH-EP-2013-069, p. 076, 2013.

[80] M. Cacciari, C. P. Salam and G. Soyez, "The anti-k_t jet clustering algorithm," *JHEP*, vol. 04, p. 063, 2008.

[81] D. Krohn, J. Thaler, and L.-T. Wang, “Jet Trimming,” *JHEP*, vol. 02, p. 084, 2010.

[82] ATLAS Collaboration, “Performance of Missing Transverse Momentum Reconstruction in ATLAS studied in Proton-Proton Collisions recorded in 2012 at 8 TeV.” ATLAS-CONF-2013-082.

[83] M. Aaboud *et al.*, “Jet energy scale measurements and their systematic uncertainties in proton-proton collisions at $\sqrt{s} = 13$ TeV with the ATLAS detector,” *Phys. Rev.*, vol. D96, no. 7, p. 072002, 2017.

[84] H.-L. Lai *et al.*, “New parton distributions for collider physics,” *Phys. Rev. D*, vol. 82, no. MSUHEP-100707, SMU-HEP-10-10, p. 074024, 2010.

[85] T. Gleisberg *et al.*, “Event generation with SHERPA 1.1,” *JHEP*, vol. 0902, no. FERMILAB-PUB-08-477-T, SLAC-PUB-13420, ZU-TH-17-08, DCPT-08-138, IPPP-08-69, EDINBURGH-2008-30, MCNET-08-14, p. 007, 2009.

[86] K. Melnikov and F. Petriello, “Electroweak gauge boson production at hadron colliders through $\mathcal{O}(\alpha_s^2)$,” *Phys. Rev. D*, vol. 74, no. UH-511-1092-06, p. 114017, 2006.

[87] T. Sjostrand, S. Mrenna, and P. Z. Skands, “PYTHIA 6.4 Physics and Manual,” *JHEP*, vol. 0605, no. FERMILAB-PUB-06-052-CD-T, LU-TP-06-13, p. 026, 2006.

[88] M. Czakon, P. Fiedler, and A. Mitov, “Total Top-Quark Pair-Production Cross Section at Hadron Colliders Through $O(a\frac{4}{S})$,” *Phys. Rev. Lett.*, vol. 110, no. CERN-PH-TH-2013-056, TTK-13-08, p. 252004, 2013.

[89] N. Kidonakis, “Next-to-next-to-leading-order collinear and soft gluon corrections for t-channel single top quark production,” *Phys. Rev. D*, vol. 83, p. 091503, 2011.

[90] N. Kidonakis, “NNLL resummation for s-channel single top quark production,” *Phys. Rev. D*, vol. 81, p. 054028, 2010.

[91] N. Kidonakis, “Two-loop soft anomalous dimensions for single top quark associated production with a W- or H-,” *Phys. Rev. D*, vol. 82, p. 054018, 2010.

[92] “EvtGen Project - Documentation.” http://evtgen.warwick.ac.uk/docs/.

[93] “ATLAS Run 1 Pythia8 tunes,” Tech. Rep. ATL-PHYS-PUB-2014-021, CERN, Geneva, Nov 2014.

[94] ATLAS Collaboration, “Selection of jets produced in 13TeV proton-proton collisions with the ATLAS detector,” Tech. Rep. ATLAS-CONF-2015-029, 2015.

[95] Carlo Pandini, “Hbb resolved 0 lepton transition update.” Presentation `https://indico.cern.ch/event/464086/contribution/1/attachments/1212157/1768328/HbbResolved_0lepton_transition_UPDATE_2015_01_15_v3.pdf`. (Unpublished).

[96] “Electron and photon energy calibration with the ATLAS detector using data collected in 2015 at $\sqrt{s} = 13$ TeV,” Tech. Rep. ATL-PHYS-PUB-2016-015, CERN, Geneva, Aug 2016. (Unpublished).

[97] ATLAS Collaboration, “Muon reconstruction performance of the ATLAS detector in proton–proton collision data at $\sqrt{s}$=13 TeV,” no. CERN-EP-2016-033, 2016.

[98] R. D. Ball *et al.*, “Parton distributions with LHC data,” *Nucl. Phys.*, vol. B867, no. EDINBURGH-2012-08, IFUM-FT-997, FR-PHENO-2012-014, RWTH-TTK-12-25, CERN-PH-TH-2012-037, SFB-CPP-12-47, pp. 244–289, 2013.

[99] A. Martin, W. Stirling, R. Thorne, and G. Watt, “Parton distributions for the LHC,” *Eur. Phys. J. C*, vol. 63, no. IPPP-08-95, DCPT-08-190, CAVENDISH-HEP-08-16, p. 189, 2009.

[100] J. Pumplin, D. Stump, J. Huston, H. Lai, P. M. Nadolsky, *et al.*, “New generation of parton distributions with uncertainties from global QCD analysis,” *JHEP*, vol. 0207, no. MSU-HEP-011101, p. 012, 2002.

[101] ATLAS Collaboration, “Search for the $b\bar{b}$ decay of the Standard Model Higgs boson in associated $(W/Z)H$ production with the ATLAS detector,” *JHEP*, vol. 1501, no. CERN-PH-EP-2014-214, p. 069, 2015.

[102] G. Cowan, K. Cranmer, E. Gross, and O. Vitells, “Asymptotic formulae for likelihood-based tests of new physics,” *Eur. Phys. J. C*, vol. 71, p. 1554, 2011.

[103] K. Cranmer, G. Lewis, L. Moneta, A. Shibata, and W. Verkerke, “HistFactory: A tool for creating statistical models for use with RooFit and RooStats,” no. CERN-OPEN-2012-016, 2012.

[104] G. Aad *et al.*, “Search for the $b\bar{b}$ decay of the Standard Model Higgs boson in associated $(W/Z)H$ production with the ATLAS detector. Search for the $b\bar{b}$ decay of the Standard Model Higgs boson in associated $(W/Z)H$ production with the ATLAS detector,” *JHEP*, vol. 01, p. 45, Sep 2014.

[105] G. Busoni *et al.*, “Recommendations on presenting LHC searches for missing transverse energy signals using simplified s-channel models of dark matter,” no. CERN-LPCC-2016-001, FERMILAB-FN-1009-CD, 2016.

[106] A. L. Read, “Presentation of search results: the cl s technique,” *Journal of Physics G: Nuclear and Particle Physics*, vol. 28, no. 10, p. 2693, 2002.

[107] S. Meehan *et al.*, “Search for Dark Matter Produced in Association with a Higgs Boson Decaying to $b\bar{b}$ at $\sqrt{s} = 13$ TeV with the ATLAS Detector,” Tech. Rep. ATL-COM-PHYS-2016-1484, CERN, Geneva, Oct 2016. (Unpublished).

APPENDIX A

Cooling Equation Derivation

The transfer of heat into a system can be modelled exponentially. The rate of energy flowing into the sensor is equal to that of the power transferred via the beam/heating element minus any energy lost through cooling. The cooling can be modelled by Newton's Law of Cooling (Equation A.1).

$$\frac{dQ}{dt} = h\Delta T = h(T - T_A) \tag{A.1}$$

where Q is the heat energy, t is time, h is a cooling coefficient, T is temperature and T_A is ambient temperature (with ΔT defined as (T - T_A)). The differential describes heat lost over time. We can then define Q_{IN} ($= mC\Delta T$, where m = mass of sensor and C = specific heat capacity of silicon) as the over all energy entering the sensor. It follows that:

$$\dot{Q_{IN}} = \tfrac{dQ_{IN}}{dt} = mC\tfrac{dT}{dt} = P - h(T - T_A)$$

$$\tfrac{mC}{h}\tfrac{dT}{dt} = -(T - T_A) + \tfrac{P}{h} = -T + T_A + \tfrac{P}{k}$$

$$\tfrac{dT}{-T+\frac{P}{h}+T_A} = \tfrac{h}{mC}dt$$

$$\int \tfrac{dT}{-T+\frac{P}{h}+T_A} = \int \tfrac{h}{mC}dt$$

$$-log\left(-T + \tfrac{P}{h} + T_A\right) = t\tfrac{h}{mC} + const$$

where P is the power of the heating element. It is known that at t = 0, T = T$_A$. Therefore:

$$-log\left(\tfrac{P}{h}\right) = const$$

$$-log\left(-T + \tfrac{P}{h} + T_A\right) + log\left(\tfrac{P}{h}\right) = t\tfrac{h}{mC}$$

$$-log\left(\tfrac{-T+\frac{P}{h}+T_A}{\frac{P}{h}}\right) = t\tfrac{h}{mC}$$

$$-T + \tfrac{P}{h} + T_A = \tfrac{P}{h}e^{-t\frac{h}{mC}}$$

From here, it is possible to model the temperature at any given time, with the following:

$$T = T_A + \frac{P}{h}\left(1 - e^{-t\frac{h}{mC}}\right) \tag{A.2}$$

APPENDIX B

Additional Pre-Fit Plots

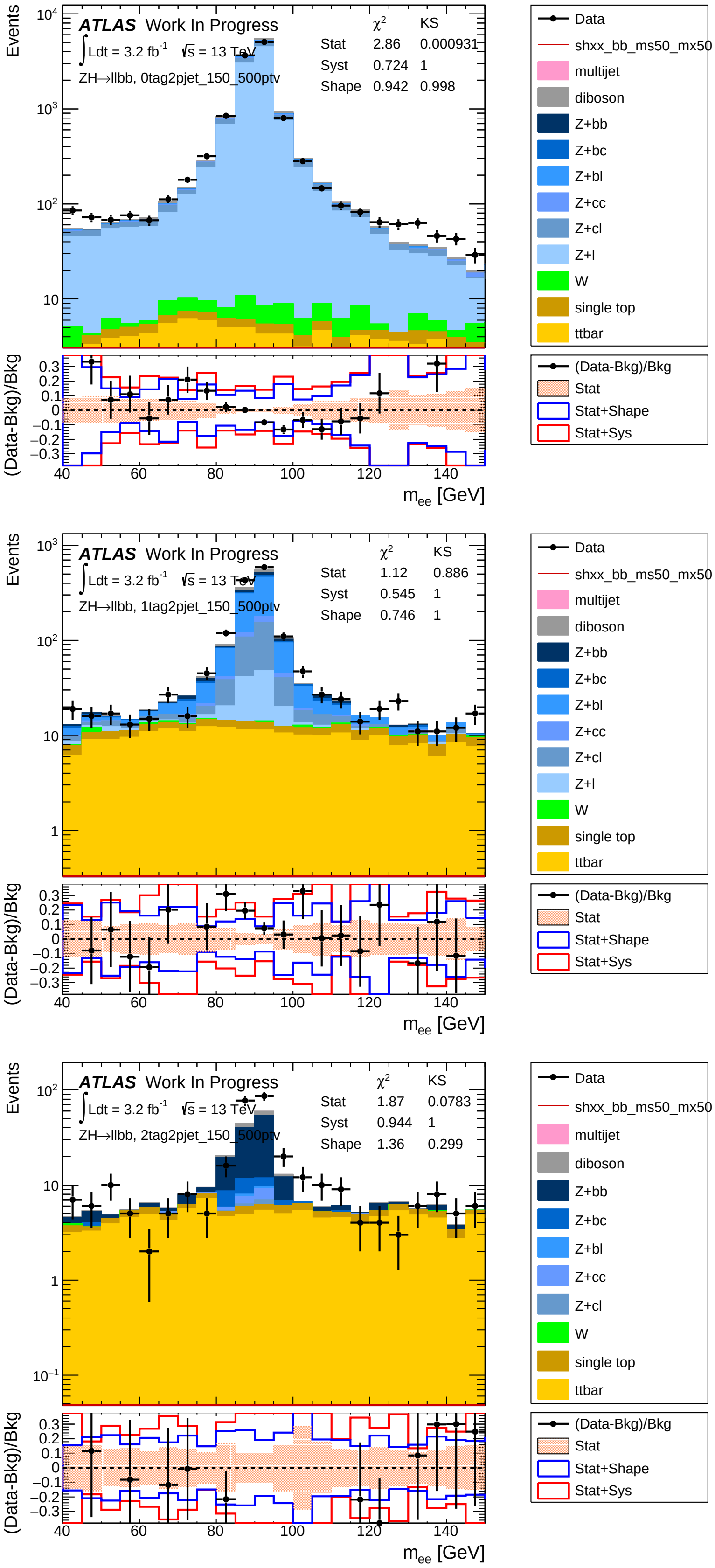

Figure B.1: The invariant mass of the two electrons for the 2 lepton resolved analysis control region for (a) 0, (b) 1 and (c) 2 tag events respectively.

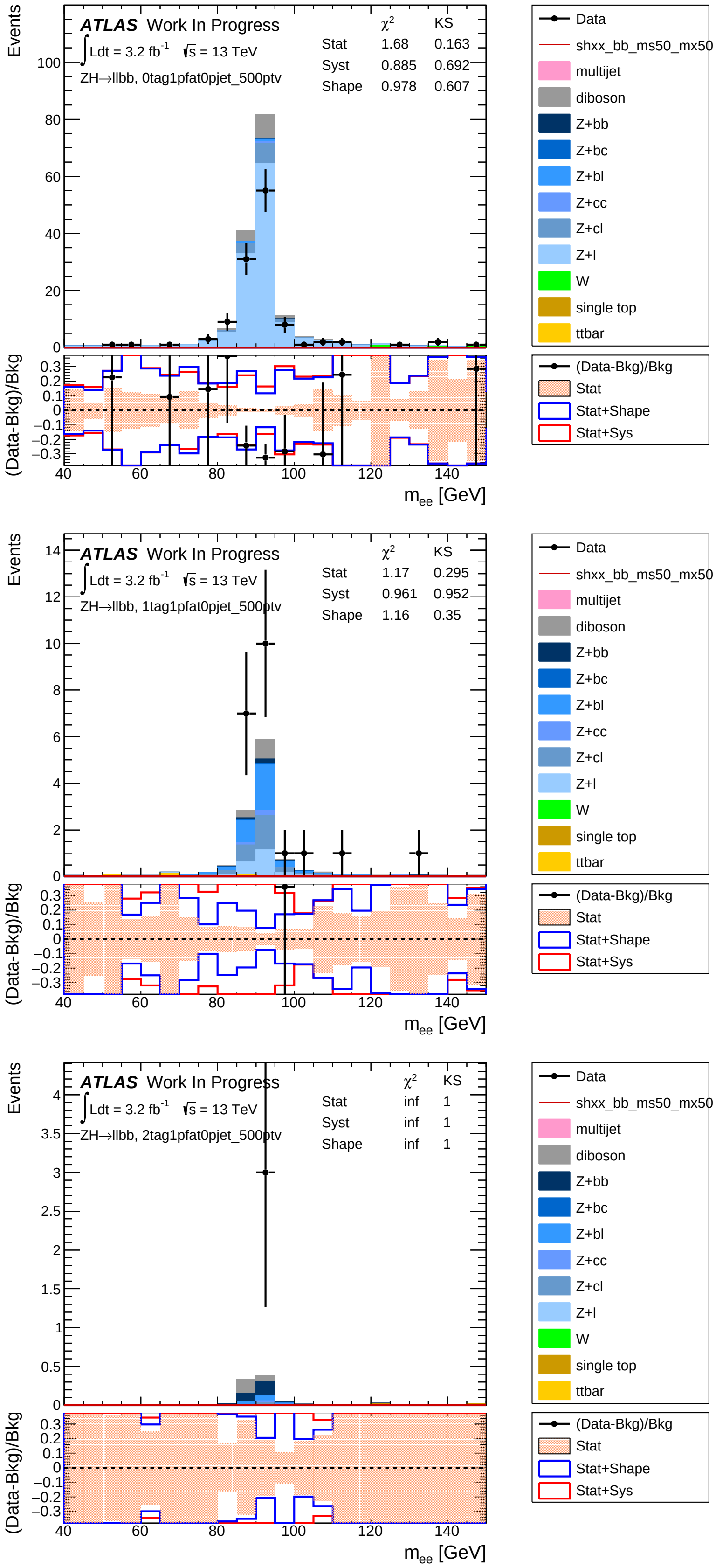

Figure B.2: The invariant mass of the two electrons for the 2 lepton merged analysis control region for (a) 0, (b) 1 and (c) 2 tag events respectively.

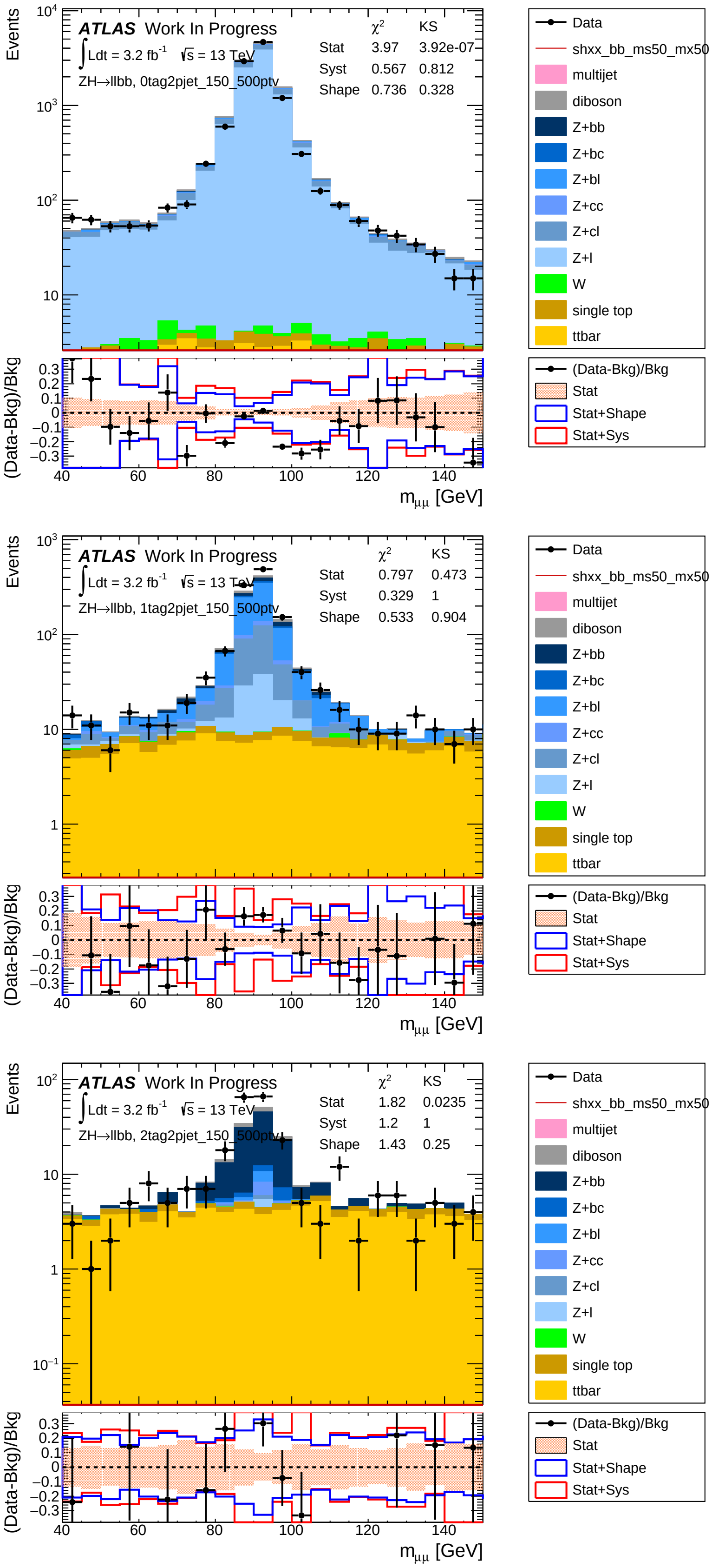

Figure B.3: The invariant mass of the two muons for the 2 lepton resolved analysis control region for (a) 0, (b) 1 and (c) 2 tag events respectively.

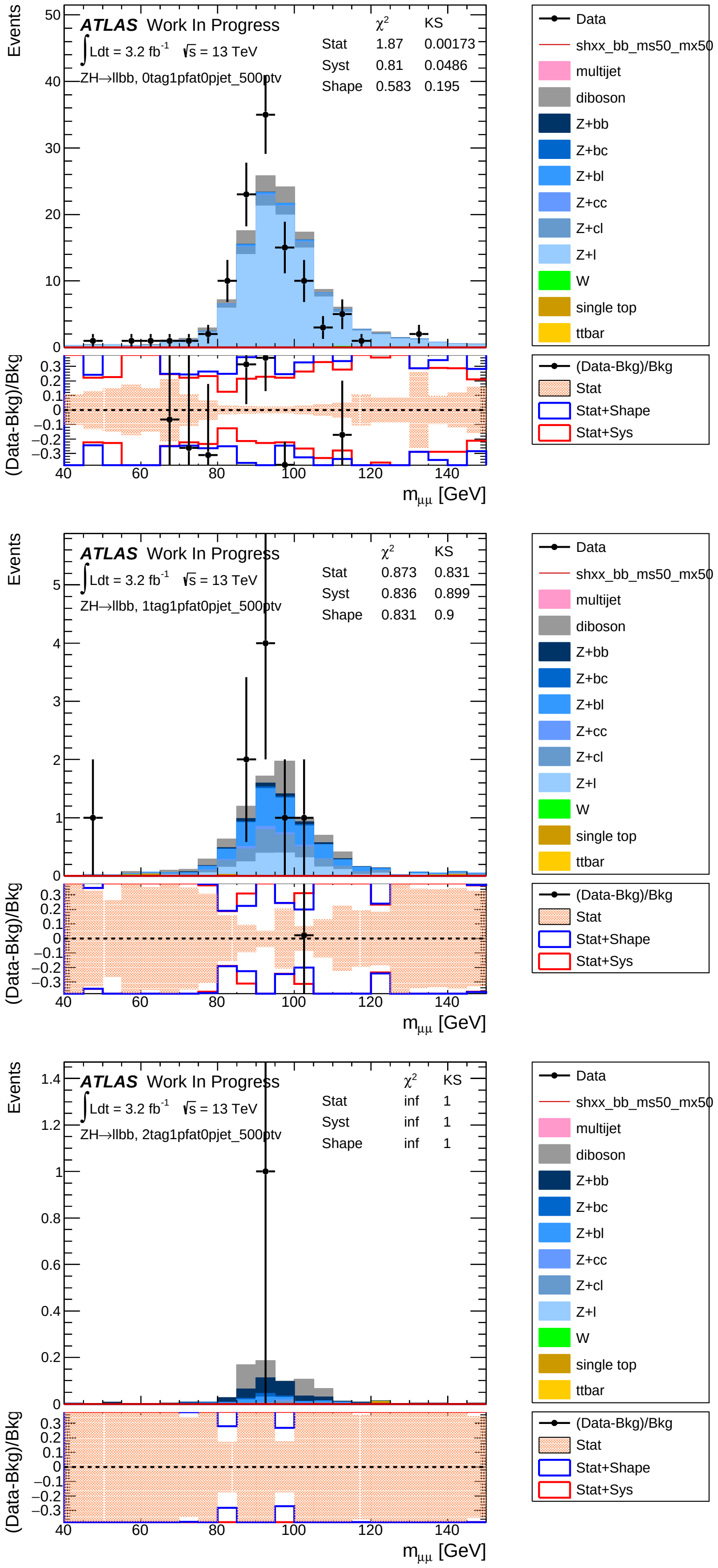

Figure B.4: The invariant mass of the two muons for the 2 lepton merged analysis control region for (a) 0, (b) 1 and (c) 2 tag events respectively.

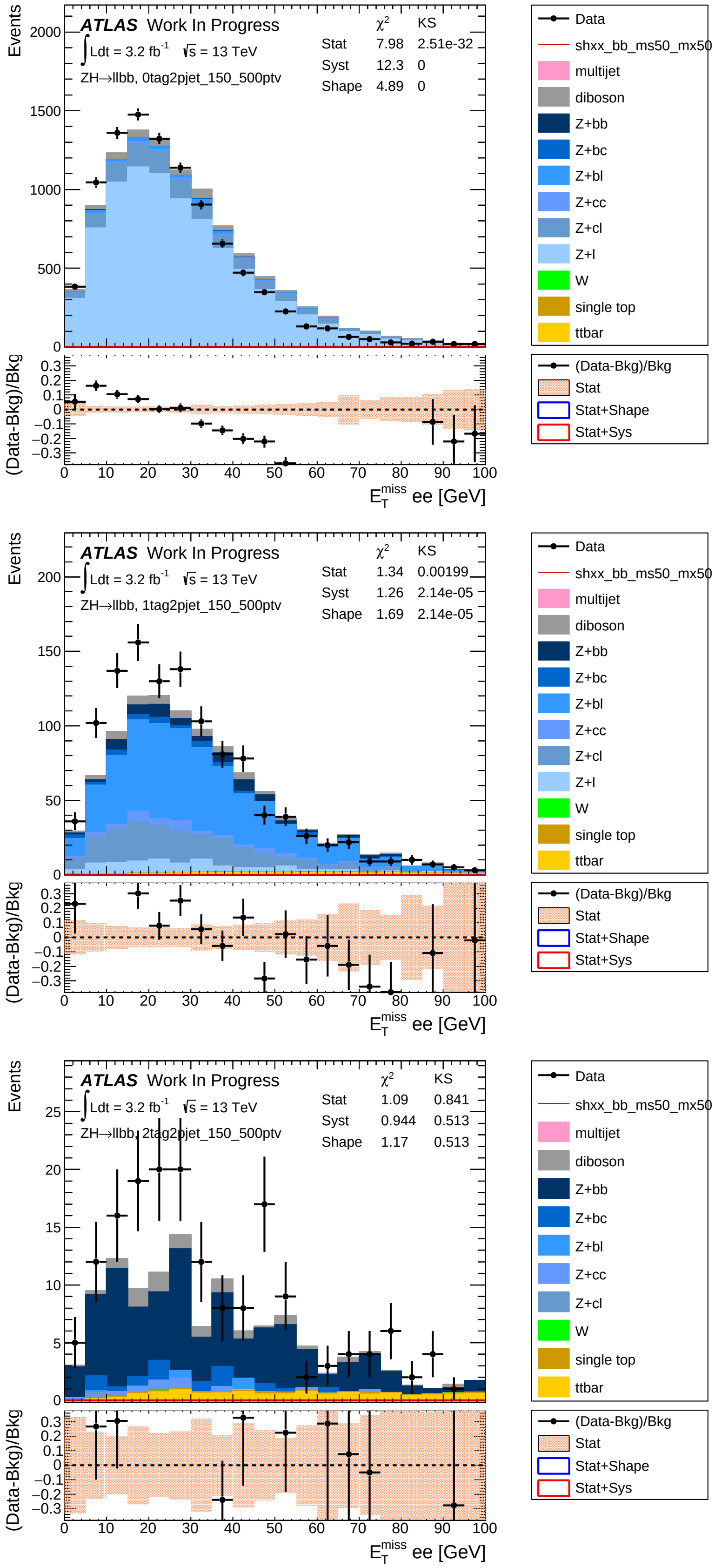

Figure B.5: The MET for the 2 lepton resolved electron analysis control region for (a) 0, (b) 1 and (c) 2 tag events respectively.

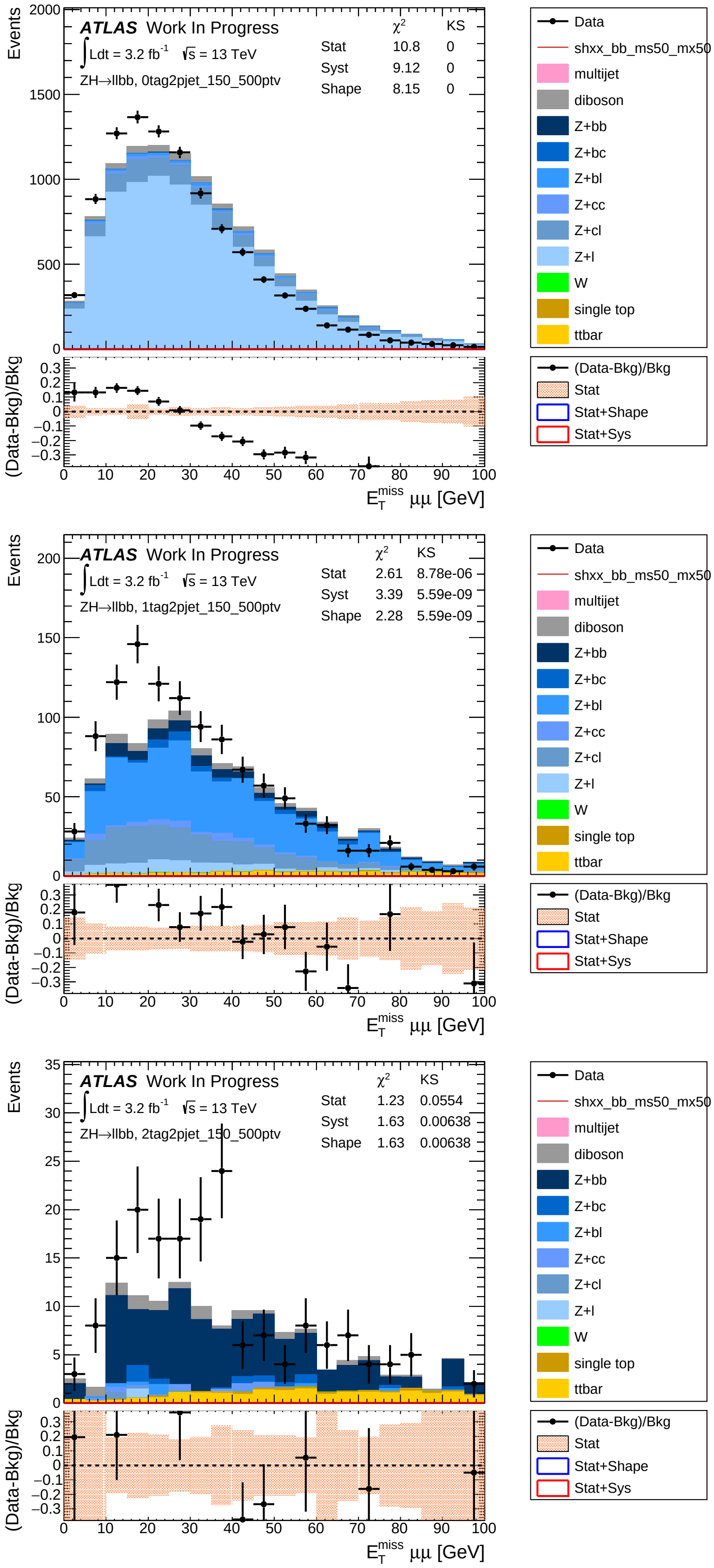

Figure B.6: The MET for the 2 lepton resolved muon analysis control region for (a) 0, (b) 1 and (c) 2 tag events respectively.

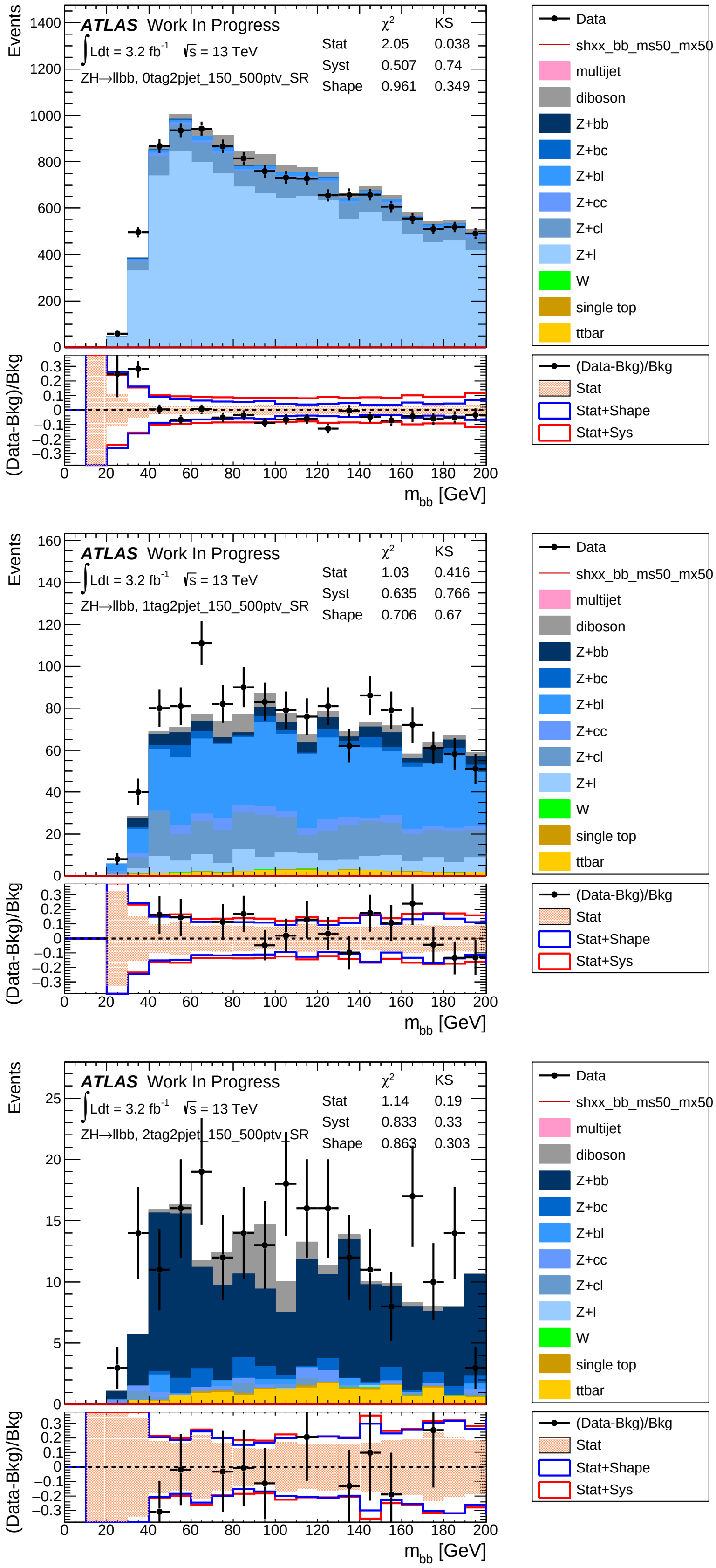

Figure B.7: The invariant mass of the two signal jets for the 2 lepton resolved analysis control region for (a) 0, (b) 1 and (c) 2 tag events respectively.

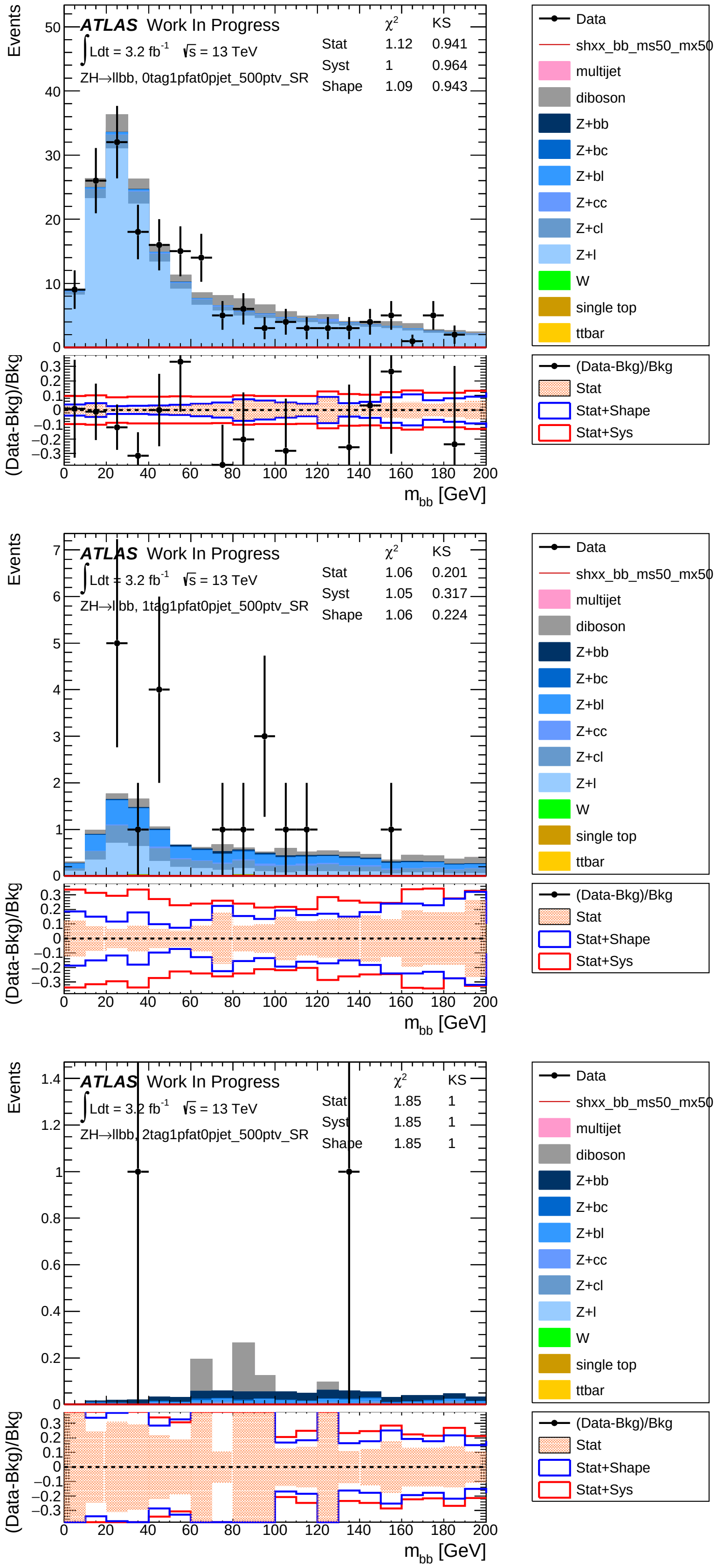

Figure B.8: The invariant mass of the two signal jets for the 2 lepton merged analysis control region for (a) 0, (b) 1 and (c) 2 tag events respectively.

APPENDIX C

Additional Background Systematics Plots

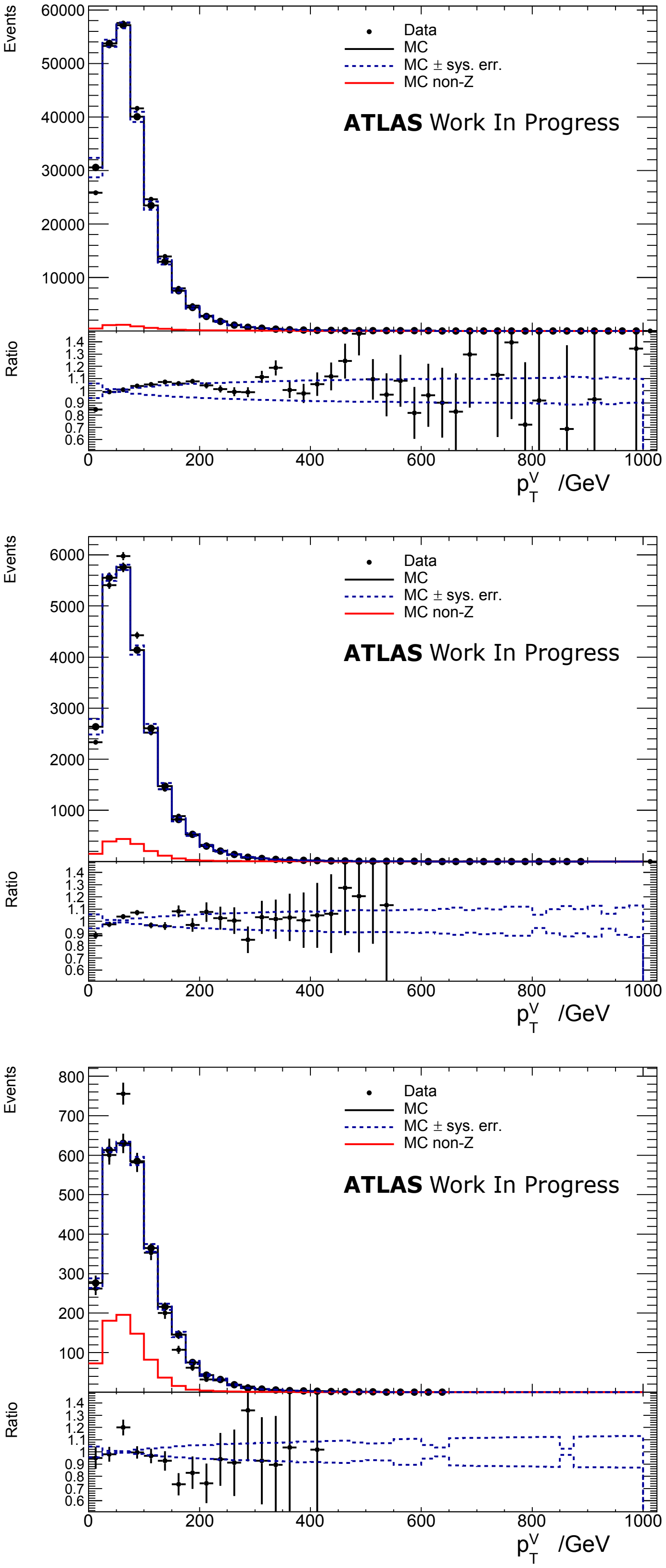

Figure C.1: The transverse momentum of the Z p_T^Z for the 2 lepton control region for 0, 1 and 2 tags.

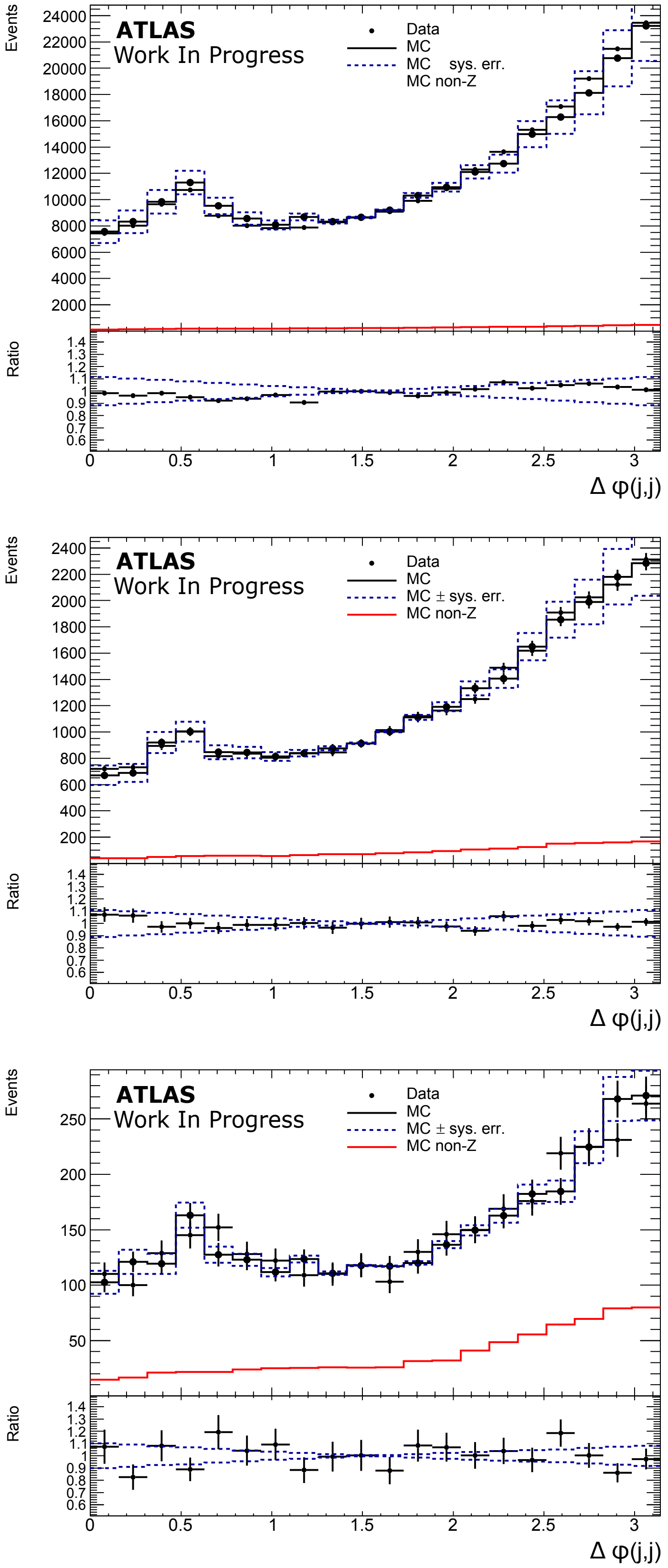

Figure C.2: The $\Delta\phi_{jj}$ between the two signal jets for the 2 lepton control region for 0, 1 and 2 tags.

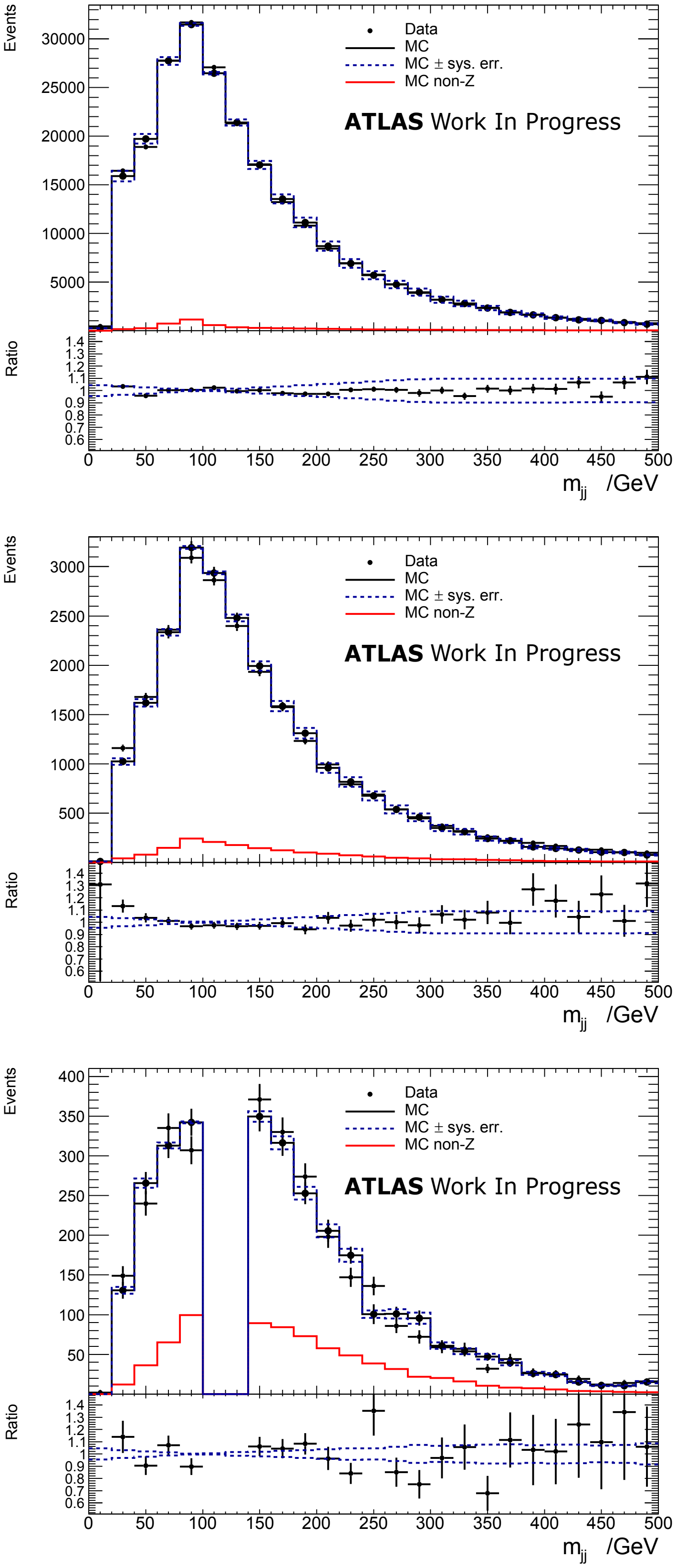

Figure C.3: The m_{jj} distribution for the 2 lepton control region for 0, 1 and 2 tags.

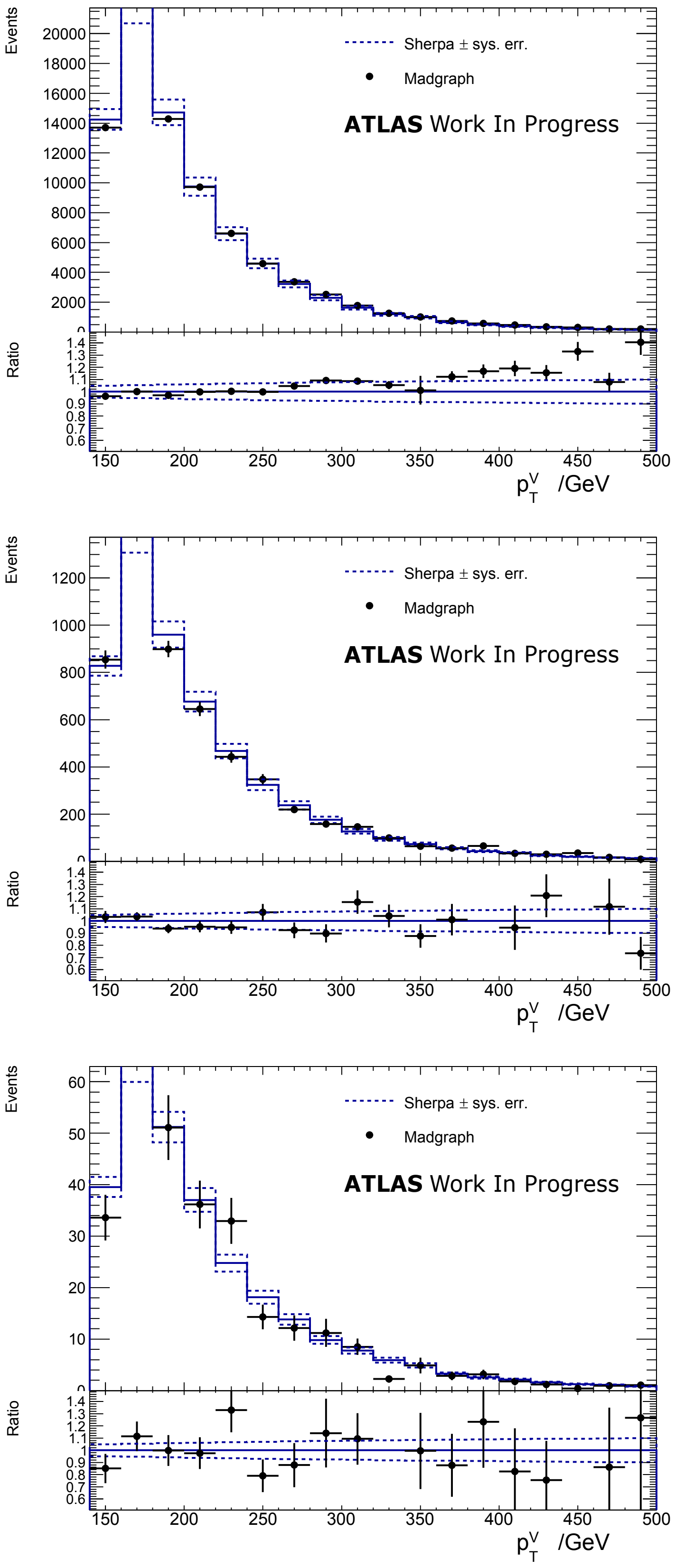

Figure C.4: Comparison of the W+jets prediction from MadGraph with that from Sherpa as a function of the transverse momentum of the W (p_T^W) for the 1 lepton control region and 0, 1 and 2 tags.

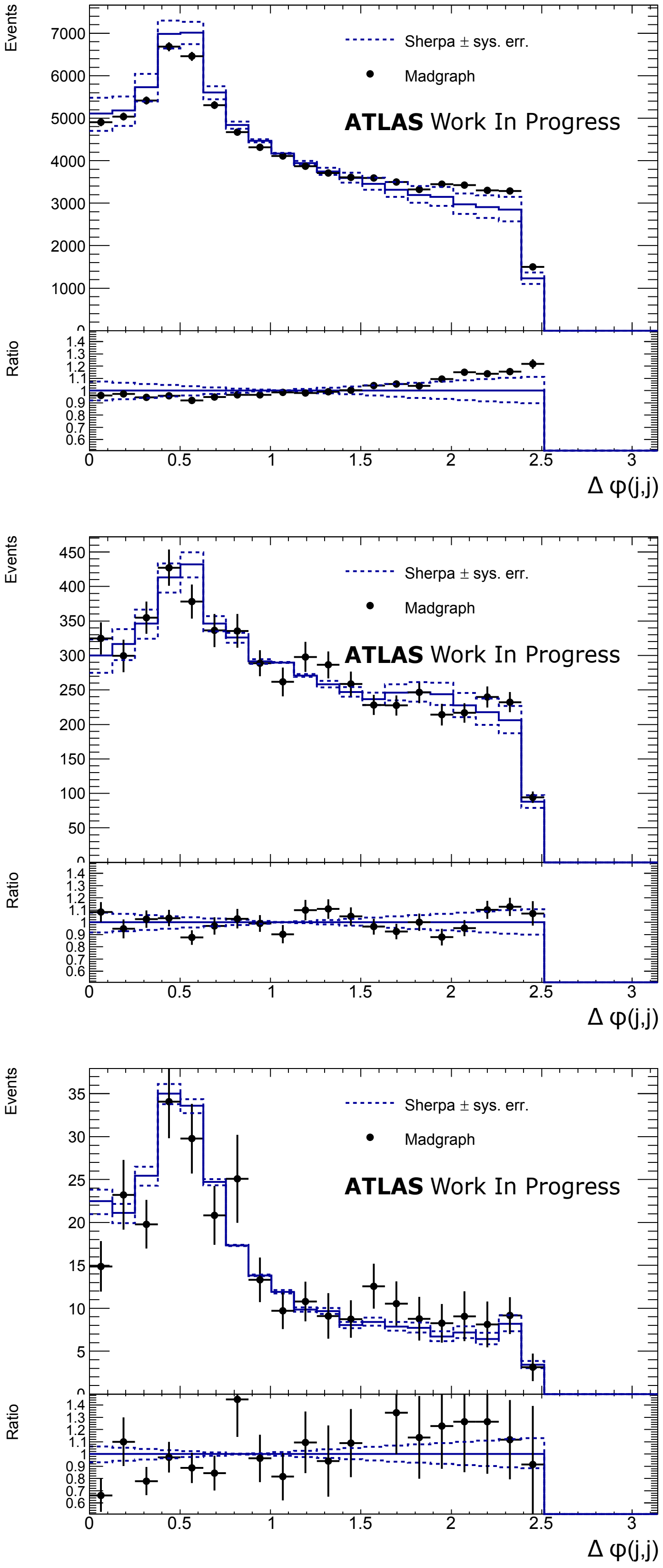

Figure C.5: Comparison of the W+jets prediction from MadGraph with that from Sherpa as a function of the $\Delta\phi_{jj}$ between the two signal jets for the 1 lepton control region and 0, 1 and 2 tags.

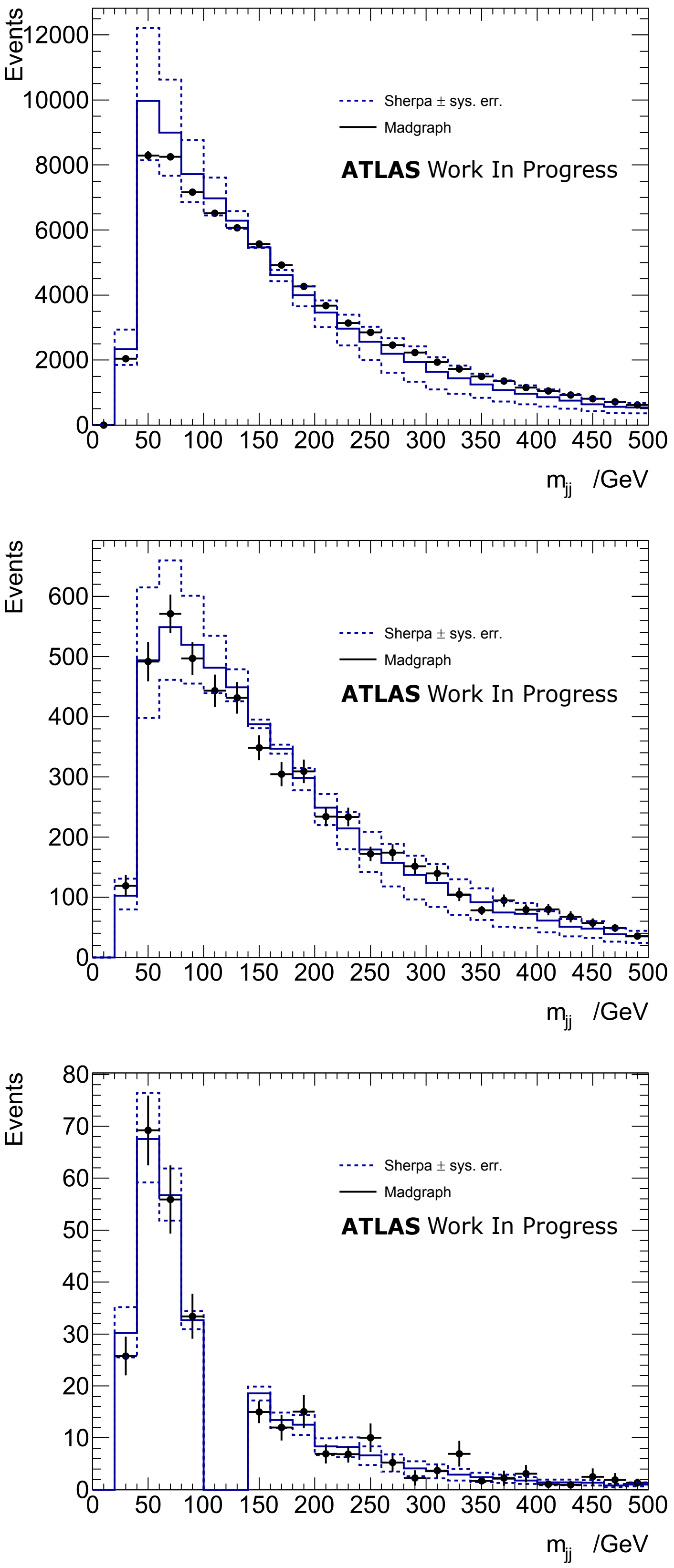

Figure C.6: Comparison of the W+jets prediction from MadGraph with that from Sherpa as a function of m_{jj} for the 1 lepton control region and 0, 1 and 2 tags.

APPENDIX D

Additional Limit Plots

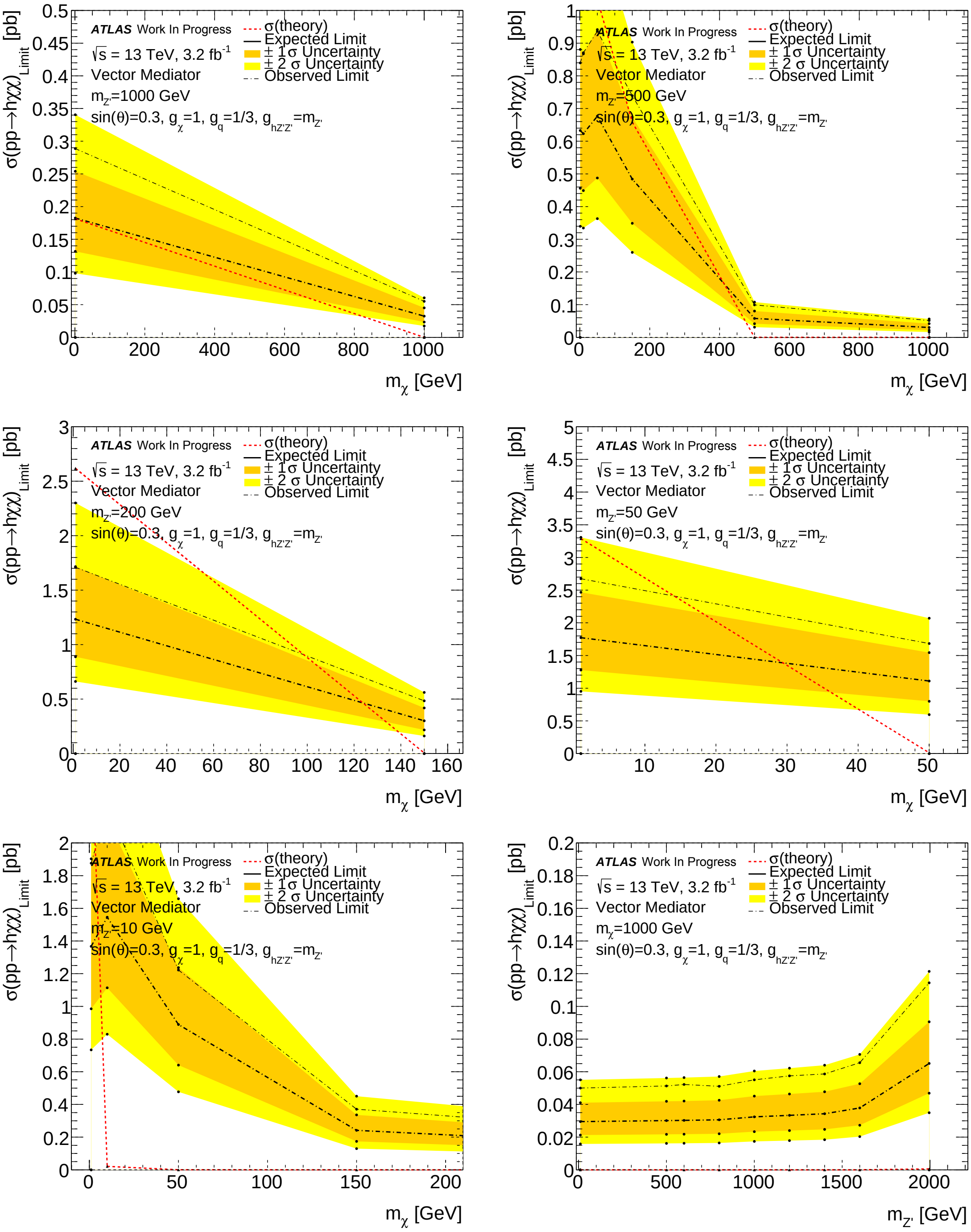

Figure D.1: Cross section limits determined for the vector simplified model shown in linear scale. Continued on next page.

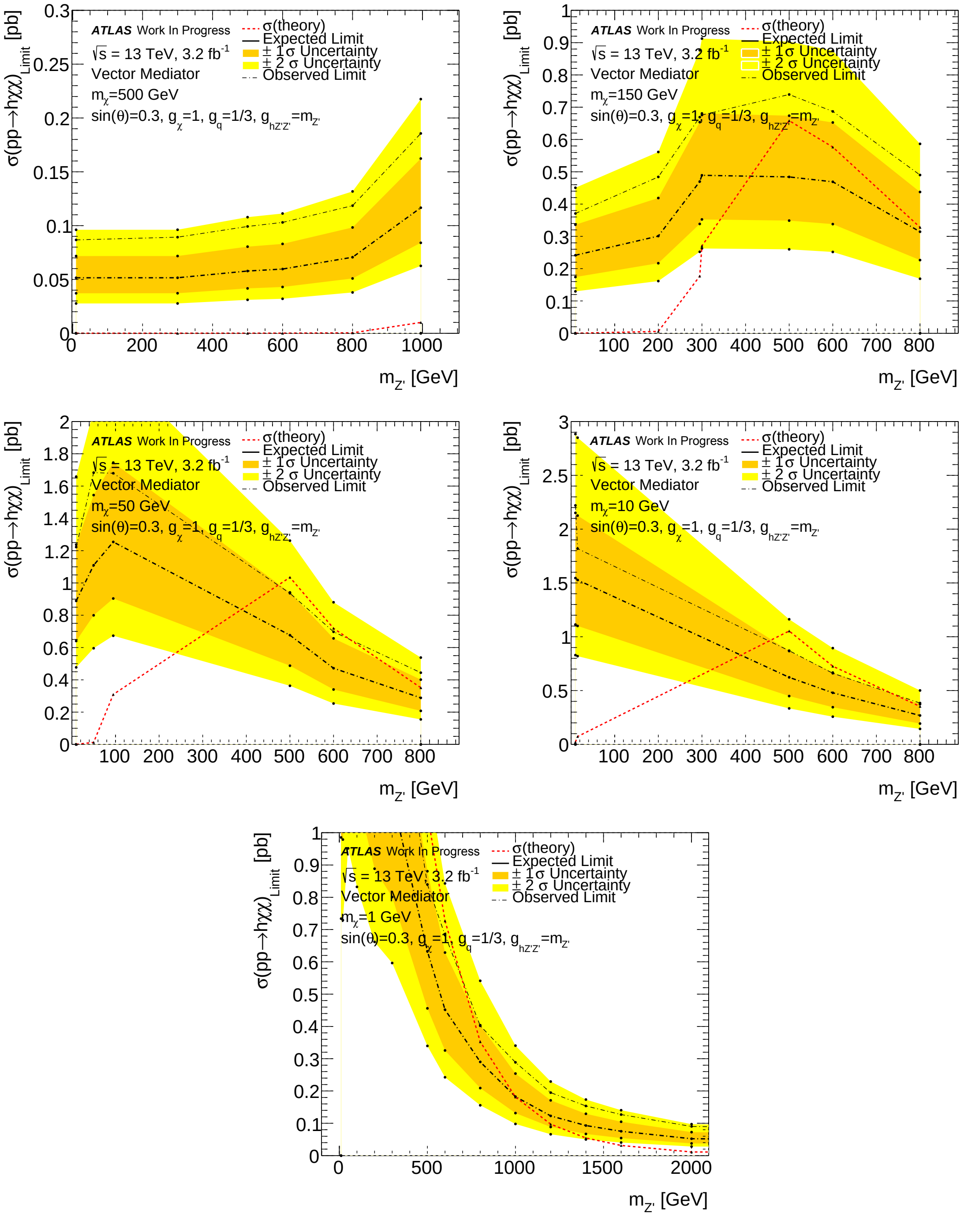

Figure D.2: Cross section limits determined for the vector simplified model shown in linear scale. Continued from previous page.

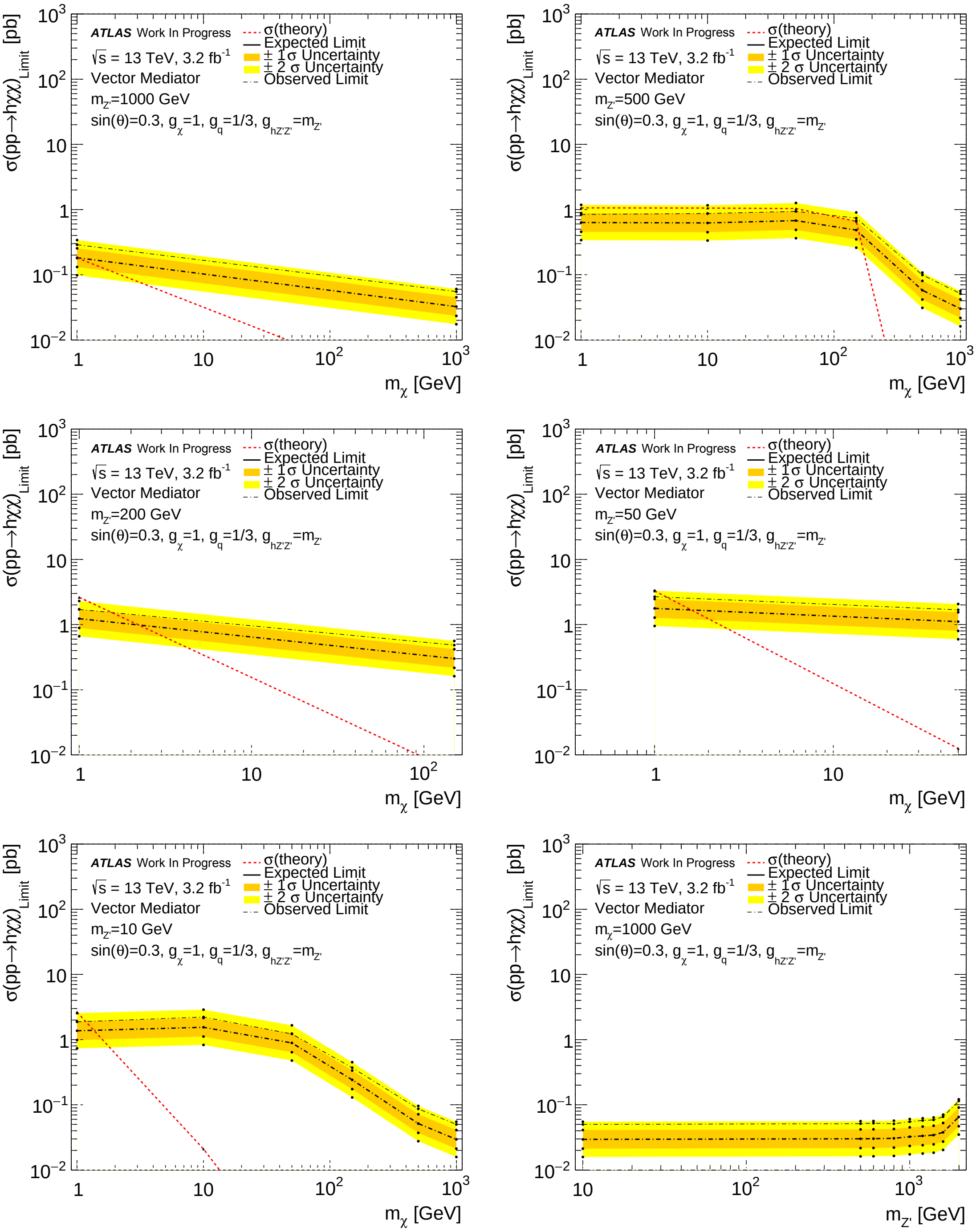

Figure D.3: Cross section limits determined for the vector simplified model shown in logarithmic scale. Continued on next page.

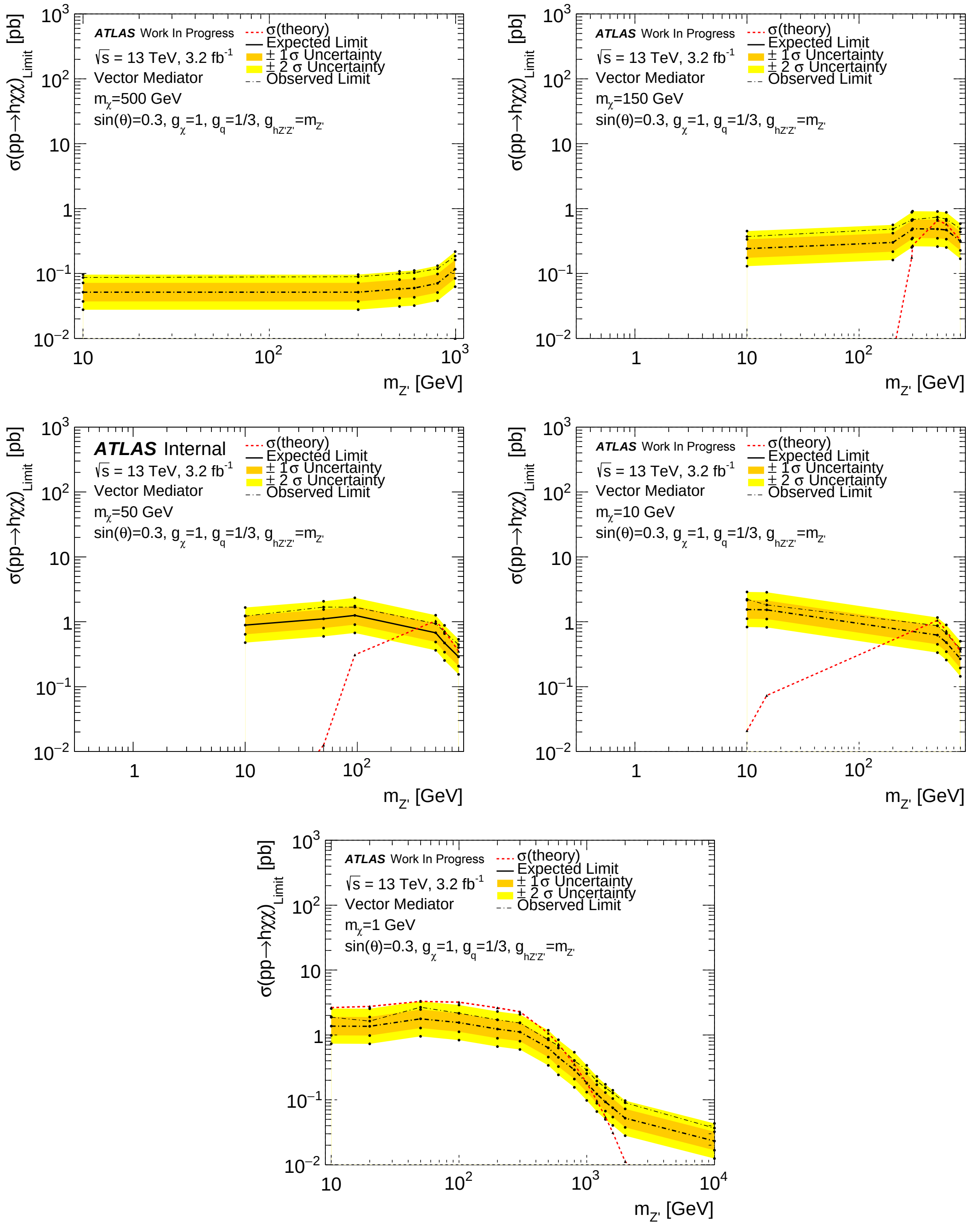

Figure D.4: Cross section limits determined for the vector simplified model shown in logarithmic scale. Continued from previous page.

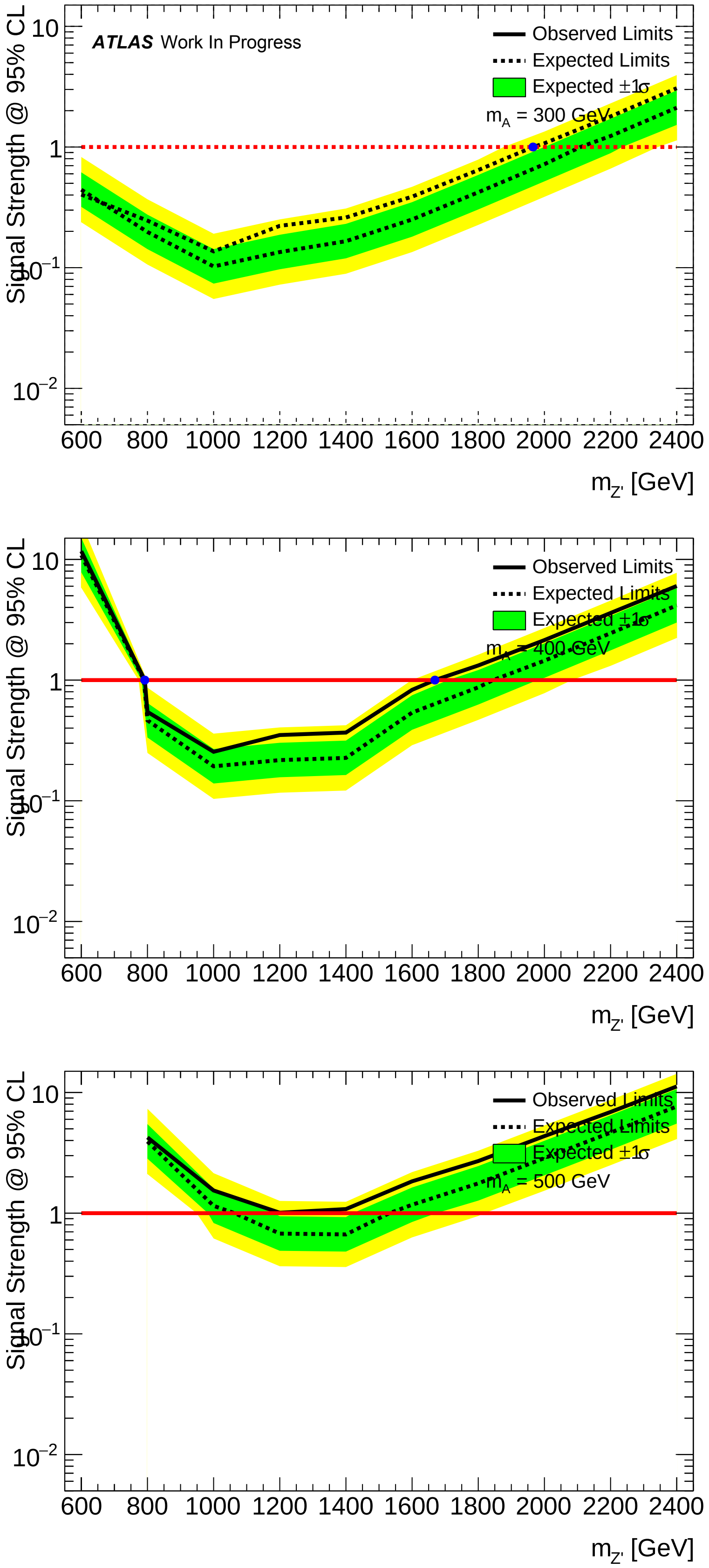

Figure D.5: Cross section limits determined for the Z'-2HDM model shown in logarithmic scale. Continued on next page.

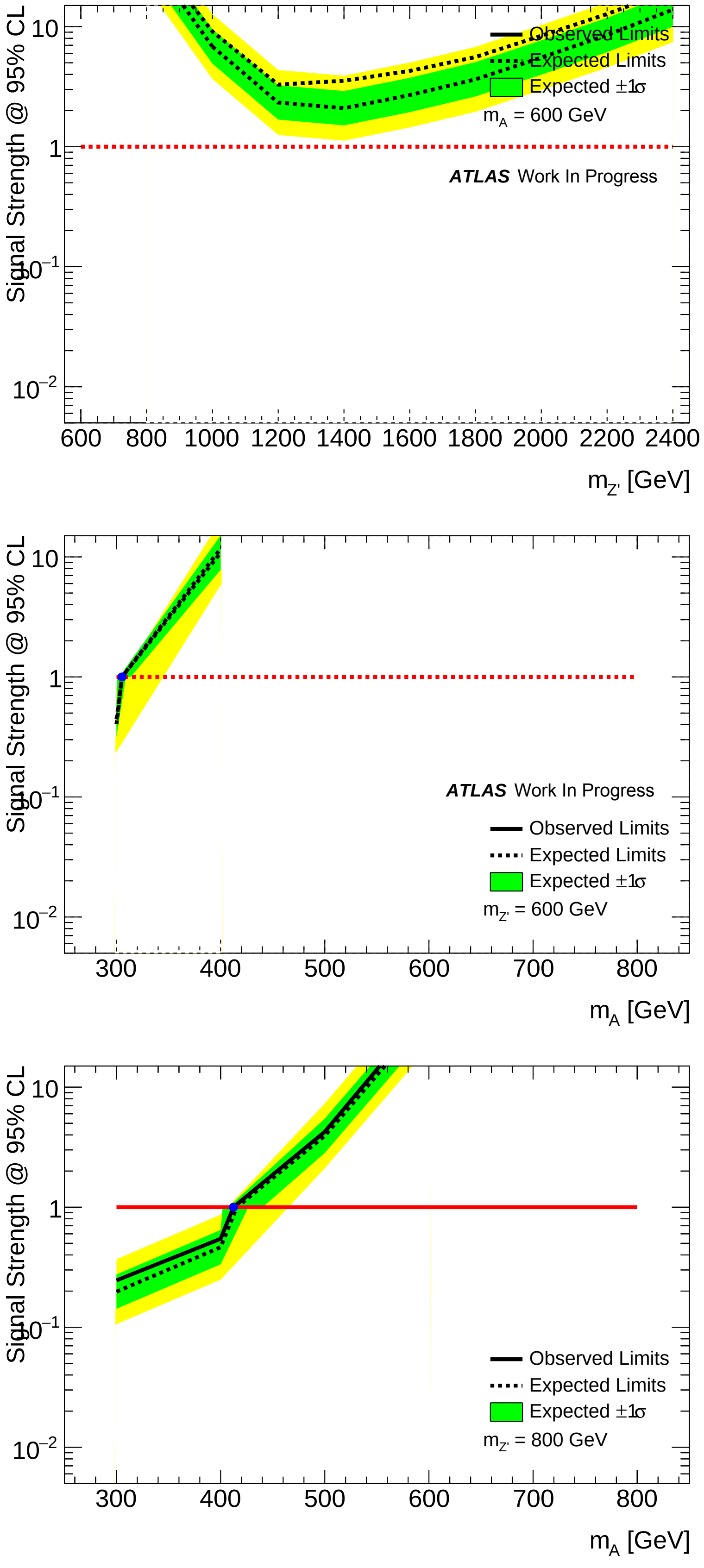

Figure D.6: Cross section limits determined for the Z'-2HDM model shown in logarithmic scale. Continued on next page.

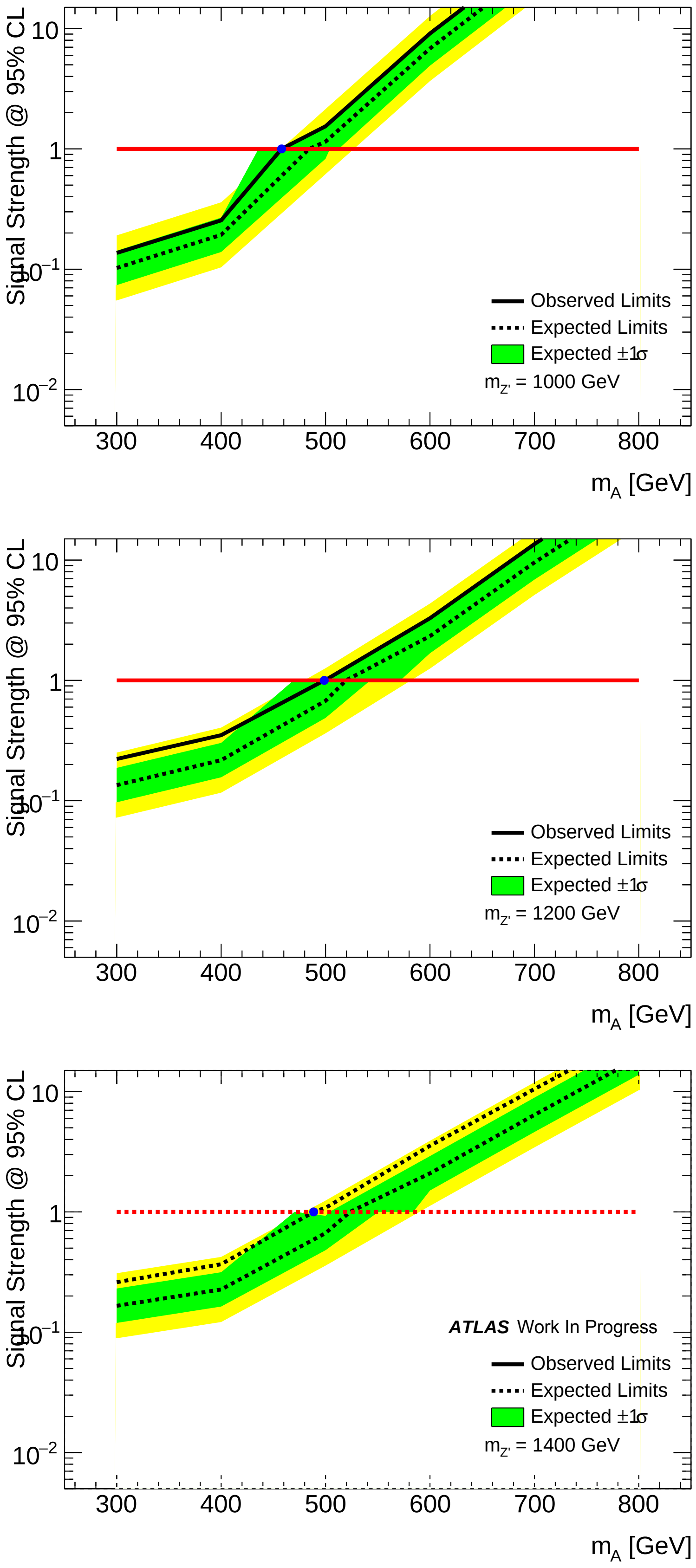

Figure D.7: Cross section limits determined for the Z'-2HDM model shown in logarithmic scale. Continued from previous page.